# Habilitationsschrift

# Efficiently Measuring Wireless Communication Systems

ausgeführt zum Zwecke der Erlangung

der Lehrbefugnis für das Fach

## Wireless Communications

eingereicht an der Technischen Universität Wien

Fakultät für Elektrotechnik und Informationstechnik

von

**Mag. Dipl.-Ing. Dr. Sebastian Caban**

geboren am 13. März 1980 in Wien

Wien, im Mai 2021

I certify that I have written this thesis on my own
and have cited the work done by other authors appropriately.
This thesis is cumulative. So the work reported in this thesis is not new
but published already in the publications cited.

Sebastian Caban
Vienna, May 1, 2021

# Abstract

This habilitation thesis is a collection of journal articles and conference papers published after my Ph.D. thesis in 2009. These 40 manuscripts summarize my journey to deeply understand the fundamentals of wireless data transmission. Inspired by a lecture of Lord Kelvin in 1883, I always measured what I was writing about throughout my journey, because "when you cannot measure it, when you cannot express it in numbers, your knowledge is of a meagre and unsatisfactory kind; it may be the beginning of knowledge, but you have scarcely, in your thoughts, advanced to the stage of science, whatever the matter may be."

Like my journey, this thesis starts with a chapter on how to design measurements and the apparatus therefore needed. The challenges we thereby faced were manifold, ranging from buying and setting up reusable hardware to developing new metrics to judge the repeatability of consecutive transmissions.

The next chapter is devoted to the transmission of data in *static* scenarios. We show how to control for a variable such as antenna-position to measure and model the effects of antenna-spacing. We carry out channel sounding experiments at 2.5 GHz and 60 GHz to model the channel investigated. We measure and compare different modulation and coding schemes as well as communication standards. Finally, we show why we are still far off the ultimate performance bound, namely the Shannon Bound.

Mobile scenarios revive the challenge of repeatability and controllability in measurements, particularly if the velocities exceed the speed one can safely drive with a car. We thus had to apply new measurement methodologies such as scaling the time, and thereby the velocity. Another fundamentally different approach we have introduced is to rotate the transmitter or receiver around a central pivot, similar to a high-G centrifuge used for flight training. Ultimately, we combined these two approaches to validate them and solve even the most demanding high-speed measurement challenges.

# Contents

# Acknowledgements

Scientists never work alone, especially when conducting large measurement campaigns. Teamwork is one of the key ingredients to scientific achievements. So I have written this thesis in the "we"-form. Nevertheless, sometimes we get pushed to stand out, forget about the others, and summarize our own work in a thesis such as this one.

After almost ten years of working on this manuscript, I now understand how Brendan Pietsch, assistant professor of religious studies at Nazarbayev University in Astana, Kazakhstan, must have felt when he could not come up with a list of all the people who had helped him. So he wrote:

"I blame all of you. Writing this manuscript has been an exercise in sustained suffering. The casual reader may, perhaps, exempt herself from excessive guilt, but for those of you who have played the larger role in prolonging my agonies with your encouragement and support, well ... you know who you are, and you owe me."

Thank you all for prolonging my years as a researcher to become the most rewarding and entertaining years of my life!

# 1 Hardware and Methodology

Autonomous vehicles, IoT, decentralized computing models, and last but not least, the desire to be always and everywhere connected drive an ever-increasing demand for high data rates, high availability, and low latency. 5G will not be the end of our journey. Millimeter waves and massive MIMO are just the beginning.

There is no "one-fits-all" solution to measure the physical layer performance of such wireless communication systems. The integrated hardware available nowadays may solve challenges that required custom build setups a few years ago. Nonetheless, we need to be prepared to buy black boxes with limited modularity and upgradeability that we may not fully understand in functionality, see Figure 1.

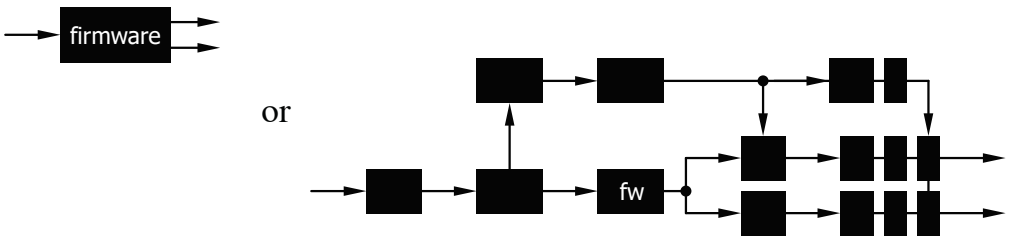


Figure 1: "The blackbox problem": Shall we buy our measurement hardware in one complex piece, in a few pieces of moderate complexity, or in many small but simple pieces that can be easily validated? (see [1])

Notably, measuring the performance of highly complex wireless communication systems is more than an engineering challenge when trying to minimize the effort to answer the questions of interest. We need to make an educated compromise, as building a prototype of the whole wireless communication system is out of scope and only simulating is not close enough to the real world until we know what effects to consider in our models.

- We employ a testbed to measure neither real-time nor offline. Instead, we efficiently combine both approaches to measure even transmissions systems with feedback.
- We combat fading not by random sampling but by equidistant sampling within a small-scale fading scenario using XY-positioning tables to minimize spatial correlation.
- We measure and plot our results against transmit power and not against signal to noise ratio at the receiver to include, for example, the gains due to beamforming at the transmitter.
- We avoid absolute measurements, as relative measurements allow us to reduce measurement variance.
- Finally, when plotting results, we always pay attention that measurement results consist of a number, a unit of measurement, *and* a measure for uncertainty

Thereby, we always remember that repeatability is a cornerstone of the scientific method, *see [1] for further reading.*

[1] **S. Caban**, J. A. G. Naya, and M. Rupp. "Measuring the Physical Layer Performance of Wireless Communication Systems". In: *IEEE Instrumentation & Measurement Magazine* 14.5 (2011), pp. 8–17. DOI: 10.1109/MIM.2011.6041377. → see Page 35

The remainder of this chapter briefly shows the testbed we have developed to *efficiently* perform measurements, the synchronization methodology we have invented to trigger transmitter and receiver *without* a cable connection, the noise bounds we are facing at *high* frequencies, and a novel metric we have developed to *to quantize* how much the wireless channel changes between consecutive measurements.

## 1.1 A Testbed

Consisting of much more than a transmitter and a receiver, a modular and carefully validated testbed is the basis to carry out even the most demanding measurements. *For more details, see [2].*

[2] M. Lerch, **S. Caban**, M. Mayer, and M. Rupp. "The Vienna MIMO Testbed: Evaluation of Future Mobile Communication Techniques". In: *Intel Technology Journal* 18 (3 2014), pp. 58–69. → see Page 45

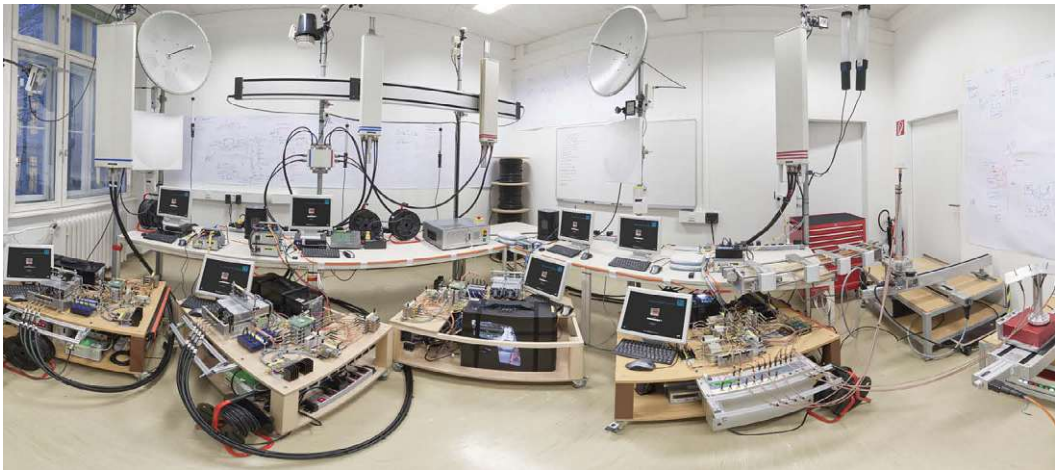


Figure 2: The Vienna MIMO Testbed [2] before deploying it on the rooftops of Vienna, Austria. We have never stopped to further enhance the testbed.

## 1.2 Synchronization

We use off-the-shelf available GPS disciplined rubidium frequency standards to synchronize the local oscillator frequency of transmitters and receivers if we cannot connect them via cables. However, we were unable to buy a device that allows triggering sample synchronous transmission and reception without cables. The methodology we have developed is shown in Figure 3.

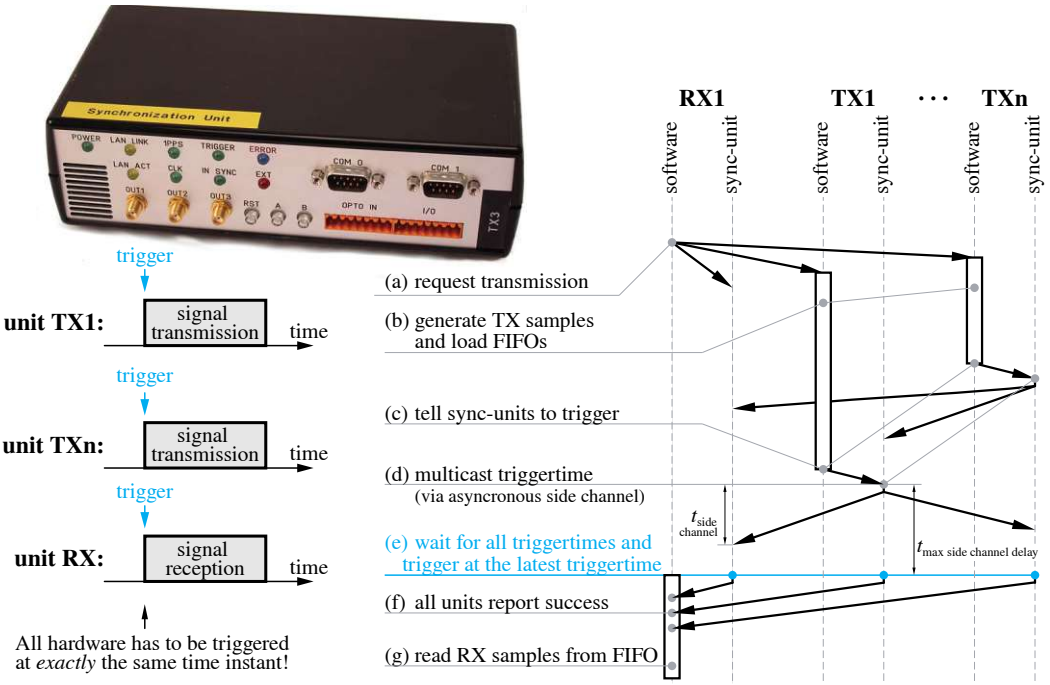


Figure 3: We have developed our own methodology and hardware to precisely trigger several transmitters and receivers, see [3].

The key idea is to use the typically already available "pulse per second" (from the GPS) and frequency (from the rubidium frequency standard) to build synchronized counters that exchange trigger-instant-counter-values via, for example, a standard internet connection. In addition, we showed that the internal clocks of standard desktop computers can be synchronized with 10µs precision. *For further details, see [3] and [4].*

[3] **S. Caban**, A. Disslbacher-Fink, J. A. G. Naya, and M. Rupp. "Synchronization of Wireless Radio Testbed Measurements". In: *Proc. International Instrumentation and Measurement Technology Conference (I2MTC)*. 2011. DOI: 10.1109/IMTC.2011.5944089. → see Page 57

[4] M. Laner, **S. Caban**, P. Svoboda, and M. Rupp. "Time Synchronization Performance of Desktop Computers". In: *Proceedings of the International Symposium on Precision Clock Synchronization ISPCS'11*. 2011. DOI: 10.1109/ISPCS.2011.6070154.

## 1.3 Noise bounds

Especially at higher center frequencies such as, for example, 60 GHz, noise may become the limiting factor in measurements. *For more details, see [5] and the references therein.*

[5] M. Lerch, E. Zöchmann, **S. Caban**, and M. Rupp. "Noise Bounds in Multicarrier mmWave Doppler Measurements". In: *European Wireless 2017 (EW2017)*. Dresden, Germany, May 2017.

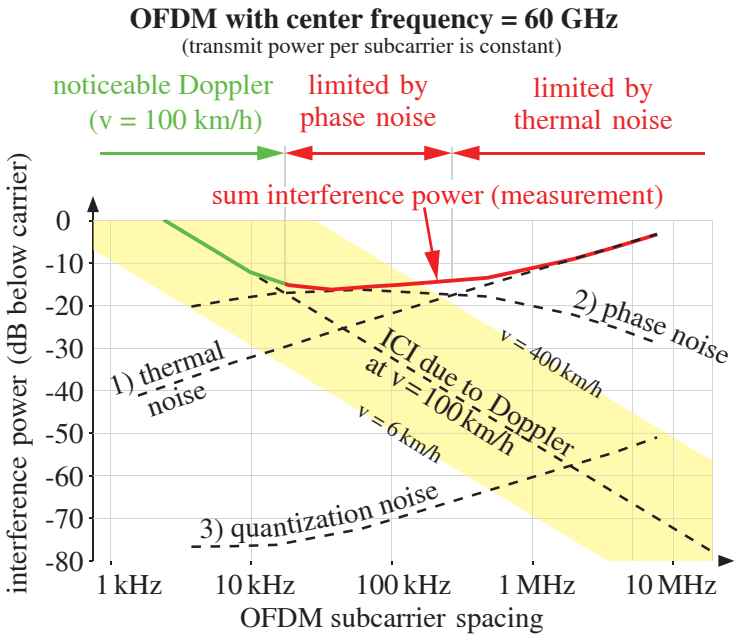


Figure 4: The measured interference power (drawn in red and green) is the result of 1) thermal noise, 2) quantization noise, 3) phase noise, and the ICI due to Doppler that we want to observe. In this example, Doppler can only be observed for a subcarrier spacing below approx. 17kHz [5].

## 1.4 How Static is Static

A real-world outdoor-to-indoor wireless channel changes over time even if the transmitter and the receiver are static and even if measuring at night when nobody moves around. To measure how fast the channel changes, we analyze

how often the channel quality indicator (CQI) for two consecutively transmitted LTE sub-frames is not equal (see Figure 5).

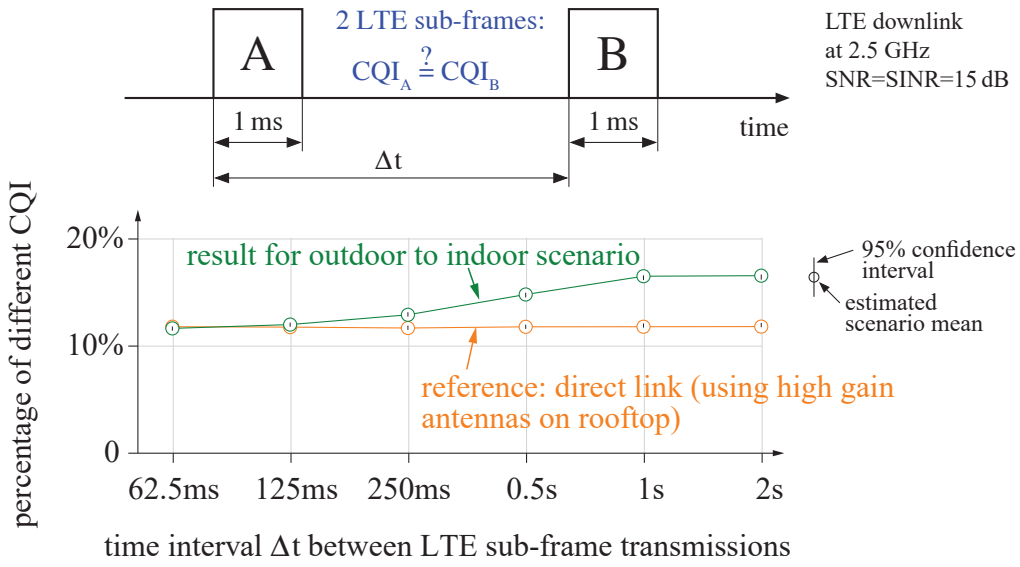


Figure 5: How similar is the channel between transmission A and B?

To overcome the quantized nature of the CQI, we vary the estimated noise power passed to the CQI calculation uniformly distributed within a range of -1.5 dB to 1.5 dB, a method similar to non-subtractive dithering. Notably, the resulting novel metric is very similar to the well-established relative average distance between two channel estimates in terms of the Frobenius norm, but with numbers more intuitive on the y-axis. For the particular scenario shown in Figure 5, there is no need to transmit two LTE sub-frames faster than approx. 125 ms to measure with feedback. *For more details, see [6].*

[6] M. Lerch, **S. Caban**, E. Zöchmann, and M. Rupp. "Quantifying the Repeatability of Wireless Channels by Quantized Channel State Information". In: *IEEE 9th Sensor Array and Multichannel Signal Processing Workshop (SAM 2016)*. Rio de Janeiro, Brazil, July 2016. DOI: 10.1109/SAM.2016.7569702. → see Page 61

# 2 Static Scenarios

This chapter is devoted to the transmission of data in *static* scenarios using a measurement setup equal or similar to the one shown in Figure 6.

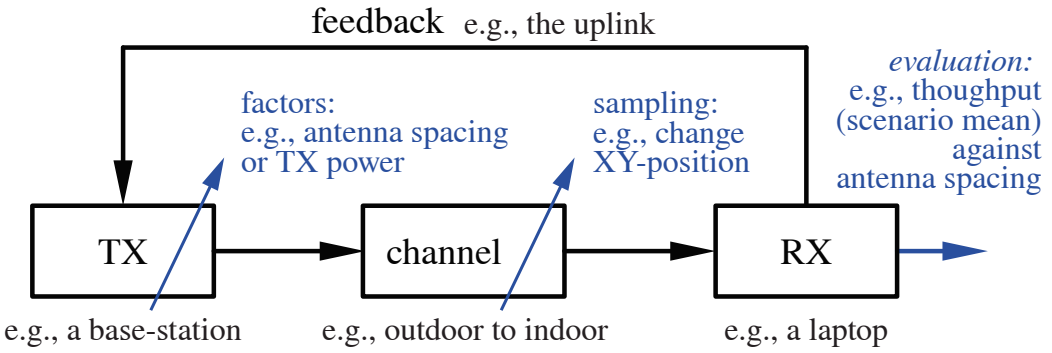


Figure 6: The measurement setup used (with slight variations) throughout this chapter.

We show how to control for a variable such as antenna-position to measure and model the effects of antenna-spacing. We carry out channel sounding experiments at 2.5 GHz and 60 GHz to model the channel investigated. We measure and compare different modulation and coding schemes as well as communication standards. Finally, we show why we are still far off the ultimate performance bound, namely the Shannon Bound.

## 2.1 Antenna Spacing at the Base-Station

Suppose we use the measurement setup shown in Figure 6 to measure channel capacity against antenna spacing at the transmitting base-station located on a rooftop. To change the antenna spacing at the base-station, we move *only* the right-hand antenna of the two antennas we have. Notably, we then measure two different effects, see Figure 7:

a. The ability to transmit more data as bigger antenna spacing decreases channel correlation

b. A change in SNR and thus a change in channel capacity that originates from repositioning the right-hand TX antenna

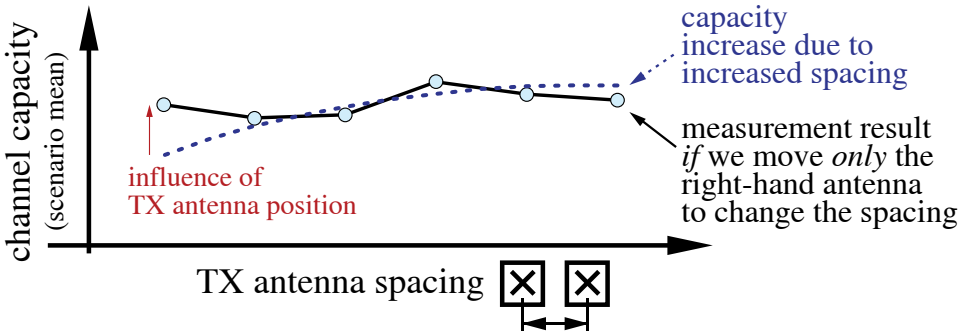


Figure 7: The outcome of our experiment is dependent on the position of the transmit antennas (confound) and not only on the spacing (exposure).

This so called confounding can be controlled in two ways:

1. **by "intelligently" designing the experiment**: We introduce the variance reduction techniques of randomization and matching with equidistant sampling as well as plotting the results relatively to reduce the influence of confounding, see Figure 8. *See [7] and the references therein for further reading on how to control for confounding ind antenna spacing measurements.*

2. **by analytically compensating the effects *after* conducting the experiment**: In previous works, we used concomitant the observations of single-channel throughput to compensate for confounding analytically. We

did so to evaluate the throughput of WiMAX and HSDPA against antenna spacing, *see [8] and [9] and the references therein.*

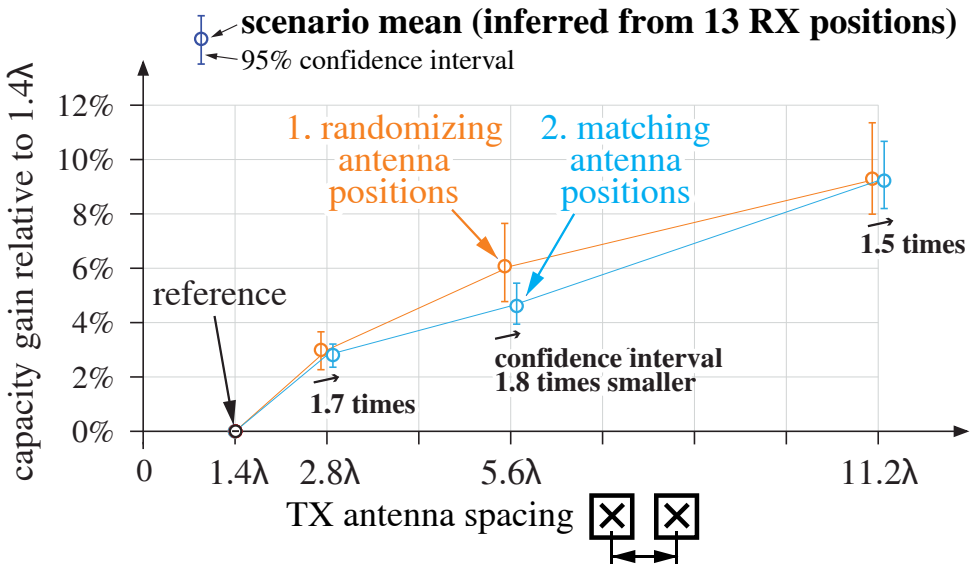


Figure 8: In the measurement scenario investigated, the proposed variance reduction methodology of matching leads to higher levels of confidence (smaller confidence intervals) compared to randomization.

[7] **S. Caban**, M. Lerch, S. Pratschner, E. Zöchmann, P. Svoboda, and M. Rupp. "Design of Experiments to Compare Base Station Antenna Configurations". In: *IEEE Transactions on Instrumentation and Measurement* 68.10 (2019), pp. 3484–3493. ISSN: 0018-9456. DOI: 10.1109/TIM.2018.2880941. → see Page 67

[8] **S. Caban**, J. A. García Naya, L. Castedo, and C. Mehlführer. "Measuring the influence of TX antenna spacing and transmit power on the closed-loop throughput of IEEE 802.16-2004 WiMAX". In: *Proc. IEEE Instrumentation and Measurement Technology Conference (I2MTC 2010)*. Austin, TX, USA, May 2010.

[9] **S. Caban**, J. A. García Naya, C. Mehlführer, and M. Rupp. "Measuring the Closed-Loop Throughput of 2x2 HSDPA over TX Power and TX Antenna Spacing". In: *Proc. 2nd International Conference on Mobile Lightweight Wireless Systems (Mobilight-2010)*. Barcelona, Spain, May 2010.

## 2.2 Spatial Correlation of Indoor Receivers

In contrast to investigating spatial correlation at the base station located on a rooftop, we have also investigated spatial correlation at the indoor-receiver site of the same scenario. We show that the sum achievable spectral efficiency of two users located indoors is lower than in the commonly employed Rican channel model (with the same K factor), even at large inter-user distances of 8 m, see Figure 9.

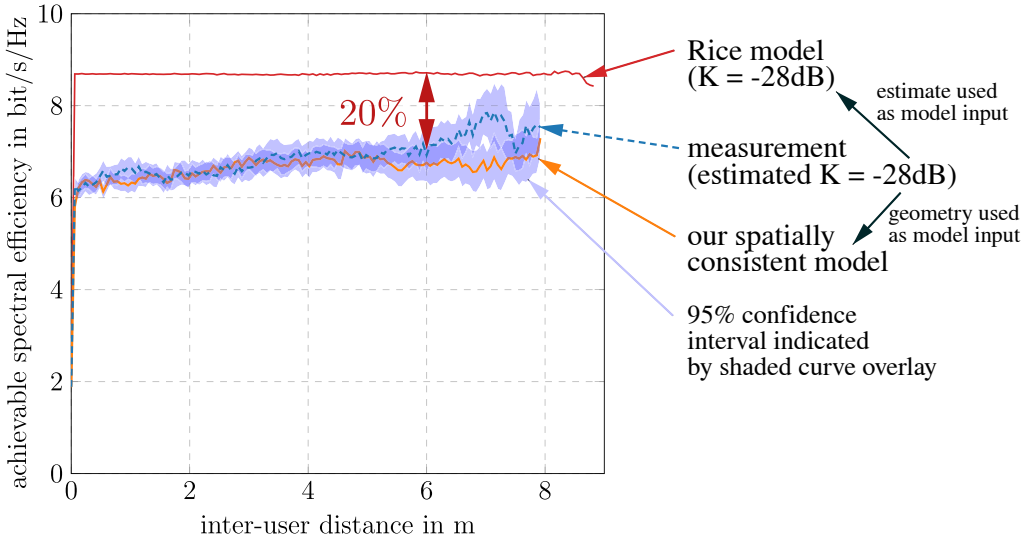


Figure 9: In a "typical" outdoor-to-indoor scenario, indoor receivers separated by distances of over six meters are still correlated. This leads to a (20%) lower spectral efficiency than suggested by the commonly employed Rican channel model.

To explain the measured effects, we introduce a spatially consistent channel model that we fit to the measurement scenario geometry. *See [10], [11] and the references therein for further reading, as well as [12, 13, 14] that set the foundation for these two works.*

[10] S. Pratschner, T. Blazek, H. Groll, **S. Caban**, S. Schwarz, and M. Rupp. "Measured User Correlation in Outdoor-to-Indoor Massive MIMO Scenarios". In: *IEEE Access* 8 (2020), pp. 178269–178282. DOI: 10.1109/ACCESS.2020.3026371. → see Page 77

[11] S. Pratschner, T. Blazek, E. Zöchmann, F. Ademaj, **S. Caban**, S. Schwarz, and M. Rupp. "A Spatially Consistent MIMO Channel Model With Adjustable K Factor". In: *IEEE Access* 7 (2019), pp. 110174–110186. DOI: 10.1109/ACCESS.2019.2934635. → see Page 91

[12] S. Pratschner, E. Zöchmann, H. Groll, **S. Caban**, S. Schwarz, and M. Rupp. "Does a Large Array Aperture Pay Off in Line-Of-Sight Massive MIMO?" In: *International Workshop on Signal Processing Advances in Wireless Communications (SPAWC)*. Cannes, France, 2019, pp. 1–5. DOI: 10.1109/SPAWC.2019.8815590.

[13] S. Pratschner, **S. Caban**, D. Schützenhöfer, M. Lerch, E. Zöchmann, and M. Rupp. "A Fair Comparison of Virtual to Full Antenna Array Measurements". In: *International Workshop on Signal Processing Advances in Wireless Communications (SPAWC)*. Kalamata, Greece, 2018, pp. 1–5. ISBN: 978-1-5386-3511-7. DOI: 10.1109/SPAWC.2018.8445923.

[14] S. Pratschner, **S. Caban**, S. Schwarz, and M. Rupp. "A mutual coupling model for massive MIMO applied to the 3GPP 3D channel model". In: *European Signal Processing Conference (EUSIPCO)*. Kos, Greece, 2017, pp. 623–627. DOI: 10.23919/EUSIPCO.2017.8081282.

## 2.3 Channel Sounding and Modelling at 60 GHz

So far, we have conducted all experiments in this thesis at a center frequency of 2.5 GHz where the wavelength is approx. 12 cm. If we increase the center frequency to 60 GHz, the wavelength shortens to 5 mm. These so-called mmWaves not only make the measurement equipment required a magnitude more expensive but also change the dominating propagation effects, especially when highly directional antennas are used in order to overcome path loss. We apply Akaike's information criterion to decide whether Rician fading still sufficiently explains the data recorded in an indoor laboratory environment. Our results favor the two-wave with diffuse power (TWDP) fading hypothesis over Rician fading in situations where our steerable antenna is pointing towards reflecting objects or is slightly misaligned at line-of-sight, see Figure 10.

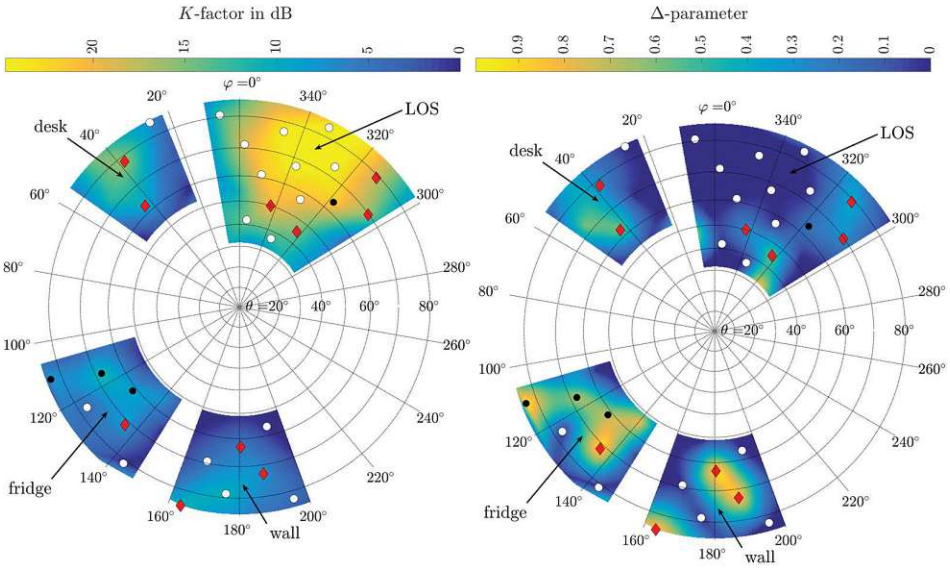


Figure 10: Akaike's information criterion favors two-wave with diffuse power fading (red diamonds, parameterized by K and $\Delta$) over Rician fading (white circles) or rejecting both distributions (black markers) when our steerable antenna is pointing towards reflecting objects or is slightly misaligned at line-of-sight.

To analyze spatial averaging in conjunction with directional channel sounding, we built an elevation-over-azimuth antenna positioner mounted on an x-y-z positioning table that rotates a horn antenna around its apparent phase center. *For further reading see [15] and the references therein, as well as [16] and [17] that set the foundation of this work.*

[15] E. Zöchmann, **S. Caban**, C. F. Mecklenbräuker, S. Pratschner, M. Lerch, S. Schwarz, and M. Rupp. "Better than Rician: modelling millimetre wave channels as two-wave with diffuse power". In: *EURASIP Journal on Wireless Communications and Networking* 2019.1 (Jan. 2019), p. 21. ISSN: 1687-1499. DOI: 10.1186/s13638-018-1336-6.
→ see Page 104

[16] E. Zöchmann, M. Lerch, S. Pratschner, R. Nissel, **S. Caban**, and M. Rupp. "Associating Spatial Information to Directional Millimeter Wave Channel Measurements". In: *IEEE 86th Vehicular Technology Conference (VTC2017-Fall)*. Toronto, Canada, Sept. 2017. DOI: 10.1109/VTCFall.2017.8287905.

[17] E. Zöchmann, M. Lerch, **S. Caban**, R. Langwieser, C. F. Mecklenbräuker, and M. Rupp. "Directional Evaluation of Receive Power, Rician K-factor and RMS Delay Spread obtained from Power Measurements of 60GHz Indoor Channels". In: *IEEE-APS Topical Conference on Antennas and Propagation in Wireless Communications (APWC 2016)*. Cairns, Australia, Sept. 2016.

## 2.4 The Shannon Bound

The supreme discipline of wireless communication measurements is, in my opinion, to implement the entire physical layer of a transmission standard to measure its physical layer throughput (in Mbit/s), thereby learning what we need to consider in simulations. For example, we found out that plotting against the signal-to-noise ratio (SNR) at the receiver leads to wrong conclusions because the adaptive feedback employed strongly influences the receive-SNR while leaving the sum transmit-power untouched. Our novel approach here is to plot measurement results against transmit power and to note the average single antenna (SISO) signal-to-noise ratio (SNR) at the receiver in a second axis, see Figure 11. In addition, when measuring a MIMO channel, the average SNR observed at each receive antenna is typically by 3 dB to 5 dB different (scenario average, one antenna may point more towards the transmitter or have a similar polarization), which is typically not reflected by channel models that assume symmetrical channels. This asymmetry leads to a an average throughput that is lower than expected, *see [18], [19], and [20] and the references therein for further reading.*

[18] **S. Caban**, M. Rupp, C. Mehlführer, and M. Wrulich. *Evaluation of HSDPA and LTE: From Testbed Measurements to System Level Performance*. Wiley & Sons, 2011. ISBN: 9780470711927. DOI: 10.1002/9781119954705.

[19] C. Mehlführer, **S. Caban**, and M. Rupp. "Measurement-based Performance Evaluation of MIMO HSDPA". In: *IEEE Transactions on Vehicular Technology* 59.9 (2010), pp. 4354–4367. DOI: 10.1109/TVT.2010.2066996.

[20] C. Mehlführer, **S. Caban**, and M. Rupp. "MIMO HSDPA Throughput Measurement Results". In: *HSDPA/HSUPA Handbook*. Ed. by B. Furht and S. A. Ahson. Boca Raton, FL, USA: CRC Press, 2010, pp. 357–377. ISBN: 1420078631.

The next step is to plot the maximum rate at which information can be transmitted via the same channel into the same graph, namely the channel capacity. The surprise is high once spotting the gap of up to 40% between the throughput measured and the channel capacity estimated, see Figure 11.

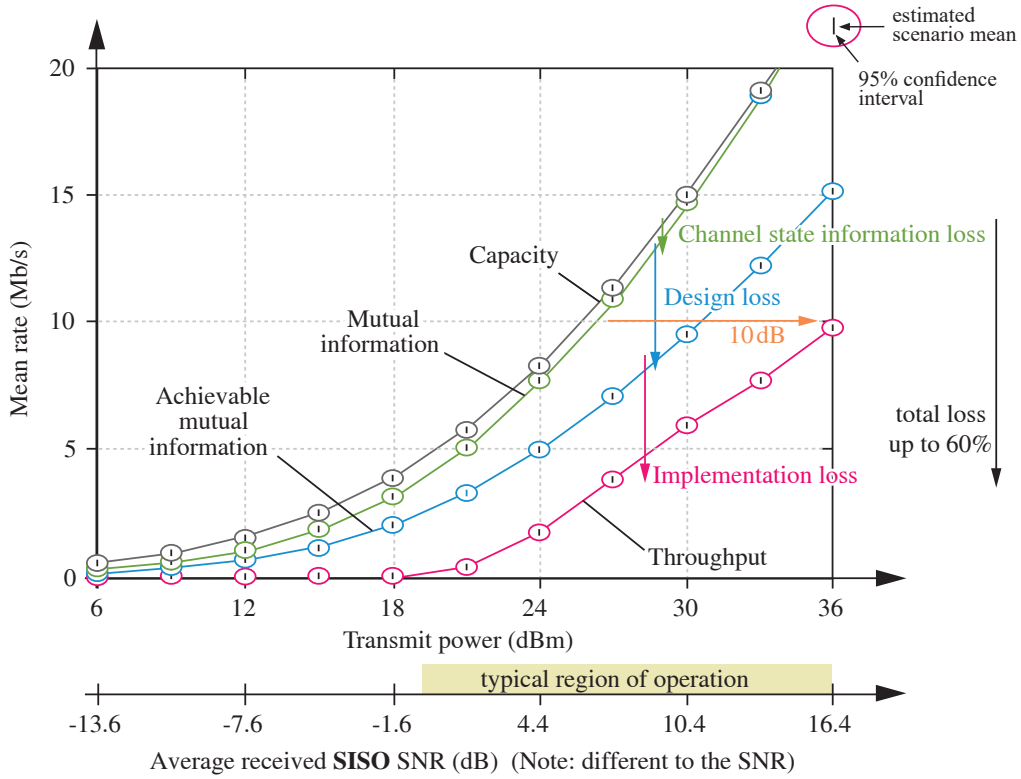


Figure 11: The physical layer throughput of WiMAX (shown in the graph above), HSDPA, and also LTE are up to 10 dB off the Shannon Bound.

We split the loss observed into three parts: The *channel state information loss* due to imperfect channel knowledge is negligible in the typical region of operation. The *design loss* is "political", caused by, for example, losses due to quantized precoding, suboptimal coding, or the transmission of pilot and synchronization symbols. The *implementation loss* that accounts for losses caused by non-optimum receivers and channel code is currently unavoidable

but could be decreased in the near future when having better models at hand to improve receivers. *For further reading see [21] and the references therein, as well as [22] and [23] that set the foundation of this work.*

[21] C. Mehlführer, **S. Caban**, and M. Rupp. "Cellular System Physical Layer Throughput: How Far Off Are We From The Shannon Bound?" In: *IEEE Wireless Communications* 18.6 (2011), pp. 54–63. DOI: 10.1109/MWC.2011.6108334. → see Page 121

[22] M. Rupp, J. A. García-Naya, C. Mehlführer, **S. Caban**, and L. Castedo. "On Mutual Information and Capacity in Frequency Selective Wireless Channels". In: *Proc. IEEE International Conference on Communications (ICC 2010)*. Cape Town, South Africa, May 2010. DOI: 10.1109/ICC.2010.5501942.

[23] M. Rupp, C. Mehlführer, and **S. Caban**. "On Achieving the Shannon Bound in Cellular Systems". In: *Proc. 20th International Conference Radioelektronika 2010*. Brno, Czech Republic, Apr. 2010.

## 2.5 Other Measurements

### Modulation and Coding Schemes

We have also investigated Filter Bank Multi-Carrier (FBMC) as a possible future transmission technique. In contrast to common belief, we show experimentally that low latency MISO works in FBMC, *see [24].* We employ auxiliary symbols to deal with the imaginary interference inherently caused in FBMC and validate our approach by real-world throughput measurements, *see [25].* Finally, we derive and validate closed-form capacity expressions for a low complexity bit-interleaved coded modulation, *see [26] and the references therein for further reading.*

[24] R. Nissel, E. Zöchmann, M. Lerch, **S. Caban**, and M. Rupp. "Low-Latency MISO FBMC-OQAM: It Works for Millimeter Waves!" In: *IEEE International Microwave Symposium (IMS)*. Hawaii, USA, June 2017. → see Page 131

[25] R. Nissel, **S. Caban**, and M. Rupp. "Experimental Evaluation of FBMC-OQAM Channel Estimation Based on Multiple Auxiliary Symbols". In: *IEEE 9th Sensor Array and Multichannel Signal Processing Workshop (SAM 2016)*. Rio de Janeiro, Brazil, July 2016.

[26] R. Nissel, **S. Caban**, and M. Rupp. "Closed-Form Capacity Expression for Low Complexity BICM with Uniform Inputs". In: *IEEE International Symposium on Personal, Indoor and Mobile Radio Communications (PIMRC)*. Hong Kong, P.R.China, 2015.

## Operational Cellular Network Measurements

Measuring the mean throughput performance of a single user in an operational cellular mobile network is a challenge entirely different from all the things presented so far in this thesis. The key problem here is:

How to measure the mean throughput performance of a single user within a short period if fading is position-dependent and the overall network load (and thus the throughput of a user) changes throughout a day?

Our three-step approach first derives the instantaneous IP-throughput within one second by using a novel packet pattern method. Next, we remove the slowly changing average network load by using side information from the network. Finally, we obtain the scenario-mean of the remaining small-scale fading scenario by statistical inference. Long time measurements show that we can estimate the *weekly* mean IP-throughput with an error of 10% by conducting only a 20-second measurement (90% level of confidence), *see [27] and the references therein for further reading.*

[27] M. Rindler, **S. Caban**, M. Lerch, P. Svoboda, and M. Rupp. "Swift Indoor Benchmarking Methodology for Mobile Broadband Networks". In: *IEEE 86th Vehicular Technology Conference (VTC2017-Fall)*. Toronto, Canada, Sept. 2017. DOI: 10.1109/VTCFall.2017.8288190.

# 3 Mobile Scenarios

The good news is, we can measure most wireless channels in motion straightforwardly by mounting the receiver and or the transmitter inside a car. The first easy to solve obstacle we thereby usually encounter is that the 12 V cigarette adapter of the car does not deliver enough power for all the measurement equipment involved. Exact time synchronization, frequency synchronization, and phase synchronization of transmitter and receiver without cables are the next items on our to-do list. Once velocities exceed 300 km/h, however, we need to rethink the measurement methodology, not only for safety reasons. Especially repeatability and controllability, which are already very hard to achieve at low velocities, become a real showstopper in experimental design for extreme velocities.

In this chapter, we first show how to measure high velocity scenarios by rotating the transmitter or the receiver around a central pivot, similar to a high-G centrifuge used for flight training. Next, we introduce the fundamentally different approach to scale the velocity of measurements down to velocities that are easier to handle. Then, we combine these two approaches to validate them and solve even the most demanding high-speed measurement challenges. Finally, we present how to perform classic drive-by measurements at 60 GHz without driving.

## 3.1 Rotation Measurements

One of the first things that comes to mind when thinking of *repeatable* wireless communication measurements at different velocities in a controllable environment is to mount the transmitter or receiver, or only their antennas on a linear guide or short rail. This way, one should be able to repeat an experiment at any desired velocity while still being able to connect transmitter and receiver through cables. While in principle not necessary, being able to use cables to connect transmitter and receiver saves a lot of time to set up and carry out experiments. Unfortunately, this all is wishful thinking, when the goal is to measure at more than 400 km/h and repeat the experiment within 125 ms to keep the channel static (remember Figure 5).

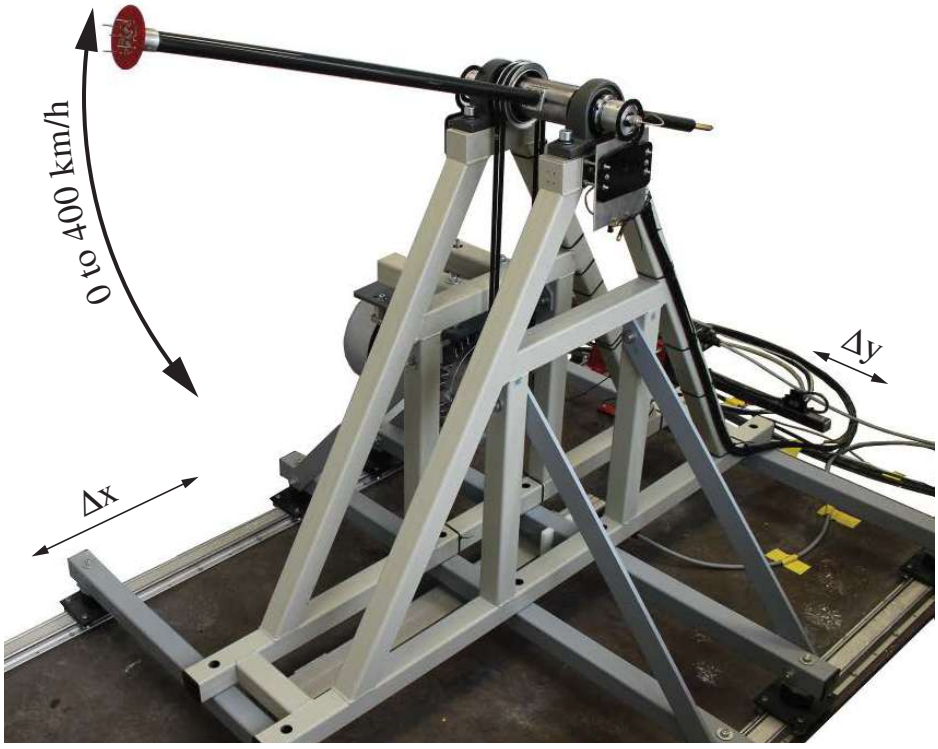


Figure 12: To carry out controlled and repeatable high speed measurements, we rotate the transmit or receive antennas around a central pivot.

As shown in Figure 12, our novel approach to measure at 400 km/h is to mount monopole antennas with a common ground plane on a one-meter long, four-centimeter thick carbon fiber rod that is rotated around a central pivot with

18 revolutions per second. The centripetal acceleration of the receive antenna is then approx. 13 000 m/s$^2$ and a 12 kilowatt electrical engine is required to overcome the drag of the rod. Nevertheless, the engineering is straight forward, even for velocities higher than 400 km/h, requiring only low-cost off-the-shelf components and welding skills. Note that, due to security concerns, one is not advised to set up a rotation unit as shown in Figure 12 in his own office.

The novelty of this set-up for experimental research is that we can carry out high velocity measurements while still being able to connect transmitter and receiver with cables. This not only enables "perfect" triggering, as well as time, phase, and frequency synchronization far beyond the precision of GPS disciplined rubidium frequency standards. There is also no need to worry about power supply, measurement time, or remote access anymore. Data can be evaluated instantly, expensive hardware does not need to be insured for accidents, and so on. Who has ever carried out measurements with cars knows that cables make a researcher's life much easier.

Next to being able to use cables, another breakthrough of measuring in a circle is controllability; in particular, we can repeatedly start measurements at the same, or a different, position in the same fading scenario at a certain velocity of the antenna. When rotating in a circle with a radius of 1 meter at 400 km/h, the path of the antennas is thereby close to linear, see Figure 13.


Figure 13: Drawn at scale, the antennas only rotate by 6 degree while moving 11 cm during the transmission of a standard compliant LTE sub-frame.

This allows us to change only single parameters, such as the maximum Doppler shift (proportional to the velocity), the signal to noise ratio, or the fading, while holding all the other parameters constant, *see [28] and [29] for further reading on the methodology. See [30] for further reading on how we extended the methodology to measure 60 GHz.*

Having full control over all parameters of the measurement, especially position and speed, allows us to execute measurements that are not possible with conventional, drive by set-ups. For example, we can compare the performance

of beamforming algorithms in standstill and different velocities by measuring at the same positions, *see [31] for further reading.* We can elaborate on estimating the Angle of Arrivals (AoAs) through Doppler measurement, *see [32] for further reading.* And finally, we can validate the time scaling techniques presented in the next section using this setup.

[28] **S. Caban**, J. Rodas, and J. A. García-Naya. "A Methodology for Repeatable, Off-line, Closed-loop Wireless Communication System Measurements at Very High Velocities of up to 560 km/h". In: *Proc. International Instrumentation and Measurement Technology Conference (I2MTC 2011)*. Binjiang, Hangzhou, China, May 2011. DOI: 10.1109/IMTC.2011.5944019. → see Page 136

[29] **S. Caban**, R. Nissel, M. Lerch, and M. Rupp. "Controlled OFDM Measurements at Extreme Velocities". In: *Proc. of ExtremeCom'2014*. Galapagos Islands, Ecuador, Aug. 2014.

[30] E. Zöchmann, R. Langwieser, **S. Caban**, M. Lerch, S. Pratschner, R. Nissel, C. Mecklenbräuker, and M. Rupp. "A Millimeter Wave Testbed For Repeatable High Velocity Measurements". In: *European Wireless 2017 (EW2017)*. Dresden, Germany, May 2017.

[31] D. Schützenhöfer, E. Zöchmann, M. Lerch, S. Pratschner, H. Groll, **S. Caban**, and M. Rupp. "Experimental Evaluation of the Influence of Fast Movement on Virtual Antenna Arrays". In: *23rd International ITG Workshop on Smart Antennas (WSA 2019)*. Vienna, Austria, Apr. 2019.

[32] E. Zöchmann, **S. Caban**, M. Lerch, and M. Rupp. "Resolving the Angular Profile of 60 GHz Wireless Channels by Delay-Doppler Measurements". In: *IEEE 9th Sensor Array and Multichannel Signal Processing Workshop (SAM 2016)*. Rio de Janeiro, Brazil, July 2016.

## 3.2 Scaled Time Measurements

The idea of scaling is not new to the wireless community. Inspired by researchers who scale airplanes in size to measure their cross sections in small anechoic chambers, we came up with a novel technique to scale the signal transmitted in time by a factor of $n$ while moving $n$ times slower. We achieve this time scaling by lowering the sampling frequency at the transmitter by a factor of $n$ and then increasing it again by $n$ after receiving, see Figure 14.

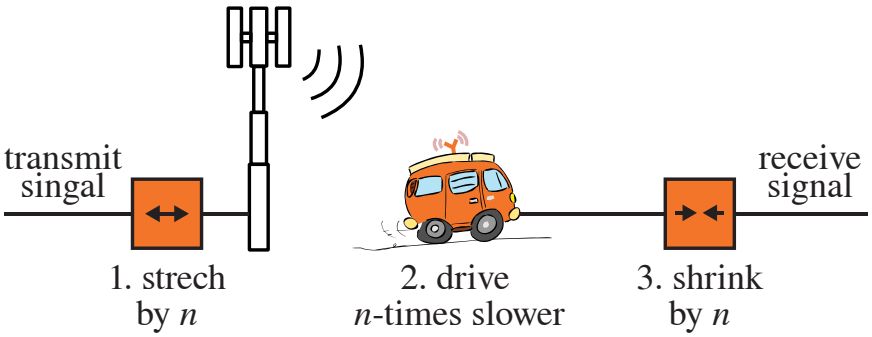


Figure 14: Instead of measuring at very high velocities, we drive $n$ times slower and scale the signal transmitted by the same factor n.

As we lower the sampling rate by a factor of $n$, the transmission of a signal lasts $n$ times longer. Therefore, we can drive $n$ times slower to still drive by the same "hills and holes of fading" during the transmission of a signal. In case there were other cars on the road, these cars also need to drive $n$ times slower. Notably, if there were interference, this idea would not work. Therefore, we either measured interference-free or created our own much stronger, scaled interference. Finally, we scaled the amplitude of the signal transmitted accordingly to obtain the same signal-to-noise ratio at the receiver.

The downsides of this approach are clear. One still has to measure using cars or trains, which imposes restrictions to repeatability and controllability. Thus we combined the time scaling technique described above with the rotation measurements from the previous section to a novel high-speed measurement methodology. Combining these two techniques also allowed us to evaluate the combined measurement error of rotational and time scale measurements, see Figure 15.

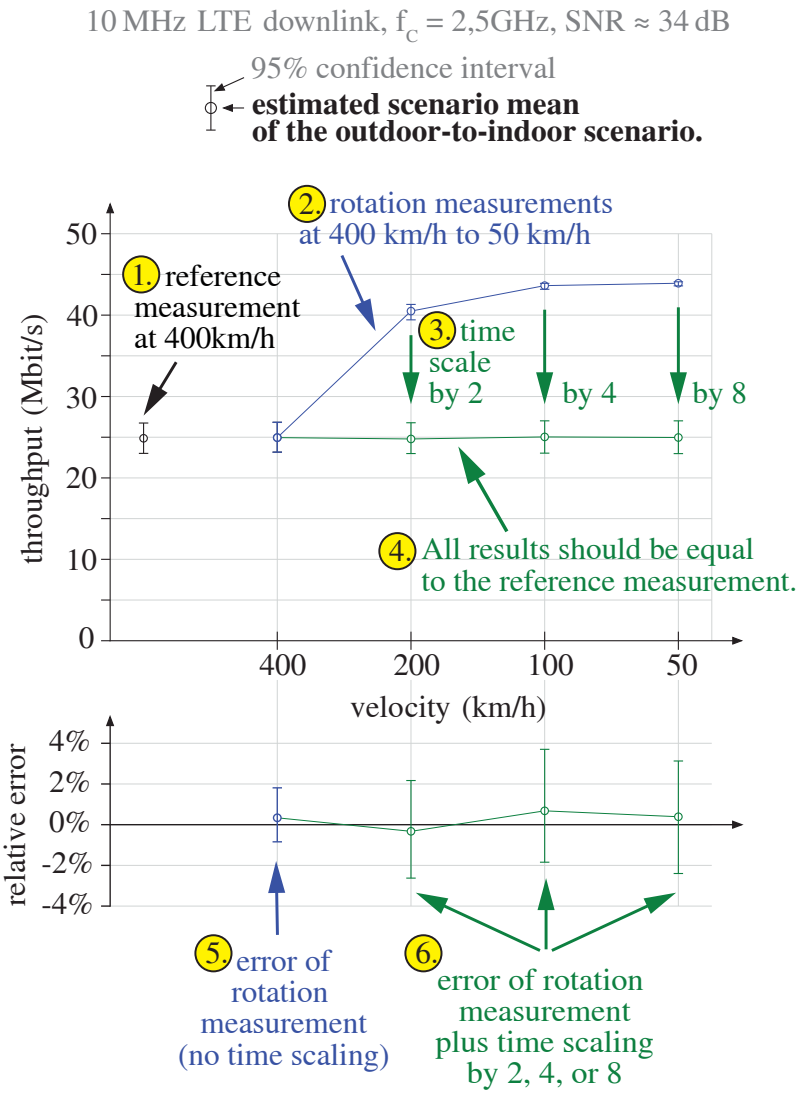


Figure 15: Controlled measurement where everything except the velocity is kept constant. The resulting measurement error is below 4% (95% confidence).

We used this new methodology to conduct LTE measurements at up to 600 km/h, *see [33] and [34] for further reading.* Being able to repeatably measure at the same positions, thereby also allowed us to compare several novel modulation schemes in high speed scenarios, *see [35] for further reading.*

Up to now, we have designed the transmitted OFDM signal "well", that is, the cyclic prefix is "long enough" so that inter-symbol-interference and inter-carrier interference due to an insufficient cyclic prefix are negligible. Thus, their

change due to time scaling is also negligible. Unfortunately, for example, relay nodes in public railway scenarios introduce significant interference outside the cyclic prefix length. We have therefore developed a time-stretching technique that preserves the effects of the insufficient cyclic prefix with negligible error and without channel knowledge, *see [36] for further reading.*

[33] J. Rodríguez-Piñeiro, M. Lerch, J. A. García-Naya, **S. Caban**, M. Rupp, and L. Castedo. "Emulating Extreme Velocities of Mobile LTE Receivers in the Downlink". In: *EURASIP Journal on Wireless Communications and Networking* 2015.106 (Apr. 2015), pp. 1–14. ISSN: 1687-1499. DOI: 10.1186/s13638-015-0343-0. → see Page 141

[34] J. Rodríguez-Piñeiro, M. Lerch, P. Suárez-Casal, J. A. García-Naya, **S. Caban**, M. Rupp, and L. Castedo. "LTE Downlink Performance in High Speed Trains". In: *Proceedings of the 81st Vehicular Technology Conference (VTC2015-Spring)*. Glasgow, Scotland, May 2015. DOI: 10.1109/VTCSpring.2015.7145924.

[35] J. Rodríguez-Piñeiro, M. Lerch, T. Domínguez-Bolaño, J. A. García-Naya, **S. Caban**, and L. Castedo. "Experimental Assessment of 5G-Candidate Modulation Schemes at Extreme Speeds". In: *IEEE 9th Sensor Array and Multichannel Signal Processing Workshop (SAM 2016)*. Rio de Janeiro, Brazil, July 2016. DOI: 10.1109/SAM.2016.7569632.

[36] M. Lerch, **S. Caban**, E. Zöchmann, P. Svoboda, and M. Rupp. "Scaled-Time OFDM Experiments for Channels Exceeding the Cyclic Prefix". In: *Electronics Letters* 55.25 (2019), pp. 1370–1373. DOI: 10.1049/el.2019.2857. → see Page 155

## 3.3 Drive-by Measurements without Driving

After measuring the performance of wireless communication systems for more than ten years, we had the equipment and the knowledge to precisely synchronize, trigger, and execute classical drive-by measurements, see Figure 16, *see [37] for further reading.*


Figure 16: Classical drive-by measurements are cumbersome to perform.

However, as a matter of fact, drive-by measurements are cumbersome and potentially unsafe, especially on public roads. Therefore, whenever feasible, we have avoided driving to minimize safety hazards, see Figure 17.

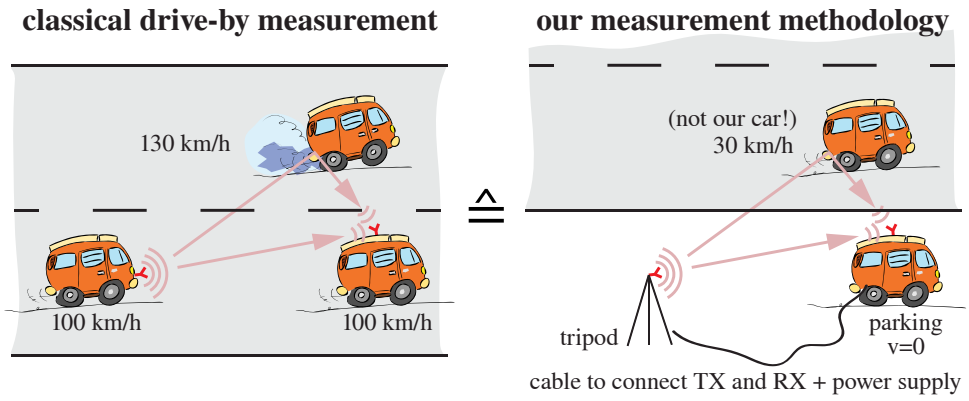


Figure 17: Capturing the effect of an overtaking vehicle without driving. At 60 GHz, our methodology is valid to characterize the large-scale fading and the small-scale fading of an overtaking vehicle.

As the measurements performed conclude, the two-wave with diffuse power (TWDP) model is more adequate to model small-scale fading than the customary used Rician fading model in such a scenario when measuring at 60 GHz. Figuratively speaking, we have only two dominant propagation paths in this setup. This proves also the validity of the chosen, simple measurement setup that avoids driving and enables the use of cables to power and connect transmitter and receiver, *see [38, 39, 40] for further reading.*

[37] H. Groll, E. Zöchmann, S. Pratschner, M. Lerch, D. Schützenhöfer, M. Hofer, J. Blumenstein, S. Sangodoyin, T. Zemen, A. Prokes, A. Molisch, and **S. Caban**. "Sparsity in the Delay-Doppler Domain for Measured 60 GHz Vehicle-to-Infrastructure Communication Channels". In: *Proceedings of the IEEE ICC 2019*. May 2019. DOI: 10.1109/ICCW.2019.8756930.

[38] E. Zöchmann, M. Hofer, M. Lerch, S. Pratschner, L. Bernadó, J. Blumenstein, **S. Caban**, S. Sangodoyin, H. Groll, T. Zemen, A. Prokes, M. Rupp, A. Molisch, and C. Mecklenbräuker. "Position-Specific Statistics of 60 GHz Vehicular Channels During Overtaking". In: *IEEE Access* 7 (2019), pp. 14216–14232. ISSN: 2169-3536. DOI: 10.1109/ACCESS.2019.2893136. → see Page 158

[39] E. Zöchmann, C. F. Mecklenbräuker, M. Lerch, S. Pratschner, M. Hofer, D. Löschenbrand, J. Blumenstein, S. Sangodoyin, G. Artner, **S. Caban**, T. Zemen, A. Prokes, M. Rupp, and A. Molisch. "Measured Delay and Doppler Profiles of Overtaking Vehicles at 60 GHz". In: *IEEE 12th European Conference on Antennas and Propagation (EuCAP 2018)*. London, UK, Apr. 2018. DOI: 10.1049/cp.2018.0470.

[40] E. Zöchmann, M. Hofer, M. Lerch, J. Blumenstein, S. Sangodoyin, H. Groll, S. Pratschner, **S. Caban**, D. Löschenbrand, L. Bernadó, T. Zemen, A. Prokes, M. Rupp, C. Mecklenbräuker, and A. Molisch. "Statistical Evaluation of Delay and Doppler Spread in 60 GHz Vehicle-to-Vehicle Channels During Overtaking". In: *Proceedings of the 2018 IEEE-APS Topical Conference on Antennas and Propagation in Wireless Communications (APWC)*. Cartagena, Colombia, Sept. 2018, pp. 1–4. DOI: 10.1109/APWC.2018.8503750.

# 4 Bibliography

## 4.1 Authored Books and Book Sections

[18] **S. Caban**, M. Rupp, C. Mehlführer, and M. Wrulich. *Evaluation of HSDPA and LTE: From Testbed Measurements to System Level Performance*. Wiley & Sons, 2011. ISBN: 9780470711927. DOI: 10.1002/9781119954705.

[20] C. Mehlführer, **S. Caban**, and M. Rupp. "MIMO HSDPA Throughput Measurement Results". In: *HSDPA/HSUPA Handbook*. Ed. by B. Furht and S. A. Ahson. Boca Raton, FL, USA: CRC Press, 2010, pp. 357–377. ISBN: 1420078631.

## 4.2 Authored Journals

[1] **S. Caban**, J. A. G. Naya, and M. Rupp. "Measuring the Physical Layer Performance of Wireless Communication Systems". In: *IEEE Instrumentation & Measurement Magazine* 14.5 (2011), pp. 8–17. DOI: 10.1109/MIM.2011.6041377. → see Page 35

[2] M. Lerch, **S. Caban**, M. Mayer, and M. Rupp. "The Vienna MIMO Testbed: Evaluation of Future Mobile Communication Techniques". In: *Intel Technology Journal* 18 (3 2014), pp. 58–69. → see Page 45

[7] **S. Caban**, M. Lerch, S. Pratschner, E. Zöchmann, P. Svoboda, and M. Rupp. "Design of Experiments to Compare Base Station Antenna Configurations". In: *IEEE Transactions on Instrumentation and Measurement* 68.10 (2019), pp. 3484–3493. ISSN: 0018-9456. DOI: 10.1109/TIM.2018.2880941. → see Page 67

[10] S. Pratschner, T. Blazek, H. Groll, **S. Caban**, S. Schwarz, and M. Rupp. "Measured User Correlation in Outdoor-to-Indoor Massive MIMO Scenarios". In: *IEEE Access* 8 (2020), pp. 178269–178282. DOI: 10.1109/ACCESS.2020.3026371. → see Page 77

[11] S. Pratschner, T. Blazek, E. Zöchmann, F. Ademaj, **S. Caban**, S. Schwarz, and M. Rupp. "A Spatially Consistent MIMO Channel Model With Adjustable K Factor". In: *IEEE Access* 7 (2019), pp. 110174–110186. DOI: 10.1109/ACCESS.2019.2934635. → see Page 91

[15] E. Zöchmann, **S. Caban**, C. F. Mecklenbräuker, S. Pratschner, M. Lerch, S. Schwarz, and M. Rupp. "Better than Rician: modelling millimetre wave channels as two-wave with diffuse power". In: *EURASIP Journal on Wireless Communications and Networking* 2019.1 (Jan. 2019), p. 21. ISSN: 1687-1499. DOI: 10.1186/s13638-018-1336-6. → see Page 104

[19] C. Mehlführer, **S. Caban**, and M. Rupp. "Measurement-based Performance Evaluation of MIMO HSDPA". In: *IEEE Transactions on Vehicular Technology* 59.9 (2010), pp. 4354–4367. DOI: 10.1109/TVT.2010.2066996.

[21] C. Mehlführer, **S. Caban**, and M. Rupp. "Cellular System Physical Layer Throughput: How Far Off Are We From The Shannon Bound?" In: *IEEE Wireless Communications* 18.6 (2011), pp. 54–63. DOI: 10.1109/MWC.2011.6108334. → see Page 121

[33] J. Rodríguez-Piñeiro, M. Lerch, J. A. García-Naya, **S. Caban**, M. Rupp, and L. Castedo. "Emulating Extreme Velocities of Mobile LTE Receivers in the Downlink". In: *EURASIP Journal on Wireless Communications and Networking* 2015.106 (Apr. 2015), pp. 1–14. ISSN: 1687-1499. DOI: 10.1186/s13638-015-0343-0. → see Page 141

[36] M. Lerch, **S. Caban**, E. Zöchmann, P. Svoboda, and M. Rupp. "Scaled-Time OFDM Experiments for Channels Exceeding the Cyclic Prefix". In: *Electronics Letters* 55.25 (2019), pp. 1370–1373. DOI: 10.1049/el.2019.2857. → see Page 155

[38] E. Zöchmann, M. Hofer, M. Lerch, S. Pratschner, L. Bernadó, J. Blumenstein, **S. Caban**, S. Sangodoyin, H. Groll, T. Zemen, A. Prokes, M. Rupp, A. Molisch, and C. Mecklenbräuker. "Position-Specific Statistics of 60 GHz Vehicular Channels During Overtaking". In: *IEEE Access* 7 (2019), pp. 14216–14232. ISSN: 2169-3536. DOI: 10.1109/ACCESS.2019.2893136. → see Page 158

## 4.3 Authored Conference Papers

[3] **S. Caban**, A. Disslbacher-Fink, J. A. G. Naya, and M. Rupp. "Synchronization of Wireless Radio Testbed Measurements". In: *Proc. International In-*

*strumentation and Measurement Technology Conference (I2MTC)*. 2011. DOI: 10.1109/IMTC.2011.5944089. → see Page 57

[4] M. Laner, **S. Caban**, P. Svoboda, and M. Rupp. "Time Synchronization Performance of Desktop Computers". In: *Proceedings of the International Symposium on Precision Clock Synchronization ISPCS'11*. 2011. DOI: 10.1109/ISPCS.2011.6070154.

[5] M. Lerch, E. Zöchmann, **S. Caban**, and M. Rupp. "Noise Bounds in Multicarrier mmWave Doppler Measurements". In: *European Wireless 2017 (EW2017)*. Dresden, Germany, May 2017.

[6] M. Lerch, **S. Caban**, E. Zöchmann, and M. Rupp. "Quantifying the Repeatability of Wireless Channels by Quantized Channel State Information". In: *IEEE 9th Sensor Array and Multichannel Signal Processing Workshop (SAM 2016)*. Rio de Janeiro, Brazil, July 2016. DOI: 10.1109/SAM.2016.7569702. → see Page 61

[8] **S. Caban**, J. A. García Naya, L. Castedo, and C. Mehlführer. "Measuring the influence of TX antenna spacing and transmit power on the closed-loop throughput of IEEE 802.16-2004 WiMAX". In: *Proc. IEEE Instrumentation and Measurement Technology Conference (I2MTC 2010)*. Austin, TX, USA, May 2010.

[9] **S. Caban**, J. A. García Naya, C. Mehlführer, and M. Rupp. "Measuring the Closed-Loop Throughput of 2x2 HSDPA over TX Power and TX Antenna Spacing". In: *Proc. 2nd International Conference on Mobile Lightweight Wireless Systems (Mobilight-2010)*. Barcelona, Spain, May 2010.

[12] S. Pratschner, E. Zöchmann, H. Groll, **S. Caban**, S. Schwarz, and M. Rupp. "Does a Large Array Aperture Pay Off in Line-Of-Sight Massive MIMO?" In: *International Workshop on Signal Processing Advances in Wireless Communications (SPAWC)*. Cannes, France, 2019, pp. 1–5. DOI: 10.1109/SPAWC.2019.8815590.

[13] S. Pratschner, **S. Caban**, D. Schützenhöfer, M. Lerch, E. Zöchmann, and M. Rupp. "A Fair Comparison of Virtual to Full Antenna Array Measurements". In: *International Workshop on Signal Processing Advances in Wireless Communications (SPAWC)*. Kalamata, Greece, 2018, pp. 1–5. ISBN: 978-1-5386-3511-7. DOI: 10.1109/SPAWC.2018.8445923.

[14] S. Pratschner, **S. Caban**, S. Schwarz, and M. Rupp. "A mutual coupling model for massive MIMO applied to the 3GPP 3D channel model". In: *European Signal Processing Conference (EUSIPCO)*. Kos, Greece, 2017, pp. 623–627. DOI: 10.23919/EUSIPCO.2017.8081282.

[16] E. Zöchmann, M. Lerch, S. Pratschner, R. Nissel, **S. Caban**, and M. Rupp. "Associating Spatial Information to Directional Millimeter Wave Channel Measurements". In: *IEEE 86th Vehicular Technology Conference (VTC2017-Fall)*. Toronto, Canada, Sept. 2017. DOI: 10.1109/VTCFall.2017.8287905.

[17] E. Zöchmann, M. Lerch, **S. Caban**, R. Langwieser, C. F. Mecklenbräuker, and M. Rupp. "Directional Evaluation of Receive Power, Rician K-factor and RMS Delay Spread obtained from Power Measurements of 60GHz Indoor Channels". In: *IEEE-APS Topical Conference on Antennas and Propagation in Wireless Communications (APWC 2016)*. Cairns, Australia, Sept. 2016.

[22] M. Rupp, J. A. García-Naya, C. Mehlführer, **S. Caban**, and L. Castedo. "On Mutual Information and Capacity in Frequency Selective Wireless Channels". In: *Proc. IEEE International Conference on Communications (ICC 2010)*. Cape Town, South Africa, May 2010. DOI: 10.1109/ICC.2010.5501942.

[23] M. Rupp, C. Mehlführer, and **S. Caban**. "On Achieving the Shannon Bound in Cellular Systems". In: *Proc. 20th International Conference Radioelektronika 2010*. Brno, Czech Republic, Apr. 2010.

[24] R. Nissel, E. Zöchmann, M. Lerch, **S. Caban**, and M. Rupp. "Low-Latency MISO FBMC-OQAM: It Works for Millimeter Waves!" In: *IEEE International Microwave Symposium (IMS)*. Hawaii, USA, June 2017. → **see Page 131**

[25] R. Nissel, **S. Caban**, and M. Rupp. "Experimental Evaluation of FBMC-OQAM Channel Estimation Based on Multiple Auxiliary Symbols". In: *IEEE 9th Sensor Array and Multichannel Signal Processing Workshop (SAM 2016)*. Rio de Janeiro, Brazil, July 2016.

[26] R. Nissel, **S. Caban**, and M. Rupp. "Closed-Form Capacity Expression for Low Complexity BICM with Uniform Inputs". In: *IEEE International Symposium on Personal, Indoor and Mobile Radio Communications (PIMRC)*. Hong Kong, P.R.China, 2015.

[27] M. Rindler, **S. Caban**, M. Lerch, P. Svoboda, and M. Rupp. "Swift Indoor Benchmarking Methodology for Mobile Broadband Networks". In: *IEEE 86th Vehicular Technology Conference (VTC2017-Fall)*. Toronto, Canada, Sept. 2017. DOI: 10.1109/VTCFall.2017.8288190.

[28] **S. Caban**, J. Rodas, and J. A. García-Naya. "A Methodology for Repeatable, Off-line, Closed-loop Wireless Communication System Measurements at Very High Velocities of up to 560 km/h". In: *Proc. International Instrumentation and Measurement Technology Conference (I2MTC 2011)*. Binjiang, Hangzhou, China, May 2011. DOI: 10.1109/IMTC.2011.5944019. → **see Page 136**

[29] **S. Caban**, R. Nissel, M. Lerch, and M. Rupp. "Controlled OFDM Measurements at Extreme Velocities". In: *Proc. of ExtremeCom'2014*. Galapagos Islands, Ecuador, Aug. 2014.

[30] E. Zöchmann, R. Langwieser, **S. Caban**, M. Lerch, S. Pratschner, R. Nissel, C. Mecklenbräuker, and M. Rupp. "A Millimeter Wave Testbed For Repeatable High Velocity Measurements". In: *European Wireless 2017 (EW2017)*. Dresden, Germany, May 2017.

[31] D. Schützenhöfer, E. Zöchmann, M. Lerch, S. Pratschner, H. Groll, **S. Caban**, and M. Rupp. "Experimental Evaluation of the Influence of Fast Movement on Virtual Antenna Arrays". In: *23rd International ITG Workshop on Smart Antennas (WSA 2019)*. Vienna, Austria, Apr. 2019.

[32] E. Zöchmann, **S. Caban**, M. Lerch, and M. Rupp. "Resolving the Angular Profile of 60 GHz Wireless Channels by Delay-Doppler Measurements". In: *IEEE 9th Sensor Array and Multichannel Signal Processing Workshop (SAM 2016)*. Rio de Janeiro, Brazil, July 2016.

[34] J. Rodríguez-Piñeiro, M. Lerch, P. Suárez-Casal, J. A. García-Naya, **S. Caban**, M. Rupp, and L. Castedo. "LTE Downlink Performance in High Speed Trains". In: *Proceedings of the 81st Vehicular Technology Conference (VTC2015-Spring)*. Glasgow, Scotland, May 2015. DOI: 10.1109/VTCSpring.2015.7145924.

[35] J. Rodríguez-Piñeiro, M. Lerch, T. Domínguez-Bolaño, J. A. García-Naya, **S. Caban**, and L. Castedo. "Experimental Assessment of 5G-Candidate Modulation Schemes at Extreme Speeds". In: *IEEE 9th Sensor Array and Multichannel Signal Processing Workshop (SAM 2016)*. Rio de Janeiro, Brazil, July 2016. DOI: 10.1109/SAM.2016.7569632.

[37] H. Groll, E. Zöchmann, S. Pratschner, M. Lerch, D. Schützenhöfer, M. Hofer, J. Blumenstein, S. Sangodoyin, T. Zemen, A. Prokes, A. Molisch, and **S. Caban**. "Sparsity in the Delay-Doppler Domain for Measured 60 GHz Vehicle-to-Infrastructure Communication Channels". In: *Proceedings of the IEEE ICC 2019*. May 2019. DOI: 10.1109/ICCW.2019.8756930.

[39] E. Zöchmann, C. F. Mecklenbräuker, M. Lerch, S. Pratschner, M. Hofer, D. Löschenbrand, J. Blumenstein, S. Sangodoyin, G. Artner, **S. Caban**, T. Zemen, A. Prokes, M. Rupp, and A. Molisch. "Measured Delay and Doppler Profiles of Overtaking Vehicles at 60 GHz". In: *IEEE 12th European Conference on Antennas and Propagation (EuCAP 2018)*. London, UK, Apr. 2018. DOI: 10.1049/cp.2018.0470.

[40] E. Zöchmann, M. Hofer, M. Lerch, J. Blumenstein, S. Sangodoyin, H. Groll, S. Pratschner, **S. Caban**, D. Löschenbrand, L. Bernadó, T. Zemen, A. Prokes, M. Rupp, C. Mecklenbräuker, and A. Molisch. "Statistical Evaluation of Delay and Doppler Spread in 60 GHz Vehicle-to-Vehicle Channels During Overtaking". In: *Proceedings of the 2018 IEEE-APS Topical Conference on Antennas and Propagation in Wireless Communications (APWC)*. Cartagena, Colombia, Sept. 2018, pp. 1–4. DOI: 10.1109/APWC.2018.8503750.

## 4.4 Publications authored during my Ph.D. thesis

### Authored Journals

[41] C. Mehlführer, **S. Caban**, and M. Rupp. "Experimental Evaluation of Adaptive Modulation and Coding in MIMO WiMAX with Limited Feedback". In: *EURASIP Journal on Advances in Signal Processing* 2008, Article ID 837102 (2008). DOI: 10.1155/2008/837102.

[42] **S. Caban** and M. Rupp. "Impact of Transmit Antenna Spacing on 2x1 Alamouti Radio Transmission". In: *Electronics Letters* 43, no. 4 (Feb. 2007), pp. 198–199. DOI: 10.1049/el:20073153.

[43] **S. Caban**, C. Mehlführer, R. Langwieser, A. L. Scholtz, and M. Rupp. "Vienna MIMO Testbed". In: *EURASIP Journal on Applied Signal Processing* 2006, Article ID 54868 (2006). DOI: 10.1155/ASP/2006/54868.

[44] M. Rupp, C. Mehlführer, **S. Caban**, R. Langwieser, L. W. Mayer, and A. L. Scholtz. "Testbeds and Rapid Prototyping in Wireless System Design". In: *EURASIP Newsletter* 17.3 (Sept. 2006), pp. 32–50. ISSN: 1687-1421.

### Authored Conference Papers

[45] C. Mehlführer, **S. Caban**, J. A. G. Naya, and M. Rupp. "Throughput and Capacity of MIMO WiMAX". In: *Conference Record of the Fourtysecond Asilomar Conference on Signals, Systems and Computers, 2009*. Pacific Grove, CA, USA, Nov. 2009. DOI: 10.1109/ACSSC.2009.5469848.

[46] Q. Wang, **S. Caban**, C. Mehlführer, and M. Rupp. "Measurement based Throughput Evaluation of Residual Frequency Offset Compensation in WiMAX". In: *Proc. 51st International Symposium ELMAR-2009*. Zadar, Croatia, Sept. 2009.

[47] **S. Caban**, C. Mehlführer, G. Lechner, and M. Rupp. "Testbedding MIMO HSDPA and WiMAX". In: *Proc. 70th IEEE Vehicular Technology Conference (VTC2009-Fall)*. Anchorage, AK, USA, Sept. 2009. DOI: 10.1109/VETECF.2009.5378995.

[48] J. A. García-Naya, C. Mehlführer, **S. Caban**, M. Rupp, and C. Luis. "Throughput-based Antenna Selection Measurements". In: *Proc. 70th IEEE Vehicular Technology Conference (VTC2009-Fall)*. Anchorage, AK, USA, Sept. 2009. DOI: 10.1109/VETECF.2009.5378992.

[49] C. Mehlführer, **S. Caban**, and M. Rupp. "MIMO HSDPA Throughput Measurement Results in an Urban Scenario". In: *Proc. 70th IEEE Vehicular Technology Conference (VTC2009-Fall)*. Anchorage, AK, USA, Sept. 2009. DOI: 10.1109/VETECF.2009.5378994.

[50] T. Zemen, **S. Caban**, N. Czink, and M. Rupp. "Validation of Minimum-Energy Band-Limited Prediction using Vehicular Channel Measurements". In: *Proc. 17th European Signal Processing Conference (EUSIPCO 2009)*. Glasgow, Scotland, UK, Aug. 2009.

[51] C. Mehlführer, **S. Caban**, M. Wrulich, and M. Rupp. "Joint Throughput Optimized CQI and Precoding Weight Calculation for MIMO HSDPA". In: *Conference Record of the Fourtysecond Asilomar Conference on Signals, Systems and Computers, 2008*. Pacific Grove, CA, USA, Oct. 2008. DOI: 10.1109/ACSSC.2008.5074632.

[52] C. Mehlführer, **S. Caban**, and M. Rupp. "Measurement Based Evaluation of Low Complexity Receivers for D-TxAA HSDPA". In: *Proc. of the 16th European Signal Processing Conference*. Lausanne, Switzerland, Aug. 2008.

[53] M. Rupp, **S. Caban**, and C. Mehlführer. "Measurements of MIMO HSDPA and WiMAX Transmissions". In: *15th International Conference on Systems, Signals and Image Processing, IWSSIP 2008*. Bratislava, Slovakia, June 2008.

[54] **S. Caban**, C. Mehlführer, L. W. Mayer, and M. Rupp. "2x2 MIMO at Variable Antenna Distances". In: *Proc. of the IEEE Vehicular Technology Conference (VTC 2008 Spring)*. Singapore, May 2008. DOI: 10.1109/VETECS.2008.276.

[55] C. Mehlführer, **S. Caban**, and M. Rupp. "An Accurate and Low Complex Channel Estimator for OFDM WiMAX". In: *3rd International Symposium on Communications, Control and Signal Processing (ISCCSP 2008)*. St. Julians, Malta, Mar. 2008. DOI: 10.1109/ISCCSP.2008.4537355.

[56] M. Rupp, **S. Caban**, and C. Mehlführer. "Challenges in Building MIMO Testbeds". In: *Proc. of the 13th European Signal Processing Conference (EUSIPCO 2007)*. Poznan, Poland, Sept. 2007.

[57] M. Wrulich, **S. Caban**, and M. Rupp. "Testbed Measurements of Optimized Linear Dispersion Codes". In: *Proc. of the ITG Workshop on Smart Antennas*. Feb. 2007.

[58] L. W. Mayer, M. Wrulich, and **S. Caban**. "Measurements and Channel Modeling for Short Range Indoor UHF Applications". In: *Proc. of the European Conference on Antennas and Propagation, EuCAP 2006*. Nov. 2007.

[59] **S. Caban**, C. Mehlführer, A. L. Scholtz, and M. Rupp. "Indoor MIMO Transmissions with Alamouti Space-Time Block Codes". In: *Proc. of the 8th International Symposium on DSP and Communication Systems, DSPCS 2005*. Noosa Heads, Australia, Dec. 2005.

[60] C. Mehlführer, **S. Caban**, M. Rupp, and A. L. Scholtz. "Effect of Transmit and Receive Antenna Configuration on the Throughput of MIMO UMTS Downlink". In: *Proc. of the 8th International Symposium on DSP and Communication Systems, DSPCS 2005*. Noosa Heads, Australia, Dec. 2005.

[61] C. Mehlführer, S. Geirhofer, **S. Caban**, and M. Rupp. "A Flexible MIMO Testbed with Remote Access". In: *Proc. of the 13th European Signal Processing Conference (EUSIPCO 2005)*. Antalya, Turkey, Sept. 2005.

[62] E. Aschbacher, **S. Caban**, C. Mehlführer, G. Maier, and M. Rupp. "Design of a Flexible and Scalable 4x4 MIMO Testbed". In: *Proc. of the 11th IEEE Signal Processing Workshop (DSP 2004)*. Taos Ski Valley, NM, USA, Aug. 2004. DOI: 10.1109/DSPWS.2004.1437937.

# 5 Publications Included

## 5.1 Hardware and Methodology

[1] **S. Caban**, J. A. G. Naya, and M. Rupp. "Measuring the Physical Layer Performance of Wireless Communication Systems". In: *IEEE Instrumentation & Measurement Magazine* 14.5 (2011), pp. 8–17. DOI: 10.1109/MIM.2011.6041377. → see Page 35

[2] M. Lerch, **S. Caban**, M. Mayer, and M. Rupp. "The Vienna MIMO Testbed: Evaluation of Future Mobile Communication Techniques". In: *Intel Technology Journal* 18 (3 2014), pp. 58–69. → see Page 45

[3] **S. Caban**, A. Disslbacher-Fink, J. A. G. Naya, and M. Rupp. "Synchronization of Wireless Radio Testbed Measurements". In: *Proc. International Instrumentation and Measurement Technology Conference (I2MTC)*. 2011. DOI: 10.1109/IMTC.2011.5944089. → see Page 57

[6] M. Lerch, **S. Caban**, E. Zöchmann, and M. Rupp. "Quantifying the Repeatability of Wireless Channels by Quantized Channel State Information". In: *IEEE 9th Sensor Array and Multichannel Signal Processing Workshop (SAM 2016)*. Rio de Janeiro, Brazil, July 2016. DOI: 10.1109/SAM.2016.7569702. → see Page 61

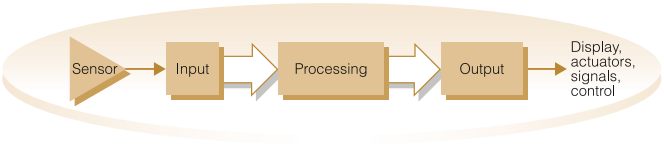


# Measuring the Physical Layer Performance of Wireless Communication Systems

**Part 33 in a series of tutorials on instrumentation and measurement**

*Sebastian Caban, José Antonio García Naya, and Markus Rupp*

Measuring the physical layer performance of wireless radio communication systems is one important step in clearly understanding their behavior in real-world, that is, non-simulation, environments. Unfortunately, measurements in wireless communications are extremely expensive and time-consuming. In fact, they require researchers to deal with non-artificial, realizable, real-world problems. They also require these researchers to have experience in computer engineering, telecommunication engineering, electrical engineering and often even mechanical engineering. Finally, they require teamwork to set up complete systems instead of dealing with single, isolated, numerical environments.

In this era of low-cost and ever more powerful personal computers, more and more research groups are abandoning hardware-based research in favor of "simpler," simulation-based research. If this tendency continues, soon, only a few research groups will be left that publish results based on large-scale measurement setups. One might think that measurements have lost most of their appeal.

At the end of the day, each research group has to decide if it is up to the challenge of measurements that cost time and money. To ease the non-financial part of this challenge, in this tutorial, we offer some advice and a few pointers based on our experience [1].


## Problem Statement

Let us examine the wireless communication system in Fig.1. This simple set-up can easily be extended to resemble a complete wireless communication system, and at the same time, it also serves as an example for the tutorial.

The set-up consists of three blocks. Data are generated in the block named 'TX'. These data are next transmitted over a wireless radio channel. Finally, the data received are processed in the 'RX' block to calculate the figure of merit of the data transmission, namely the throughput typically expressed in Mbit/s. We are interested in the physical-layer throughput that can be achieved in a given, specific, real-world scenario – with actual


1094-6969/11/$25.00©2011IEEE

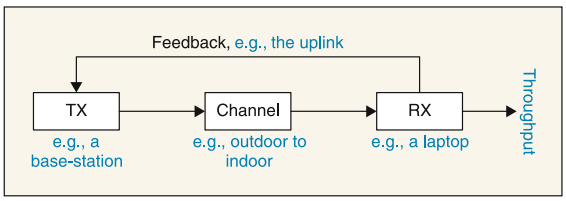


***Fig. 1.*** A sample problem set-up; the downlink of the physical layer of a wireless communication system.

physical channels, transmitters, receivers, and a standard-conforming transmission.

## Measurement Result

Fig. 2 shows the result of a measurement following the ideas described in this tutorial. The measurement was carried out in 2009 in downtown Vienna, Austria. On the y-axis, we plot the figure of merit, namely, the physical-layer throughput of the wireless radio transmission under investigation. As the system under investigation adaptively improves the signal-to-noise ratio (SNR) at the receiver, we do not measure over SNR. Therefore, on the x-axis, we plot the total transmit power, that is, the power transmitted by all active transmit antennas. As a lead, we also plot the SNR and received power for a transmission that does not adaptively improve the SNR (the two additional x-axes) and point out the area of typical operation.

Our research target is the throughput of a wireless communication system using two antennas at the transmitter and two antennas at the receiver (the '2x2' curve). We compare this throughput to the throughput of a reference system having only one antenna at the transmitter but still two antennas at the receiver (the '1x2' curve). We conclude that the 2x2 system is significantly better than the 1x2 system in the area of typical operation (see the '2x2 minus 1x2' curve). Furthermore, we compare the measured throughput to a theoretical bound, namely in this case, the estimated capacity of the channel (the orange '2x2 capacity' curve), that is, the maximum theoretical throughput allowed by the channel for the 2x2 transmission. To visualize the precision of our measurement, we draw confidence intervals (the small black vertical lines).

As simple as it may look at first glance, it took us several years to obtain such figures efficiently in a reproducible and repeatable fashion for modern wireless communication standards such as WiMAX, HSDPA (the example in Fig. 2), LTE, and LTE advanced. As space is limited, we are only able to roughly sketch what steps we took to obtain such measurement results in real-world scenarios.

## Still the First Step: Simulation

Starting with the work of Ronald A. Fisher in 1935, there exist many excellent books on the design of experiments [2], [3]. They all advise us of the importance of carefully planning experiments and of following the scientific method. Reality, however, is different. Expensive hardware is often purchased only to lie unused in the corner of a laboratory. Therefore, browsing catalogs and homepages of several manufacturers to

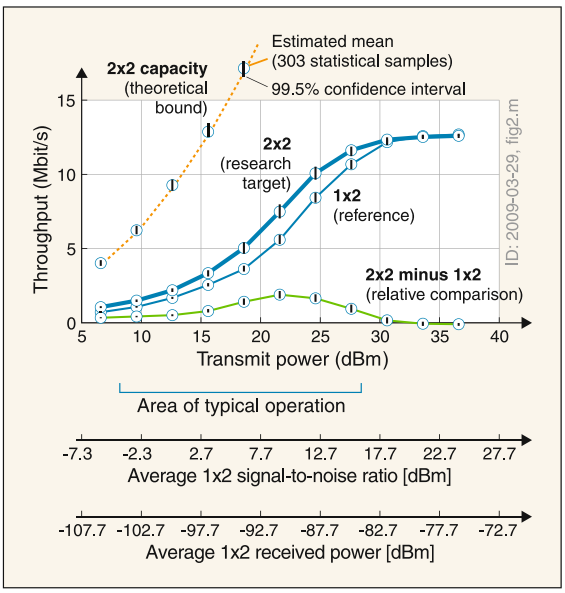


***Fig. 2.*** A sample measurement result.

buy "fancy hardware" is not the most intelligent starting point for experimentally evaluating wireless communication systems. Rather, after a thorough experiment design, simulation is the first and most important step to avoid unnecessary costs as well as efforts. Such simulations should not only concentrate on the "kernel" of the problem to be investigated but should be designed to simulate the measurement environment.

Let us now reexamine the set-up shown in Fig. 1. Being only one among many possible setups, we use it as an example to highlight important properties of the simulation to be carried out (see Fig. 3).

At first, the whole set-up has to be split up into distinct blocks. These blocks should be implemented as separated software modules, for example functions. A strict separation of the different blocks is necessary, as in the next step these simulated blocks will be mapped onto different hardware devices such as a transmitter and a receiver. These devices are often physically separated; therefore, global information cannot be used to control them. Only for settings that do not change during the course of an experiment (for example, the name of a computer or the identifier of the measurement), global information

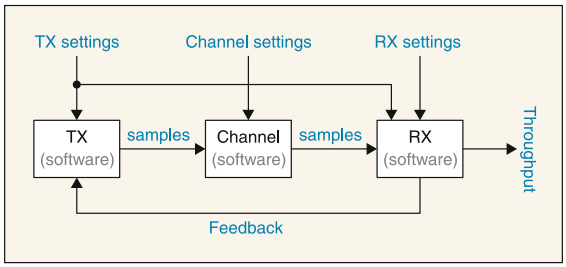


***Fig. 3.*** A sample simulation/measurement set-up. Every block represents a software-function/hardware-block. Note the limited information passed between the different blocks.

may be used to simplify the measurement software. However, because it is fixed throughout an experiment, such global information decreases flexibility and should be avoided as much as possible. Instead, data structures containing the settings should be passed between the different blocks. This leads to increased flexibility when very different sets of settings have to be selected repeatedly during a measurement (for example, the set of transmit power levels or the set of antenna configurations).

Often, the information passed between different blocks has to be very restricted, as in the final experiment, where signaling bandwidths may be limited and subject to significant latency. Sometimes, it may also happen that desired information cannot be passed at all between different blocks as this information will not be available in the measurement. For example, in Fig. 3, channel properties are generated inside the channel block without the possibility of passing them to and from the channel. In the simulation, as in the measurement, the true noise power and channel are both unknown. The noise realization is also not kept equal for consecutive blocks as preferred in Monte Carlo simulations that compare different transmission schemes. On the other hand, the same set of blocks (chosen from a large pre-generated set of blocks) may always be transmitted. This saves time by not having to generate them on-line at the transmitter.

Still, even if a simulation is carried out with the greatest care, unforeseen effects may be revealed later in the measurement. For example, using commercial-grade radio-frequency components may result in in-phase to quadrature imbalance and non-flat frequency responses next to nonlinearities. Whether such effects should be calibrated out of the hardware, if this is possible at all, depends on the problem statement. Whether such effects should be included in or neglected in the simulation once the effects are discovered depends on the degree of their impact on the result.

Other than this, one may be able to infer key parameters of the hardware set-up from the simulation. Accurate knowledge of such parameters, for example the peak SNR at the receiver, may guide the design and implementation of the hardware required for the measurement. Still, in academic research, it may sometimes be better to design the hardware one magnitude more precise than required such that a "bound" can be measured and compared to a practical, meaningful implementation.

Last but not least, one should not forget the unloved step of verification and validation that should be natural in research.

## How to Combat Fading?

Isolated, absolute throughput measurements of wireless communication links tend to lead to different results in practice depending on exactly when and where they are carried out. This happens for two reasons:

- First, channels observed in wireless communications experience "small scale fading". In other words, the received signal power may change by several orders of magnitude when moving the receiver or objects in its vicinity only slightly. For a signal transmitted at 2.5 GHz, moving objects on the order of 6 cm, namely half a wavelength, can cause a large change in the power of the received signal.
- Second, channels observed in wireless communication experience "large scale fading". That is, moving behind an obstruction, such as a wall, building, or hill, will lead to fundamentally different received signal strengths depending on the observed shadowing.

To combat large and small scale fading, one may carry out so-called drive test measurements. That is, one can make measurements at several positions on a path driven with the receiver or the transmitter and use the data recorded to plot empirical cumulative distributions of the values observed.

In this tutorial, we focus on another way of dealing with fading in wireless measurements. The basic idea is simple, and Fig. 2 shows the results of such a measurement taken using the technique we describe now. Detailed reasons for the steps we recommend taking will be given in the following sections.

- Step 1: Fix the physical position of the transmitter TX (the base-station).
- Step 2: Fix the total transmit power; that is, the total power transmitted on all available transmit antennas. Using a power meter, this power can be easily measured at the input of the transmit antennas and it is plotted on the last x-axis of Fig. 2.
- Step 3: Move the receiver (the laptop) to a distinct position within an area of approximately three times three wavelengths (36 cm times 36 cm for a transmission at 2.5GHz) by the use of an accurate XY-positioning table. By doing so, the receiver experiences small-scale fading but avoids large-scale fading.
- Step 4: Transmit all schemes of interest "quickly". In the example, to measure the values plotted in Fig. 2, we conducted a "2x2 transmission" and a "1x2 transmission" using exactly the same set-up: exactly the same transmitter position, total transmit-signal power, and receiver position. But more important, as we transmit all schemes consecutively within the channel coherence time, they experience exactly the same channel realization.
- Step 5: Repeat Steps 3 and 4 to obtain more throughput values of the same small-scale fading scenario at the same transmit power. Each of these throughput values represents a statistical sample and, if not too many of them are taken in the limited area available, the samples are statistically independent [4].

  The results shown in Fig. 2 were obtained from 303 statistical samples taken uniformly in a grid of three times three wavelengths. Choosing random positions would also have been an option, but when measuring many realizations, systematic sampling tends to minimize the correlation between the samples obtained. In the end, the choice of sampling procedure is a trade-off between the loss of precision due to correlation and possible errors introduced by a systematic sampling approach [3, pg. 221].
- Step 6: Average the (in our example 303) throughput values for each scheme to obtain the best estimate for the


"mean throughput" at each transmit-power level (the circles shown in Fig. 2), as no additional information other than independent samples is available. Of course, any other estimator, as for example "the median", would also work with this methodology.

- Step 7: Bootstrap (resample) the throughput values to obtain $BC_a$ confidence intervals for the mean (the small black vertical lines shown in Fig. 2) [5], [6].
- Step 8: Repeat Steps 2 to 7 for different transmit power levels (the primary x-axis in Fig. 2) to obtain the mean throughput over transmit power. In the measurements we performed, we achieved these different power levels by precisely attenuating the transmit signal using a combination of digital and analog attenuation which we calibrated for linearity prior to the measurement. Note that this step accounts for the avoided large scale fading.
- Step 9: Name each measurement uniquely (see the measurement identifier "ID: 2009-03-29" at the right-hand side of Fig. 2). Next, automatically backup all scripts and source code with the measurement results, and take many pictures of the measurement set-up. Experience has shown that when measurement results are reused years later, such information is indispensible, especially when details of the measurements that were not important during the initial measurement become relevant, as for example, if a door were open.

Over the course of the last few years we have repeatedly and successfully tested this methodology on most modern wireless communication systems in several urban and non-urban scenarios. In contrast to other methodologies, for example drive test measurements, this methodology does not allow for an *efficient* comparison of how a transmission scheme behaves in very different scenarios, even though this would be possible by repeating all of the steps above over and over. On the other hand, if such a comparison is not intended and only the behavior of a communications system in specific scenarios is of interest, the above-presented methodology may be the methodology of choice.

## Why to Measure Over Transmit Power?

In wireless communications, the figure of merit (for example, the throughput) is usually thought of as a function of SNR or signal-to-interference noise ratio (the first additional x-axis in Fig. 2). We do things a bit differently for a few reasons.

First, modern wireless communication standards employ multiple antennas at the transmitter and combine this change with techniques such as channel adaptive precoding or beam-forming. While keeping the transmit power fixed, such techniques adaptively modify the transmit signal to increase the SNR at the position of the receiver. As a consequence, the performance of the wireless transmission is improved. Plotting the corresponding performance curve over the SNR at the receiver would cancel out all of this improvement, thus giving a misleading picture of reality (although still a correct picture for a given SNR).

Second, assume that your task is to compare two equal wireless communication links employing different antennas at the transmitter. The first antenna has a gain of 20 dBi, while the second one offers a gain of 5 dBi. Consequently, the communication system with the 20 dBi antenna will experience a higher throughput. But, if one plots the throughput of these two communication systems over the SNR at the receiver, their performance will be exactly equal (as the scenario is linear and equal in both cases, the throughput is only a function of the SNR). This reasoning also holds for different antenna orientations, different antenna polarizations, different noise figures of the receiver, and for different shadowing by walls, for example.

Third, channels in wireless communication experience fading. This leads to an instantaneous SNR at the receiver that is different for measurements at different receive antenna positions. Therefore, in simulations, researchers usually plot the 'expected SNR' on the x-axis which may typically even be known beforehand as the channel follows a given known model with clearly defined parameters. In measurements, however, this value first has to be estimated over time and space, assuming that the system observed is ergodic. But even more problematic, a specific value for the expected SNR at the receiver cannot be set but only be observed with the precision of possibly only a few measurements.

On the other hand, even if we measure over transmit power, we still express the results additionally in terms of SNR at the receiver. Therefore, we plot the SNR in Fig. 2 (the second additional x-axis) only for the 1x2-link and call it "average 1x2-SNR". As the 2x2 link operates using channel adaptive beam-forming, its SNR at the receiver is significantly better, and, therefore, the throughput curve is shifted to the left. This effect, that may even vary in magnitude with SNR, is not cancelled out by plotting over transmit power rather than plotting over the SNR. As a general rule: Never plot systems that adaptively improve the SNR over SNR.

## Everything is Relative

Let us rethink the setup in Fig. 2, this time from a slightly different point of view. Are we really interested in the absolute performance of a communication system at a specific transmit power or SNR, or are we actually interested in the improvement that a new system delivers over its predecessor or any other reference we have in mind? The difference between these two viewpoints changes the way we should measure and present our results.

First, the absolute values on the x-axis loose importance. We know beforehand in which region the old, known system (for example, the 1x2-system in Fig. 2) was operated. Therefore, its successor will be operated in the same region of the x-axis as the total transmit power will not change when upgrading from one system to the next one. Whether a certain throughput is achieved at a certain SNR is one thing, but what is of more interest is the performance increase of the new system (or more generally, the performance relative to a known system).

Second, we always draw at least two curves: one for a system that is known and a second one for the system under investigation. At best, we choose a well-known curve as a reference so our results can be compared to others by placing the two results on top of each other in image editing software and matching them (which turned out to be a convenient way for validating our own results). Sometimes we prefer a different reference curve, namely the unconstrained mean channel capacity assuming Gaussian input signals and full/no channel knowledge at the transmitter. As this curve is only a property of the channel (and not the communication system) it is handy as a reference that is not linked to the transmission scheme being investigated. We have also plotted this curve in Fig. 2. It is the orange dotted curve that represents what the 2x2-system could theoretically achieve. In fact, it is "quite far away" from the achieved throughput, leaving much room for improvement in the years to come.

**Whether a certain throughput is achieved at a certain SNR is one thing, but what is of more interest is the performance increase of the new system (or more generally, the performance relative to a known system).**

On the other hand, focusing on relative results also influences the measurement method as we can easily reduce the uncertainty in our results by a technique often referred to as blocking [3]. The basic idea is simple: when we compare the throughput performance of a 2x2-system to the performance of a 1x2-system, we measure these two systems in rapid succession. Instead of first measuring the 2x2-system for several receive antenna positions and then the 1x2-system for several receive antenna positions, we make sure that the transmissions are performed over the same channels. Therefore, when subtracting the two performance curves from each other (the green curve in Fig. 2) the standard deviations of the error do not add. In fact, as the two throughput curves are correlated, the uncertainty of the throughput difference is less than the uncertainty of the 2x2-system throughput or the 1x2-system throughput alone (as long as the systems are not saturated). This behavior can be easily observed in Fig. 2 by inspecting the decreased confidence intervals of the difference of the two schemes.

Making all measurements relative to an initial power simplifies the measurement procedure in another way as we do not need to know the absolute level of the transmit power anymore. We only have to make sure that we can precisely attenuate the transmit signal. If required at all, the absolute scale of the x-axis can be inferred afterwards from the reference curve or a reference measurement.

## The Real World Is Not Symmetric

Modern wireless communication systems employ multiple antennas at the transmitter site and at the receiver site. Unlike the situation that is all-too-frequently found in simulations, in real life, the polarization as well as the beam patterns of these antennas will never all be equal. Therefore, the expected channel attenuation of a MIMO system will be different for every transmit-receive antenna pair. More technically speaking, the channel matrix will not be independently and identically distributed.

Let us now take again a closer look at Fig. 2. In this figure, we compare the throughput of a system with two transmit antennas (the 2x2 curve) to the throughput of a system with only one transmit antenna (the 1x2 curve). In reality, it is now very unlikely that each of the two transmit antennas of the 2x2 system will deliver the same fraction of the total performance given by the whole system. For example, one of the transmit antennas might have the same polarization as the receive antennas or point more towards their direction. Consequently, a direct comparison of the 2x2 system with a 1x2 system using just one of the two possible transmit antennas would be unfair.

Fig. 4 illustrates this issue. Next to the throughput of the 2x2 system, we have also plotted the performance of a 1x2 system using the first of the two transmit antennas, as well as the performance of a 1x2 system using the second transmit antenna (the bottom dashed curve in Fig. 4). Note that the performance of the two different 1x2 systems is significantly different, although both are measured over exactly the same channels as the 2x2 system.

In our experiments, to make a fair comparison between the 2x2 and the 1x2 systems, we always compare the 2x2 system to the average performance of the two possible 1x2 subsystems, both measured over the same channels as the 2x2 system (see the bottom solid curve in Fig. 4 that is also plotted in Figs. 2 and 5). By doing so, we ensure that all four possible transmission links of the 2x2 transmission are also measured equally often during the two 1x2 transmissions in which we measure two links each.

When comparing, for example, a 4x4 transmission to a

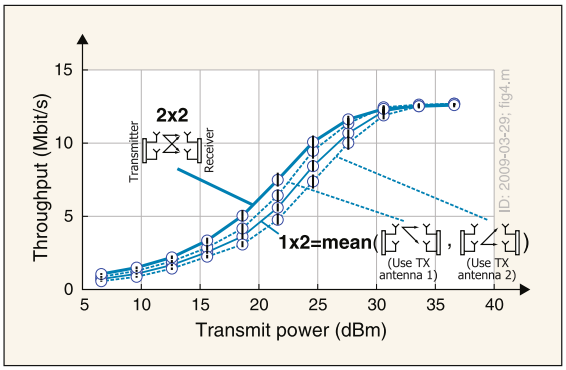


***Fig. 4.*** When comparing a transmission with two transmit antennas (2x2) to a transmission using only one transmit antenna (1x2), we average over the two possible 1x2 transmissions to make the comparison fair.

1x1 transmission, we perform one 4x4 transmission and sixteen 1x1 transmissions. To speed things up we only measure four transmissions from one transmit antenna to four receive antennas and evaluate from this data the sixteen 1x1 transmissions. In simulations, we proceed similarly. We first create a 4x4 channel matrix that is not independently and identically distributed. Next, we use this channel matrix to simulate the 4x4 transmissions as well as the sixteen 1x1 transmissions. The same holds true for any other comparison. In the end, each element of the channel matrix should be used equally often to make the comparison fair.

## How Precise Is Accurate Enough?

Remember, every simulation and measurement result consists of a value (the best estimate of the particular quantity of interest) and an associated measurement uncertainty (the probability distribution characterizing a reasonable dispersion of the value, visualized, for example, by the confidence intervals in Fig. 2). Whereas beginners are typically only interested in the measurement values, dealing with uncertainty has always been state of the art and it has been standardized since 1993 in the "Guide to the Expression of Uncertainty in Measurement" [7].

As explained above, the results shown in Fig. 2 were obtained from 303 statistical samples *(namely independent throughput measurements)* for each transmit-power level and for each transmission scheme. The dots represent the best estimate for the mean throughput at each transmit-power level *(namely, the average throughput, as no knowledge other than the samples was available)*. The black vertical lines represent the corresponding 99.5% confidence intervals for the mean. That is, if the measurement were to be repeated, in 99.5% of the repetitions, the unknown true, average, mean-scenario-throughput would lie within these confidence intervals *(namely, the 99.5% $BC_a$ confidence intervals obtained by bootstrapping the throughput values obtained)*.

Next, remember, the precision of a sample mean in a Monte Carlo simulation can be increased by a factor of $n$ by simulating $n^2$ samples (given that the samples drawn from the same distribution are independent). The same holds true for a well-designed measurement up to the point when the samples become correlated as they are measured in a small area. Unfortunately, techniques such as multi-core-measuring or cluster-measuring usually do not exist. Then, the only solution to keep the measurement time at a reasonable level is a more careful experiment design and the implementation of, for example, so-called variance reduction techniques [2], [3], [4].

Still, it is not beneficial to simulate the throughput of a wireless communication system with a precision of 0.001%, even if this were possible for a given model at the expense of needing to use a fast computer; the relevance of the last digits of this result will be questionable. In other words, the conclusions to be drawn would typically not change if the result were simulated only with a precision of 1%. The simulation time, on the other hand, will change by a factor of a million.

As the old saying goes, "5% is pretty good; 1% is wrong anyway." Of course, these numbers should not be taken for granted. Still, there is more truth in them than we might think at first glance. Anyone who has ever tried to reproduce an outdoor wireless measurement in another city will see the accuracy of the results obtained with a different perspective. Even repeating a measurement indoors can be a difficult endeavor.

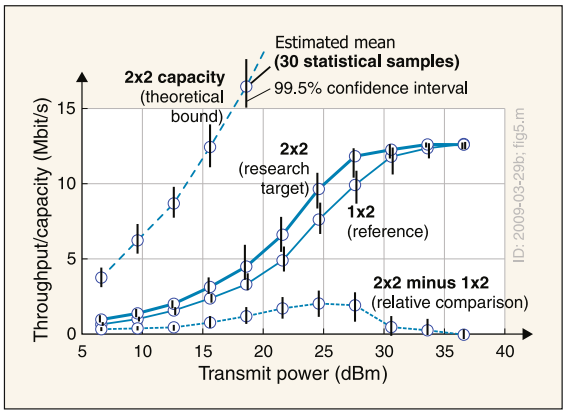


***Fig. 5.*** The same scenario as in Fig. 2, but only a tenth of the statistical samples were measured this time. Note that the confidence intervals for the relative comparison are smaller than those of the 2x2 curve and the 1x2 curve that already overlap. Compared to Fig. 2, the confidence intervals are about three times larger, the measurement time is reduced by a factor of 10, and the conclusion (the relative comparison is greater than zero) does not change.

To test the ideas presented above, we repeated the measurement shown in Fig. 2, but in contrast, only measured a tenth of the statistical samples for each transmit-power level, that is, 30 samples (see Fig. 5). As a consequence, on the one hand, the measurement time was reduced by a factor of ten. On the other hand, the confidence intervals increased only by a factor of roughly three. Note that the conclusion that the transmission with two antennas is significantly better (99.5% significance level) than the transmission using only one transmit antenna can still be drawn up to a transmit-power level of approximately 30 dBm (as the confidence intervals for the difference do not touch the x-axis). Note again that the confidence intervals of the difference curve are much smaller than those of the other curves as the latter are correlated. Of course, 30 samples are only sufficient if we are interested in these relative results. But frequently, only relative results are of interest.

## Buying Expensive Black Boxes

Once the initial simulation is finished, the next step consists of browsing the catalogs of different vendors and starting to spend lots of money on "fancy" hardware. But wait! There is one thing that we have learned during the last years the hard way: hardware does not work out of the box!

So we should rethink our strategy and carefully consider *how* to buy hardware for a wireless communications test bed and what important points need to be considered.

Let us, for example, take a closer look at the digital baseband hardware. Such hardware can be bought from a variety of vendors in very different price ranges. In contrast to standard personal computer parts, for example, such specialized hardware is sold in very small quantities. Sometimes, it is even

assembled directly for the paying customer. Still, that does not hinder most companies in this field from pushing out new and more powerful products on a regular basis. So how is it possible for these hardware manufacturers to keep up with ever-shorter product life cycles?

On the one hand, the price for digital signal processing hardware in wireless communications is premium, as it has to include not only a large portion of the company's profit but also of the development costs. On the other hand, *you* will be the alpha tester, typically even for demo examples and user manuals. The effort required to make such hardware work properly is often substantially underestimated. In our experience, if good support is not included and you do not have months of time to debug somebody else's hardware, there is little you can do.

Recently, the advent of reprogrammable hardware enriched the quest for buying hardware that really works by so-called firmware upgrades. A really wonderful idea in principle, but the possibility of firmware upgrades did not actually increase the quality of hardware but rather actually decreased it. The reason is very simple. Before the concept of firmware upgrades existed, a company had to take back a product if it did not work properly, which implied high costs. Now, all a company has to do is to release a firmware upgrade on their homepage. Continuing this train of thought, companies *could* now even sell reprogrammable products that are not thoroughly tested or even refuse to work at all. Looking at the bug-fix lists of certain products, no other conclusion seems reasonable for us besides that a product with such a long bug-fix list could have never worked flawlessly at the time it was introduced to the market. Fortunately, this argument can also be turned around. In our experience, hardware that does not allow for firmware upgrades tends to be more robust than hardware that allows for firmware upgrades. While experience has shown that this hypothesis might be true, the reason for this could also be that products without firmware are just simpler and therefore do not fail as often. Still, the general trend is undeniable. When buying a product that allows for firmware upgrades, one should be prepared to wait for the updates and even to fight for them (and based on our experience, this can take years, and holds true for almost every product).

Summarizing, one has to be prepared to buy hardware with inputs and outputs and little to no documentation on the inside. In other words, one has to be prepared to buy expensive black boxes that allow for firmware upgrades and typically do not work out of the box (see Fig. 6).

Knowing about this, the key task in buying hardware for a test bed is not only to choose the right black box from the right vendor, but more importantly, the right black box size (see Fig. 7):

- One way is to buy the hardware in one complex piece: At first glance, this also seems to be the least-time demanding task. All that has to be done is to search for an appropriate piece of usually very powerful and flexible hardware that suits the desired purpose, next to maybe writing an application for funding this piece of hardware.

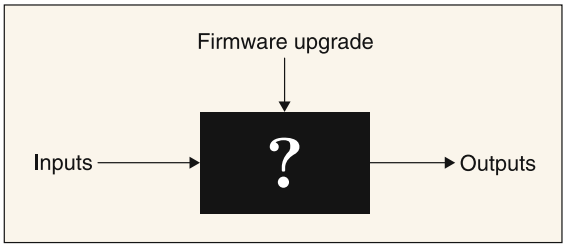


***Fig. 6.*** Every piece of hardware bought is more or less a black box. It has inputs, outputs, and the possibility of a firmware upgrade, but little or nothing is documented about what is inside.

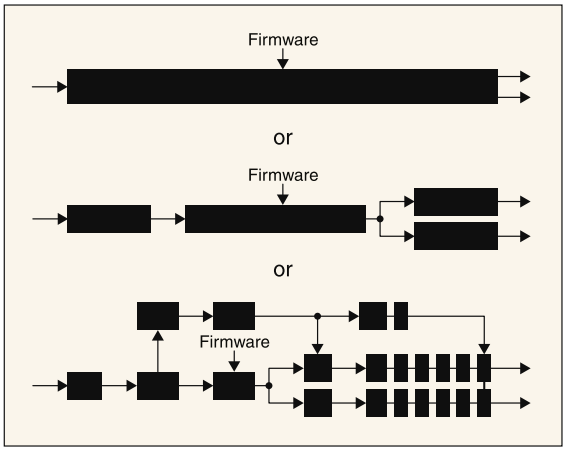


***Fig. 7.*** "The black box problem": should we buy the hardware in one complex piece, in a few pieces of moderate complexity, or in a lot of very small but simple pieces that can be easily checked and repaired?

  However, this approach will be prone to fail for the reasons outlined above: Almost certainly, the hardware will simply not work as desired out of the box. Unfortunately, a researcher is then at the mercy of the hardware manufacturer to release new firmware. Trying to correct the problem will, on the other hand, typically also fail because of poor documentation.
- The other extreme is to assemble the hardware from many small and simple pieces. These small pieces of hardware are relatively cheap. They can be bought from a variety of different vendors. And most important, it is possible to exactly specify their functionality and interfaces prior to purchase. The implications for the time after purchase are straightforward. First, it is relatively easy to understand and check the functionality of the hardware bought. Second, it is also relatively easy to prove to the vendor by measurements that the hardware does not fulfill its advertised specifications. Therefore, experience has shown that vendors will (have to) correct their products. Third, if a product does not live up to its expectations, buying a better-suited product from a different vendor is a suitable option. Fourth, if a product does not work as advertised and the vendor refuses to repair it for obscure reasons, writing it off and buying an alternative product may be preferred over any


legal actions. Fifth, because they are less complex and, therefore, often more thoroughly tested, small pieces of hardware are less likely to fail in general. Finally, the different pieces of hardware can be reused for different experiments, assembled in a different way, and so on. In other words, the investment made in a small piece of hardware is not lost after the measurements which it was purchased for are finished.

Note that we do not consider a carrier board with several different modules interconnected by proprietary interfaces as modular. In our opinion, this is one black box featuring interchangeable modules that might fail because it is very unlikely that they have been tested in the way you will assemble them. Conversely, a rubidium frequency normal connected to an oscillator via a 50 ohm coaxial cable (a well-defined standard) or a power meter connected to a PC via a local area network connection (also, a well-defined standard) is very likely to work as expected.

On the downside, assembling small black boxes to obtain a complex piece of hardware takes considerable time, expert knowledge, and expensive (measurement) equipment for testing. There is absolutely no need to redesign things that others have designed, such as a GPS receiver where only its outputs are of interest and it is very unlikely that "half a GPS receiver" might be needed in a future experiment.

The art of efficiently and effectively buying hardware for a measurement is now, in our opinion, to maximize the size of the black boxes purchased while still being able to fully specify and test their functionality and to maintain flexibility for both present and future experiments.

## Real-Time, Off-Line, or Even Both?

Programming digital signal processing algorithms into real-time hardware such as digital signal processors and field programmable gate arrays requires time. Debugging and testing algorithms programmed into such hardware requires even more time. Finally, modifying these algorithms once they are inside the hardware also seems to be very time consuming. Even worse, people researching algorithms are usually not trained and experienced in programming real-time hardware. Even if they were, the tools available are, at least in our opinion, not the most convenient and stable. As long as researching on how to implement algorithms in real-time hardware is not needed or of interest, there is no real benefit in doing so other than decreased execution time (that can be combated with cluster processing on standard PCs) and publicity (that can be restricted to a few, simple, nice-to-show setups).

On the other hand, coding algorithms in a high-level programming language is convenient. This is especially true when utilizing a numerical computing environment such as MATLAB that comes with a lot of toolboxes. Furthermore, as such an environment may have been used to test the algorithms in an initial simulation, the idea of reusing this code for a measurement seems obvious.

Consequently, in our measurements, we avoid programming algorithms into real-time hardware at all cost. Instead, we execute all algorithms off-line on personal computers and use the same high-level language code that has already been used in the initial simulations.

To do so, we prepare a transmission in which:

- We organize all signals to be transmitted in blocks.
- We always transmit the same data and ensure by simulation that the measurement result, namely in our case the throughput, is not altered by this simplification of reality. Furthermore, we design the experiment in such a way that only a limited number of different blocks needs to be transmitted during the course of the whole experiment. Whether or how often these different blocks will be transmitted in the experiment can be decided later; for now, we only have to decide on a finite set of blocks.
- We calculate the baseband data samples of all these different blocks and store them on fast hard disk drives or in the memory of the transmitter.

Next, we carry out several transmissions during an experiment in which:

- We load the block to be transmitted, namely, the baseband data samples, into a real-time-capable buffer.
- We transmit this data block in real-time over the wireless channel.
- We receive the data block into a real-time-capable buffer.
- We store the data block on a hard disk drive (rather than evaluating it immediately).

Finally, we evaluate the stored data blocks off-line in a cluster of personal computers.

Having the data readily available at a transmitter that is synchronized with the receiver not only allows for the transmission of single blocks of data. Interestingly, it also allows for techniques such as retransmissions (see Fig. 8), adaptive modulation and coding (see Fig. 9), and adaptive modulation and coding combined with pre-coding and retransmissions (see Fig. 10). The only requirement to do so is a channel that is static during one measurement or a non-static channel that can be repeated.

## Measurement Results

Our real-world wireless communication system scenario was obtained in 2009 in downtown Vienna, Austria. We used a 2x2-transmission: a transmission using two antennas at the

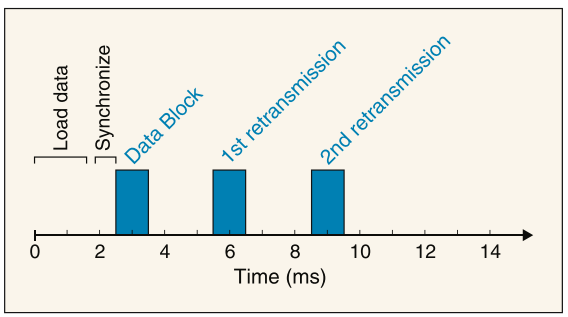


***Fig. 8.*** We always transmit all possible retransmissions even if they are not required. Later, during the off-line evaluation, we decide whether we need them or not.

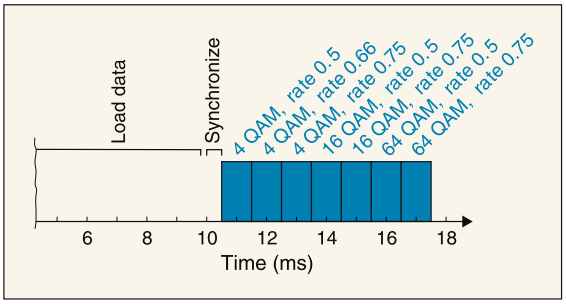


***Fig. 9.*** We always transmit all possible adaptive modulation and coding schemes (faster than the channel coherence time) even though only one would be transmitted in a real-world transmission. Later, during the off-line evaluation, we decide which one to choose based on the estimated channel.

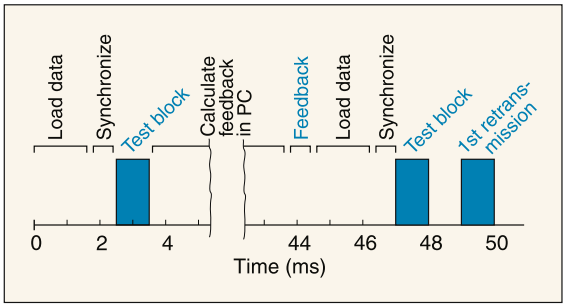


***Fig. 10.*** If the number of possible schemes exceeds the channel coherence time, we first transmit a training block. Next, we let the receiver evaluate the channel conditions (but not more) and estimate which blocks should be transmitted under these channel conditions. Then we feed this information back to the transmitter and transmit the blocks selected (with the retransmissions that may be required or not) by loading pre-generated blocks from the memory or fast hard-disk drives. Finally, we evaluate not only the whole measurement offline, but also if the channel has changed between the training block and the actual transmission. If the channel has changed, we discard the result of this transmission.

transmitter and two antennas at the receiver site, and a 1x2-transmission: a transmission using only one antenna at the transmitter but still using two antennas at the receiver site. The 1x2-transmission is the reference system.

Fig. 2 shows the measurement results. The '**2x2** (research target)' curve and the '**1x2** (reference)' curve graph the throughput performance of the transmission over the transmit power. The '**2x2 capacity** (theoretical bound)' is the dotted orange curve which represents the unconstrained channel capacity of the 2x2-transmission: the maximum theoretical throughput allowed by the channel for this transmission.

We compared the 2x2 and 1x2 throughput with the '**2x2 minus 1x2** (relative comparison)' curve and it showed gain. We concluded that the 2x2 throughput is significantly better in a typical operation by having one additional antenna at the transmitter.

We also compared this throughput to the '**2x2 capacity** (theoretical bound)' curve. As the system under investigation adaptively improves the signal-to-noise ratio (SNR) at the receiver, we measure over transmit power and plot the SNR (see the first additional x-axis). We also measure the receive power of the 1x2 system that does not adaptively improve the SNR (see the second additional x-axis).

## Reality Is Too Complex

Up to now we have shown how to measure basic setups like the one outlined in Fig 1. While such setups allow us to gain a deep understanding of parts of the system being investigated, real-world wireless communication systems are typically far more complex. The art of designing measurement setups for investigating the performance of such systems is now, in our opinion, to simplify reality as far as possible while still including all the ''important'' parts.

Let's take a closer look at cellular systems employing several base stations that actively coordinate the signals transmitted in order to maximize the throughput for several users in their vicinity. If the hardware for the transmitter and for the receiver is assembled from several black boxes of reasonable size, duplicating them and adding another black box for synchronization of the different sites (see for example [10]) is only a matter of money, manpower, and time. In reality, money is always scarce, manpower not available, time is devoted to more important tasks than assembling hardware, and motivation is lost once the hardware has been built for the first time. Therefore, one will try to simplify and employ the minimum setup that still allows for research output. Regarding the number of base stations, three seems to be a reasonable lower bound for still being able to obtain interesting results. Regarding the number of receivers, the potential for savings is a lot higher. There, the idea is to record beforehand, one by one, the channels observed by as many receivers as desired and to assume that these channels are still the same in the final measurement. This final measurement is also taken with only one receiver but the transmitters assume that all the other receivers are present when calculating the optimal transmit signal. The performance of the transmission is then evaluated for the only existing receiver. Then the receiver is moved to a new position, and the performance of a new user is measured, again assuming that all the other users are present where, in fact, they are not. The whole process could then be automatized by switching between several receive antennas using RF switches.

While base stations are typically employed on a roof, the receiver is likely to be operated in the vicinity of humans. The past has shown that even multinational companies forget to test their handhelds while actually being hand-held. The same holds true for the measurement methodology described in this tutorial where we sometimes mount laptop replacements with antennas on their back on linear guides or use very small and compact antennas as in a final product. The real challenge here is to design these antennas in such a way that the signal is captured by the antennas and not by the cables that connect the antennas to the rest of the measurement hardware.

Furthermore, experience has shown that the presented methodology is robust to people walking around and doors opening or closing. We, therefore, do not avoid such interactions by measuring at night. Rather, we discard single measurements afterwards during the off-line evaluation in

case the channel did change too much within the time of a single measurement. This might be the case if the feedback, and thus the adaptation to the channel, is wrong or the systems to be compared experience different channels. Remember that we always measure the systems to be compared in a rapid succession, typically within milliseconds. Therefore, long term drifts, such as changes in the scenario, do not impact our relative measurement result.

At the end of the day, one is likely to fill up three rooms. One to actually work in and build the hardware, one to store the tools and spare parts, and another room to test the hardware built before putting it on the roofs of several buildings that also need to be occupied and adapted. The hardware built might consist of three transmitters, one receiver, many different antennas, a fiber optic and wireless backbone, servers for data storage, PCs and servers for controlling the measurement and evaluation, a cluster of PCs to evaluate the results, sensors for capturing the environmental conditions, linear guides for moving the antennas, RF switches for switching between different antennas, roofs adapted to attach antennas as well as install base stations, and much more. Whether such a setup reflects a real-world wireless communication system remains to be seen, but that is how close we could come in six years.

## The Wrong Metric?

Next to other metrology related issues, building complex measurement setups in wireless communication requires considerable experience and engineering knowledge. Because the art of engineering setups has not been widely covered in scientific literature, one may only be able to find books on certain areas of interest, for example, for designing radio frequency hardware [8], [9]. Besides such books, the literature on how other groups have set up their hardware for measurements is either limited or non-existent. So carefully note that this will also apply to your "research."

Let us take a look at, for example, the steps required for synchronizing several transmitters and receivers in a wireless communication system measurement. This issue becomes non-trivial if measuring outdoors, over large distances, or at high velocities. Sooner or later, every research group will have to spend a considerable amount of time and manpower in developing and testing an engineering-solution that serves no other purpose than synchronizing the measurement set-up. Then, some time later, they may find that there are new features required by this hardware and that the whole set-up must be redesigned. Comparing the manpower and time invested to the scientific output achieved by this particular synchronization hardware (that is, zero), it would have been more efficient to buy somebody else's design and to copy it. Unfortunately, typically this possibility does not exist. In addition, governmental funding often make it less complicated to spend one man-year on developing mid-priced hardware from scratch rather than to buy it [10].

Summarizing: In order to make measurements, a lot of time is "lost" that could have been otherwise devoted to research. On the other hand, it is not really lost, because it allows us to measure.

## Some Years Later...

Did we not mention it at the beginning? Measurements cost time and money. In return, they provide us with invaluable insights into real-world problems. Whether a paper could have been published more easily by submitting only the initial simulation and skipping all the measurement effort is another (very sad) story.

## References


[1] S. Caban, C. Mehlführer, M. Rupp, and M. Wrulich, *Evaluation of HSDPA and LTE: From Testbed Measurements to System Level Performance*, 1st ed. Wiley, 2011. ISBN: 0470711922.

[2] R. Fisher, *The Design of Experiments*, 1st ed. New York: Wiley, 1935.

[3] R. L. Mason, R. F. Gunst, and J. L. Hess, *Statistical Design and Analysis of Experiments*, 2nd ed. Wiley-Interscience, 2003, p. 221. ISBN: 0471372161.

[4] W. G. Cochran, *Sampling Techniques*, 3rd ed. Wiley, 1977. ISBN: 047116240X.

[5] B. Efron and D. V. Hinkley, *An Introduction to The Bootstrap (CRC Monographs on Statistics & Applied Probability 57)*, 1st ed. Chapman & Hall, 1994. ISBN: 0412042312.

[6] A. M. Zoubir and D. R. Iskander, *Bootstrap Techniques for Signal Processing*, 1st ed. Cambridge University Press, 2004. ISBN: 052183127X.

[7] *Guide to the Expression of Uncertainty in Measurement, International Organization for Standardization (ISO)*, 1993.

[8] A. Behzad, *Wireless LAN Radios*, 1st ed. Wiley & Sons, 2007. ISBN: 0471709646.

[9] A. Luzzatto and G. Shirazi, *Wireless Transceiver Design*, 1st ed. Wiley & Sons, 2007. ISBN: 047006076X.

[10] S. Caban, A. Disslbacher-Fink, J. A. García-Naya, and M. Rupp, "Synchronization of wireless radio testbed measurements", *Proc. of International Instrum. Meas. Technology Conf.*, I2MTC 2011, Binjiang, Hangzhou, China.



***Sebastian Caban*** (scaban@nt.tuwien.ac.at) is a postdoc researcher at the Vienna University of Technology. In this productive environment, he is now busy perfecting the art of building testbeds for wireless radio communication systems for more than six years, seven days a week.

***José Antonio García Naya*** (jagarcia@udc.es) is an assistant professor at the University of A Coruña. He came to Vienna to learn the art of wireless engineering and has returned several times to continue with the fruitful research collaboration that started at his first visit.

***Markus Rupp*** (mrupp@nt.tuwien.ac.at) is a full professor at the Vienna University of Technology. He invests most of his time in bureaucracy and raising funds, which enables researchers to build wireless testbeds for experimental research.

Intel® Technology Journal | Volume 18, Issue 3, 2014

# THE VIENNA MIMO TESTBED: EVALUATION OF FUTURE MOBILE COMMUNICATION TECHNIQUES

## Contributors

**Martin Lerch**
Vienna University of Technology

**Sebastian Caban**
Vienna University of Technology

**Martin Mayer**
Vienna University of Technology

**Markus Rupp**
Vienna University of Technology

In order to evaluate current and upcoming mobile communications standards and to investigate new transmission as well as receiver techniques in a real-world environment, a very flexible testbed was set up at the Vienna University of Technology, comprised of multiple base stations, each equipped with several antennas. After providing an overview of this testbed and its capabilities, different kinds of measurements and their underlying methodologies are described in the context of 3GPP Long Term Evolution (LTE) transmissions. These are, on the one hand, point-to-point LTE Multiple-Input Multiple-Output (MIMO) throughput measurements, employing a single base station and, on the other hand, modern interference alignment measurements, utilizing up to three base stations simultaneously.

## Introduction

The decades after Marconi's invention were filled with wireless experiments. Although we understand many physical phenomena of wireless propagations today much better than in the past, the channel models we use still capture only a part of the complex physical process. Nevertheless, in the last two decades, it has become a common method to entirely skip experimental validation and trust existing channel models when designing mobile communication systems. As the complexity of mobile communication standards also increases, simulation methods appear to be the Holy Grail to solve open design questions. While these methods deliver quantitative results in acceptable time, many important issues are simplified or not modeled at all, trading off timely results for accuracy. Converting new algorithmic ideas into hardware on the other hand is quite time consuming and often lacks flexibility so that experimental evaluation remains no longer an attractive choice. We show that with our testbed approach, we essentially combine the advantages of both worlds: design flexibility and timeliness under true physical conditions.

*"As the complexity of mobile communication standards also increases, simulation methods appear to be the Holy Grail to solve open design questions."*

*"We show that with our testbed approach, we essentially combine the advantages of both worlds: design flexibility and timeliness under true physical conditions."*

In this article, we explain briefly our testbed approach[1] and our optimized measurement methodology that allows the deducing of results based on a minimal number of sampling points in the following section, "The Vienna MIMO Testbed: A Marriage of Hardware and Software." Experimental examples based on 3GPP Long Term Evolution (LTE) are then provided in the section "LTE Measurements," and finally experimental results for the interference alignment (IA) transmission scheme[2] are presented in the section "Interference Alignment Measurements." The article briefly sums up the findings with a "Conclusion" section.

## The Vienna MIMO Testbed: A Marriage of Hardware and Software

The Vienna MIMO testbed consists of various hardware components that couple data generating and capturing PCs, radio frequency front ends, antennas, and a suite of software tools, the so-called Vienna LTE Simulators.[3][4][5] While the LTE simulators help in designing optimal algorithms, the same signals can be fed into the testbed in order to transmit them over the air. The captured data are then input to the receiver part of the simulators and can be evaluated offline later on. It is important to note that the Vienna MIMO testbed is not limited to LTE transmissions. The LTE simulator can be easily replaced by software implementations of any desired communication system that meets the constraints of the testbed.

*"While the LTE simulators help in designing optimal algorithms, the same signals can be fed into the testbed in order to transmit them over the air."*

### Hardware

Figure 1 exhibits the main hardware components required to convert *a priori* generated data into electromagnetic waves, transmitting them over the air and finally capturing them before storing them in digital form for further evaluation. The major hardware components are:

- Three rooftop transmitters supporting four antennas each. The digital signal samples are converted with a precision of 16 bits and are transmitted with adjustable power within a continuous range of about −35 dBm to 35 dBm per antenna.
- One indoor receiver with four channels that converts the received signals with a precision of 16 bits before the raw signal samples are saved to hard disk. The receive antennas are mounted on a positioning table, which allows for measurements at different positions within an area of about 1 m × 1 m.
- The carrier frequency, the sample clock, and the trigger signals are generated separately at each station utilizing GPS synchronized rubidium frequency standards. The synchronization of the triggers is based on exchanging timestamps in the form of UDP packets over a trigger network.[6] The precision of this trigger mechanism does not require any further

*"The carrier frequency, the sample clock, and the trigger signals are generated separately at each station utilizing GPS synchronized rubidium frequency standards."*

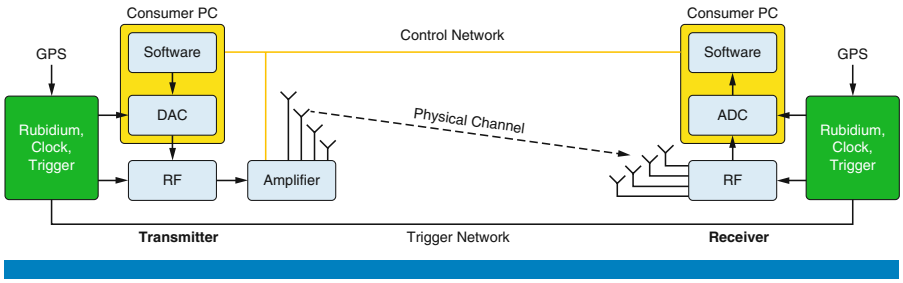


**Figure 1:** Testbed setup showing GPS-controlled rubidium clocks at both ends of the transmission chain (Source: Vienna University of Technology, 2014)

Intel® Technology Journal | Volume 18, Issue 3, 2014

post-synchronization at the receiver. It is sufficient to measure the delay once and time-shift all signals according to the measured delay.

- A dedicated fiber-optic network is utilized to exchange synchronization commands as well as feedback information and general control commands.

The current setup supports a transmission bandwidth of up to 20 MHz at a center frequency of 2.503 GHz.

**LTE Simulators**

Along with the hardware setup, a suite of software-based simulators are employed. Currently we support:

- The Vienna LTE-A Downlink Link Level Simulator (DL-LL)
- The Vienna LTE Uplink Link Level Simulator (UL-LL)
- The Vienna LTE Downlink System Level Simulator (DL-SL)

*"Our simulators together with published results were released under an open license agreement, free of charge for academic research."*

Our simulators together with published results were released under an open license agreement, free of charge for academic research. Over the years, many thousand users have formed a Web-based exchange forum where open problems were posed and solutions discussed. Due to these efforts in reproducibility, our simulators not only increased in functionality but also gained substantial quality. Many companies are now also using the simulators because they offer a convenient platform to exchange results between partners. The DL-SL simulator is only listed here to provide a complete list; this simulator uses link-level abstractions and supports simulations with hundreds of users since such complexity would not lead to acceptable run times in link-level precision. Both link-level simulators can be used to generate inputs to the testbed and testbed outputs can be fed back into them, hence providing an LTE-compliant transmission chain whose data can be directed to the transmit antennas and captured at the receive antennas instead of running transmissions over simulated channels such as ITU or Winner. Although the transmission only allows a burst mode, we can continuously generate such data bursts and mimic accurately continuous transmissions. The received symbols are time-stamped and can later be fed back into the simulator chain for evaluation. By this we can directly compare simulations with measured results based on identical transmit data and identical receiver algorithms, allowing very rigorous research results.

**Measurement Methodology**

*"As a rule of thumb, in a typical scenario approximately 30 measurements of different receive antenna positions are necessary to get sound results for an LTE signal with a bandwidth of 10 MHz."*

In typical measurements, the transmission of desired signals, or rather signals generated according to parameters of interest, is repeated with different values of transmit power in order to obtain results for a certain range of receive signal-to-noise ratios (SNR). Furthermore, the transmission of such signals at all values of transmit power is repeated at different receive antenna positions in order to average over small-scale fading scenarios. As a rule of thumb, in a typical scenario approximately 30 measurements of different receive antenna positions are necessary to get sound results for an LTE signal with a bandwidth of 10 MHz. In order to check whether we have measured enough channel realizations, we always

include BCa bootstrap confidence intervals in our results (see the following section and Caban et al.[7]). While this process is usually the same for different kinds of measurements, they may differ in the way transmit signals are generated.

As illustrated in Figure 2, two different methodologies are utilized as detailed in the following:

- *Brute force measurements:* All signals of interest are pre-generated, transmitted over the physical channel, and saved as raw signal samples to hard disk. The received signals are then evaluated offline. This approach is only feasible as long as the time duration of all the different transmit signals is small compared to the channel variations so that successively transmitted data sets appear to be transmitted over the same channel.
- *Measurements with feedback:* The transmit signals are generated on the fly utilizing channel state information obtained via a preceding transmission of training symbols. While the processing and evaluation of the actual data symbols can be computed offline, the demodulation of the training symbols, evaluation, and decision about the generation of the next transmit signal has to be performed in (quasi-) real time.

*"This approach is only feasible as long as the time duration of all the different transmit signals is small compared to the channel variations so that successively transmitted data sets appear to be transmitted over the same channel."*

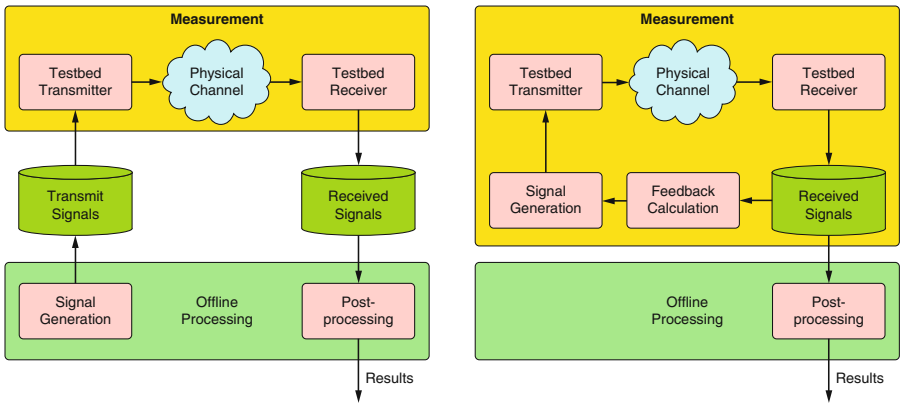


**Figure 2:** Measurement process without (left) and with feedback (right) (Source: Vienna University of Technology, 2014)

While brute force measurements typically take longer than the feedback approach and the number of different signals that need to be evaluated is much higher, results obtained by brute force measurements are typically more detailed and are certainly not contaminated by the quality of the feedback function. If the number of different transmit signals is not too large, a combination of both methodologies is possible. All signals of interest are pre-generated, but only those a feedback function decides for are transmitted. This approach reduces the number of signals that have to be evaluated and signals do not have to be generated during the measurement. Nevertheless, it should be noted that if the number of possible

Intel® Technology Journal | Volume 18, Issue 3, 2014

transmit signals is rather large or infinite (for example, zero-forcing Multi-User MIMO mode), only a feedback approach is feasible.

*"While LTE cellular systems are already being rolled out and operated in many countries around the world, there are still unresolved issues in transmission technology."*

## LTE Measurements

While LTE cellular systems are already being rolled out and operated in many countries around the world, there are still unresolved issues in transmission technology. Focusing on point-to-point single-user LTE transmissions, there exist many open questions that can be best tackled by LTE measurements:

- Comparison of different kinds of receivers (receiver algorithms)
- Performance of novel and modified transmission schemes following the LTE standard
- Performance measurements at extreme channels (for example, very high speed) for which channel models are very crude or even nonexistent
- Comparison of different penetration scenarios or different antenna configurations

In the following, we present two measurements comparing on the one hand two different transmit antenna configurations and two different scenarios on the other hand. For both measurements the brute force approach using the DL-LL simulator as software implementation of the base station and the user equipment was used. We chose the open loop spatial multiplexing transmission mode where no feedback of the preferred precoder is performed. Thus the number of different transmit signals is small enough to apply the brute force approach.

### A Comparison of Different Antenna Configurations

We were interested in evaluating the influence of the transmit antenna configuration on the performance of the LTE MIMO downlink. Possible configurations for the case of two transmit antennas are cross-polarized antennas, as they are used in today's base station antennas, and equally polarized antennas. For the measurements presented below, we utilized an off-the-shelf double cross-polarized sector antenna (Kathrein 800 10543) whose four antenna elements were used for implementing both a cross-polarized antenna pair and two equally polarized antennas with a spacing of 1.24 wavelengths (see legend of Figure 3).

*"…spatial multiplexing outperforms single-stream transmission only above a certain average SNR we observe that a cross-polarized configuration outperforms an equally polarized configuration."*

Figure 3 shows the measured throughput of the LTE open-loop downlink. In the left plot the results are shown over measured average SNR for a fixed transmission rank (1 or 2) where for single-stream transmission (rank 1) both antenna configurations performed similarly. The results for two spatial streams (rank 2) show on the one hand that spatial multiplexing outperforms single-stream transmission only above a certain average SNR. On the other hand, we observe that a cross-polarized configuration outperforms an equally polarized configuration. In the right plot, the throughput was maximized over the number of spatial streams for every channel realization, resembling a feedback selection scheme. More details on measurements comparing different vertical and horizontal setups for 2x2 as well as for 4x4 transmissions are described by Lerch and Rupp.[8]

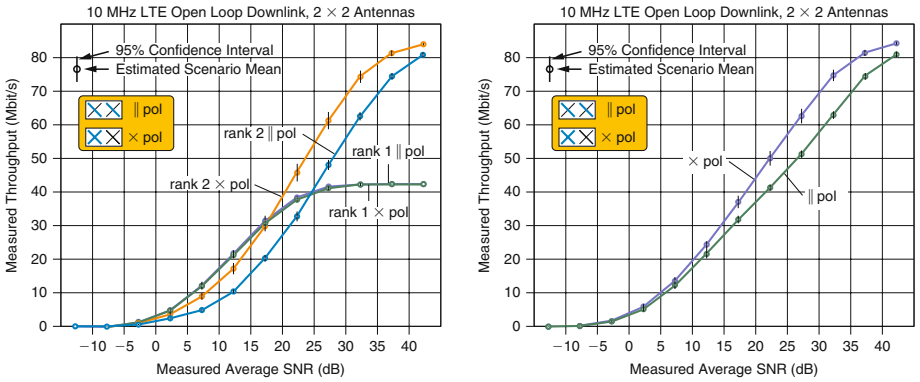


**Figure 3:** Comparison of cross-polarized and equally polarized transmit antennas in terms of LTE throughput (Source: Vienna University of Technology, 2014)

### A Comparison of Different Scenarios

While the previous results were obtained in a certain scenario given by the location of the transmitter and the receiver, we were further interested in a comparison of different scenarios. Therefore the measurement was repeated placing a transmitter at a different location and keeping the receiver location. In the previous scenario there was no line-of-sight path between the transmitter and the receiver. We considered a second scenario with a significant line-of-sight path. These two scenarios will be referred to as Non-Light-of-Sight (NLOS) and Line-of-Sight (LOS).

The left plot of Figure 4 shows the results considering two transmit antennas. While the cross-polarized antennas perform similarly in both scenarios, an even worse performance is obtained when considering equally polarized antennas in the LOS scenario, although only in the higher SNR regions where data is transmitted over two spatial streams. At lower SNRs, where only a single data stream is transmitted, the performance is quite independent of the scenario and the transmit antenna configuration used. Finally, the right plot of Figure 4 shows a comparison of both scenarios considering four transmit antennas. The results are similar to those for two antennas. While in the lower SNR regions the difference is negligible; at higher SNRs, where data is transmitted over multiple spatial streams, the performance in the NLOS scenario is better than in the LOS scenario.

*"While in the lower SNR regions the difference is negligible; at higher SNRs, where data is transmitted over multiple spatial streams, the performance in the NLOS scenario is better than in the LOS scenario."*

## Interference Alignment Measurements

Interference alignment (IA)[2] is an example of a system setup that utilizes all three transmitters simultaneously with feedback. IA measurements fully exploit all capabilities of the Vienna MIMO testbed.

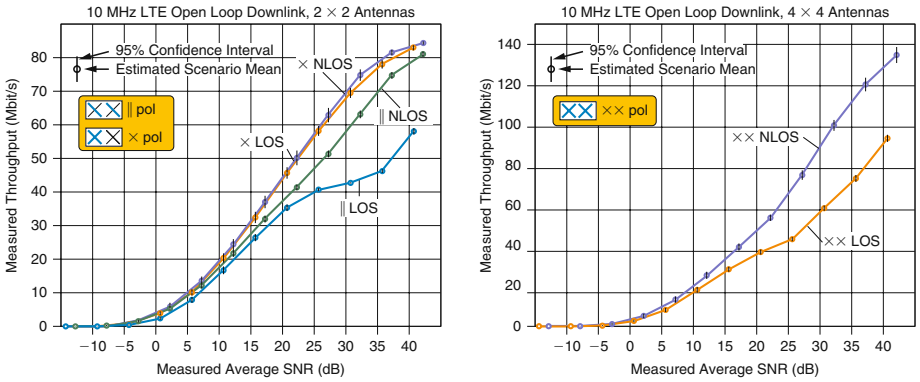


**Figure 4:** LTE throughput measurement results comparing LOS and NLOS scenarios for two and four transmit antennas.
(Source: Vienna University of Technology, 2014)

*"All three users experience heavy interference from the other base stations approximately as strong as the desired downlink signal."*

*"In the ideal case, half of the capacity of the interference-free case with four data streams can be achieved, which is more than what is obtained by using resource sharing."*

### The Concept of Interference Alignment

Consider the cellular scenario shown in Figure 5 where three mobile users at the cell edges wish to communicate with a different base station. All three users experience heavy interference from the other base stations approximately as strong as the desired downlink signal. An emerging MIMO technique to cope with such a scenario is called *interference alignment.* Based on the knowledge of the channels between every user and every base station, a joint calculation of precoding matrices, $V_i$ i = 1, 2, and 3 and receive filters, $U_i$ i = 1, 2, and 3, is performed, by which half of the degrees of freedom of the MIMO channels are utilized for data transmission while the other half are exploited to align the interferences at the receiver. By applying the receive filters, interferences are eliminated and only the data signal of interest is retained. Thus, instead of transmitting the maximum number of four data streams over a 4x4 MIMO channel, only two data streams are transmitted. In the ideal case, half of the

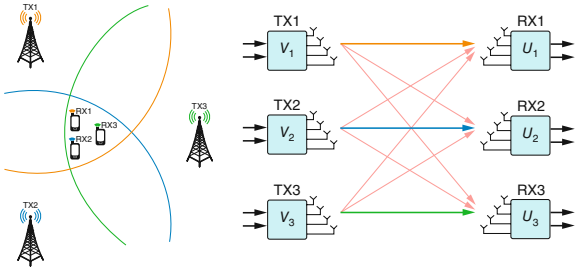


**Figure 5:** Interference alignment scenario and setup
(Source: Vienna University of Technology, 2014)

capacity of the interference-free case with four data streams can be achieved, which is more than what is obtained by using resource sharing. (Orthogonal multiple access schemes like time division multiple access can only offer a third of the capacity for each of the three users).

**Measurements**

Measurements with the Vienna MIMO testbed were carried out to show the feasibility of IA in a real-world scenario and to provide a basis for further investigations on the impact of different kinds of practical issues on the performance of IA. In order to evaluate IA on our testbed, we implemented the ideas below:

- While all three base stations are needed in order to transmit at the same time, one receiver that can act as any of the three receivers is indeed sufficient. The other two receivers can be virtual receivers and the respective channels can either be generated randomly or can be results of past channel measurements.
- Every mobile user has to estimate the channels to all transmitters. Therefore, not only must the training symbols from different antennas of each base station be orthogonal among themselves, but the training symbols of all different base stations must also be orthogonal. In the case of three base stations, each having four antennas, the channels from twelve transmit antennas have to be estimated simultaneously. Thus, standard compliant LTE, whose pilot structure only supports up to four transmit antennas, is not applicable, and therefore we implemented our own transmission scheme described below.
- Each transmit frame consists of a pilot preamble followed by the data payload. The pilot preamble is constructed to estimate the channels to all transmit antennas simultaneously and the data payload is designed to estimate the mutual information of the transmission. The precoders applied to the data payload are based on the channel estimates obtained from the respectively previous transmission. In order to keep the time between the channel measurement and the application of the respective precoders short (less than 20 ms), we took only a single subcarrier into account.

IA requires all involved transmitters and receivers to be synchronous in terms of carrier frequency and time. On our testbed, rubidium frequency standards at every station combined with a GPS based trigger network provide the required synchronicity. In order to receive the signals from different transmitters perfectly synchronous at the receiver, the transmit signals are time shifted according to the delays between the respective transmitter and the receiver. For a more detailed discussion of IA measurements on the Vienna MIMO testbed, the reader is referred to Mayer et al.[9]

*"IA requires all involved transmitters and receivers to be synchronous in terms of carrier frequency and time."*

**Results**

The left plot of Figure 6 shows the mutual information results of a measurement for a fixed signal-to-interference ratio (SIR) of −3 dB, that is, the signals from all three base stations are received equally strongly at the receivers. In order to compare the performance of IA to a non-cooperative scheme, a full rank

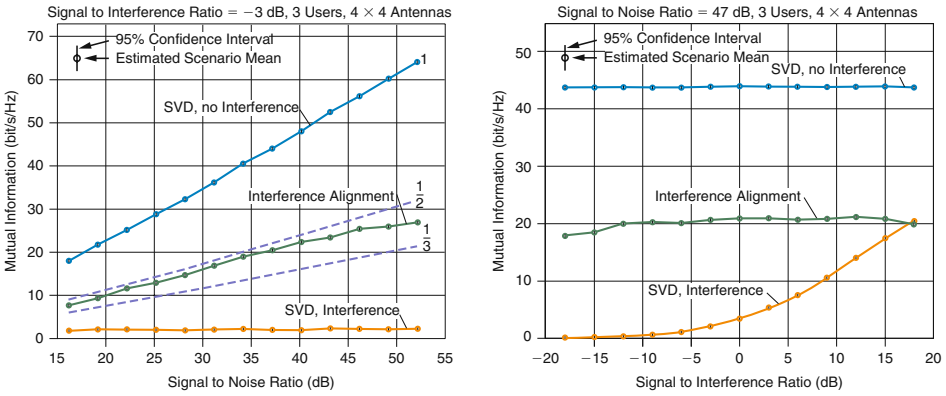


**Figure 6:** Performance of IA for a fixed SIR (left) and a fixed SNR (right). (Source: Vienna University of Technology, 2014)

*"IA reaches, almost half of the mutual information of the interference-free full rank case IA is very sensitive to channel estimation errors…"*

transmission based on the Singular Value Decomposition (SVD) of the channel utilizing all four available data streams was measured in the same scenario. In the case of interference, the performance of the SVD transmission (orange curve) is solely determined by the rather low SIR and therefore quite constant over the observed SNR region. IA (green curve) reaches, following the theory (dashed blue curve), almost half of the mutual information of the interference-free full rank case (blue continuous line). At high SNR, a saturation of mutual information is observed in the IA case. This is due to the fact that IA is very sensitive to channel estimation errors as mentioned by Garcia-Naya et al.[10] The precoders are always computed from the channel estimate of the previous transmission, and since our feedback is only finitely fast, the channels have time to change between transmissions. Thus, despite the high SNR, there will always be residual interference power due to imperfect alignment that limits mutual information, as long as the channel is not perfectly static.

*"With increasing SIR (decreasing interference) the performance of the non-cooperative full rank transmission increases and outperforms IA…"*

The results for a fixed signal-to-noise ratio of 47 dB are shown on the right plot of Figure 6. With increasing SIR (decreasing interference) the performance of the non-cooperative full rank transmission increases and outperforms IA at a certain level of SIR. Above this level, a mobile user should rather be scheduled for a different transmission scheme than IA.

## Conclusion

The article describes a testbed methodology that combines the rapid development speed of software with the precise measurements results including physical wireless channels.

The capability of our testbed to measure over a wide range of transmit power within the same scenario allows for deep insights into the performance of

modern mobile communication systems. As an example, we demonstrated in terms of LTE throughput that the performance of MIMO techniques does not only depend on the signal-to-noise ratio. It also depends on the actual transmit antenna configuration and the scenario. Our measurement based evaluation of interference alignment provides viable information regarding its possible fields of application and the entailed constraints. The inherent precoder feedback delay and the extensive channel knowledge requirement narrow the field down to applications that comprise reliable feedback and coordination. Fully exploiting the capabilities of the Vienna MIMO Testbed, interference alignment was shown to be feasible, achieving results close to theory and outperforming orthogonal access schemes in case of intermediate to strong interference at fairly high SNR.

*"…the performance of MIMO techniques does not only depend on the signal-to-noise ratio. It also depends on the actual transmit antenna configuration and the scenario."*

## References


[1] Caban, S., C. Mehlführer, M. Rupp, and M. Wrulich, *Evaluation of HSDPA and LTE: From Testbed Measurements to System Level Performance* (New York: John Wiley & Sons, 2012), p. 404.

[2] Cadambe, V. R. and S. A. Jafar, "Interference Alignment and Degrees of Freedom of the K-User Interference Channel," *IEEE Transactions on Information Theory,* vol. 54, no. 8, pp. 3425–3441, 2008.

[3] Mehlführer, C., J. Colom Ikuno, M. Simko, S. Schwarz, M. Wrulich, and M. Rupp, "The Vienna LTE Simulators - Enabling Reproducibility in Wireless Communications Research," *EURASIP Journal on Advances in Signal Processing*, vol. 2011, pp. 1–13, 2011.

[4] Schwarz, S., J. Colom Ikuno, M. Simko, M. Taranetz, Q. Wang, and M. Rupp, "Pushing the Limits of LTE: A Survey on Research Enhancing the Standard," *IEEE Access,* vol. 1, pp. 51–62, 2013.

[5] "The Vienna LTE simulators," Institute of telecommunications, Vienna University of Technology, [Online]. Available: www.nt.tuwien.ac.at/ltesimulator.

[6] Caban, S., A. Disslbacher-Fink, J. A. Garcia Naya, and M. Rupp, "Synchronization of Wireless Radio Testbed Measurements," in *IEEE International Instrumentation and Measurement Technology Conference,* Binjiang, 2011.

[7] Caban, S., J. A. Garcia Naya, and M. Rupp, "Measuring the Physical Layer Performance of Wireless Communication Systems," *IEEE Instrumentation & Measurement Magazine, v*ol. 14, pp. 8–17, 2011.

[8] Lerch, M. and M. Rupp, "Measurement-Based Evaluation of the LTE MIMO Downlink at Different Antenna Configurations," in *17th International ITG Workshop on Smart Antennas*, Stuttgart, 2013.

[9] Mayer, M., G. Artner, G. Hannak, M. Lerch, and M. Guillaud, "Measurement Based Evaluation of Interference Alignment on the Vienna MIMO Testbed," in *The Tenth International Symposium on Wireless Communication Systems*, Ilmenau, 2013.

[10] Garcia-Naya, J. A., L. Castedo, O. Gonzalez, I. Ramirez, and I. Santamaria, "Experimental evaluation of Interference Alignment under imperfect channel state information," in *9th European Signal Processing Conference (EUSIPCO),* Barcelona, Spain, 2011.

## Acknowledgements

The authors would like to thank the LTE research group and in particular Prof. Christoph Mecklenbräuker for continuous support. This work has been funded by the Christian Doppler Laboratory for Wireless Technologies for Sustainable Mobility, KATHREIN Werke KG, and A1 Telekom Austria AG. The financial support by the Austrian Federal Ministry of Economy, Family and Youth and the National Foundation for Research, Technology and Development is gratefully acknowledged.

## Author Biographies

**Martin Lerch** studied electrical and communication engineering at the Vienna University of Technology where he received his master's degree in 2008. During this time and later, Martin developed several database, Web, and desktop applications before he returned to the Vienna University of Technology in 2011 to work on the Vienna MIMO testbed. Martin's work focuses on the development of new measurement methodologies for static and high mobility mobile communication scenarios. Contact him at mlerch@nt.tuwien.ac.at

**Sebastian Caban** works as a consultant for operational excellence next to being a postdoctoral researcher at the Vienna University of Technology. He holds a BSc, MSc, and PhD in Telecommunication Engineering as well as a BBA and MBA in business administration. His research focuses on developing measurement methodologies and building testbeds to quantify the *actual* performance of wireless communication systems. He can be contacted at scaban@nt.tuwien.ac.at

**Martin Mayer** is a research assistant at the Vienna University of Technology. He holds a BSc degree in Electrical Engineering and Information Technology and an MSc degree in Telecommunication Engineering, both received at the Vienna University of Technology in 2011 and 2013, respectively. For his master's degree,

his research focused on evaluating interference alignment on the Vienna MIMO testbed. In 2014, his field of interest shifted to advanced signal processing in RFID. Martin can be contacted at mmayer@nt.tuwien.ac.at

**Markus Rupp holds** the chair for signal processing in mobile communications at the Vienna University of Technology. His research is devoted to digital wireless communication systems with a focus on cellular communications but also addressing near field communications as well as traffic modelling. He can be contacted at mrupp@nt.tuwien.ac.at

# Synchronization of Wireless Radio Testbed Measurements

Sebastian Caban*, Armin Disslbacher-Fink*, José A. García-Naya‡, and Markus Rupp*
*Institute of Communications and Radio-Frequency Engineering, Vienna University of Technology, Vienna, Austria
‡Department of Electronics and Systems, University of A Coruña, A Coruña, Spain
Contact e-mail: scaban@nt.tuwien.ac.at

***Abstract*—Measuring the physical layer performance of a wireless radio transmission is straightforward: Firstly, a transmitter generates the signal-samples to be transmitted. Secondly, these samples are broadcasted in real-time and captured by the receiver. Thirdly, the received signal is evaluated and the desired figure of merit is calculated. If only isolated blocks of data are transmitted and the received signal is evaluated off-line to simplify implementation, the receiver has to know when to actually acquire the data. The situation becomes more complicated when several transmitters and receivers have to be synchronized in time.**

**In this paper we will present a method to synchronize an arbitrary number of transmitters and receivers that is swift (e.g. 1 ms, the latency of an already exiting LAN infrastructure) as well as accurate (e.g. ±30 ns, the relative accuracy of GPS).**

## I. Motivation

In currently employed wireless radio transmission systems, receivers usually capture the input signal on a continuous basis [1]. In a next step, more or less complex digital signal processing algorithms continuously estimate the most likely start of data blocks to then decode the received information. This important step of finding where the blocks of data actually are is usually referred to as "timing synchronization".

*In contrast*, a well established way to infer the performance of complex wireless communications systems is to create the blocks to be transmitted off-line in a high-level programming language, transmit and receive only single blocks of data, and then evaluate the received blocks off-line [2]. Such "testbed measurements" avoid the cumbersome implementation of algorithms in hardware while still allowing for transmissions over real-world channels, therefore capturing real-world effects.

When now only a single block of data is to be transmitted, and the receiver is only capturing data for a limited amount of time (that is, in the optimum, approximately the time required for the transmission), the receiver has to know somehow when to actually receive the data. If data processing is carried out only off-line after the acquisition has finished, the received data itself cannot be used for this purpose and, therefore, an external triggering mechanism has to be employed. Such triggering mechanism does not necessarily have to be very accurate if more data is captured than actually required. In this case, accurate timing synchronization can be carried out later off-line in software. On the other hand, accurate hardware-triggering and therefore hardware-synchronization may simplify the work of the researchers as either the off-line timing synchronization can be omitted or the not-omitted timing synchronization can be compared to the perfect reference of a hardware trigger.

Things change when several time-synchronous transmitters are used in an experiment as software-aided synchronization techniques cannot be employed anymore. This may be for example the case when measuring the performance of interference alignment[1] techniques [3].

[1]The key idea of interference alignment is to shape multiple transmit signals in such a way that they cast "shadows" on other users, while the user(s) of interest can still decode them.

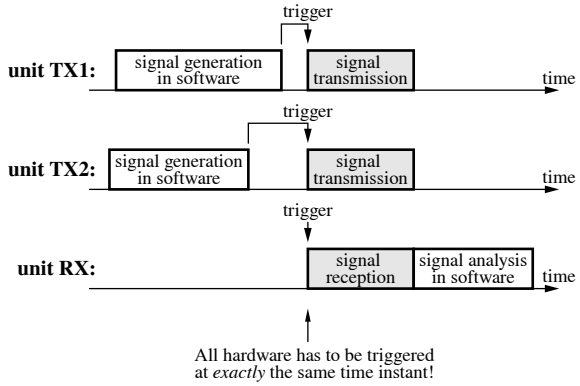


Fig. 1. After calculating the data to be transmitted in software, the data has to be transmitted and received at exactly the same time instant.

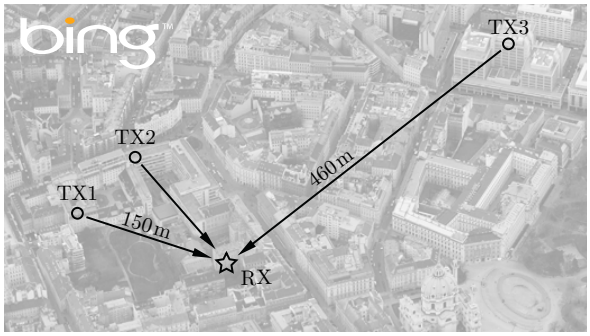


Fig. 2. Birds eye view showing our most recent hardware set-up, namely the three transmitters (set up on roofs) and the receiver (set up in an office) in downtown Vienna, Austria. The fastest existing connection between them is the local area network provided by the Vienna University of Technology.

The goal is therefore to design a "distributed piece of hardware" that allows for precise synchronization of several transmitters and receivers at a low cost while still allowing for the flexibility of an off-line measurement approach. Specifically, it should be possible to transmit blocks of data immediately upon request, and not only at full seconds as it could be easily realized by using a PPS[2] signal from a GPS reference.

Indoors, or when the sites of the measurement system are not located far from each other, the probably easiest implementation of such a distributed timing synchronization system is a 50 ohm coaxial cable to spread a common trigger signal. If however, as shown for example in Figure 2, the transmit sites are located on different

[2]A Pulse Per Second (PPS) is an electrical signal that is high for a certain period starting at exactly each full second. It does, therefore, not specify the time but only the start of each second.

buildings in a city, laying dedicated cables becomes non feasible, calling for a new, innovative approach.

## II. The Concept

The simplest way to exchange information between different sites is to use/extend a typically already existing LAN/WAN[3] infrastructure and/or maybe also set up dedicated wireless LAN bridges to connect different LAN segments. Unfortunately, if not specially designed for this purpose[4], LAN connections suffer from a typically non-constant delay. Therefore, they can only be used for information exchange between the geographically separated sites of a testbed but not for supplying the trigger instant itself.

Precise timing ($\pm 30$ ns relative difference[5]) at very different sites can be easily obtained using the PPS signal provided by commercial-grade GPS devices. However, these devices do not allow for additional information exchange between the different transmitter and receiver sites.

The basic idea now is to use a GPS at each site to acquire the current time precisely, and a local area network connection between all sites to handshake at what time to trigger the transmission. Figure 3 shows the proposed set-up, employing a dedicated timing synchronization unit at each testbed site:

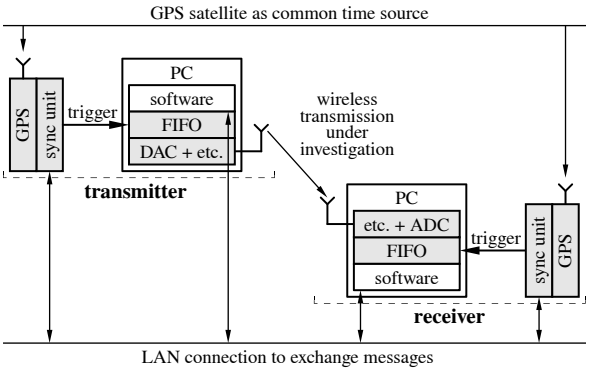


Fig. 3. Block diagram of the set-up proposed. Parts operating in real-time are shown in gray. We actually employ three transmitters and one receiver. The methodology proposed works with any number of transmitters and receivers.

### A. Initial Preparation

Prior to a measurement (and not during a measurement), the following steps have to be carried out:

(1) All GPS units acquire a satellite fix. *(Duration: sometimes up to several minutes but not relevant for the measurement)*

(2) The master PC (typically a receiver) tells its own sync-unit via a UDP datagramm[6] that all sync-units shall acquire the a common reference time. In order to do so, the sync-unit receiving the UDP datagram waits for the next PPS pulse to then multicast through the LAN connection to all other sync-units that they shall set their internal clocks to zero with the next PPS pulse (it is assumed that the multicast takes less than one second.) The result of this procedure is that all sync-units share a common, precise, relative time. Of course, the absolute time could also have been obtained from the GPS devices, but this additional effort is not required for the proposed set-up. *(Duration: from one to two seconds but not relevant for the measurement)*

### B. Triggering Procedure

The transmission of a single data block works as described below (see also Figure 4). Note that the proposed set-up only reveals its full potential if multiple, pre-generated data blocks have to be transmitted from multiple transmitters:

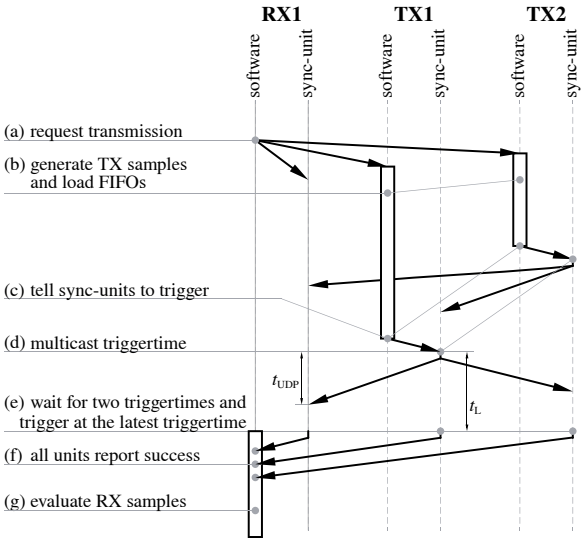


Fig. 4. UDP datagrams on the LAN (arrows) plotted over time (Y-direction).

(a) The master PC (typically a receiver) tells all other PCs that the transmission of a specific data block shall be performed. *(UDP multicast, duration: maximum LAN latency)*

(b) - In all transmitters, the specific data block to be transmitted is created off-line in the block named software (see Figure 3). In the form of samples, this data is then stored in the block named FIFO[7] to be transmitted exactly when the external trigger originated in the sync-unit is applied. *(Software execution, start: when UDP multicast is received, duration: unknown)*
- All receivers get ready for reception.

(c) - Each transmitter tells its own sync-unit that a transmission shall be triggered in $t_L$ milliseconds. The time $t_L$ is to be determined

[3] A Wide Area Network (WAN) is, in contrast to a Local Area Network (LAN), covering a much larger geographical area. For simplicity, we will refer to both, WANs and LANs, as LANs throughout this paper.

[4] Defined in IEEE 1588 [4], the Precision Time Protocol (PTP) allows for precise timing synchronization using "special" network cards and switches. While at laboratory conditions a timing performance close to GPS devices can be achieved, already existing networks do not allow for such performance [5].

[5] We measured this value using commercial of-the-shelf equipment [6, Figure 3.14.]. Data sheets of GPS devices typically report the standard deviation of this difference, which is obviously lower than its maximum values.

[6] A User Datagram Protocol (UDP) datagram is a basic transfer unit of the packet-switched LAN. In contrast to Transmission Control Protocol (TCP) packet transmission, UDP datagram transmission does not provide reliability, ordering, and data integrity. On the other hand, avoiding the therefore required overhead, it is more suited for real-time applications.

[7] FIFO... In our case a dual-port memory is set up as a First In First Out buffer (FIFO buffer) to first store the off-line generated samples and then forward these samples to the DAC in real-time. The buffer is required as the software is not capable of generating the data samples fast enough.

by the user beforehand or to be optimized adaptively during operation.
- The receivers are assumed to be ready and do not necessarily notify their sync-unit. In case this assumption is not valid, an error is reported in Step (f). *(UDP unicast, start: when samples are in FIFO, duration: single switch latency as PC and corresponding sync-unit are not geographically separated)*

(d) Each sync-unit receiving a trigger command looks up its own internal clock and multicasts this time plus $t_L$ as the earliest possible trigger time to all sync-units. *(UDP multicast, duration: maximum LAN latency)*

(e) All sync-units wait until they receive from every transmitter (the number of transmitters is known beforehand) the desired trigger time. Then they trigger at the latest time received. This time is exactly the same for all units and all units must be able to trigger at this time if $t_L$ is higher than the maximum UDP datagram delay $t_{UDP}$ observed (see Figure 4). *(Wait until trigger which happens exactly $t_L$ after the slowest PC has requested a trigger)*

(f) In case the datagram with the message to trigger has arrived after the triggering time contained in it (this happens if $t_L$ was set too low), the units report an error and the transmission has to be repeated, otherwise the successful triggering is reported back. By increasing $t_L$, the rate of success can be increased while at the same time the duration of the triggering procedure is incremented. The optimal $t_L$ (that is the unknown non-deterministic $t_{UDP}$) can be set adaptively as a tradeoff between the time required for repeating a transmission and the time $t_L$ that is lost for carrying out the triggering procedure.

(g) The data received is evaluated. Note that the evaluation already starts when the data is received. It is not necessary to wait for the "successful triggering" reported in Step (f) to start the evaluation. In case an error is reported instead of a "successful triggering," the evaluation is aborted.

If an UDP datagram is lost during the above procedure, neither a successful triggering nor an error is reported back. In this case, a timeout occurs at the receiver, all sync-units are reset, and the whole procedure is repeated.

### C. GPS (+ Rubidium) as Time Reference

In order to trigger at the same time instant, all sync-units need very stable internal clocks. Low cost (commercially available) GPS modules that provide a PPS output next to a stabilized 10 MHz oscillator output (for example [7, 8]) may be already sufficient to provide precise timing information in most measurement set-ups.

If, however, a higher short time phase and frequency stability is required, a rubidium standard may be the device of choice. Commercially available frequency standards (for example [9]) provide long-term (via a GPS) and short-term (via the rubidium) stabilized 10 MHz as well as PPS outputs (see Figure 5). The price to be paid for a time stability factor of $\pm 5 \times 10^{-11}$ is in the magnitude of 3 kEUR per sync-unit to stabilize.

### D. Precise DAC Triggering and Frequency Synchronization

Although the trigger pulse generated with the set-up proposed in Figure 5 is very precise, the output of the DAC itself will experience a timing uncertainty of one DAC clock cycle[8] as the DAC will quantize the trigger pulse to the "next" edge of the DAC clock. To avoid this uncertainty, the DAC has to operate on the same clock as the sync-unit.

[8]Note that with some DACs this uncertainty is even higher.

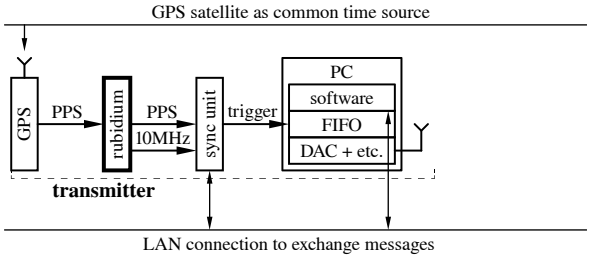


Fig. 5. Enhanced by a rubidium frequency standard at each site (only one transmitter is shown in the figure) the proposed set-up is able to trigger with a short-time precision factor of approximately $5 \times 10^{-11}$. The long term accuracy of approximately $\pm 30$ ns is defined by the GPS used.

Figure 6 shows such a set-up where DAC and sync-unit are operated on the same externally generated clock, allowing for a trigger pulse that has a constant timing relation to the DAC clock. If this externally generated clock (see the block labeled "oscillator" in Figure 6) is stabilized by the 10 MHz output of the rubidium, hardware frequency synchronization of all units in a testbed can be achieved as a side effect. If desired, the local oscillator of the up-conversion can also be locked to the rubidium reference. The resulting set-up can then even be used for channel sounding.

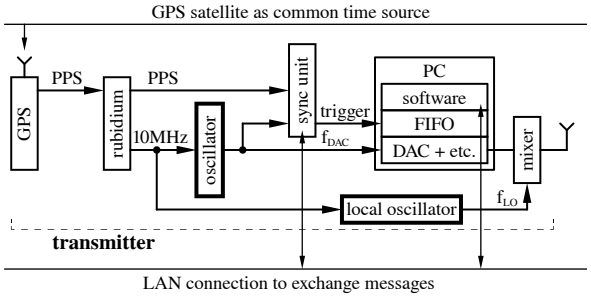


Fig. 6. If the sync-unit and the DAC are operated on the same external clock, precise triggering is possible. If all oscillators are locked to the rubidium reference and the scenario is static, consecutive transmissions will experience the same channel. Note that we define the channel from the DAC to the ADC, not from TX antennas to RX antennas.

## III. Discussion of the Set-Up Proposed

### A. Applicability

The set-up proposed allows for timing synchronization of several transmitters and receivers over an already existing LAN connection. With less triggering speed (equal to the network latency), synchronization can be even achieved over low-cost 3G/4G wireless modems (e.g. 50 ms per trigger in HSDPA).

Please note that the units do not need to be connected directly by a cable in order to synchronize precisely. A LAN connection, a GPS, and a rubidium frequency standard that is at best never turned off[9] is sufficient.

### B. Validation and Verification

The set-up can be easily validated[10] by displaying the trigger pulses of all units on an single oscilloscope.

[9]We power each rubidium frequency standard via a Uninterruptible Power Supply (UPS) so that we never have to turn them off.

[10]Validation: "Has the thing been built right?" Verification: "Has the right thing been built?"

As we are interested in testing wireless communication systems, a way to verify the proposed set-up is to transmit a signal from several transmitters, acquire it, and then estimate (1) the beginning of the received block as well as (2) the channel. When repeating the transmission, these two estimates should not change significantly in a static environment.

### C. Repeatability

If repeating an experiment requires a transmission to happen at a specific time the proposed set-up may not be sufficient. The reason is that firstly, in Step (c) in Figure 4, a packet has to be sent to the sync-unit resulting in an unknown delay next to the fixed time $t_L$ that cannot be avoided. Secondly, it is very hard to time UDP datagrams in software more accurately than in a microseconds [10]. We therefore implemented an external hardware input into the sync-unit.

### D. Achievable Triggering Speed

When transmitting blocks of data, the latency introduced by the triggering is the sum of:

1) the time required to tell the sync-unit to trigger (Step (c) in Figure 4), that is, the delay of a network switch,
2) the time required by the sync-unit to receive and transmit UDP packets as well as to read the internal clock (the vertical lines of Steps (d) and (e) in Figure 4), that can be made negligible by employing high-speed hardware, and
3) the estimated maximum time required to broadcast the trigger time over the network (Step (d) in Figure 4).

*) Note that the time required to receive the success report (step (e) in Figure 4) is not included in the sum, as the received data can already be evaluated (Step (f) in Figure 4) while waiting for the success report.

Therefore, if only triggering, triggering speeds of more than one trigger per millisecond can be easily achieved in typical LANs.

However, in a real measurement, the transmission not only has to be triggered but data also has to be generated, transmitted, and received. If employing off-line processing of data, the triggering itself will only account for a negligible part of the overall measurement time (far less than 10%). It is therefore not necessary to optimize the speed of the triggering procedure anymore.

## IV. Our Hardware Implementation of the Sync-Unit

The synchronization unit has been implemented in hardware (see Figure 7) and tested in various local area network environments. For example, if "generating the TX samples and loading them into the FIFOs" (step b in Figure 4) takes 4 ms and the data is transmitted while the next block is already loaded, a rate of 233 transmitted data blocks per second has been reached in a local area network. A detailed analysis can be found in [11].

## V. Conclusions

In this paper we presented a method to synchronously trigger hardware at different locations using a GPS and a dedicated sync-unit at each site, as well as an already existing LAN infrastructure. We showed that the precision of the overall set-up can be further increased by employing rubidium frequency standards and external local oscillators.

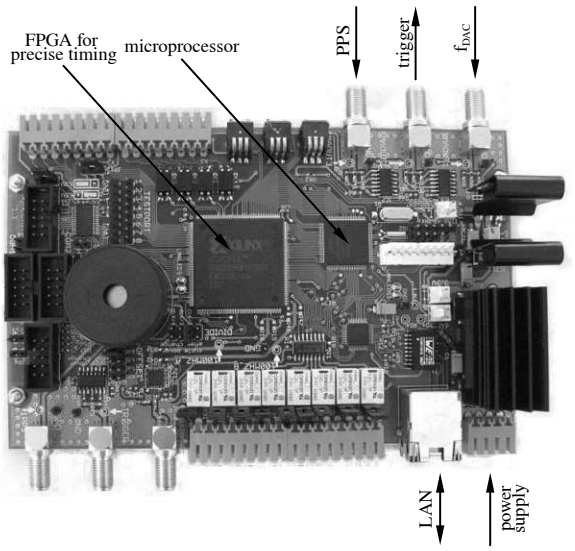


Fig. 7. Sync-unit built. The unit incorporates a host of additional input/output connections in order to control other hardware such as step attenuators, linear guides, rotation units, and radio frequency switches.

## VI. Acknowledgements

This work has been funded by the Christian Doppler Laboratory for Wireless Technologies for Sustainable Mobility, the A1 Telekom Austria AG, and the KATHREIN-Werke KG. It has also been supported by the Xunta de Galicia, the Ministerio de Ciencia e Innovación of Spain, and the FEDER funds of the European Union under the grants 10TIC003CT, TEC2007-68020-C04-01, and CSD2008-00010. The financial support by the Federal Ministry of Economy, Family and Youth and the National Foundation for Research, Technology and Development is gratefully acknowledged.

## References

[1] V. Jungnickel, T. Wirth, M. Schellmann, T. Haustein, and W. Zirwas, "Synchronization of cooperative base stations," in *IEEE International Symposium on Wireless Communication Systems*, pp. 329 –334, Oct. 2008, doi: 10.1109/ISWCS.2008.4726071.

[2] S. Caban, C. Mehlführer, G. Lechner, and M. Rupp, "Testbedding MIMO HSDPA and WiMAX," in *Proc. 70th IEEE Vehicular Technology Conference (VTC2009-Fall)*, Anchorage, AK, USA, Sept. 2009, doi: 10.1109/VETECF.2009.5378995. http://publik.tuwien.ac.at/files/PubDat_176574.pdf

[3] V. R. Cadambe and S. A. Jafar, "Interference alignment and degrees of freedom of the $k$-user interference channel," *IEEE Trans. Information Theory*, vol. 54, no. 8, pp. 3425–3441, Aug. 2008, doi: 10.1109/TIT.2008.926344.

[4] "IEEE standard for a precision clock synchronization protocol for networked measurement and control systems," IEEE Std 1588-2008 (Revision of IEEE Std 1588-2002), 2008.

[5] L. Cosart, "Precision packet delay measurements using IEEE 1588v2," in *ISPCS 2007, IEEE International Symposium on Precision Clock Synchronization for Measurement, Control and Communication*, pp. 85 –91, Oct. 2007, doi: 10.1109/ISPCS.2007.4383778.

[6] S. Caban, "Testbed-based evaluation of mobile communication systems," Ph.D. dissertation, Technische Universität Wien, Institut für Nachrichtentechnik und Hochfrequenztechnik, Sept. 2009, supervisor: Markus Rupp.

[7] "Thunderbolt(R) E GPS disciplined clock," available from Trimble Navigation Limited. http://www.trimble.com/timing/thunderbolt-e.aspx

[8] "Accurate frequency & timing solutions." http://www.accubeat.co.il/

[9] "Fs725 – benchtop rubidium frequency standard," available from Stanford Research Systems, Inc. http://www.thinksrs.com/products/FS725.htm

[10] S. Donnelly, "Endance DAG time-stamping whitepaper," White paper, Endance Technology Ltd., 2006, available online (8 pages). http://www.endace.com

[11] A. Disslbacher-Fink, "Hardware-based timing synchronization," Master's thesis, Vienna University of Technology, Vienna, Austria, 2011. http://publik.tuwien.ac.at/files/PubDat_195758.pdf

# QUANTIFYING THE REPEATABILITY OF WIRELESS CHANNELS BY QUANTIZED CHANNEL STATE INFORMATION

*Martin Lerch**, Sebastian Caban**, Erich Zöchmann**† and Markus Rupp**

*Institute of Telecommunications, TU Wien, Vienna, Austria
†Christian Doppler Laboratory for Dependable Wireless Connectivity for the Society in Motion
{mlerch,scaban,ezoechma,mrupp}@nt.tuwien.ac.at

## ABSTRACT

Repeatability is the prerequisite for scientific evaluation of wireless measurements. However, in real-world scenarios, the channel always slightly changes with time as, for example, trees move in the wind. In this paper, we propose a methodology that uses quantized channel state information and a technique similar to non-substractive SNR-dithering to quantify the repeatablility of wireless channels. Thereby, we introduce a new metric that allows for a comparison of different setups and scenarios in terms of repeatability. In a measurement campaign, we compare (1) a directional link to (2) an outdoor to indoor urban scenario with a fixed receiver and (3) the same scenario with the receiver moving in a circle, thereby experiencing the same high speed channel again and again.

## 1. INTRODUCTION

"Being able to repeat experiments is considered a hallmark of the scientific method, used to confirm or refute hypotheses and previously obtained results" [1]. The authors of [2] provide a broad overview of topics arising in the context of repeatable experiments in the field of wireless research. Such experiments include but are not limited to comparing different transmit modes at different values of Signal-to-Noise Ratio (SNR) [3, 4], the experimental evaluation of MIMO handsets [5], the experimental evaluation of the coexistence of different mobile standards [6], experimental evaluation of multiuser beamforming [7] and certain channel sounding techniques [8, 9].

Repeatability[1] of wireless transmissions requires the channel to be time invariant over repetitions. Time invariant channels are commonly referred to as static. Even if the receiver might not be fixed at a certain position, time invariant channels are realizable by sampling of periodic movements at the same point within the fundamental period. System theory names this *lifting* of time periodic systems [11–13].

In order to analyze the repeatability of wireless channels and especially, to compare different scenarios in terms of channel repeatability, we consider the approach illustrated in Figure 1.

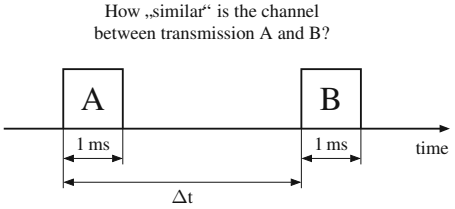


**Fig. 1**. Motivation.

We compare the Channel State Information (CSI) obtained through the transmission of a single 3GPP Long Term Evolution (LTE) downlink [14] subframe A to the CSI obtained through the transmission of an equal subframe B. Thereby, full CSI is given by the combination of the estimated channel matrix $\widehat{\mathbf{H}}$ and the estimated noise power $\widehat{\sigma}_z^2$ while the Channel Quality Indicator (CQI) reflects CSI in a quantized way. The actual type of CSI that is available depends on the application and the implementation of the LTE receiver. In contrast to lifting, within our LTE system, we do not sample at one point. The LTE subframes we measure extend over 1 ms. Thus, we investigate time invariance of the channel quality captured by the change of the CSI.

### Contribution and outline

In this contribution, we propose a new metric to quantify the repeatability of wireless channels based on the CQI and introduce a technique similar to non-subtractive dithering [15] to overcome the quantized nature of the CQI. After introducing this new metric in Section 2, we use it in a measurement

This work has been funded by the Christian Doppler Laboratory for Wireless Technologies for Sustainable Mobility, KATHREIN Werke KG. The financial support by the 'Austrian Federal Ministry of Economy, Family and Youth', the 'Austrian Federal Ministry of Science, Research and Economy' and the 'National Foundation for Research, Technology and Development' is gratefully acknowledged.

[1] repeatability…"The closeness of agreement between independent results obtained with the same method on identical test material, under the same conditions (same operator, same apparatus, same laboratory and after short intervals of time)" [10]

campaign described in Section 3, where we compare different scenarios in terms of repeatability of channels. The results are compared to a metric that uses full CSI. Finally, we conclude our findings in Section 4 and highlight further research questions.

## 2. THE CQI$_{\neq}$ METRIC

In LTE, the CQI is used to report CSI to the transmitter in order to adapt the transmit signal to the actual channel state. In the Vienna LTE Link Level Simulator [16, 17], the LTE implementation of this work, the CQI is calculated by first mapping the actual channel state to the equivalent AWGN channel and then determing the CQI for the equivalent AWGN channel [18]. This mapping, as well as the quantized characteristics of the CQI, is illustrated in Figure 2.

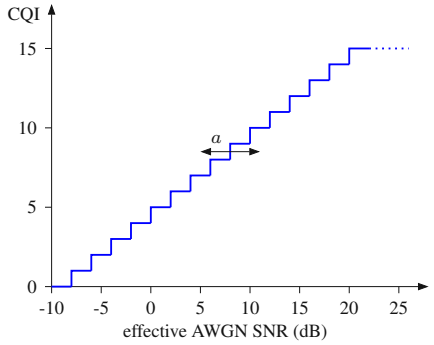


**Fig. 2**. Schematic relation between the CQI and the SNR for a frequency-flat AWGN channel.

Plotted over received SNR, the actual slope and the SNR step size depend on the actual channel charateristics and the receiver implementation. In order to capture channel fluctuations between two transmissions based on the CQI we introduce the CQI$_{\neq}$ metric

$$\mathrm{CQI}_{\neq} = \begin{cases} 0, & \mathrm{CQI_A} = \mathrm{CQI_B} \\ 1, & \mathrm{CQI_A} \neq \mathrm{CQI_B} \end{cases}. \qquad (1)$$

Due to the quantized characteristics of the CQI, the sensitivity of this metric depends on the actual effective AWGN SNR and therefore on the characteristics of the underlying channel and the noise power.

In order to overcome CQI quantization we propose a method similar to non-subtractive dithering. Thereby, we vary the estimated noise power $\widehat{\sigma}_z^2$ passed to the CQI calculation within a certain range of a factor $a$. This scaling of the noise power corresponds to a shift of the CQI characteristics in Figure 2. In this work, we randomize $a$ uniformly distributed within a range of -1.5 dB. . .1.5 dB [19]. The whole procedure to calculate the CQI$_{\neq}$ metric is illustrated in Figure 3. Thereby, for each set of channel estimates $\widehat{\mathbf{H}}_\mathrm{A}$ and $\widehat{\mathbf{H}}_\mathrm{B}$, the calculation of CQI$_{\neq}$ is repeated for every value of $a$. The results are then averaged over all measurements with the same time interval $\Delta$t between two consecutive transmissions. Note, that the actual SNR is left unchanged and therefore the impact of noise is independent of $a$.

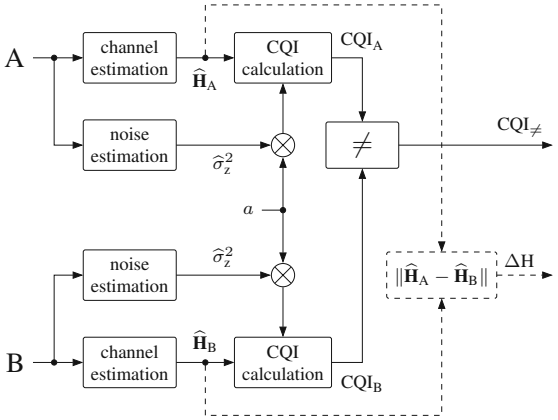


**Fig. 3**. Calculation of the CQI$_{\neq}$ metric.

## 3. MEASUREMENTS

In a measurement campaign, we use the proposed CQI$_{\neq}$ metric to compare different scenarios in terms of repeatability of wireless channels. These measurements were performed at TU Wien in downtown Vienna by the Vienna MIMO testbed [20]. Thereby, we compared a directional link, a fixed indoor receiver and a fast moving indoor receiver. On the transmitter side, we use for all scenarios the same off-the-shelf sector antenna located on a rooftop location, see Figure 4.

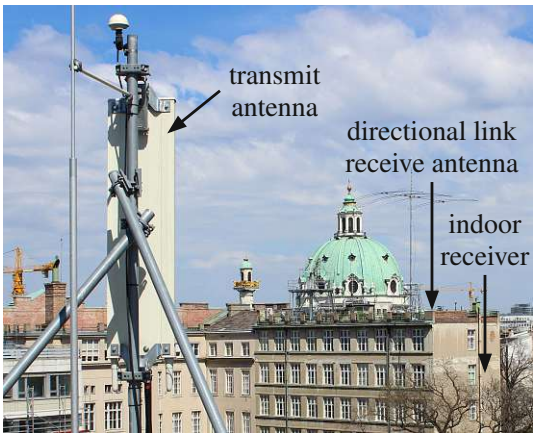


**Fig. 4**. Measurement setup.

### 3.1. Directional link

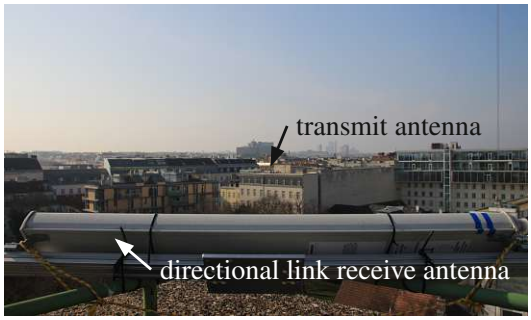


**Fig. 5**. Setup for the directional link measurement in downtown Vienna, Austria. The receive antenna is mounted on a rooftop opposite the building the transmitter is located.

In order to generate a static baseline scenario where slowly time-varying reflections from the surrounding area are suppressed, we setup an outdoor-to-outdoor directional link. Therefore, at the receiver side, we use an antenna similar to the transmit antenna but mounted 90° rotated and tilted upwards as shown in Figure 5. Reflections from the surrounding buildings are suppressed due to the rather small horizontal beamwidth of about 10° while reflections from the ground are suppressed by the uptilt of the antenna. The $\mathrm{CQI}_{\neq}$ metrics retrieved from this measurement plotted in Figure 6 are independent of the time interval between consecutive transmissions and reflect the properties of a directional link. Simulations show, that the fluctuations in the results are due to noise only.

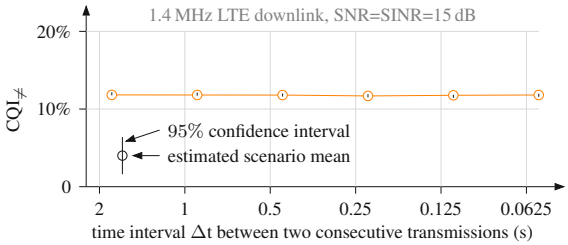


**Fig. 6**. Results for the directional link.

### 3.2. Fixed receiver

In this scenario, we measure the outdoor-to-indoor scenario of the fast moving receiver scenario described in Section 3.3 but without actually moving the receive antenna. Thereby, the receiver is located in an unpopulated office building opposite the building the transmit antenna is mounted on. In between, there is a courtyard with several trees. The measurements were performed in the evening on December 24th, 2015, at a wind speed of 10 km/h.

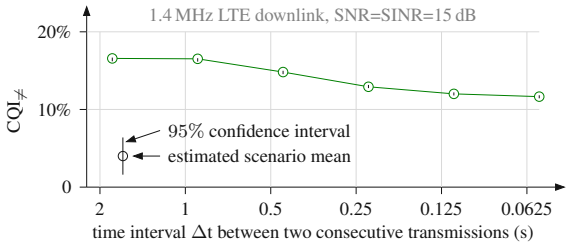


**Fig. 7**. Results for the fixed receiver.

For small $\Delta t$, we see results similar to the results for the directional link. With increasing time between two consecutive transmissions, the channel fluctuations increase caused by a slowly changing environment, e.g. trees moving in the wind.

### 3.3. Fast moving receiver

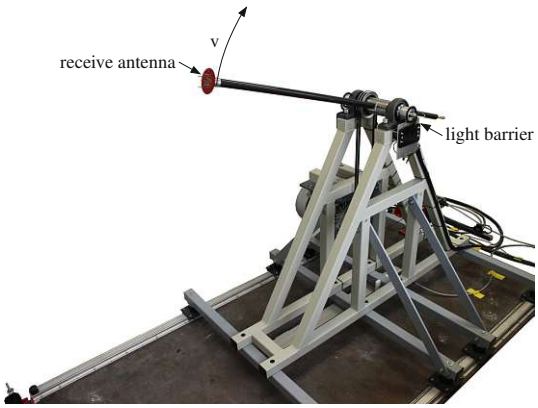


**Fig. 8**. The rotary unit, located indoors, generates time-variant channels by rotating the receive antenna around a central pivot.

The rotary unit [21–25] shown in Figure 8 generates repeatable time-variant channels by rotating the receive antenna around a central pivot. The received signals are then fed through the rod and rotary joints mounted inside the axis to the receiver hardware. A light barrier mounted on the axis captures the start of each turn and triggers the signal transmission. Thereby, the actual velocity and therefore the round-trip time of the antenna determines the minimum time interval between two consecutive transmissions over the same channel. For the maximum velocity of 400 km/h this time interval is ≈56 ms. In order to compare the fast moving receiver to the other scenarios, the time intervals for these measurements were chosen such that they correspond to the velocities in the measurement of the fast moving receiver.

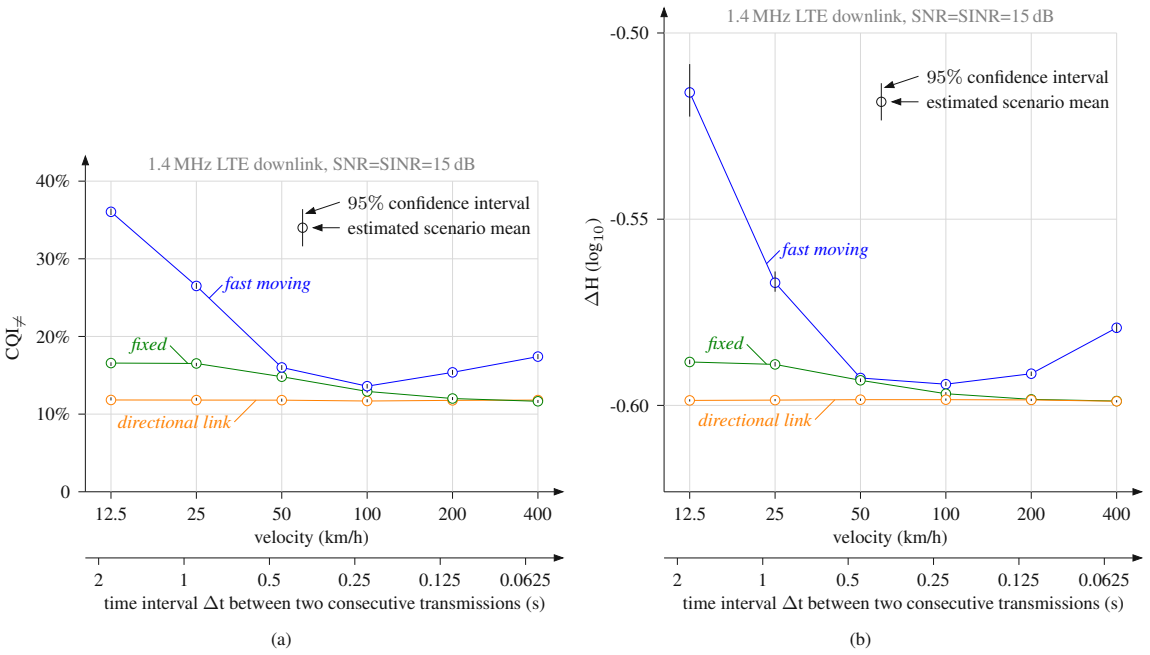


**Fig. 9**. Results in terms of (a) $\mathrm{CQI}_{\neq}$ and (b) $\Delta\mathrm{H}$. The axis were scaled such that they allow for a qualitative comparison.

A comparison of the results for the fast moving receiver and the results for the other scenarios is given by Figure 9a. We observe, that for velocities above 50 km/h, our fast moving receiver is able to accurately reproduce a fast fading channel. Simulations with equal channels and different thermal noise show that the slight increase in the $\mathrm{CQI}_{\neq}$ metric at very high velocities is only the result of an increase in channel diversity. On the other hand, for velocities below 50 km/h, the variable-frequency drive powering the AC motor is not able to move the receive antenna at a constant velocity anymore, thus the channel cannot be repeated precisely anymore.

### 3.4. Channel distance metric

Finally, we compare the measurement results in terms of the $\mathrm{CQI}_{\neq}$ metric to results obtained through evaluation of unquantized channel information. We therefore define the channel distance as the relative average distance between two channel estimates in terms of the Frobenius norm[2]

$$\Delta\mathrm{H} = \frac{\|\widehat{\mathbf{H}}_\mathrm{A} - \widehat{\mathbf{H}}_\mathrm{B}\|_\mathrm{F}}{\sqrt{\|\widehat{\mathbf{H}}_\mathrm{A}\|_\mathrm{F} \cdot \|\widehat{\mathbf{H}}_\mathrm{B}\|_\mathrm{F}}}. \qquad (2)$$

Thereby, $\Delta\mathrm{H}$ considers differences in the magnitude as well as differences in the phase of the channel estimates. This means in turn, that in contrast to the $\mathrm{CQI}_{\neq}$ metric, this metric is only applicable on measurements performed with phase synchronized equipment or if knowledge of the actual phase difference between the transmitter and the receiver is available. We use the latter approach by simultaneously measuring a reference phase over the directional link and phase-shift the channel estimates obtained from the receive antennas under investigation by this reference phase. Comparing the results plotted in Figure 9b to the results in terms of the $\mathrm{CQI}_{\neq}$ metric in Figure 9a, we find a qualitative accordance between the results based on full CSI and the results in terms of the $\mathrm{CQI}_{\neq}$ metric that is based on quantized CSI.

[2] $\|\mathbf{H}\|_\mathrm{F} := \sqrt{\mathrm{trace}(\mathbf{H}^H\mathbf{H})}$

## 4. DISCUSSION AND CONCLUSIONS

The proposed $\mathrm{CQI}_{\neq}$ metric together with the underlying methodology allows to quantify the repeatability of wireless channels based on quantized channel state information. Performance bounds of the proposed method along with the optimal SNR-based dithering are still subject to future research and investigating the influence of interference. The replacement of SNR dithering with dithering through statistical dispersion of receiver hardware, for example, imperfections from off-the-shelf cell phones, is currently under research. The conducted measurement campaign verifies the applicability of the proposed method.

## 5. REFERENCES


[1] D. G. Feitelson, "From Repeatability to Reproducibility and Corroboration," *ACM SIGOPS Operating Systems Review*, vol. 49, no. 1, pp. 3–11, 2015.

[2] A. Abedi, A. Heard, and T. Brecht, "Conducting repeatable experiments and fair comparisons using 802.11 n MIMO networks," *ACM SIGOPS Operating Systems Review*, vol. 49, no. 1, pp. 41–50, 2015.

[3] M. Lerch and M. Rupp, "Measurement-Based Evaluation of the LTE MIMO Downlink at Different Antenna Configurations," in *Proc. of the 17th International ITG Workshop on Smart Antennas 2013 (WSA 2013)*, Stuttgart, Germany, Feb. 2013.

[4] R. Nissel, S. Caban, and M. Rupp, "Experimental evaluation of FBMC-OQAM channel estimation based on multiple auxiliary symbols," in *IEEE 9th Sensor Array and Multichannel Signal Processing Workshop (SAM 2016)*, Rio de Janeiro, Brazil, Jul. 2016.

[5] F. Harrysson, J. Medbo, A. F. Molisch, A. J. Johansson, and F. Tufvesson, "Efficient experimental evaluation of a MIMO handset with user influence," *IEEE Transactions on Wireless Communications*, vol. 9, no. 2, pp. 853–863, February 2010.

[6] Y. Jian, C.-F. Shih, B. Krishnaswamy, and R. Sivakumar, "Coexistence of Wi-Fi and LAA-LTE: Experimental evaluation, analysis and insights," in *Communication Workshop (ICCW), IEEE International Conference on*, June 2015, pp. 2325–2331.

[7] E. Aryafar, N. Anand, T. Salonidis, and E. W. Knightly, "Design and Experimental Evaluation of Multi-user Beamforming in Wireless LANs," in *Proceedings of the Sixteenth Annual International Conference on Mobile Computing and Networking*, ser. MobiCom '10. New York, NY, USA: ACM, 2010, pp. 197–208.

[8] E. Zöchmann, S. Caban, M. Lerch, and M. Rupp, "Resolving the angular profile of 60 GHz wireless channels by Delay-Doppler measurements," in *IEEE 9th Sensor Array and Multichannel Signal Processing Workshop (SAM 2016)*, Rio de Janeiro, Brazil, Jul. 2016.

[9] E. Zöchmann, M. Lerch, S. Caban, R. Langwieser, C. F. Mecklenbräuker, and M. Rupp, "Directional evaluation of receive power, Rician K-factor and RMS delay spread obtained from power measurements of 60GHz indoor channels," in *IEEE-APS Topical Conference on Antennas and Propagation in Wireless Communications (APWC 2016)*, Cairns, Australia, Sep. 2016.

[10] A. D. Mcnaught and A. Wilkinson, *IUPAC. Compendium of Chemical Terminology, 2nd ed. (the "Gold Book").* Wiley-Blackwell; 2nd Revised edition, Aug. 1997.

[11] M. S. Allen, "Frequency-domain identification of linear time-periodic systems using LTI techniques," *Journal of Computational and Nonlinear Dynamics*, vol. 4, no. 4, pp. 041 004.1–041 004.6, 2009.

[12] R. A. Meyer and C. S. Burrus, "A unified analysis of multirate and periodically time-varying digital filters," *Circuits and Systems, IEEE Transactions on*, vol. 22, no. 3, pp. 162–168, 1975.

[13] F. Felici, J.-W. Van Wingerden, and M. Verhaegen, "Subspace identification of MIMO LPV systems using a periodic scheduling sequence," *Automatica*, vol. 43, no. 10, pp. 1684–1697, 2007.

[14] 3rd Generation Partnership Project (3GPP), "Evolved Universal Terrestrial Radio Access (E-UTRA) physical channels and modulation," 3rd Generation Partnership Project (3GPP), TS 36.211, Jan. 2015.

[15] S. P. Lipshitz, R. A. Wannamaker, and J. Vanderkooy, "Quantization and Dither: A Theoretical Survey," *Journal of the Audio Engineering Society*, vol. 40, no. 5, pp. 355–375, 1992.

[16] M. Rupp, S. Schwarz, and M. Taranetz, *The Vienna LTE-Advanced Simulators: Up and Downlink, Link and System Level Simulation*, 1st ed., ser. Signals and Communication Technology. Springer Singapore, 2016.

[17] E. Zöchmann, S. Schwarz, S. Pratschner, L. Nagel, M. Lerch, and M. Rupp, "Exploring the physical layer frontiers of cellular uplink," *EURASIP Journal on Wireless Communications and Networking*, vol. 2016, no. 1, pp. 1–18, 2016.

[18] S. Schwarz, C. Mehlführer, and M. Rupp, "Calculation of the Spatial Preprocessing and Link Adaption Feedback for 3GPP UMTS/LTE," in *Wireless Advanced (WiAD), 2010 6th Conference on*, London, UK, June 2010, pp. 1–6.

[19] P. Csordás, A. Mersich, and I. Kollár, "Digital Dither: Decreasing Round-off Errors in Digital Signal Processing," in *Intelligent Signal Processing, 2003 IEEE International Symposium on*, Sept 2003, pp. 9–14.

[20] M. Lerch, S. Caban, M. Mayer, and M. Rupp, "The Vienna MIMO testbed: Evaluation of future mobile communication techniques," *Intel Technology Journal*, vol. 18, pp. 58–69, 2014.

[21] S. Caban, J. Rodas, and J. A. García-Naya, "A Methodology for Repeatable, Off-line, Closed-loop Wireless Communication System Measurements at Very High Velocities of up to 560 km/h," in *Proc. International Instrumentation and Measurement Technology Conference (I2MTC 2011)*, Binjiang, Hangzhou, China, May 2011.

[22] R. Nissel and M. Rupp, "Doubly-selective MMSE channel estimation and ICI mitigation for OFDM systems," in *IEEE International Conference on Communications (ICC)*, London, UK, Jun. 2015.

[23] M. Lerch, "Experimental comparison of fast-fading channel interpolation methods for the LTE uplink," in *Proc. of the 57th International Symposium ELMAR-2015*, Zadar, Croatia, Sep. 2015.

[24] R. Nissel, M. Lerch, and M. Rupp, "Experimental validation of the OFDM bit error probability for a moving RX antenna," in *IEEE Vehicular Technology Conference (VTC)*, Vancouver, Canada, Sep. 2014.

[25] J. Rodríguez-Piñeiro, M. Lerch, J. A. García-Naya, S. Caban, M. Rupp, and L. Castedo, "Emulating Extreme Velocities of Mobile LTE Receivers in the Downlink," *special issue JWCN*, 2015.

## 5.2 Static Scenarios

[7] **S. Caban**, M. Lerch, S. Pratschner, E. Zöchmann, P. Svoboda, and M. Rupp. "Design of Experiments to Compare Base Station Antenna Configurations". In: *IEEE Transactions on Instrumentation and Measurement* 68.10 (2019), pp. 3484–3493. ISSN: 0018-9456. DOI: 10.1109/TIM.2018.2880941. → see Page 67

[10] S. Pratschner, T. Blazek, H. Groll, **S. Caban**, S. Schwarz, and M. Rupp. "Measured User Correlation in Outdoor-to-Indoor Massive MIMO Scenarios". In: *IEEE Access* 8 (2020), pp. 178269–178282. DOI: 10.1109/ACCESS.2020.3026371. → see Page 77

[11] S. Pratschner, T. Blazek, E. Zöchmann, F. Ademaj, **S. Caban**, S. Schwarz, and M. Rupp. "A Spatially Consistent MIMO Channel Model With Adjustable K Factor". In: *IEEE Access* 7 (2019), pp. 110174–110186. DOI: 10.1109/ACCESS.2019.2934635. → see Page 91

[15] E. Zöchmann, **S. Caban**, C. F. Mecklenbräuker, S. Pratschner, M. Lerch, S. Schwarz, and M. Rupp. "Better than Rician: modelling millimetre wave channels as two-wave with diffuse power". In: *EURASIP Journal on Wireless Communications and Networking* 2019.1 (Jan. 2019), p. 21. ISSN: 1687-1499. DOI: 10.1186/s13638-018-1336-6. → see Page 104

[21] C. Mehlführer, **S. Caban**, and M. Rupp. "Cellular System Physical Layer Throughput: How Far Off Are We From The Shannon Bound?" In: *IEEE Wireless Communications* 18.6 (2011), pp. 54–63. DOI: 10.1109/MWC.2011.6108334. → see Page 121

[24] R. Nissel, E. Zöchmann, M. Lerch, **S. Caban**, and M. Rupp. "Low-Latency MISO FBMC-OQAM: It Works for Millimeter Waves!" In: *IEEE International Microwave Symposium (IMS)*. Hawaii, USA, June 2017. → see Page 131

3484 IEEE TRANSACTIONS ON INSTRUMENTATION AND MEASUREMENT, VOL. 68, NO. 10, OCTOBER 2019

# Design of Experiments to Compare Base Station Antenna Configurations

Sebastian Caban, Martin Lerch, Stefan Pratschner, Erich Zöchmann, Philipp Svoboda, and Markus Rupp

***Abstract*— Publishing measurement results without elaborating on the uncertainty included is a common practice in the wireless community. Therefore, it is not surprising that the application of state-of-the-art variance reduction techniques to wireless research is rarely seen. In this paper, we discuss, exemplarily, the benchmarking of the average link capacity of a 4 × 4 multiple-input multiple-output (MIMO) downlink resulting from different base station (BS) antenna configurations. We show that the capacity of this downlink is not only dependent on the antenna spacing (the effect we want to measure), but also on the position of the antennas (an effect we need to control for). Unfortunately, once we change the antenna spacing, we cannot avoid changing the position of the antennas as well. We show that by applying the variance reduction technique of randomizing BS antenna positions, we get more accurate results. We further show that without increasing the effort, our favored method of matching completely eliminates the systematic error of position dependence. Both methodologies can also be applied to throughput measurements and larger antenna arrays, especially to virtual antenna array measurements for massive MIMO.**

***Index Terms*— 5G mobile communication, antenna arrays, antenna measurements, beamforming, massive multiple-input multiple-output (MIMO), MIMO, wireless communication.**

## I. Introduction

When carrying out mobile cellular network measurements, either by using only a few antennas [1]–[8] or a massive multiple-input multiple-output (MIMO) configuration [9]–[20], the mean scenario-performance of the links measured is influenced by the base station (BS) antenna configuration (the effect we want to investigate in this paper) and the physical position of the antennas.

### A. Problem Formulation

The mean scenario performance of a radio link can be expressed in many different ways. For example, to determine physical layer throughput, the entire protocol stack (including the channel state information feedback in the uplink) has to be implemented [3], [21]–[24]. In this paper, we simplify the measurements by applying channel capacity as a performance metric [25]–[28], knowing that the ideas presented in the following are also valid for throughput measurements [29], [30] and for other performance metrics.

Manuscript received May 3, 2018; revised October 20, 2018; accepted October 22, 2018. Date of publication December 17, 2018; date of current version September 13, 2019. This work was supported in part by the Austrian Federal Ministry of Science, Research and Economy, in part by the National Foundation for Research, Technology and Development, in part by the Czech Science Foundation through future transceiver techniques for the society in motion under Project 17-18675S, in part by the Czech Ministry of Education in the frame of the National Sustainability Program under Grant LO1401, and in part by the INWITE Project. The Associate Editor coordinating the review process was Dr. Huang-Chen Lee. *(Corresponding author: Sebastian Caban.)*

S. Caban, M. Lerch, S. Pratschner, and E. Zöchmann are with the Christian Doppler Laboratory for Dependable Wireless Connectivity for the Society in Motion, 1040 Vienna, Austria, and also with the Institute of Telecommunications, TU Wien, 1040 Vienna, Austria (e-mail: sekretariat@nt.tuwien.ac.at).

P. Svoboda and M. Rupp are with the Institute of Telecommunications, TU Wien, 1040 Vienna, Austria.

Color versions of one or more of the figures in this article are available online at http://ieeexplore.ieee.org.

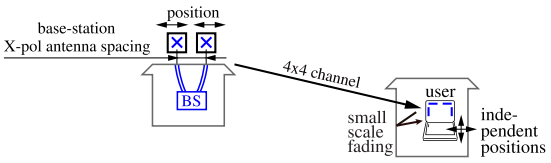


Fig. 1. Representative Measurement Scenario. A BS, connected with four cables to two X-pol antennas on a roof, transmits to four RX antennas hidden inside a laptop located indoors.

Without loss of generality, let us investigate the outdoor-to-indoor down-link channel of the simple scenario shown in Fig. 1. On the transmitter side, we have a BS with two dual cross-polarized flat-panel antennas mounted on the roof of a building. In the sequel, we refer to one "dual cross-polarized flat-panel antenna" as "X-pol antenna." We connect our four-channel TX hardware to the four antenna ports of the BS's two X-pol antennas. On the receiver side, we have a laptop, also equipped with four antenna ports, placed in an office room.

Again, without loss of generality, let us investigate the capacity of this link only against the spacing of the X-pol antennas at the BS in Fig. 1 (the antenna configuration).

Typically, there are many scattering objects around an indoor user. To make such an investigation independent of the antenna positions of the indoor receiver, the receiver can be moved by a few wavelengths in-between measurements in order to obtain uncorrelated measurement samples in a small-scale fading scenario [30].

On the transmitter side, the situation is different: outdoor BSs are (in most cases and also in our case) purposely placed on the roof of buildings with no reflecting objects within the vicinity. Repositioning relatively heavy transmit antennas (for example, to other rooftops) in a timely and repeated fashion is not an option. Therefore, it is not feasible to take uncorrelated measurements at different transmit antenna locations in order to be independent of transmit antenna placement.

Consequently, when measuring the channel capacity against TX antenna spacing, the average link capacity no longer changes exclusively due to the spacing (Figs. 2 and 3).

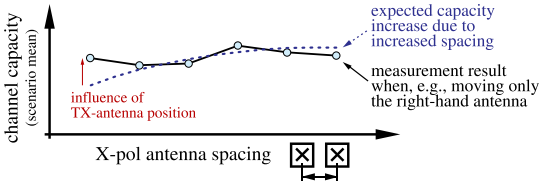


Fig. 2. Channel capacity against antenna spacing. To measure the channel capacity of a 4×4 channel against antenna spacing, we move the right-hand TX antenna in-between each measurement to change the antenna spacing. Thus, we measure two different effects: 1) the ability to transmit more data as bigger antenna spacing decreases channel correlation and 2) a change in SNR and thus a change in channel capacity that originates from repositioning the right-hand TX antenna.

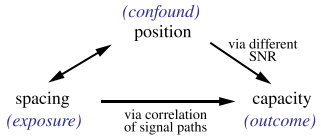


Fig. 3. Confounding by position. We are interested in inferring the mean 4×4 link capacity as function of the X-pol antenna spacing (horizontal arrow from the left to the right). However, we deal with confounding, as the antenna spacing is associated with antenna position (illustrated by the double arrow). Changing the position of the antennas will change the link capacity due to a change in SNR.

The qualitative results shown in Fig. 2 represent only the specific TX antenna positions we have used to measure against TX antenna spacing. If we move the left-hand TX antenna to measure against TX antenna spacing (instead of the right-hand TX antenna), then we get a slightly different result despite measuring with the same TX antennas at the same antenna spacings, just at different positions (this will be detailed in Fig. 10 in the measurement results section). The same holds true if we move both TX antennas symmetrically and keep their center position constant. Thus, how do we measure only the capacity increase due to an increased spacing, as shown dotted curve in Fig. 2?

### B. Work on Antenna Configurations

The amount of data that can be transmitted on a radio channel increases with transmit antenna spacing as the signal paths originating in the transmit antennas become less and less correlated. This behavior has been found to happen throughout the literature in measurements regarding indoor scenarios [31]–[34], outdoor scenarios [32], [35], [36], reverberation chambers [37], and virtual antenna arrays [38]. These results are supplemented by ray tracing techniques [39], [40] and theoretical analyses (see [41]–[47] and the references therein). The 4×4 capacity sketched in Fig. 2 shows this behavior, which is common knowledge [31]–[47] and therefore not within scope of this paper.

In the context of massive MIMO, the topic of antenna configurations has recently regained research interest [9]–[20]. Massive MIMO channel characterization has been carried out via measurements with virtual antenna arrays [9]–[12], [48], [49]. The authors of [17]–[19] and [50] have investigated the impact of different antenna configurations. Deployment aspects of massive MIMO have been considered in [15], [16], and [51]. Massive MIMO with physical space constraints has been theoretically analyzed in [52] and [53].

However, it still seems generally accepted in the wireless community to publish measurement results without elaborating on the uncertainty included (for example, by plotting confidence intervals). Thus, we can only speculate whether "something" has been just measured in a publication or whether the experiments have been designed thoroughly.

As outlined earlier, in real-world measurements, the capacity of a specific antenna configuration can be—by chance—higher or lower than the capacity of the same antenna configuration at a different position. As there are not many scattering objects around an outdoor BS, it seems to be accepted (including our past measurements [1], [2], [54]) to just measure at different spacings, by, for example, moving only one antenna [1], [2], [54] or both antennas symmetrically [32] without systematically compensating the position dependence in the design of experiments.

*Our Contribution:* In this paper, we propose experimental designs to reduce the effect of confounding by BS antenna position.

### C. This Work

We present our measurement setup in Section II. In Section III, we propose two experimental designs to efficiently quantify the influence of BS antenna spacing on channel capacity. We thereby isolate the effects of antenna spacing on capacity from the effects of antenna position on capacity to cancel the latter. In Section IV, we report the results of a measurement campaign to quantify the performance of both methodologies. Our contribution ends in Section V with a note on how our proposed methodologies can be applied to arrays with more antennas.

## II. Measurement Scenario and Setup

All measurements in this paper are conducted at 2.5 GHz, a frequency currently used for Long-Term Evolution (LTE) (band B7). We use a custom-built wireless testbed [55]–[58] to generate and receive data with a bandwidth of 9 MHz, which corresponds to 10-MHz LTE. We neither use virtual transmitters nor receivers, as we can directly measure a 4×4 MIMO channel with our testbed. Aside from the size of the custom-built transmit-and-receive hardware, our measurement setup represents a possible real-word LTE downlink setup (Fig. 4). Table I summarizes the channel sounding parameters.

### A. Transmitting Base Station

At the TX site, we connect our hardware with four cables to two commercially available Kathrein 80010438 flat-panel X-pol antennas. They transmit with a total transmit power of 36 dBm from the roof of a building. As shown in Fig. 5, the only modification we have made to what one would expect from a possible real-world LTE downlink scenario is that we have mounted both transmit antennas on a 3-m-long linear guide such that we can freely move both transmit antennas in-between measurements with a repeat accuracy of 0.02 mm.

TABLE I
CHANNEL SOUNDING PARAMETERS

| | |
|---|---|
| transmit antennas | Kathrein 80010438 |
| transmit power | 30 dBm per antenna |
| center frequency | 2.5 GHz |
| transmit signal | OFDM, random QPSK symbols |
| subcarrier spacing | 15 kHz |
| number of subcarriers $K$ | 600 |
| bandwidth $B$ | 9 MHz (corresponds to 10 MHz LTE) |
| receive antennas | printed dipole antennas |
| frequency synchronization | rubidium frequency standards |
| timing synchronization | over LAN with GPS plus custom-built hardware [59], [60] |
| evaluation | off-line in Matlab |

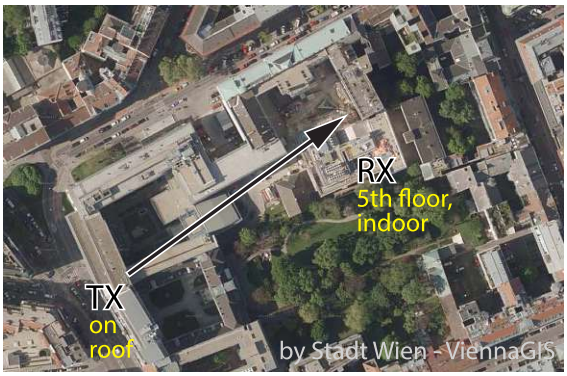


Fig. 4. Bird's eye view of the measurement scenario. The two X-pol antennas of the BS are located on a roof approximately 150 m away from the indoor receiver in downtown Vienna, Austria.

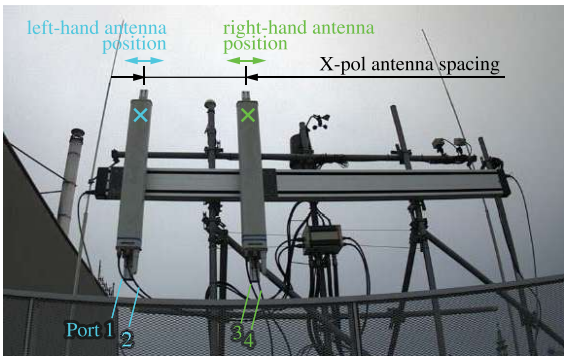


Fig. 5. Transmitting BS. At the BS, we mount two kathrein 80010438 X-pol flat-panel antennas on a 3-m-long linear guide to freely move both X-pol antennas in-between measurements.

At a wavelength of $\lambda$ =12 cm, this corresponds to a repeat accuracy of $\pm 0.02\%$ of $\lambda$.

### B. Receiving Indoor User

The receiver is placed inside an office building approximately 150 m away from the TX site. As shown in Fig. 6, we use two vertically and two horizontally polarized printed dipole antennas inside an off-the-shelf laptop. The antennas are connected via four cables to an external receiving hardware. During a measurement, the laptop is randomly moved and

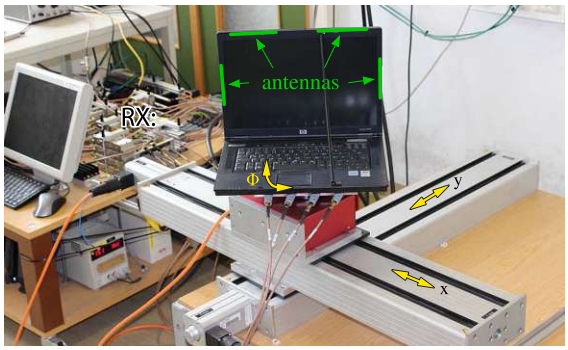


Fig. 6. Receiving indoor user. The indoor receiver utilizes two vertically and two horizontally polarized receive antennas, which are mounted inside an off-the-shelf laptop. This laptop is placed on an $xy\Phi$-positioning table to sample different receiver positions.

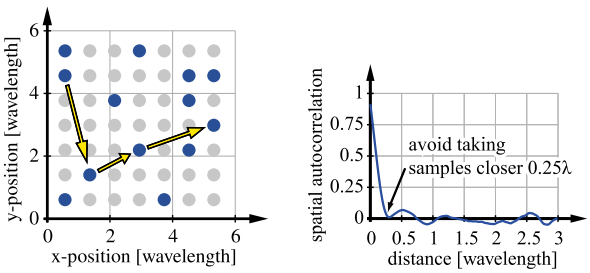


Fig. 7. Sampling positions at the receiver. Bird's eye view of the $XY\Phi$-positioning table in Fig. 6 (left). We measure at 13 random RX locations (blue dots, fixed during the whole measurement) on a grid spaced according to a distance coprime to half a wavelength in order to avoid sampling periodic variations of the scenario. If we need more samples, then we continue to measure at the remaining positions of equidistantly spaced grid, thereby minimizing correlation. The spatial autocorrelation of the measurement scenario (right). See [65] on how the correlogram is constructed.

rotated to sample 13 independent realizations of a fading scenario as shown in Fig. 7.

### C. Sample Size and Sampling Strategy

A sample size of less than 10 is "usually too small to rely on sample estimates, even in "nice"[1] parametric cases" [61]. Therefore, we usually follow a simple strategy to minimize

[1]Transmitting with a signal bandwidth of 9 MHz, averaging over 4×4 antennas, and plotting relative results prevents "deep fading holes."

sample size, and thus measurement time: we measure 10 samples to calculate a first estimate of the results online in the field. We check whether the results are significant or not. If not, we measure another 10 samples and then check again. If the results are significant, we measure only three additional samples to check for divergence.

If time allows, especially in a research in which there is no past experience on what to expect, measuring more samples ("till the end of the day") is never a bad idea. By measuring $n$ times more "effectively independent samples," we decrease the size of the confidence intervals for the mean by $\sqrt{n}$ [62]. For our specific case, we will see in the results section that having more than 13 samples is not necessary as the favored method of matching is "accurate enough" with very small sample sizes.

When sampling, we need to avoid spatial correlation by sampling with a fair amount of distance on the $xy\Phi$-positioning table. When taking only a few samples, using systematic sampling may be a dangerous procedure, especially when periodic variations exist in the area to be sampled [63]. Therefore, when we sample only a few positions, we do this randomly. When sampling many positions, the literature suggests systematically sampling a grid of fixed size, particularly in such cases of autocorrelated populations experiencing negative exponential correlation functions. This strategy minimizes correlation by maximizing the distance between samples [64].

## III. Reducing Position Dependence by Intelligent Experiment Design

Several approaches exist to reduce confounding (by position) [66], [67]. In principle, confounding can be controlled in two ways: 1) by "intelligently" designing the experiment to reduce the influence of confounding or 2) by analytically compensating the effects of confounding after conducting the experiment if the former method is impractical. In this paper, we focus only on intelligent experiment design to inherently compensate the confounding effect instead of relying on a model to reduce it.

### *A. Methodology 1—Randomizing Antenna Positions*

In the last century, the development of randomized controlled trials [68] has been one of the most important achievements in the study of the effect of treatment in medical research [69]. Applying this methodology to our problem, it works as follows. If we give any transmit antenna position an equal chance to occur by moving both transmit antennas at every measurement to a random position with the desired spacing, we average out the effect of position.

Although this sounds straightforward in theory, we need to ensure that for each antenna spacing, the chance that each antenna is moved to a certain position is equal. Obviously, this is not possible as shown in Fig. 8, since positions at both ends of the (noninfinitely long) linear guide are less likely to occur the larger the antenna spacing.

Randomizing antenna positions, therefore, has two limiting factors.

1) *Unequal Position Distribution:* Measuring each spacing with unequal position distributions leads to biased results if the SNR changes over antenna center position. According to the position distribution (probability density function) shown in Fig. 8, positions close to both ends of the linear guide are less likely to occur the larger the antenna spacing is. For example, if the SNR is highest in the middle of the linear guide, then the SNR, and thus the capacity, will decrease as antenna spacing increases. This capacity decrease is not due to antenna correlation or mutual coupling but due to different measurement positions only. To combat this scenario-dependent systematic error, we aim to measure all spacings with equal antenna position distributions.
2) *Spatial Correlation:* The measurements are (highly) spatially correlated since there are not many scattering objects around an outdoor BS. As the spatial correlation decreases with distance, randomly sampling the limited range available does not minimize the variance. Thus, in order to combat spatial correlation, a uniform sampling approach (which maximizes the distance between samples) is preferable in this case of autocorrelated populations experiencing negative exponential correlation functions [64].

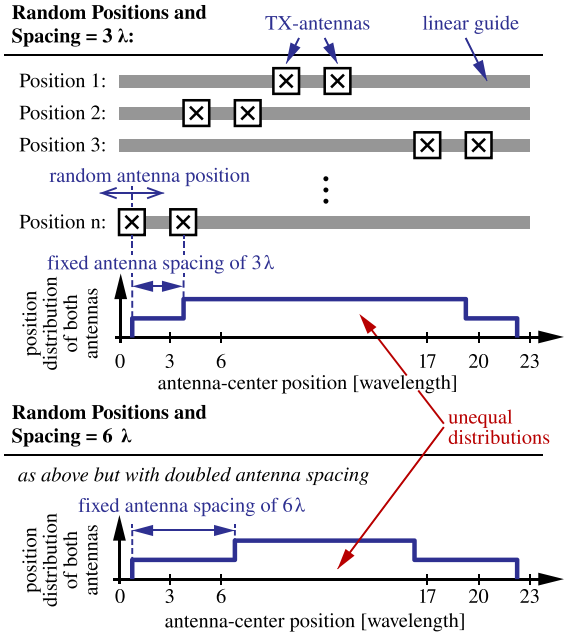


Fig. 8. Randomizing antenna positions. When randomizing positions on a linear guide, the antenna positions cannot be distributed equally for different antenna spacings.

### *B. Methodology 2—Matching Antenna Positions With Equidistant Sampling*

To overcome the two aforementioned downsides of randomizing antenna positions, we propose five prerequisites to: 1) measure at exactly the same transmit antenna positions for

each antenna spacing[2] and 2) reduce spatial correlation by sampling equidistantly.

1) *Quantize Antenna Positions:* We restrict the possible positions of both transmit antennas to a grid of spacing $\Delta$ (the vertical gray lines in Fig. 9). The grid spacing $\Delta$ can be chosen arbitrarily but needs to be equal to or greater than the width of a transmit antenna.
2) *Quantize Antenna Spacings:* If we restrict the possible positions of both transmit antennas to a grid of spacing $\Delta$, then we also automatically restrict the antenna spacings that can be measured to integer multiples of the grid spacing $\Delta$.
3) *Assume that both TX Antennas are Identical:* If we use two identical (with identical antenna patterns) antennas at the transmitter, then we do not need to differentiate between the left-hand and the right-hand antenna positions. Mass-produced BS antennas typically fulfil this prerequisite. If the antennas are not identical but are instead interchangeable, then exchanging their positions at the end of the experiment, repeating the whole measurement, and then averaging the results is also an option.
4) *Measure Only Once at each Grid Position for Each Antenna Spacing s:* Looking exemplarily at the measurement with an antenna spacing $s = 4\Delta$ in Fig. 9, we need to measure at eight grid positions to obtain a uniform position distribution (note the green building block with a size of $2s = 8\Delta$). This building block is then repeated to obtain a uniform position distribution for the overall guide.
5) *Set the Guide Length to an Integer Multiple of 2s:* Consequently, to measure and compare multiple antenna spacings, we require a linear guide with a minimum length that is the least common multiple (LCM) of all the building block sizes, for example,

| antenna spacings $s$ to be measured (examples) | | | | | minimum linear guide length required |
|---|---|---|---|---|---|
| $1\Delta$ | $2\Delta$ | $3\Delta$ | $4\Delta$ | | $12\Delta$ |
| $1\Delta$ | $2\Delta$ | | $4\Delta$ | $8\Delta$ | $16\Delta$ |
| $1\Delta$ | $2\Delta$ | $3\Delta$ | $4\Delta$ | $8\Delta$ | $48\Delta$ |

Thus, all we need to do now is to measure at all the transmit antenna positions in Fig. 9. Finally, we average the channel capacities of each antenna spacing.

### C. Intermediate and Other Methodologies

Matching with equidistant sampling overcomes the two downsides of randomizing antenna positions, namely, unequal position distributions and spatial correlation. In between randomizing and matching with equidistant sampling, we can think of a variety of intermediate methodologies. For example, one technique that can be used is to relocate the antennas uniformly (for example, in terms of array center) instead of relocating randomly. The uniform sampling approach reduces spatial correlation as it maximizes the distance between the samples. We can also ensure that the array is moved to positions within the same range. Unfortunately, we will not be able to achieve equal antenna position distributions through these methods as positions close to the end of the linear guide are less likely to occur the larger the spacing is (similar to

[2]In our problem, we apply the method of matching treated units to similar nontreated units, as promoted by Professor Rubin in the 1980s [70].

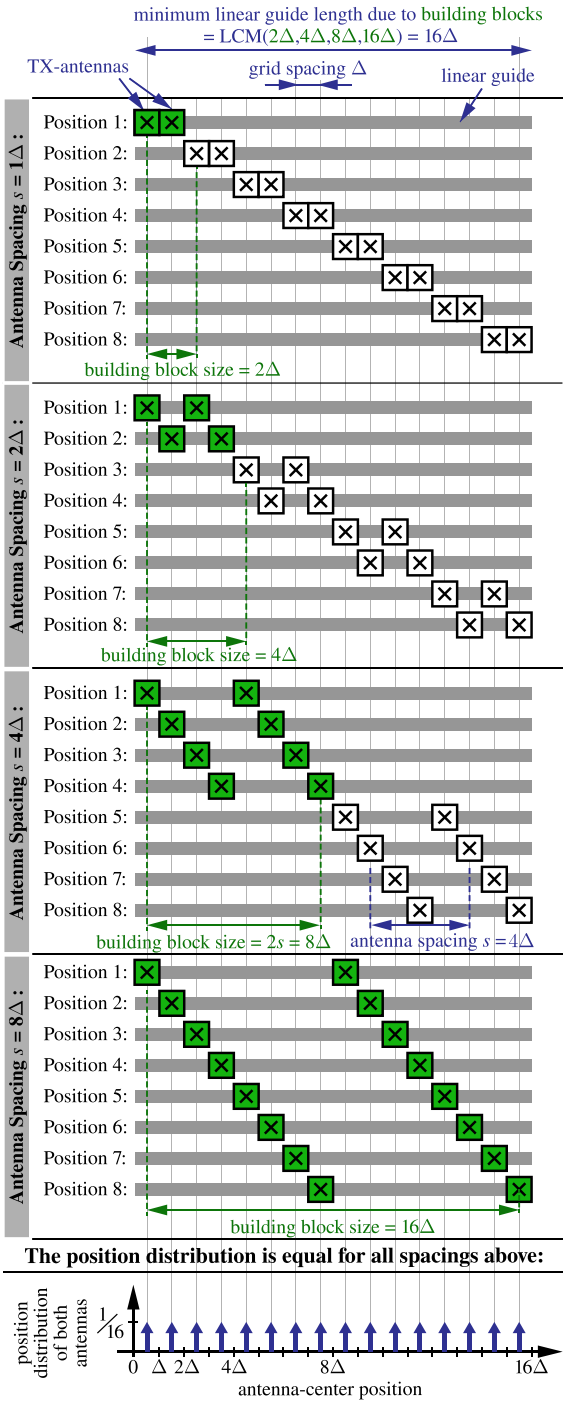


Fig. 9. Measurement procedure to measure four different antenna spacings with equally distributed and equally spaced antenna positions.

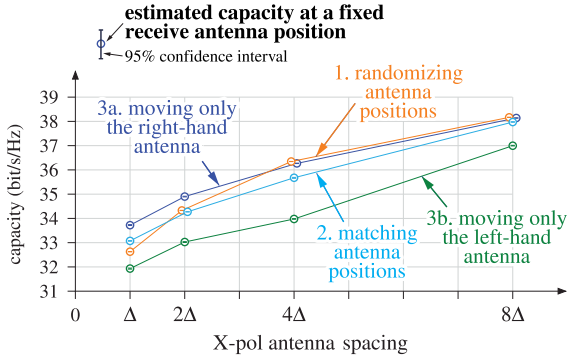


Fig. 10. Real-world measurement at a single receive antenna position. 4×4 channel capacity against X-pol antenna spacing is measured with the same transmit antennas at the same antenna spacings of 1Δ, 2Δ, 4Δ, and 8Δ. The four-element receive antenna is static at a fixed position. The uncertainty of the measurement results (random error), presented as 95% confidence intervals, is a consequence of the interference and the noise captured by the receiver. Different results (systematic error) of Methodologies 1 and 3 compared to those of matching originate only from different transmit antenna positions. (Measurement points are shifted off-grid for better visibility.)

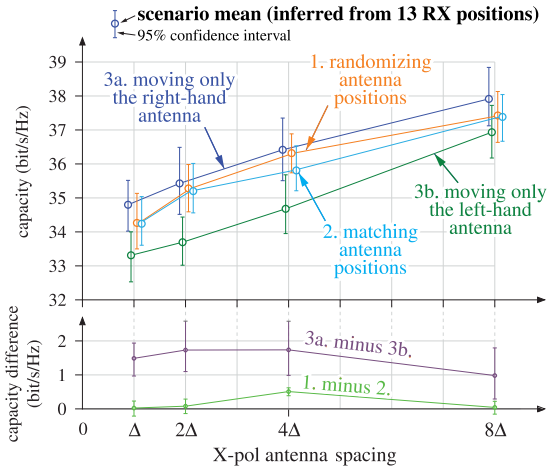


Fig. 11. Real-world measurement at 13 receive antenna positions. The same setup as shown in Fig. 10 but showing the scenario mean inferred from 13 receive antenna positions. Significantly different results obtained from Methodologies 3a and 3b (bottom part) originate *only* from different transmit antenna positions. The difference between Methodologies 1 and 2 is statistically significant only for an antenna spacing of 4Δ. (Measurement points are shifted off-grid for better visibility.)

Fig. 8). When the SNR is highest or lowest in the middle of the array (as, for example, in Fig. 12), a systematic error will occur due to different average SNRs. In the measurement campaign in the following, we do not include the above-outlined intermediate methodologies; we present, for simplicity reasons, only the two "extremes" of matching and randomization.

## IV. Measurement, Measurement Results, and Discussion

This section shows how to use the measurement setup described in Section II, together with the methodologies of randomizing antenna positions and matching antenna positions (both with eight positions per antenna spacing) presented in Section III, to compare different antenna spacings. In addition, we show the measurement results when moving only the right-hand antenna and moving only the left-hand antenna. We show these additional results to represent all cases in which rooftop transmit antennas are not mounted on linear guides to avoid confounding by moving them in a repeatable fashion.

The width of our X-pol BS antennas expressed in wavelengths is slightly below $1.4\lambda$. In our measurements, we thus choose a grid spacing of $\Delta = 1.4\,\lambda$. We decided to measure antenna spacings of $1\,\Delta$, $2\,\Delta$, $4\,\Delta$, and $8\,\Delta$ to take full advantage of our $22\lambda \approx 16.4\,\Delta$ long linear guide while maximizing the ratio between the lowest spacing and highest spacing we can measure.

*Step A (Measuring at a Single Receive Antenna Position):* Measuring at a single, fixed receive antenna position, we obtain the result shown in Fig. 10. To capture measurement uncertainty, we repeated the whole measurement at the same position. By means of bootstrap analysis [71], we then calculated the 95% bias-corrected and accelerated bootstrap confidence intervals.

*Step B (Measuring at Independent Receive Antenna Positions to Infer the Scenario Mean):* A measurement at a single receive antenna position is not representative of an outdoor-to-indoor scenario since fading is present at the indoor

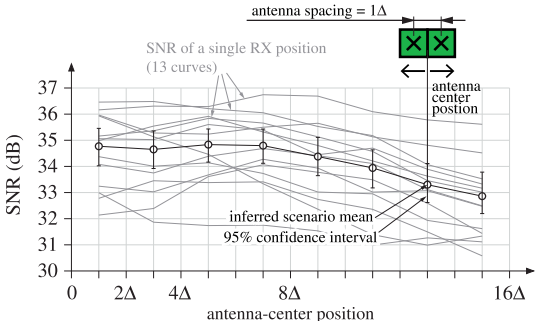


Fig. 12. Real-world measurement of the SNR against antenna center position: The large-scale fading trend of our exemplary scenario is demonstrated by the mean SNR, inferred from 13 RX positions. The SNR has been measured with a fixed X-pol antenna spacing of 1Δ by jointly moving both TX antennas. Note that we do not move the transmit antennas only by "a few wavelengths" but by $14\Delta = 14 \cdot 1.4\lambda = 19.6\lambda = 2.4\,\text{m}$ [48].

receiver. To infer the mean scenario performance shown in Fig. 11, we repeat the overall measurement at 13 spatially uncorrelated positions of the four-element receive antenna (as discussed in Section II-B).

We could then extend this procedure of sampling a single user location by sampling many possible user locations in a cell (stratified sampling [67]) until we are again confident enough of the results. However, in this paper, we only conduct measurements at a single user location by taking samples within close proximity of the single user.

Note that the X-pol antenna spacings are equal in all four curves of Fig. 11. The difference between the curves is scenario dependent. In this specific example, the mean SNR shown in Fig. 12 is lowest on the right-hand side of the guide. Consequently, as shown in Curve 3b in Fig. 11, the capacity is lowest when the right-hand antenna is fixed on the right edge of the guide while moving only the left-hand

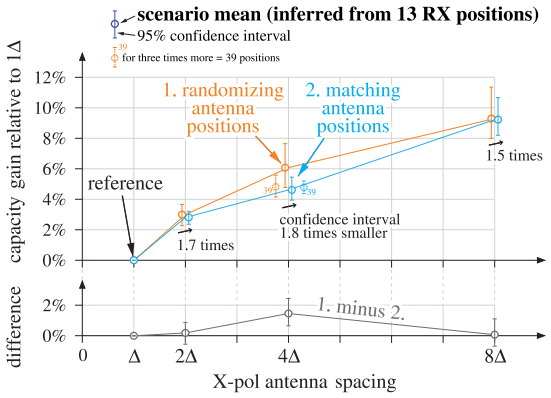


Fig. 13. Real-world measurement of the capacity gain relative to the capacity at 1Δ. Compared to Fig. 11, where the confidence intervals partly overlap, we can now be confident that there is a capacity gain when increasing antenna spacing. We further observe that matching antenna positions is more precise (smaller confidence intervals) than randomizing antenna positions. At an antenna spacing of 4Δ, the inferred means are significantly different (bottom plot). (Measurement points are shifted off-grid for better visibility.)

antenna. In Curve 3a, we observe the opposite. Fig. 11 (bottom part) shows the difference between these two curves due to confounding by position. The difference is significant as the confidence intervals do not include the null hypothesis value of 0 [72].

The shape of the individual SNR curves per RX position in Fig. 12 is dependent on the position of the receiver. This means that the RX position also confounds our measurement results. We avoid confounding by RX position by fixing the RX position while measuring all different transmit antenna configurations. Hence, we implicitly apply the method of matching to the RX antenna positions.

*Step C (Plotting the Results Relative for Comparison):* Note that the curves in Fig. 11 show a very smooth (relative) increase over antenna spacing, whereas the confidence intervals look large. Although the (absolute) confidence intervals in Fig. 11 are correct, they are misleading—there is a common fluctuation in all of the points in Fig. 11. The uncertainty caused by measuring 13 different positions is larger than the uncertainly caused by measuring using a different methodology or at a different spacing. The resulting curves in Fig. 11 are very smooth (with a certain offset common to all points), but we cannot infer from the confidence intervals whether the increase over antenna spacing is significant.

Consequently, if we are interested in comparing antenna configurations, then we need to plot the relative capacity increase against antenna spacing, and not the absolute capacity inferred from our specific measurement scenario. In other words, we need to cancel out the common fluctuation in Fig. 11 by normalizing the results to the capacity measured at 1Δ as shown in Fig. 13.

Note that although the absolute confidence intervals of Methodologies 1 and 2 on the top part of Fig. 11 partly overlap, the relative capacity gain plotted on the top part of Fig. 13 is significantly larger than 2% for 2Δ, 4% for 4Δ, and 6% for 8Δ.

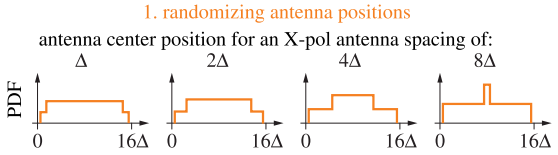


Fig. 14. Position distribution when randomizing antenna positions. Positions at the edge of the guide are less likely to occur when randomizing (Fig. 8). If the SNR in a specific scenario is not distributed equally against position (Fig. 12), then a systematic measurement error will occur. In our case, the error is highest at 4Δ.

*Precision:* Looking at the length of the confidence intervals, we observe that matching antenna positions results in a smaller variance (smaller intervals) than randomizing antenna positions does. For example, at an antenna spacing of 4Δ, the confidence interval is 1.8 times smaller using the methodology of matching antenna positions than that of randomizing antenna positions. The reason is that when matching, we measure each antenna spacing at exactly the same transmit antenna positions (Fig. 9), thereby eliminating the effects of a change in position when plotting the results relative to 1Δ. We do not and cannot measure at exactly the same positions when randomizing transmit antenna positions.

As the size of the confidence intervals for the mean decreases with the square root of the number of effectively independent samples [62], in this scenario, we need to measure approximately $1.8^2 \approx 3$ times more effectively independent receiver positions (at a spacing of 2Δ) using the methodology of randomizing antenna positions in order to get the same precision as that in matching antenna positions. To verify this claim, we plot the result of randomly sampling 13×3 = 39 RX positions in Fig. 13 (labeled with "39"). The size of the confidence interval is approximately equal to that in the matching approach with 13 positions.

*Accuracy:* At a spacing of 4Δ, we also observe a significant difference in the inferred means resulting from the matching and randomization approaches (bottom part of Fig. 12). The reason is that at a spacing of 4Δ, the position distribution when randomizing is very different from the always-equal, uniform distribution that we have when matching (Fig. 14). This can introduce (dependent on the scenario) a systematic error to the results when randomizing positions. In our example, small deviations from the uniform distribution (for example, at 2Δ) do not result in a significant difference.

Looking again at the result of 39 RX positions (markers labeled "39" in Fig. 13), the systematic error got smaller (by chance). Measuring at other RX locations where the SNR changes differently against antenna position, the situation may look different.

Compared with not adjusting for confounding and with randomizing, the matching methodology delivers more accurate results in a substantially reduced measurement time.

## V. Generalization to Antenna Arrays

Up to now, we have utilized two X-pol antennas at the transmitter. As exemplarily shown in Fig. 15 for a 1-D array consisting of four X-pol antennas, randomizing and matching antenna positions work also analogously for 1-D,

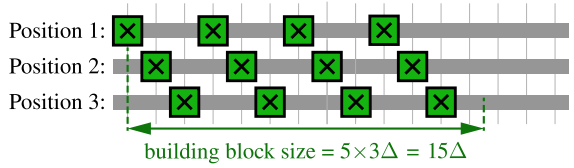


Fig. 15. Building block for an array with $N=4$ X-pol Antennas spaced by $3\Delta$. The measurement works analogous to Fig. 9.

and 2-D arrays of any size as long as all antennas are equally spaced. The required guide length increases only linearly with the number of antennas $N$, to $N$ times the LCM of all antenna spacings measured.

When comparing arrays with a few elements to larger arrays with more elements, similar matching methodologies can be found to reduce the effect of confounding by position. Exemplarily, Fig. 16 shows how to compare a single X-pol antenna to an array of two and an array of four X-pol antennas. The straightforward approach is to mount the three arrays on a roof to measure, for example, throughput. However, analogous to the observations in Sections III and IV, the measured throughput is also influenced by antenna position. Therefore, we again propose to measure multiple times such that the positions of the antennas are distributed equally for each antenna size, and then average the results for each antenna size as shown in Fig. 16.

### *A. On Confounding in Virtual Antenna Array Measurements for Massive MIMO*

Deploying massive MIMO technologies in the future mobile communications systems will increase the number of antennas at the BS by an order of magnitude. For feasibility reasons, measurements for massive MIMO channel characterization are often carried out by using virtual antenna arrays [10], [48], [49] rather than by using conventional antenna arrays. In both cases, the (virtual) antenna array is physically much larger than a wavelength; thus, the SNR changes for different elements within the array, that is, different path loss states are experienced on the array [48].

If one wants to obtain measurement results (for example, channel capacity), depending on the number of antenna elements (for example, by comparing different subarrays of one large array [10], [48]), again the number of antenna elements per subarray is confounded by the position of this subarray (analogous to Fig. 16). Zhang *et al.* [10], for example, mitigated this effect by averaging the different subarray choices created through randomization or through sliding antenna positions. Depending on the scenario, randomization may lead to a small systematic error as discussed in Section III-A. Synthesizing antenna arrays with 2, 4, 8, … up to 256 antennas and then matching antenna positions (to measure equally often at the same positions analogous to Fig. 16) further improves the confidence level of the results obtained.

## VI. Conclusion

In realistic outdoor-to-indoor scenarios, we have shown that when comparing different antenna configurations, the systematic error caused by measuring at different BS antenna

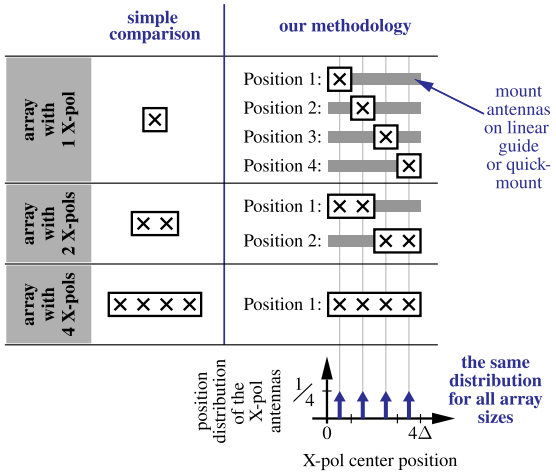


Fig. 16. Comparing arrays consisting of 1, 2, and 4 antennas. To make the comparison of antenna arrays consisting of 1, 2, and 4 X-pol antennas' fair, we propose to measure with equal position distribution per array size.

positions can be and needs to be separated from all the other effects we want to observe. Unfortunately, measuring at many independent transmit antenna positions and then averaging the results is not always feasible. Therefore, we have shown how to reduce position dependence by randomization (with similar antenna position distributions). Matching (with exactly equal antenna positions) will completely eliminate the systematic error caused by different transmit antenna positions in substantially less measurement time.

Controlling the confounding by position is not only key in the measurement we have shown but also in all other real-world outdoor-to-indoor mobile communication measurements, particularly when different antenna configurations are to be benchmarked in order to characterize, for example, the performance of an antenna array relative to the performance of a subset of the same antenna array. Ignoring this fundamental point leads to inaccurate results.

## References

[1] S. Caban, J. A. García-Naya, L. Castedo, and C. Mehlführer, "Measuring the influence of TX antenna spacing and transmit power on the closed-loop throughput of IEEE 802.16-2004 WiMAX," in *Proc. IEEE Instrum. Meas. Technol. Conf. (I2MTC)*, May 2010, pp. 1545–1550.

[2] S. Caban, J. A. García-Naya, C. Mehlführer, L. Castedo, and M. Rupp, "Measuring the closed-loop throughput of 2×2 HSDPA over TX power and TX antenna spacing," in *Proc. 2nd Int. Conf. Mobile Lightweight Wireless Syst. (Mobilight)*, May 2010, pp. 388–399.

[3] M. Lerch and M. Rupp, "Measurement-based evaluation of the LTE MIMO downlink at different antenna configurations," in *Proc. 17th Int. ITG Workshop Smart Antennas (WSA*, Stuttgart, Germany, Mar. 2013, pp. 1–6.

[4] S. Caban, C. Mehlführer, G. Lechner, and M. Rupp, "Testbedding MIMO HSDPA and WiMAX," in *Proc. 70th IEEE Veh. Technol. Conf. (VTC-Fall)*, Anchorage, AK, USA, Sep. 2009, pp. 1–5.

[5] S. Caban, M. Rupp, C. Mehlführer, and M. Wrulich, *Evaluation of HSDPA and LTE: From Testbed Measurements to System Level Performance*. Hoboken, NJ, USA: Wiley, 2011.

[6] E. Zöchmann, M. Lerch, S. Caban, R. Langwieser, C. F. Mecklenbräuker, and M. Rupp, "Directional evaluation of receive power, Rician K-factor and RMS delay spread obtained from power measurements of 60 GHz indoor channels," in *Proc. IEEE-APS Top. Conf. Antennas Propag. Wireless Commun. (APWC )*, Cairns, QLD, Australia, Sep. 2016, pp. 246–249.

[7] E. Zöchmann, M. Lerch, S. Pratschner, R. Nissel, S. Caban, and M. Rupp, "Associating spatial information to directional millimeter wave channel measurements," in *Proc. IEEE 86th Veh. Technol. Conf. (VTC-Fall)*, Toronto, ON, Canada, Sep. 2017, pp. 1–5.

[8] R. Nissel, E. Zöchmann, M. Lerch, S. Caban, and M. Rupp, "Low-latency MISO FBMC-OQAM: It works for millimeter waves!" in *Proc. IEEE Int. Microw. Symp. (IMS)*, Honololu, HI, USA, Jun. 2017, pp. 673–676.

[9] X. Gao, O. Edfors, F. Tufvesson, and E. G. Larsson, "Massive MIMO in real propagation environments: Do all antennas contribute equally?" *IEEE Trans. Commun.*, vol. 63, no. 11, pp. 3917–3928, Nov. 2015.

[10] B. Zhang *et al.*, "Multi-user channels with large-scale antenna arrays in a subway environment: Characterization and modeling," *IEEE Access*, vol. 5, pp. 23613–23625, 2017.

[11] Q. Wang *et al.*, "Spatial variation analysis for measured indoor massive MIMO channels," *IEEE Access*, vol. 5, pp. 20828–20840, 2017.

[12] B. Ai *et al.*, "On indoor millimeter wave massive MIMO channels: Measurement and simulation," *IEEE J. Sel. Areas Commun.*, vol. 35, no. 7, pp. 1678–1690, Jul. 2017.

[13] J. Flordelis, F. Rusek, X. Gao, G. Dahman, O. Edfors, and F. Tufvesson, "Spatial separation of closely-located users in measured massive MIMO channels," *IEEE Access*, vol. 6, pp. 40253–40266, 2018.

[14] S. Gunnarsson, J. Flordelis, L. van der Perre, and F. Tufvesson, "Channel hardening in massive MIMO—A measurement based analysis," in *Proc. 19th Int. Workshop Signal Process. Adv. Wireless Commun. (SPAWC)*, Apr. 2018, pp. 1010–1014.

[15] C.-M. Chen, A. P. Guevara, and S. Pollin, "Scaling up distributed massive MIMO: Why and how," in *Proc. 51st Asilomar Conf. Signals, Syst., Comput.*, Oct. 2017, pp. 271–276.

[16] C.-M. Chen, V. Volskiy, A. Chiumento, L. van der Perre, G. A. E. Vandenbosch, and S. Pollin, "Exploration of user separation capabilities by distributed large antenna arrays," in *Proc. Globecom Workshops (GC Wkshps)*, Dec. 2016, pp. 1–6.

[17] M. Gauger, J. Hoydis, C. Hoek, H. Schlesinger, A. Pascht, and S. ten Brink, "Channel measurements with different antenna array geometries for massive MIMO systems," in *Proc. 10th Int. ITG Conf. Syst., Commun. Coding*, 2015, pp. 1–6.

[18] S. Zhang, P. Harris, A. Doufexi, A. Nix, and M. Beach, "Massive MIMO real-time channel measurements and theoretic TDD downlink throughput predictions," in *Proc. 27th Annu. Int. Symp. Pers., Indoor, Mobile Radio Commun. (PIMRC)*, Sep. 2016, pp. 1–6.

[19] À. O. Martínez, E. De Carvalho, and J. Ø. Nielsen, "Massive MIMO properties based on measured channels: Channel hardening, user decorrelation and channel sparsity," in *Proc. 50th Asilomar Conf. Signals, Syst. Comput.*, Nov. 2016, pp. 1804–1808.

[20] À. O. Martínez, P. Popovski, J. Ø. Nielsen, and E. De Carvalho, "Experimental study of the benefits of a second antenna at the user side in a massive MIMO system," *IEEE Access*, vol. 6, pp. 2899–2907, 2018.

[21] C. Mehlführer, S. Caban, and M. Rupp, "Measurement-based performance evaluation of MIMO HSDPA," *IEEE Trans. Veh. Technol.*, vol. 59, no. 9, pp. 4354–4367, Nov. 2010.

[22] R. Nissel, S. Caban, and M. Rupp, "Closed-form capacity expression for low complexity BICM with uniform inputs," in *Proc. IEEE Int. Symp. Pers., Indoor Mobile Radio Commun. (PIMRC)*, Hong Kong, Aug. 2015, pp. 678–682.

[23] S. Schwarz, J. C. Ikuno, M. Simko, M. Taranetz, Q. Wang, and M. Rupp, "Pushing the limits of LTE: A survey on research enhancing the standard," *IEEE Access*, vol. 1, pp. 51–62, 2013.

[24] E. Zöchmann, S. Schwarz, S. Pratschner, L. Nagel, M. Lerch, and M. Rupp, "Exploring the physical layer frontiers of cellular uplink," *EURASIP J. Wireless Commun. Netw.*, vol. 2016, no. 1, p. 118, 2016.

[25] C. Mehlführer, S. Caban, and M. Rupp, "Cellular system physical layer throughput: How far off are we from the Shannon bound?" *IEEE Wireless Commun.*, vol. 18, no. 6, pp. 54–63, Dec. 2011.

[26] R. S. Thomä, D. Hampicke, A. Richter, G. Sommerkorn, and U. Trautwein, "MIMO vector channel sounder measurement for smart antenna system evaluation," *Trans. Emerg. Telecommun. Technol.*, vol. 12, no. 5, pp. 427–438, 2001.

[27] K. Sakaguchi, J.-I. Takada, and K. Araki, "A novel architecture for MIMO spatio-temporal channel sounder," *IEICE Trans. Electron.*, vol. 85, no. 3, pp. 436–441, 2002.

[28] A. Taparugssanagorn, X. Yin, J. Ylitalo, and B. H. Fleury, "Phase noise mitigation in channel parameter estimation for TDM MIMO channel sounding," in *Proc. IEEE 41st Asilomar Conf. Signals, Syst. Comput.*, Nov. 2007, pp. 656–660.

[29] M. Rindler, S. Caban, M. Lerch, P. Svoboda, and M. Rupp, "Swift indoor benchmarking methodology for mobile broadband networks," in *Proc. IEEE 86th Veh. Technol. Conf. (VTC-Fall)*, Toronto, ON, Canada, Sep. 2017, pp. 1–5.

[30] S. Caban, J. A. García-Naya, and M. Rupp, "Measuring the physical layer performance of wireless communication systems: Part 33 in a series of tutorials on instrumentation and measurement," *IEEE Instrum. Meas. Mag.*, vol. 14, no. 5, pp. 8–17, Oct. 2011.

[31] A. Intarapanich, P. L. Kafle, R. J. Davies, A. B. Sesay, and J. McRory, "Spatial correlation measurements for broadband MIMO wireless channels," in *Proc. VTC-Fall*, vol. 1, Sep. 2004, pp. 52–56.

[32] V. Jungnickel, V. Pohl, and C. V. Helmolt, "Capacity of MIMO systems with closely spaced antennas," *IEEE Commun. Lett.*, vol. 7, no. 8, pp. 361–363, Aug. 2003.

[33] S. Caban, C. Mehlführer, L. W. Mayer, and M. Rupp, "2×2 MIMO at variable antenna distances," in *Proc. IEEE Veh. Technol. Conf. (VTC Spring)*, Singapore, May 2008, pp. 1311–1315. [Online]. Available: http://publik.tuwien.ac.at/files/PubDat_167444.pdf

[34] S. Caban and M. Rupp, "Impact of transmit antenna spacing on 2×1 Alamouti radio transmission," *Electron. Lett.*, vol. 43, no. 4, pp. 198–199, Feb. 2007.

[35] N. Skentos, A. G. Kanatas, G. Pantos, and P. Constantinou, "Capacity results from short range fixed MIMO measurements at 5.2 GHz in urban propagation environment," in *Proc. IEEE Int. Conf. Commun. (ICC)*, vol. 5, Jun. 2004, pp. 3020–3024.

[36] D. Chizhik, J. Ling, P. W. Wolniansky, R. A. Valenzuela, N. E. Costa, and K. Huber, "Multiple-input-multiple-output measurements and modeling in Manhattan," *IEEE J. Sel. Areas Commun.*, vol. 21, no. 3, pp. 321–331, Apr. 2003.

[37] P.-S. Kildal and K. Rosengren, "Correlation and capacity of MIMO systems and mutual coupling, radiation efficiency, and diversity gain of their antennas: Simulations and measurements in a reverberation chamber," *IEEE Commun. Mag.*, vol. 42, no. 12, pp. 104–112, Dec. 2004.

[38] J. Medbo, M. Riback, and J.-E. Berg, "Validation of 3GPP spatial channel model including WINNER wideband extension using measurements," in *Proc. IEEE 64th Veh. Technol. Conf. (VTC-Fall)*, Sep. 2006, pp. 1–5.

[39] V. Pohl, V. Jungnickel, T. Haustein, and C. von Helmolt, "Antenna spacing in MIMO indoor channels," in *Proc. IEEE 55th Veh. Technol. Conf. (VTC-Spring)*, vol. 2, May 2002, pp. 749–753.

[40] J. Lv, Y. Lu, Y. Wang, H. Zhao, and C. Y. Han, "Antenna spacing effect on indoor MIMO channel capacity," in *Proc. Asia–Pacific Microw. Conf.*, Dec. 2005, pp. 1–3.

[41] D. Chizhik, F. Rashid-Farrokhi, J. Ling, and A. Lozano, "Effect of antenna separation on the capacity of BLAST in correlated channels," *IEEE Commun. Lett.*, vol. 4, no. 11, pp. 337–339, Nov. 2000.

[42] D.-S. Shiu, G. J. Foschini, M. J. Gans, and J. M. Kahn, "Fading correlation and its effect on the capacity of multielement antenna systems," *IEEE Trans. Commun.*, vol. 48, no. 3, pp. 502–513, Mar. 2000.

[43] T. D. Abhayapala, R. A. Kennedy, and J. T. Y. Ho, "On capacity of multi-antenna wireless channels: Effects of antenna separation and spatial correlation," in *Proc. 3rd Austral. Commun. Theory Workshop (AusCTW)*, Feb. 2002, pp. 1–5.

[44] C. Waldschmidt, C. Kuhnert, S. Schulteis, and W. Wiesbeck, "Analysis of compact arrays for MIMO based on a complete RF system model," in *Proc. IEEE Top. Conf. Wireless Commun. Technol.*, Oct. 2003, pp. 286–287.

[45] A. M. Tulino, A. Lozano, and S. Verdù, "Impact of antenna correlation on the capacity of multiantenna channels," *IEEE Trans. Inf. Theory*, vol. 51, no. 7, pp. 2491–2509, Jul. 2005.

[46] M. T. Ivrlac and J. A. Nossek, "Toward a circuit theory of communication," *IEEE Trans. Circuits Syst. I, Reg. Papers*, vol. 57, no. 7, pp. 1663–1683, Jul. 2010.

[47] E. Zöchmann, S. Schwarz, and M. Rupp, "Comparing antenna selection and hybrid precoding for millimeter wave wireless communications," in *Proc. IEEE 9th Sensor Array Multichannel Signal Process. Workshop (SAM)*, Rio de Janeiro, Brazil, Jul. 2016, pp. 1–5.

[48] S. Payami and F. Tufvesson, "Channel measurements and analysis for very large array systems at 2.6 GHz," in *Proc. 6th Eur. Conf. Antennas Propag. (EUCAP)*, Mar. 2012, pp. 433–437.

[49] X. Gao, F. Tufvesson, and O. Edfors, "Massive MIMO channels—Measurements and models," in *Proc. Asilomar Conf. Signals, Syst. Comput.*, Nov. 2013, pp. 280–284.

[50] B. L. Ng *et al.*, "Fulfilling the promise of massive MIMO with 2D active antenna array," in *Proc. IEEE Globecom Workshops (GC Wkshps)*, Dec. 2012, pp. 691–696.

[51] B. Panzner *et al.*, "Deployment and implementation strategies for massive MIMO in 5G," in *Proc. Globecom Workshops (GC Wkshps)*, Dec. 2014, pp. 346–351.
[52] C. Masouros, M. Sellathurai, and T. Ratnarajah, "Large-scale MIMO transmitters in fixed physical spaces: The effect of transmit correlation and mutual coupling," *IEEE Trans. Commun.*, vol. 61, no. 7, pp. 2794–2804, Jul. 2013.
[53] C. Masouros and M. Matthaiou, "Space-constrained massive MIMO: Hitting the wall of favorable propagation," *IEEE Commun. Lett.*, vol. 19, no. 5, pp. 771–774, May 2015.
[54] M. Lerch and M. Rupp, "Measurement-based evaluation of the LTE MIMO downlink at different antenna configurations," in *Proc. 17th Int. ITG Workshop Smart Antennas (WSA)*, Stuttgart, Germany, Feb. 2013, pp. 1–6.
[55] M. Lerch, S. Caban, M. Mayer, and M. Rupp, "The Vienna MIMO testbed: Evaluation of future mobile communication techniques," *Intel Technol. J.*, vol. 18, no. 3, pp. 58–69, 2014.
[56] C. Mehlführer, S. Geirhofer, S. Caban, and M. Rupp, "A flexible MIMO testbed with remote access," in *Proc. 13th Eur. Signal Process. Conf. (EUSIPCO)*, Antalya, Turkey, Sep. 2005, pp. 1–5. [Online]. Available: http://publik.tuwien.ac.at/files/pub-et_9732.pdf
[57] S. Caban, J. Rodas, and J. A. García-Naya, "A methodology for repeatable, off-line, closed-loop wireless communication system measurements at very high velocities of up to 560 km/h," in *Proc. Int. Instrum. Meas. Technol. Conf. (I2MTC)*, Hangzhou, China, May 2011, pp. 1–5.
[58] J. Rodríguez-Piñeiro, M. Lerch, J. A. García-Naya, S. Caban, M. Rupp, and L. Castedo, "Emulating extreme velocities of mobile LTE receivers in the downlink," *EURASIP J. Wireless Commun. Netw.*, vol. 2015, p. 106, Dec. 2015. [Online]. Available: http://jwcn.eurasipjournals.com/content/pdf/s13638-015-0343-0.pdf
[59] S. Caban, A. Disslbacher-Fink, J. A. García-Naya, and M. Rupp, "Synchronization of wireless radio testbed measurements," in *Proc. IEEE Int. Instrum. Meas. Technol. Conf. (I2MTC)*, May 2011, pp. 1–4.
[60] M. Laner, S. Caban, P. Svoboda, and M. Rupp, "Time synchronization performance of desktop computers," in *Proc. Int. Symp. Precis. Clock Synchronization (ISPCS)*, Sep. 2011, pp. 78–85.
[61] M. R. Chernick, *Bootstrap Methods: A Guide for Practitioners and Researchers*, 2nd ed. Hoboken, NJ, USA: Wiley, 2007.
[62] M.-J. Fortin and M. Dale, *Spatial Analysis: A Guide For Ecologists*. Cambridge, U.K.: Cambridge Univ. Press, 2005.
[63] W. G. Cochran, *Sampling Techniques*, 3rd ed. Hoboken, NJ, USA: Wiley, 1977.
[64] R. P. Haining, *Spatial Data Analysis in the Social and Environmental Sciences*. Cambridge, U.K.: Cambridge Univ. Press, 1990.
[65] O. N. Bjørnstad and W. Falck, "Nonparametric spatial covariance functions: Estimation and testing," *Environ. Ecol. Statist.*, vol. 8, no. 1, pp. 53–70, 2001.
[66] S. P. Glasser, *Essentials of Clinical Research*. Switzerland: Springer, 2014.
[67] R. Fisher, *Design Experiments*. New York, NY, USA: Wiley, 1935.
[68] R. A. Fisher, "048: The arrangement of field experiments," *J. Ministry Agricult. Great Britain*, vol. 33, pp. 503–513, 1926.
[69] I. Masic, M. Miokovic, and B. Muhamedagic, "Evidence based medicine–new approaches and challenges," *Acta Inf. Medica*, vol. 16, no. 4, p. 219, 2008.
[70] L. L. Kupper, J. M. Karon, D. G. Kleinbaum, H. Morgenstern, and D. K. Lewis, "Matching in epidemiologic studies: Validity and efficiency considerations," *Biometrics*, vol. 37, no. 2, pp. 271–291, 1981.
[71] B. Efron and R. Tibshirani, *An Introduction to the Bootstrap*. Boca Raton, FL, USA: CRC Press, 1994.
[72] M. Wood, "Statistical inference using bootstrap confidence intervals," *Significance*, vol. 1, no. 4, pp. 180–182, 2004.

**Sebastian Caban** received the master's degree in business administration from the University of Vienna, Vienna, Austria, and the master's and Ph.D. degrees in telecommunications from TU Wien, Vienna.

His current research interests include measurements in wireless communications.

**Martin Lerch** received the master's degree in telecommunications from TU Wien, Vienna, Austria.

He is currently with the Institute of Telecommunications, TU Wien, where he is currently developing testbeds and measurement methodologies for controlled and reproducible wireless experiments at high velocities.

**Stefan Pratschner** received the master's degree in telecommunications from TU Wien, Vienna, Austria, where he is currently pursuing the Ph.D. degree with the Institute of Telecommunications, with a focus on massive multi-in multi-out technologies for mobile communications.

**Erich Zöchmann** received the master's degree in telecommunications from TU Wien, Vienna, Austria.

From 2017 to 2018, he was a Visiting Scholar with The University of Texas at Austin, Austin, TX, USA. He is currently involved in experimental characterization and modeling of millimeter-wave propagation. His current research interests include wireless propagation, physical layer signal processing, and array signal processing.

**Philipp Svoboda** received the master's and Ph.D. degrees in telecommunications from TU Wien, Vienna, Austria.

He is currently a Senior Scientist with TU Wien, with a research focus on the performance aspects of mobile cellular technologies. His current research interests include a common framework for evaluating the performance of mobile networks, guaranteeing reliable, and fair connectivity for end users.

**Markus Rupp** received the Dr. Ing. degree in electrical engineering from Technische Universität Darmstadt, Darmstadt, Germany, in 1993.

From 1993 to 1995, he was a Post-Doctoral Researcher with the University of California at Santa Barbara, Santa Barbara, CA, USA. From 1995 to 2001, he was a Technical Staff Member with the Wireless Technology Research Department, Bell Labs at Crawford Hill, NJ, USA. Since 2001, he has been a Full Professor of digital signal processing in mobile communications with TU Wien, Vienna, Austria.

IEEE Access
Multidisciplinary ⋮ Rapid Review ⋮ Open Access Journal

Received September 3, 2020, accepted September 19, 2020, date of publication September 24, 2020,
date of current version October 8, 2020.

*Digital Object Identifier 10.1109/ACCESS.2020.3026371*

# Measured User Correlation in Outdoor-to-Indoor Massive MIMO Scenarios

**STEFAN PRATSCHNER[1,2], (Member, IEEE), THOMAS BLAZEK[3], (Member, IEEE), HERBERT GROLL[2], (Graduate Student Member, IEEE), SEBASTIAN CABAN[1,2], (Member, IEEE), STEFAN SCHWARZ[1,2], (Senior Member, IEEE), AND MARKUS RUPP[2], (Fellow, IEEE)**

[1]Christian Doppler Laboratory for Dependable Wireless Connectivity for the Society in Motion, 1040 Vienna, Austria
[2]Institute of Telecommunications, Technical University of Vienna (TU Wien), 1040 Vienna, Austria
[3]Silicon Austria Labs, 4040 Linz, Austria

Corresponding author: Stefan Pratschner (stefan.pratschner@tuwien.ac.at)

This work has been funded by the Christian Doppler Laboratory for dependable Wireless Connectivity for the Society in Motion. The financial support by the Austrian Federal Ministry for Digital and Economic Affairs, the National Foundation for Research, Technology and Development and the Christian Doppler Research Association is gratefully acknowledged. The authors acknowledge the TU Wien University Library for financial support through its Open Access Funding Programme.

**ABSTRACT** The performance of a multi-user multiple-input multiple-output (MIMO) system is mainly determined by the correlation of user channels. Applying channel models without spatial correlation or spatially inconsistent channel models for performance analysis leads to an under-estimation of spatial correlation and therefore to overly optimistic system performance. This is especially pronounced when the wireless channel is modeled as i.i.d. Rayleigh fading for users in a rich scattering environment, for example, for indoor users. To analyze the spatial channel correlation in massive MIMO systems, we performed wireless channel measurements in three different scenarios. In each scenario, we measure 148 receiver positions, spread over a length of almost 9 m. Since the wireless channel statistics change with receiver position, we perform a stationarity analysis. We provide a statistical analysis of the measured channel in terms of amplitude distribution and user-side spatial correlation within the region of stationarity. This analysis shows that, even for a deep-indoor user location, the spatial correlation is significantly higher compared to a Rician channel model with the same $K$ factor. We model the measured channel by means of a Rician channel model and a spatially consistent channel model, which is based on the scenario geometry, to provide an insight for the observed propagation phenomena. Results show that the user correlation is not negligible for massive MIMO in outdoor-to-indoor scenarios. The achievable spectral efficiency with linear precoding is 20% lower compared to the Rician channel model, even for large inter-user distances of 6 m.

**INDEX TERMS** MIMO, mobile communications, channel measurements, channel modeling.

## I. INTRODUCTION

The challenge to meet all requirements of envisioned future mobile communications networks is manifold. Typical use cases for 5th generation (5G) mobile communications and beyond are: ultra-reliable low-latency communication (uRLLC) for mission critical applications such as vehicular-to-vehicular (V2V) communication, enhanced mobile broadband (eMBB) to meet the steadily increasing demand for data volume and data rate, and massive machine type communication (mMTC) for the implementation of the Internet of things (IoT). A key technology for tackling these diverse challenges is enhancing the well-established technology of MIMO communication to a large-scale, which is then referred to as massive MIMO [1], [2]. As the number of antennas at the base station (BS) side is increased and many users are served in a multi-user MIMO way, the sum rate and the energy efficiency are promised to increase simultaneously [3]–[5]. Since a large-scale antenna array at the BS leads to channel hardening in a wireless fading channel, the reliability and latency are also enhanced when scaling up a MIMO system with respect to the number of BS antennas [6].

Many of the theoretical works reporting the aforementioned desired improvements assume wireless channels following an i.i.d. Rayleigh fading behavior [1], [3], [6]. Especially for indoor mobile users, an uncorrelated i.i.d. channel model

The associate editor coordinating the review of this manuscript and approving it for publication was Maurizio Magarini.

is justified with the argument of a dense scattering environment around the users. Since massive MIMO is a multi-user technology, the spatial channel correlation of simultaneously served users is an important factor for the performance of such systems [7]. The assumption of uncorrelated user channels is an optimistic one that leads to an over-estimation of system performance as spatial correlation hampers spatial multiplexing of users in close proximity. Measurements show that real-word wireless MIMO channels differ from i.i.d. Rayleigh fading channels in terms of spatial correlation [8]. Several works investigate the problem of spatial separation in MIMO communications [9]–[15], showing that users can be separated in line of sight (LOS) channel conditions.

The importance of spatial inter-user channel correlation has led to research in the area of spatially consistent wireless channel models [15]–[20]. Spatial consistency in this context refers to the fact that two users experience correlated channels when they are physically close to each other. These channel models provide a representation of spatially correlated channels that is more realistic than i.i.d. Rayleigh fading channel models and, therefore, facilitate more accurate performance analysis of massive MIMO systems.

To investigate propagation characteristics of real-world wireless channels in the context of massive MIMO, many measurements were conducted in the past years, see [8], [12], [21]–[28] to name just a few examples. Many of these measurement campaigns were performed entirely outdoors [8], [12], [21]–[24], or indoors [12], [25]–[27], while only few consider an outdoor-to-indoor scenario, for example [28].

### *CONTRIBUTION*

We sounded the wireless channel of one outdoor-to-outdoor and two outdoor-to-indoor, large-scale MIMO scenarios at 2.5 GHz. Measuring the channel at 148 user positions per scenario, located on straight lines of 8.82 m length, allows us to investigate the spatial channel correlation depending on inter-user distance. We perform a stationarity analysis in the spatial domain and characterize the regions of wide-sense stationarity in terms of fading distribution and spatial correlation. We also provide a fit of a spatially consistent channel model, which is based on the measurement scenario geometry, to explain the observed propagation effects. We show that the achievable spectral efficiency of two users in an outdoor-to-indoor massive MIMO system is 20% lower compared to a Rician channel model with the same $K$ factor, even at large inter-user distances of 6 m.

### *NOTATION*

We denote vectors by lowercase boldface letters, such as $\mathbf{x}$, and matrices by uppercase boldface letters, such as $\mathbf{X}$. The entry from the $n^{\text{th}}$ row and the $k^{\text{th}}$ column of matrix $\mathbf{X}$ is denoted by $\mathbf{X}[n, k]$. We denote the Frobenius norm by $\|\cdot\|$. The absolute value of a scalar as well as the cardinality of a set are denoted by $|\cdot|$. The transpose of a vector or matrix is denoted by $(\cdot)^{\mathrm{T}}$ while the conjugate transpose of a vector or matrix is denoted by $(\cdot)^{\mathrm{H}}$. The expectation of a random variable $X$ is denoted by $\mathbb{E}\{X\}$ and the trace of a matrix is denoted by $\mathrm{tr}(\cdot)$. The operator $\lfloor\cdot\rfloor$ rounds down to the nearest integer and the operator $\lceil\cdot\rceil$ rounds up to the nearest integer.

## II. MEASUREMENT CAMPAIGN

A wireless channel measurement campaign with three different measured scenarios was conducted in January 2020 at TU Wien in downtown Vienna, Austria. The scenarios measured will be described in detail later in this section. Channel sounding measurements are performed with the Vienna MIMO testbed [30], [31] at a center frequency of 2.5 GHz (free space wavelength $\lambda \approx 120$ mm). The transmit side antenna array is located outdoors on a rooftop and is oriented parallel to the building's facade, facing the receiver location, see Fig. 1. The distance between the transmit antenna array and the array at the receive side is $R \approx 155$ m.


**FIGURE 1.** Aerial photograph of the measurement scenario at TU Wien [29]. The red lines indicate the orientation of the antenna arrays. The coordinate system orientation is indicated in blue.

To obtain measurements of a massive MIMO channel, a uniform linear array with 40 elements at half-wavelength spacing is employed at the transmitter side. Since the Vienna MIMO Testbed is limited to four radio frequency (RF) chains, the transmit side array is implemented as a virtual antenna array. This means that a single antenna element is sequentially re-positioned in order to virtually assemble an antenna array, given that the wireless channel and the measurement hardware behave time-invariant [32]. The antenna element at the transmit array is a vertical dipole in front of the center of a 75 cm × 75 cm square aluminum reflector plate, see Fig. 2(a). We sound the wireless channel at 148 receiver positions per measurement scenario to investigate the spatial correlation as a function of inter-user distance. The receive antenna is mounted on a mechanical guide with a total length of 9 m, see Fig. 2(b). These receiver positions are arranged on a line with half a wavelength in between measurement points, resulting in a total user range of 8.82 m. As receive antenna element, an omni-directional monopole antenna with a circular groundplane with a diameter of approximately 2.5 $\lambda$ is employed.

An orthogonal frequency division multiplexing (OFDM) signal with a subcarrier spacing of $F = 15$ kHz is employed as channel sounding sequence. To keep the peak-to-average power ratio of the sounding sequence low, the transmit signal

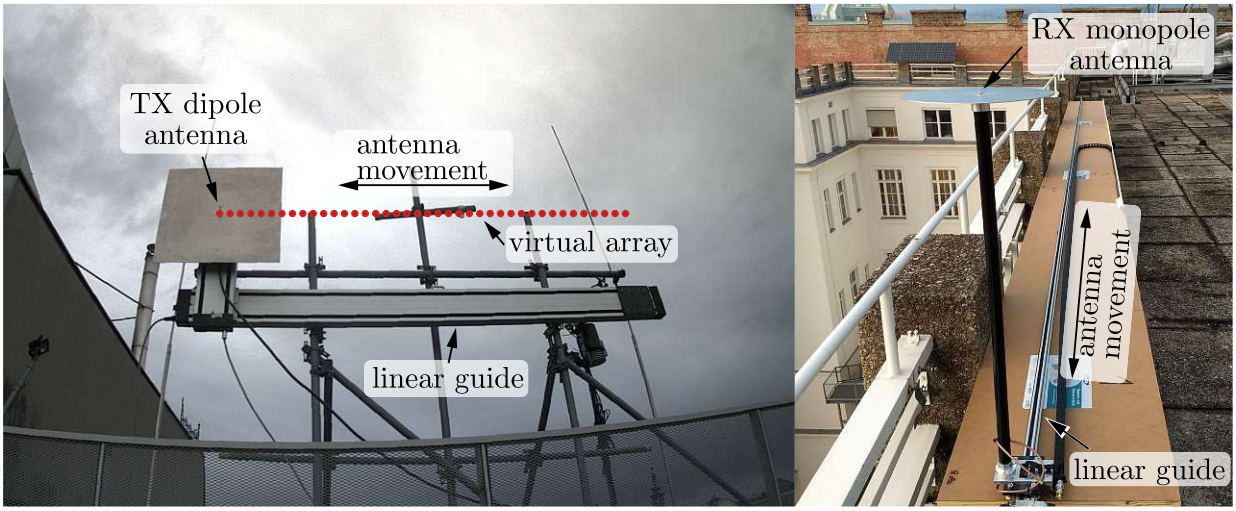


(a) transmit antenna array (b) *LOS* scenario

**FIGURE 2.** **(a) Transmit side virtual antenna array. (b) Receiver side for the *LOS* scenario. The LOS path is unblocked in this scenario.**

is designed using Newman phases, as in [33]. A transmit symbol is given by

$$x(m) = \mathrm{Re}\left( \sum_{q=-Q/2}^{Q/2-1} e^{-\mathrm{i}2\pi q \frac{m}{M}} e^{\mathrm{i}\pi \frac{q^2}{Q}} \right), \tag{1}$$

where i is the imaginary unit, $Q$ is the number of subcarriers, $m = 0, \ldots, M-1$ denotes the time index and $q$ is the subcarrier index. Here, $M$ is the number of samples per OFDM symbol.

A sounding sequence consists of 101 repetitions of the described OFDM symbol. The first symbol is exploited as cyclic prefix (CP) and is discarded at the receiver. Given the scenario geometry and the CP duration, this leads to inter-symbol interference free transmission [34]. Assuming the channel to be time-invariant, we average over the remaining 100 received symbols in order to achieve an averaging gain of 20 dB in terms of signal to noise ratio (SNR).

To measure the phase drift between the transmitter clock and the receiver clock, an additional reference radio link is established. This reference link employs directional antennas at fixed positions on both ends to obtain a wireless channel that is flat in time and frequency. More details of the measurement system's phase stability are provided in Appendix A.

We employ $Q = 10$ subcarriers for the wireless channel of interest and $Q = 20$ subcarriers for the reference link. Channel estimates for both wireless links are obtained via least squares estimation. The phases of the channel estimates obtained via the reference link are averaged over all 20 subcarriers and employed to compensate the phase drift of the channel estimates of the desired wireless channel. The phase compensated channel estimates of the desired radio link are averaged over all 10 subcarriers since the channel's coherence bandwidth is much larger than 150 kHz. This improves the channel estimation error by 10 dB.

In total, we achieve 20 dB SNR at the receiver with the Vienna MIMO Testbed, additional 20 dB SNR through averaging in time and another 10 dB improvement in channel estimation error through averaging in frequency. This yields a total normalized mean squared channel estimation error of approximately −50 dB.

### A. LOS SCENARIO

In this scenario, the transmitter and the receiver are located on rooftops with no obstacles or blockages in between them. This scenario is therefore considered as a LOS propagation scenario. A photograph of the receive antenna on the building's rooftop and the mechanical linear guide for antenna positioning is provided in Fig. 2(b). Buildings in between the transmitter and receiver location, see Fig. 1, are lower in height compared to the rooftops at transmit and receive sites. The first Fresnel zone, with a maximum diameter of $D = \sqrt{R\lambda}/2 \approx 2$ m, is undisturbed. The receive antenna height above the rooftop is 1.7 m. At both, the transmitter and the receiver, the antennas are located sufficiently high above the handrails to obtain an unobstructed connection. Let us assume a coordinate system with its origin located at the first antenna position of the transmit side antenna array as shown in Fig. 1. In this coordinate system, the first user position is located at $(x, y, z) = (151\,\mathrm{m}, 31\,\mathrm{m}, 0\,\mathrm{m})$ for this scenario.

### B. LABORATORY SCENARIO

This scenario is an outdoor-to-indoor scenario with the receiver located in an indoor laboratory environment. A photograph of the receive antenna in the laboratory is shown in Fig. 3(a). The receiver positions in terms of a floorplan

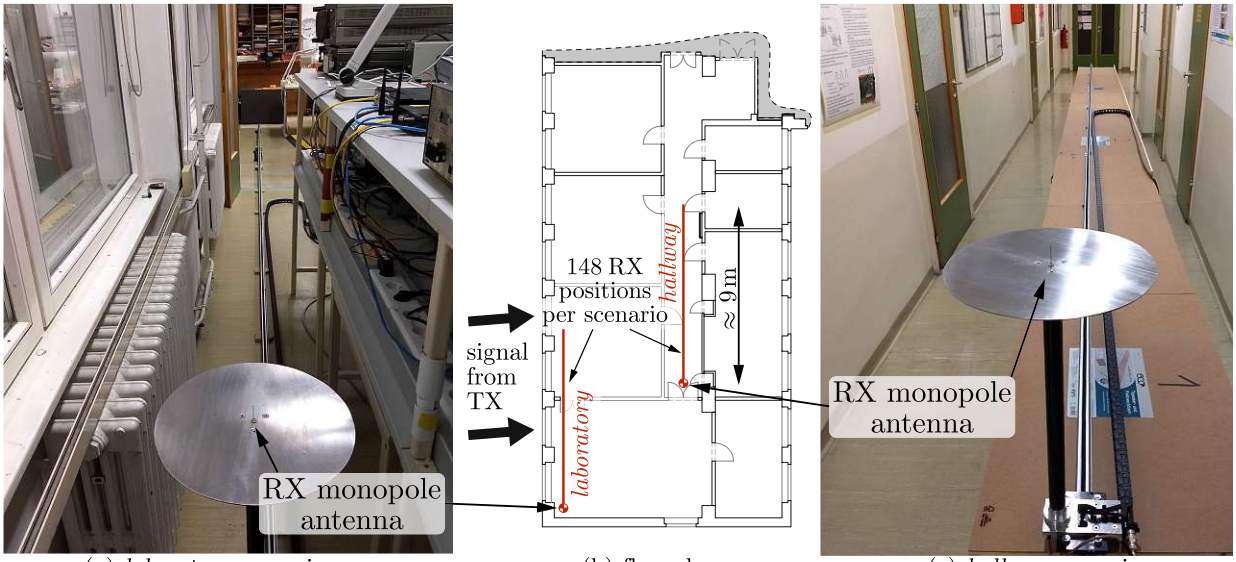


**FIGURE 3.** **(a) Receiver side for the *laboratory* environment scenario. The receive antenna positions are located next to the laboratory's windows. (b) Floor plan of the indoor receiver positions for the *laboratory* and *hallway* scenarios. The *hallway* positions are deep indoor. (c) Receiver side for the *hallway* measurement scenario. There are no obstacles in the hallway.**

of the 5th floor (two floors below the roof) of the receiver site building are shown in Fig. 3(b). In this scenario, the receiver positions are parallel to a wall, which is facing the transmitter array. The receive antenna height above the floor is 1 m, while the lower end of the windows is 90 cm above the floor. All window shades were in a fully opened position during the measurement. Therefore, there is a visual LOS path between the transmitter and the receiver for receive antenna positions directly in front of a window, obstructed only by two layers of uncoated glass. The first user position is at $(x, y, z) = (152\,\text{m}, 25\,\text{m}, -8\,\text{m})$.

### C. HALLWAY SCENARIO

In this scenario, the receiver is located indoors in an empty hallway. The receiver positions are shown in Fig. 3(b) in terms of a floorplan. Looking at this floorplan, the *hallway* scenario is "deep indoor" compared to the *laboratory* scenario. A photograph of the receiver environment is shown in Fig. 3(c). All doors were closed during the measurement. The receive antenna height above the floor is 1.3 m. The first user position is at $(x, y, z) = (157\,\text{m}, 31\,\text{m}, -8\,\text{m})$.

## III. STATISTICAL ANALYSIS

We perform a stationarity analysis and identify regions of spatial quasi-stationarity in the sense of wide-sense stationarity (WSS) in this section. To identify these regions, we employ the channel matrix collinearity metric [35]. We analyze the channel statistics in terms of amplitude distribution, spatial correlation and time correlation within the stationary regions. We illustrate the spatial and the temporal channel correlation within the stationary regions by means of the channel vector inner product.

### A. STATIONARITY ANALYSIS

Previous massive MIMO channel measurements show that the wireless channel is not stationary in the spatial domain across the entire aperture of a large scale antenna array [21], [25], [26]. Due to the large physical size of such an array, not all antenna elements see the same scattering elements or even users. Such non-stationary effects are not captured by most current MIMO channel models, but are important for massive MIMO transceiver design. In the recent work [36], the authors consider different channel statistics across a huge antenna array for the design of hybrid beamforming schemes. In our measurements, the channel statistics change across the receiver positions since they are arranged on a long line of 8.82 m length. For example in the *laboratory* scenario, the channel statistics depend on whether a receiver position is located in front of a window or not.

The performance of a multi-user MIMO system is mainly determined by the correlation of user channels. Therefore, we analyze our channel measurements in terms of spatial correlation with respect to inter-user distance. We aim to find stationary regions at the receiver side and evaluate the wireless channel statistics within them. There exist two popular metrics for the stationarity analysis of measured wireless channels [37]: the mean channel power from [38] or the correlation matrix distance (CMD) from [39]. The former metric calculates the mean channel power through the average power delay profile (APDP). The latter metric is the similarity of channel correlation matrices. Since a measured

wireless channel is never perfectly stationary, these metrics need to be compared against a threshold after evaluating them in time, frequency or space. In our case, the domain of interest is the spatial domain. Authors of [26] apply both metrics for their massive MIMO channel stationarity analysis. They conclude that the channel's spatial variation can be equally well characterized with both metrics. Since APDP is calculated by averaging in the delay domain, the CMD is better suited for our narrow-band channel measurements.

From the channel measurements, we obtain the MIMO channel matrix $\mathbf{H} \in \mathbb{C}^{N\times U}$, describing the wireless channel between all $N$ transmit antenna positions and all $U$ user positions. Please note that we obtain one MIMO channel matrix per measured scenario. We, however, omit a scenario index of the MIMO channel matrix for readability. We consider the channel coefficients, obtained via measurement, to be from a random process, sampled in space. We assume this process to be stationary in the spatial domain at the transmitter side. This is an intuitive assumption, as there are no obstacles in close proximity of the transmit antennas, which therefore all see the same scattering objects within the wireless channel. Under this assumption, the sample auto-correlation matrix is given by

$$\mathbf{R} = \frac{1}{N}\sum_{n=1}^{N} \check{\mathbf{h}}_n \check{\mathbf{h}}_n^{\mathrm{H}} \in \mathbb{C}^{U\times U}, \tag{2}$$

which serves as an estimate for the user-side auto-correlation matrix. In (2), $\check{\mathbf{h}}_n^{\mathrm{T}} \in \mathbb{C}^{1\times U}$ denotes the $n^{\text{th}}$ row vector of the channel matrix $\mathbf{H}$. Please note that the spatial correlation is of course analyzed for each measurement scenario individually, however, the scenario index of the correlation matrix is omitted in this section for readability.

By comparing a local auto-correlation at different positions, we identify regions of spatial quasi-stationarity in the WSS sense. Therefore, we introduce the CMD [39] between the correlation matrices $\mathbf{A}$ and $\mathbf{B}$ as

$$\mathrm{CMD}\,(\mathbf{A},\mathbf{B}) = \frac{\mathrm{tr}\left(\mathbf{A}^{\mathrm{H}}\mathbf{B}\right)}{\|\mathbf{A}\|\,\|\mathbf{B}\|}. \tag{3}$$

Due to the properties of the correlation matrices $\mathbf{A}$ and $\mathbf{B}$, $0 \le \mathrm{CMD} \le 1$, as shown in Appendix B. Equality, that is, $\mathrm{CMD} = 1$, is achieved if the matrices $\mathbf{A}$ and $\mathbf{B}$ are collinear, that is, $\mathbf{A} = \alpha\mathbf{B}$ with $\alpha \in \mathbb{R}$.

Let us consider a spatial averaging region of size $W$, with $W$ being a positive integer. For the ease of notation we define $L_L = \left\lfloor \frac{W-1}{2} \right\rfloor$ and $L_U = \left\lceil \frac{W-1}{2} \right\rceil$, such that $W = L_L + L_U + 1$. A local mean auto-correlation vector $\bar{\mathbf{r}}_p^W \in \mathbb{C}^{W\times 1}$ at position index $p$ is then obtained by averaging along the diagonals of the sample auto-correlation matrix $\mathbf{R}$ in a region from $p - L_L$ to $p + L_U$. The $l^{\text{th}}$ element of $\bar{\mathbf{r}}_p^W$ is given by the mean over the $l^{\text{th}}$ diagonal of $\mathbf{R}$, that is

$$\bar{\mathbf{r}}_p^W[l] = \frac{1}{W-l+1}\sum_{u=p-L_L}^{p+L_U-l+1} \mathbf{R}[u+l-1,u] \tag{4}$$

for $l \in \{1,\ldots,W\}$ and $p \in \{L_L+1,\ldots,U-L_U\}$.

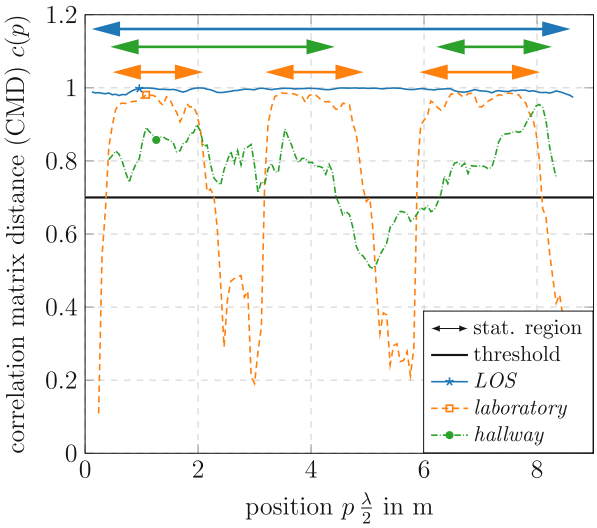


**FIGURE 4.** CMD for all three scenarios with the corresponding threshold. We chose a threshold that results in few large quasi stationary regions for further analysis.

The spatial averaging region size $W$ impacts the local mean auto-correlation vector $\bar{\mathbf{r}}_p^W$. Averaging the auto-correlation matrix $\mathbf{R}$ over large spatial region sizes $W$ reduces fluctuations in the local mean correlation, thereby making it a smooth function. As we increase $W$, however, $\bar{\mathbf{r}}_p^W$ becomes more similar to the global mean scenario correlation. Small spatial averaging regions make the local mean correlation representative for a local spatial region, but also lead to strong fluctuations of the local correlation with respect to location. We therefore choose the spatial averaging region size just large enough to identify few but large stationarity regions through a threshold on the CMD, see below. For the *LOS* and the *laboratory* scenario, a small value of $W = 5$ leads to a sufficiently smooth CMD curve. In the *hallway* scenario, we employ a larger value of $W = 15$ to obtain a smooth result in terms of CMD. Our chosen values for $W$ are summarized in Tab. 1 for all measured scenarios.

A locally averaged auto-correlation matrix $\overline{\mathbf{R}}_p^W$ is defined as a Hermitian Toeplitz matrix, with $\bar{\mathbf{r}}_p^W$ as its first column vector and $\left(\bar{\mathbf{r}}_p^W\right)^{\mathrm{H}}$ as its first row vector. For a globally averaged auto-correlation function, an averaging region size of $U$ is employed, which leads to the mean correlation vector $\bar{\mathbf{r}}_{(U/2)}^U$. Defining a squared Hermitian Toeplitz matrix through the first $W$ elements of $\bar{\mathbf{r}}_{(U/2)}^U$ as explained before, yields the globally averaged auto-correlation matrix $\overline{\mathbf{R}} \in \mathbb{C}^{W\times W}$. To identify regions of spatial stationarity, we calculate the CMD between the globally averaged auto-correlation matrix $\overline{\mathbf{R}}$ and the local average $\overline{\mathbf{R}}_p^W$ as

$$c(p) = \mathrm{CMD}\left(\overline{\mathbf{R}}_p^W, \overline{\mathbf{R}}\right) \tag{5}$$

for $p \in \{L_L+1,\ldots,U-L_U\}$.

For a stationary channel, the CMD equals one for all possible positions. Since a measured channel, however, is not perfectly stationary and also contains measurement noise, the CMD is smaller than one. Therefore, we consider quasi-stationarity for the measured wireless channel. High values of the CMD (close to one) indicate a high level of quasi-stationarity, that is, an almost stationary channel. We employ a threshold on the CMD to determine the regions of quasi-stationarity that will be considered for the evaluation of the mean spatial correlation function. If this threshold is chosen low, the resulting correlation function is not representative for the quasi-stationarity region, since a high level of fluctuation in the second order statistic is still included in the same stationarity region. Choosing the threshold too high, only a small spatial region is considered as quasi-stationary, containing a small number of measured samples. Calculating the correlation function from a small number of samples leads to a mean correlation function that is again not representative for the measured scenario. The choice of the threshold level is therefore a trade-off.

The CMD is plotted against the receiver position in Fig. 4 for the three measured scenarios. The position $p\frac{\lambda}{2}$ on the abscissa consists of the position index $p$ and the spacing of $\frac{\lambda}{2}$ between two receiver positions. We chose a threshold of $t = 0.7$ for the CMD to determine regions of quasi-stationarity. For this threshold, only few but large regions of quasi-stationarity are obtained, facilitating the calculation of a mean correlation function for the measured scenarios. The quasi-stationarity regions are indicated with arrows in Fig. 4. A stationary region $\mathcal{S}_i$ for scenario $i$ is therefore defined as

$$\mathcal{S}_i = \{p \in \{L_L + 1, \ldots, U - L_U\} \mid c(p) \geq t\}. \qquad (6)$$

For the *LOS* scenario, the CMD is flat and the entire measured scenario is considered stationary. This is not surprising as there are no scattering objects in between the transmitter and the receiver or around the receiver.

In the *laboratory* scenario, the CMD shows three clearly distinguishable stationary regions, which coincide with the physical positions of the windows in the measured indoor office environment, see Fig. 3(a)-(b). Therefore, the three stationary regions show a high similarity to the scenario mean in terms of receiver side auto-correlation.

The *hallway* scenario is considered as a deep indoor scenario, which explains that the CMD does not show clearly distinguishable regions compared to the *laboratory* scenario. Since there is no position in this scenario that allows a direct LOS path to the transmitter, the hallway scenario is expected to be invariant with respect to the position within the hallway. There are no obstacles present in the hallway that would explain a local change of second order statistics. Still, there is a region at approximately 5 m which shows a lower CMD compared to the overall scenario mean.

Please note that low values of the CMD in Fig. 4 do not indicate non-stationary regions. Since we compare the scenario averaged correlation function to a locally averaged correlation, averaged within a region of size $W$, high values of the plotted CMD indicate a high self-similarity of the local correlation. Therefore, a CMD $c(p)$ value of one means that the local correlation is identical to the average scenario correlation. This is approximately the case for *LOS* scenarios. Although low values of $c(p)$ do not mean that the channel behaves non-stationary at position index $p$, we focus our remaining analysis to the regions where the CMD exceeds the chosen threshold. These regions dominate the second order statistics of the respective scenario.

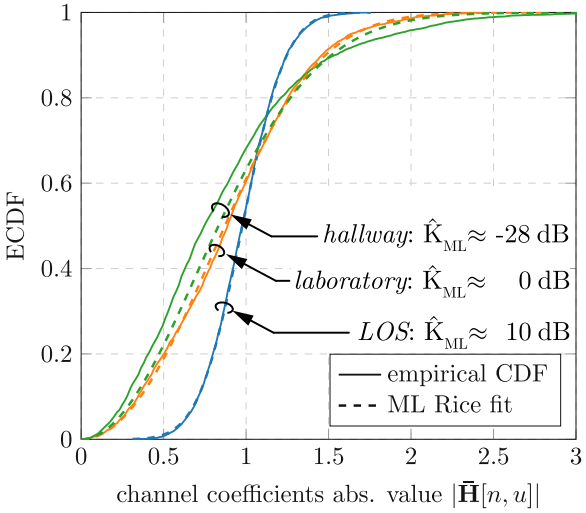


**FIGURE 5.** Channel coefficient amplitude distribution within stationary regions together with corresponding ML fits to a Rician distribution. The amplitude distributions of the measured channels are well approximated by a Rician distribution.

### B. CHANNEL COEFFICIENT DISTRIBUTION

For the channel coefficient distribution analysis, we normalize the channel coefficients per stationary region as $\bar{\mathbf{H}} = c\mathbf{H}$. We chose the scaling coefficient $c > 0$ such that

$$\frac{1}{N\,|\mathcal{S}_i|} \sum_{n=1}^{N} \sum_{u \in \mathcal{S}_i} \left|\bar{\mathbf{H}}\,[n,u]\right|^2 = 1. \qquad (7)$$

The empirical cumulative distribution functions (ECDFs) of the channel coefficients' magnitude $\left|\bar{\mathbf{H}}\,[n,u]\right|$ with $n \in \{1,\ldots,N\}$ and $u \in \mathcal{S}_i$ for the respective scenario $i$ are shown in Fig. 5. We perform maximum likelihood (ML) estimation with the measured channel's amplitudes as data set to obtain a fit to a Rician distribution. We parametrize the Rician probability density function (PDF) with the Rician $K$ factor and the power $\Omega$, see [40, p. 76]. Therefore, the ML estimate yields the estimate $\hat{K}_{\mathrm{ML}}$ for the Rician $K$ factor and the estimate $\hat{\Omega}_{\mathrm{ML}}$ for the power $\Omega$. Due to the channel normalization (7), the estimated power is $\hat{\Omega}_{\mathrm{ML}} = 1$. The fitted Rice distributions and the respective estimated Rician $K$ factors are also shown in Fig. 5. The estimated Rician $K$ factors for all measured scenarios are further summarized in Tab. 1.

**TABLE 1. Channel parameters of the measured wireless channel, the Rician channel model and the scattering channel model.**

| | *LOS* | *laboratory* | *hallway* |
|---|---|---|---|
| Rician $K$ factor | 10 dB | 0 dB | -28 dB |
| averaging region size $W$ | 5 | 5 | 14 |
| number of scattering objects $\lvert\mathcal{K}\rvert$ | 200 | 60 | 56 |
| scattering object gain $\gamma$ | 2.5 | 12 | 50 |

The fit to a Rician distribution is perfect for the *LOS* scenario where the estimated $K$ factor is high with $\hat{K}_{\mathrm{ML}} \approx 10\,\mathrm{dB}$. In the indoor *laboratory* scenario, the amplitude distribution also shows a good fit to a Rician distribution. The estimated $K$ factor here, $\hat{K}_{\mathrm{ML}} \approx 0\,\mathrm{dB}$, is significantly lower compared to the *LOS* scenario although the considered region of quasi-stationarity is located next to the windows. For the *hallway* scenario, the Rician amplitude distribution provides a reasonable approximation for the observed amplitude distribution. The deviation from a Rician distribution comes from the fact that the channel statistics change more severely depending on the position within the quasi-stationary region as they do in the other two scenarios, see Fig. 4. As one would expect, the estimated Rician $K$ factor of $\hat{K}_{\mathrm{ML}} \approx -28\,\mathrm{dB}$ is very low in this deep indoor scenario.

### C. CHANNEL CORRELATION

#### 1) TEMPORAL CORRELATION

To demonstrate the time stability of our measurement hardware, we performed the previously described measurement of channel coefficients twice for each user position. For the acquisition of all channel coefficients, the user side antenna is moved across the linear guide once, sequentially stopping at $U = 148$ positions to enable channel sounding. At each of these positions, the transmit antenna is sequentially moved to the $N = 40$ antenna positions. In the second measurement run, the receive antenna is moved sequentially across the linear guide again, in reverse direction. During this second run, the same wireless channel is observed once more, at the same physical antenna position $u$ but with a time difference $\Delta T_u$ compared to the first measurement run. Since the direction of movement is reversed, the time in between two channel measurements $\Delta T_u$, taken at the same user position index $u$, depends on the user position. This dependence is expressed via the subscript $u$ of $\Delta T_u$. For user positions at the end of the linear guide (large position indices), the time difference to the second measurement is smaller compared to the beginning (small position indices) of the linear guide. We denote the $u^{\mathrm{th}}$ column vector of the channel matrix $\mathbf{H}$ by $\mathbf{h}_u \in \mathbb{C}^{N\times 1}$. Further, we denote the channel vector obtained in the second measurement at a time difference $\Delta T_u$ later compared to the first measurement run by $\mathbf{h}_u(\Delta T_u) \in \mathbb{C}^{N\times 1}$.

To investigate the change in correlation of channel coefficients at the same positions over time, we again employ the normalized inner product of channel vectors at identical positions, measured at different times

$$r_t(u) = \frac{|\mathbf{h}_u^{\mathrm{H}}\mathbf{h}_u(\Delta T_u)|}{\|\mathbf{h}_u\|\,\|\mathbf{h}_u(\Delta T_u)\|}. \tag{8}$$

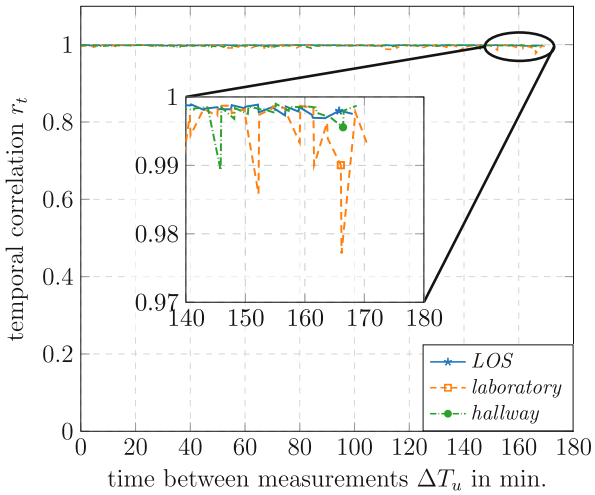


**FIGURE 6. Magnitude of the temporal channel correlation for channel vectors measured at the same position but at different times. The lowest measured value of channel correlation is 0.977, showing the high temporal stability of the measurement system.**

The magnitude of (8) is plotted over time in between two channel vector measurements in Fig. 6 for all three scenarios. Please mind the axis scaling in this figure. The smallest value of $r_t(u)$ is approximately 0.977. The plot shows that the measurement setup is approximately constant for the measurement duration of almost three hours. This includes all effects, such as, the observed wireless channel, time stability of the measurement hardware, noise, position accuracy of the virtual antenna arrays and the phase stability of cables that are bent during re-positioning of antennas. A detailed description of the measurement hardware time and frequency stability is provided in Appendix A.

#### 2) SPATIAL CORRELATION

We employ the channel matrix collinearity as metric for spatial user correlation, similar to other works in the context of correlation of MIMO channels [27], [41]–[43]. This collinearity measure is defined via (3) with the matrices $\mathbf{A}$ and $\mathbf{B}$ being two MIMO channel matrices [44]. In our special case of massive MIMO with $N$ antennas at the base station and users with a single antenna, the absolute value of this metric simplifies to the normalized inner product of channel vectors for users $u$ and $u'$

$$r(u,u') = \frac{|\mathbf{h}_u^{\mathrm{H}}\mathbf{h}_{u'}|}{\|\mathbf{h}_u\|\,\|\mathbf{h}_{u'}\|} \tag{9}$$

where $\mathbf{h}_u \in \mathbb{C}^{N\times 1}$ again denotes the $u^{\mathrm{th}}$ column vector of channel matrix $\mathbf{H}$. Please note that the squared inner product corresponds to the interference power in a MIMO downlink system with two users and maximum ratio transmission, see Appendix C. Similar to (4), a mean channel vector inner product is then estimated as

$$\bar{r}(d) = \frac{1}{U-d+1}\sum_{u=1}^{U-d+1} r(u+d-1,u), \tag{10}$$

for inter-user distances $d \in \{1,\ldots,U\}$.

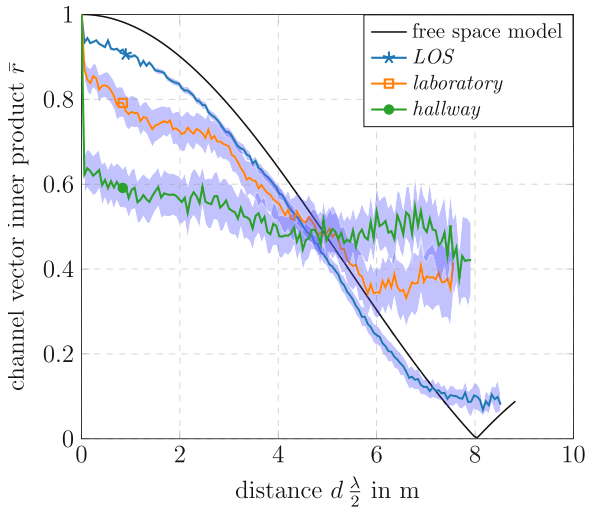


**FIGURE 7.** Mean channel vector inner product (spatial channel correlation) of the measured channel plotted against distance. The indoor scenarios *laboratory* and *hallway* show a high correlation, even for large distances. The 95% confidence interval of the mean is indicated via a shaded curve underlay.

Plots for the mean channel vector inner product (10) within the respective stationary region are provided in Fig. 7. The inner product for a free space propagation model is also provided as a reference. This free space channel model is a small scale fading model, considering the phase between the transmit and the receive antennas. A channel coefficient from transmit antenna $n \in \{1, \ldots, N\}$ to user $u \in \{1, \ldots, U\}$ of the free space channel $\mathbf{H}_{\text{free}} \in \mathbb{C}^{N \times U}$ is given by

$$\mathbf{H}_{\text{free}}[n, u] = \exp\left(-\mathrm{i}\frac{2\pi}{\lambda}\xi_{n,u}\right), \tag{11}$$

with distance $\xi_{n,u}$ between the $n^{\text{th}}$ transmit antenna and the $u^{\text{th}}$ user positions.

For the *LOS* scenario, the channel correlation is similar to a free space propagation model. The channel vector inner product is slightly lower compared to the pure LOS case, indicating that there are scattering objects present in the wireless channel.

For the *laboratory* scenario, the measured correlation function is very different from the correlation obtained from the free space channel model, since the estimated Rician $K$ factor is only approximately 0 dB in this scenario. The decorrelation occurs slower with distance compared to the *LOS* scenario. The channel vector inner product behaves similar to the free space case in a region of 3 m to 6 m, but remains higher at larger distances.

This situation becomes even more pronounced for the *hallway* scenario. The spatial channel correlation starts out (for the first non-zero distance) at a lower level compared to the other measured scenarios, but shows almost no decorrelation with increasing distance. This is a remarkable result as one expects the spatial correlation to decrease quickly with distance in an indoor scenario.

## IV. PERFORMANCE RESULTS AND CHANNEL MODELING

In this section, we present results for the achievable spectral efficiency within the stationary regions for all three scenarios. We also model the measured channel by means of a Rician channel model and a geometry based scattering channel model. We compare these channel models to the measured channel in terms of channel correlation and achievable spectral efficiency.

The Rician channel model is given by

$$\mathbf{H}_{\text{Rice}} = \sqrt{\frac{K}{1+K}}\mathbf{H}_{\text{free}} + \frac{1}{\sqrt{1+K}}\mathbf{H}_{\text{iid}}, \tag{12}$$

where $K$ denotes the Rician $K$ factor. The free space channel $\mathbf{H}_{\text{free}}$ is defined through (11). The i.i.d. Rayleigh channel matrix $\mathbf{H}_{\text{iid}} \in \mathbb{C}^{N \times U}$ consists of independent complex Gaussian random variables with $\mathbf{H}_{\text{iid}}[n, u] \sim \mathcal{CN}\{0, 1\} \forall n \in \{1, \ldots, N\}, u \in \{1, \ldots, U\}$. Please note that the Rician channel model includes spatial correlation through the free space channel component. The amount of spatial correlation is dependent on the Rician $K$ factor.

For a comparison with a spatially consistent channel model, we employ the channel model from [15]. Since this model is based on the multiple scattering channel model idea [45], we will refer to this model as *scattering* model within this work. For this channel model, a channel coefficient from transmit antenna $n \in \{1, \ldots, N\}$ to user $u \in \{1, \ldots, U\}$ is given by

$$\mathbf{H}_{\text{scatter}}[n, u] = \alpha_{u,n} + \sum_{k \in \mathcal{K}} \beta_{u,k}\alpha_{k,n}\,, \tag{13}$$

where $\mathcal{K}$ denotes the set of scattering objects. The coefficient $\alpha_{u,n}$ describes the propagation from transmit antenna $n$ to user $u$, the coefficient $\alpha_{k,n}$ describes the propagation from transmit antenna $n$ to scattering object $k$ and the coefficient $\beta_{u,k}$ describes the propagation from scattering object $k$ to user $u$. These propagation coefficients are defined as

$$\alpha_{k,j} = \frac{\lambda}{4\pi\|\mathbf{r}_k - \mathbf{r}_j\|} e^{\mathrm{i}\frac{2\pi}{\lambda}\|\mathbf{r}_k - \mathbf{r}_j\|}, \tag{14a}$$

$$\beta_{j,k} = \frac{\delta_k}{\sqrt{4\pi}\|\mathbf{r}_j - \mathbf{r}_k\|} e^{\mathrm{i}\frac{2\pi}{\lambda}\|\mathbf{r}_j - \mathbf{r}_k\|}. \tag{14b}$$

The vectors $\mathbf{r}_j \in \mathbb{R}^2$ contain the position of either transmit antenna $j$, user $j$ or scattering object $j$. The scattering event is modeled via the scattering factor $\delta_k = \gamma e^{\mathrm{i}\phi_k}$, where the scattering gain $\gamma$ describes the strength of the scattering events and $\phi_k$ is a uniformly distributed angle, that is, $\phi_k \sim \mathcal{U}[0, 2\pi)$. Please note that this channel model is defined via the actual position of the transmit antennas, scattering objects and user positions. This model is therefore inherently spatially consistent [15].

There are three major channel parameters for the scattering channel model: the scattering gain $\gamma$, the number of scattering elements $|\mathcal{K}|$ and the position of the scattering elements. We employ a uniformly distributed random placement of scattering elements within a limited spatial region for each

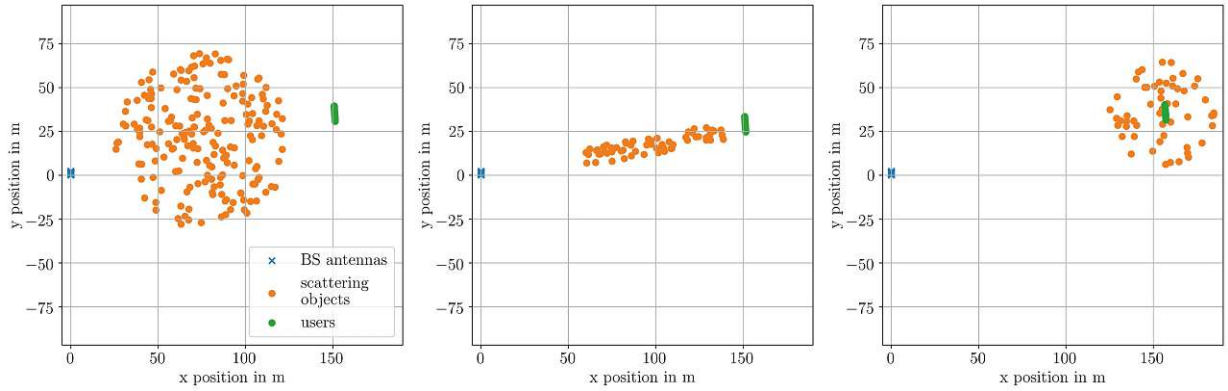


(a) *LOS* scenario (b) *laboratory* scenario (c) *hallway* scenario

**FIGURE 8.** **Environments for the scattering channel model. (a) For the *LOS* scenario, scattering objects are uniformly distributed between transmitter and receiver. (b) In the *laboratory* scenario, the scattering object placement is restricted to positions that are visible through the window. (c) In the *hallway* scenario, scattering objects are uniformly distributed around the receiver positions.**

scenario. These regions correspond to the positions of dominant scattering objects within the measured wireless channel. We provide further details on the scattering element placement in the scenario descriptions below.

To fit the scattering channel model to the channel measurements, we perform Monte Carlo simulations to find a match in terms of Rician $K$ factor and spatial channel correlation. The employed values for the number of scattering elements $|\mathcal{K}|$ and the scattering gain $\gamma$ for each measurement scenario are summarized in Tab. 1. A large scattering gain and a high number of scattering elements yields dominant non-line of sight (NLOS) components and therefore a small Rician $K$ factor. When scattering elements are spread out widely in space, dominant NLOS components lead to a low spatial correlation. In case the scattering elements form a concentrated cluster, dominant NLOS paths result in high spatial correlation. This allows to fit wireless channels with low Rician $K$ factor that still show a large spatial correlation.

For the *LOS* scenario, the positions of the scattering objects are two dimensional uniformly distributed on a disk with radius 50 m in between the transmitter and the receiver, see Fig. 8(a). These scattering objects account for the fact that the measured propagation environment is not a free space one. As the scattering elements are spread out widely in space, the NLOS components have a large angular spread and low correlation. Since, however, the Rician $K$ factor in this scenario is high, the LOS component is dominating in the channel model. The specific spatial distribution of the scattering elements has therefore little impact on the channel correlation in this scenario.

For the *laboratory* scenario, the scattering objects are clustered densely and closely to the direct LOS path, see Fig. 8(b). This models the fact that only scattering objects within a limited angular region are visible to the receiver through the windows. The positions of the scattering objects correspond to a building in between the transmitter and the user positions, see Fig. 1. The similar incident angles of scattered paths lead to a high level of spatial correlation over extended inter user distances at the receiver side, even at a low $K$ factor.

In the *hallway* scenario, a host of scattering objects is uniformly distributed within a disk of radius 30 m around the user positions, see Fig. 8(c). The radius of this disk has negligible impact on the channel model as long as the scattering elements are uniformly distributed around the user positions. This element placement models a dense scattering environment with a low Rician $K$ factor. A large scattering gain of $\gamma = 50$ and a rather small number of scattering elements of $|\mathcal{K}| = 56$ allows a good fit of the large spatial correlation in this scenario.

### A. SPATIAL CHANNEL CORRELATION

We provide results for the spatial channel correlation of the measured channel within the stationarity regions, the Rician channel model (12) and the scattering channel model (13) in Fig. 9. The Rician $K$ factors for both of these channel models are chosen to fit the ML estimated $K$ factor of the respective measured channel. The channel correlation of the free space channel model (11) is also provided as reference.

The spatial channel correlation for the *LOS* scenario is shown in Fig. 9(a). Although there are no obstacles in between the transmitter and the user in the measured *LOS* scenario, there are inevitably scattering objects present in the measured scenario. Therefore, the spatial channel correlation deviates from the free space model. Both, the Rician channel model as well as the scattering channel model, show a good fit to the measured channel in terms of the spatial channel correlation for the *LOS* scenario.

For the *laboratory* scenario, the resulting spatial correlation is shown in Fig. 9(b). The measured spatial correlation is not well explained by the fitted Rician channel model due to the low $K$ factor in this scenario. Scattering objects in the

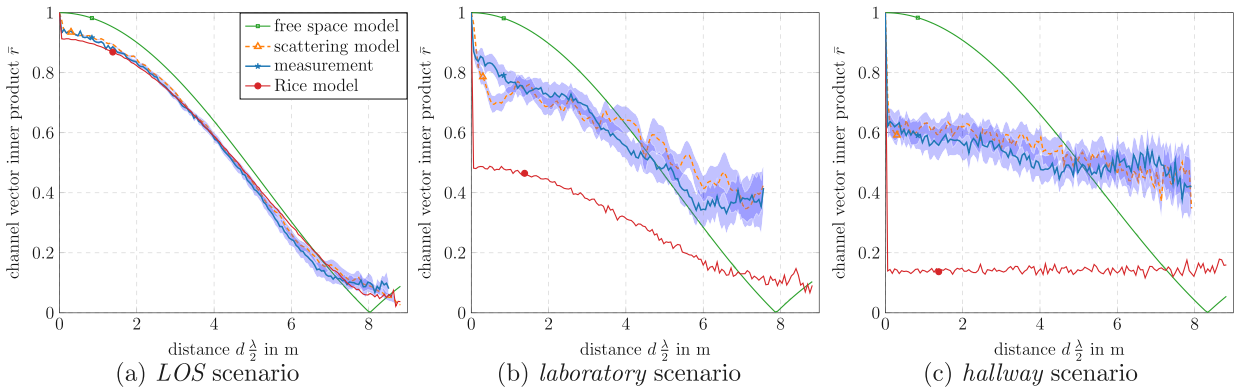


**FIGURE 9.** Mean channel vector inner product for: (a) the *LOS* scenario, (b) the *laboratory* scenario and (c) the *hallway* scenario. The 95% confidence interval of the mean is indicated via a shaded curve underlay.

corresponding scattering channel model scenario are located within a narrow angular range around the direct path. Thereby we achieve a higher spatial correlation for a low $K$ factor with the scattering channel model, providing a good match with the measured channel.

In case of the deep indoor *hallway* scenario, the spatial correlation function is shown in Fig. 9(c). Since the estimated Rician $K$ factor is very low with approximately $-28$ dB, the fitted Rician channel model is very close to an i.i.d. Rayleigh fading channel. Therefore, the Rician channel model shows almost zero spatial correlation, independent of the user separation distance. While the measured channel also shows a low level of spatial correlation, it is still significantly higher compared to the Rician channel model. For the scattering channel model, we model the indoor environment by scattering elements distributed uniformly all around the receiver positions. This scattering element placement leads to scattered paths arriving from all directions at the receiver. This yields scattered paths with low spatial correlation as the randomly fading channel has no self-similarity for different receiver positions. To fit the comparably large spatial correlation of the measured channel with the scattering channel model, we employ few scattering elements with large scattering gain in this model. Achieving a spatial correlation as low as in an i.i.d. Rayleigh channel requires a scattering environment with a huge number of scatterers. Our results show that such a large number of scattering elements is not necessarily found in a deep indoor scenario. The fact that we achieve a match with scattering elements uniformly distributed around the receiver additionally shows that the spatial correlation behavior does not necessarily come from waveguiding effects along the hallway.

### B. ACHIEVABLE SPECTRAL EFFICIENCY

In order to illustrate the impact of channel correlation on a massive MIMO mobile communications system, we provide results for the achievable spectral efficiency (SE) within the regions of WSS in this section. A system model and the definition of the achievable SE [46, p. 9], [47], employed for the simulations in this section, are provided in Appendix C.

The mean achievable sum SE for the case of two users with minimum mean squared error (MMSE) precoding is shown in Fig. 10. This mean is plotted against the distance $d$ between the users for the measurement within the stationary regions, the scattering channel model, the Rician channel model and the free space channel model. The mean value of achievable sum SE is inferred by averaging over all possible positions pairs with distance $d$, similar to the mean channel inner product (10).

The SNR without beamforming gain in this simulation scenario is set to 0 dB. Please note that although the SNR varies between the scenarios, the SNR was set to the same value for all scenarios in this simulation for a better comparison.

In the *LOS* scenario, the achievable SE curve for the measured channel is very close to the free space channel model since this scenario is a LOS one, see Fig. 10(a). The presence of scattering objects leads to an SE that is higher than the SE of the free space channel model for small inter-user distances. The Rician channel model and the scattering channel model provide a good fit to the measured channel in the *LOS* scenario.

The achievable SE for the *laboratory* scenario is shown in Fig. 10(b). The measured channel decorrelates with inter-user distance, leading to an increased SE at large distances. As a consequence of the low Rician $K$ factor in this scenario, the Rician channel model includes little spatial correlation and therefore leads to a too high SE compared to the measurement. The scattering channel model includes higher spatial correlation (having the same, low Rician $K$ factor) and therefore describes the trend in sum SE better.

The SE for the *hallway*, or deep-indoor, measurement scenario is shown in Fig. 10(c). The measured wireless channel in this scenario has an amplitude distribution with a very low Rician $K$ factor and is therefore similar to an uncorrelated i.i.d. Rayleigh channel in terms of channel coefficient distribution. Still, the measured spatial correlation is much higher

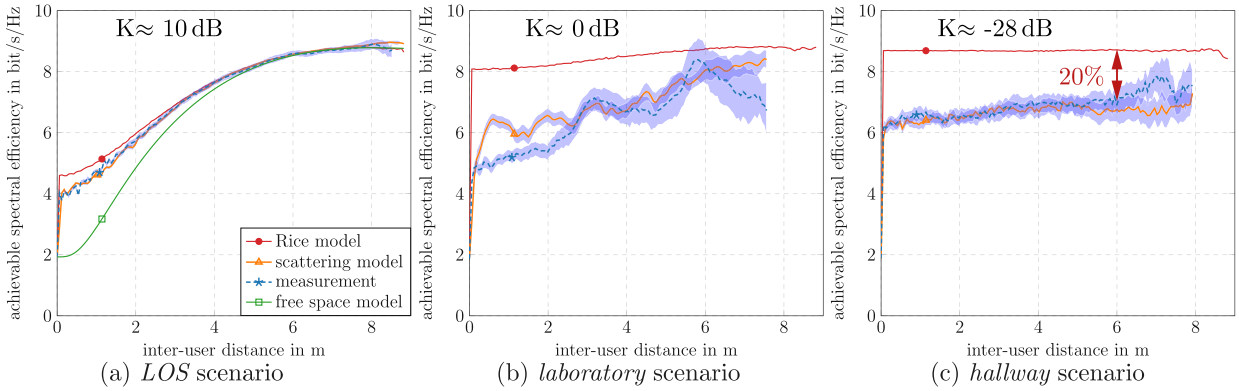


**FIGURE 10.** Mean achievable sum SE for the Rician chsssannel model, the scattering channel model, the measured channel and the free space channel model at an SNR of 0 dB. The 95% confidence interval of the mean is indicated via a shaded curve underlay.

compared to the fitted Rician channel model with the same $K$ factor. Therefore, the resulting SE of the Rician channel model is too high. The scattering channel model provides more accurate spatial correlation. Therefore, the SE obtained by the scattering channel model matches the measurement.

Further, the achievable SE shows little dependence on inter-user distance in the *hallway* scenario. While one expects that a deep-indoor channel decorrelates quickly with distance, the effect of spatial correlation remains significant for several meters in this scenario. The achievable SE of the measured channel is 20% lower than the achievable SE of the Rician channel model with the same $K$ factor for an inter-user distance as large as 6 m, see Fig. 10(c).

Similar numbers were found in other MIMO measurements before. In [48], the authors measure an outdoor-to-outdoor massive MIMO scenario. Their results show that approximately 80% of the i.i.d. Rayleigh sum rate is achieved with MMSE precoding at 0 dB SNR with 112 antennas. Authors of [8] also report to achieve 80-90% of the i.i.d. Rayleigh channel dirty paper coding capacity in an outdoor-to-outdoor scenario with zero forcing (ZF) precoding and 128 antennas. In [49], the authors measure a $4 \times 4$ MIMO outdoor-to-indoor scenario. They report a median capacity of 80% compared to an i.i.d. Rayleigh channel at an SNR of 5 dB. We observe this remarkable performance gap also for a deep indoor user in an outdoor-to-indoor scenario where one would expect a low spatial correlation.

## V. CONCLUSION

Spatial correlation heavily depends on the scenario and the user environment. The amount of spatial correlation and the decorrelation behavior with distance are mainly determined by the location of scattering objects visible to the receiver. When incident paths arrive from a narrow angular range at a certain user location, a high level of spatial correlation is experienced even when the amplitude statistic shows a very low Rician $K$ factor. For the measured outdoor-to-indoor *hallway* scenario, the observed amount of spatial correlation is significantly higher than one would obtain when modeling such a rich scattering environment with a Rician (or i.i.d. Rayleigh) channel model. Since spatial correlation between users occurs even in such dense scattering environments, user scheduling is an important tool for massive MIMO systems. Further, when a scattering environment yields spatially correlated channels for large user distances, massive MIMO with LOS is preferable to massive MIMO with NLOS. The achievable SE of a multi-user MIMO system is significantly over-estimated when using Rician channel models, such as (12), or spatially inconsistent channel models. The spatially consistent scattering channel model (13), based on the positions of the scattering elements, leads to a good match with the measurement. Thus, one is advised to use spatially consistent channel models to predict the performance of multi-user MIMO systems accurately.

## APPENDIX A
## MEASUREMENT HARDWARE STABILITY

The measurement principle of virtual antenna array measurements reduces hardware complexity in terms of number of required RF chains since only a single antenna is employed. However, the virtual array concept requires a measurement system that is stable over time, since channel measurements are performed sequentially. The obtained channel measurements are then joined into a channel matrix or channel vector as if they were all measured at the same time with a full antenna array. This requires both, a time-invariant wireless channel and measurement hardware that behaves completely stable over time. The former condition is achieved by performing wireless channel measurements out of office hours, during night, when there are no persons present at the faculty where the measurements were performed. The latter requirement on time stability of the measurement hardware includes the considerations below [50]:

- **Time Synchronization:** Since triggered measurements are performed at each transmit antenna position and each

receiver position, a repeatable triggering mechanism and time synchronization is required. The Vienna MIMO Testbed employs a hardware based timing synchronization unit [51], [52] that achieves a timing accuracy of ±10 ns. This timing offset is negligible compared to the employed OFDM symbol duration of approximately 66.67 µs.

- **Frequency Synchronization:** Global Positioning System (GPS) disciplined Rubidium frequency standards at the transmitter and the receiver ensure a frequency deviation of $\pm 5 \cdot 10^{-11}$. At a center frequency of 2.5 GHz this leads to a worst case frequency difference between transmitter and receiver of $\Delta f = 10 \cdot 10^{-11} \times 2.5\,\text{GHz} = 0.25\,\text{Hz}$. Compared to the employed subcarrier spacing of 15 kHz of the employed OFDM channel sounding signal, this frequency deviation is negligible.
- **Phase Synchronization:** To obtain a measured MIMO channel matrix with correct phase relation between all transmit antennas and all receive antennas from a virtual array measurement, phase stability is required. Although our testbed employs highly accurate Rubidium frequency standards, the worst case frequency difference $\Delta f$ between transmitter and receiver leads to a phase drift of $\frac{d\phi}{dt} = 2\pi\Delta f = \frac{\pi}{2}\,\text{s}^{-1}$. Since the re-positioning of the transmit antenna with a mechanical guide requires an amount of time in the order of a second, this phase drift is significant for the channel sounding procedure. To compensate the phase offset due to the phase drift during the virtual array measurement, a second directive radio link between the transmitter and the receiver was established. Since the Vienna MIMO Testbed has four RF channels available, the wireless channel of this directive reference link and the actual wireless channel of interest can be measured at the same time. To avoid interference between the wireless channel of interest and the reference link, the sounding sequences were frequency multiplexed. By establishing a direct LOS connection with stationary directive antennas at both ends of the reference link, we ensure that the reference link is time-invariant. Therefore, the estimated phase of the reference link provides an estimate for the phase difference between transmitter and receiver. Neglecting the phase change of at most 0.6° over the 67 ms long channel sounding sequence, the phase estimate of the reference link is exploited to compensate the phase drift of the wireless channel estimates.

## APPENDIX B
## PROPERTIES OF THE CMD

Let's assume matrices $\mathbf{A}, \mathbf{B} \in \mathbb{C}^{n\times n}$ are correlation matrices and therefore Hermitian and positive definite. Due to properties of the $\text{tr}(\cdot)$ operator and Hermitian matrices

$$\text{tr}\left(\mathbf{A}^{\text{H}}\mathbf{B}\right) = \text{tr}\left(\mathbf{A}\mathbf{B}^{\text{H}}\right) = \text{tr}\left(\mathbf{B}^{\text{H}}\mathbf{A}\right) = \text{tr}\left(\mathbf{A}^{\text{H}}\mathbf{B}\right)^{\text{H}}, \quad (15)$$

from which follows $\text{tr}\left(\mathbf{A}^{\text{H}}\mathbf{B}\right) \in \mathbb{R}$. Let us consider the matrix factorizations $\mathbf{B} = \mathbf{U}\mathbf{D}\mathbf{U}^{\text{H}}$ and $\mathbf{A} = \mathbf{V}\mathbf{Q}\mathbf{V}^{\text{H}}$, where $\mathbf{D}, \mathbf{Q} \in \mathbb{R}^{n\times n}$ are diagonal matrices and the matrices $\mathbf{U}$ and $\mathbf{Q}$ are unitary. The square root of $\mathbf{B}$ is given by $\mathbf{B}^{\frac{1}{2}} = \mathbf{U}\mathbf{D}^{\frac{1}{2}}\mathbf{U}^{\text{H}}$ such that $\mathbf{B} = \mathbf{B}^{\frac{1}{2}}\mathbf{B}^{\frac{\text{H}}{2}}$. From this follows

$$\text{tr}\left(\mathbf{A}^{\text{H}}\mathbf{B}\right) = \text{tr}\left(\mathbf{B}^{\frac{\text{H}}{2}}\mathbf{A}^{\text{H}}\mathbf{B}^{\frac{1}{2}}\right) = \text{tr}\left(\mathbf{B}^{\frac{\text{H}}{2}}\mathbf{V}\mathbf{Q}\mathbf{V}^{\text{H}}\mathbf{B}^{\frac{1}{2}}\right). \quad (16)$$

Since the argument of the $\text{tr}(\cdot)$ is positive-definite, it further follows that $\text{tr}\left(\mathbf{A}^{\text{H}}\mathbf{B}\right) > 0$ and therefore $\text{tr}\left(\mathbf{A}^{\text{H}}\mathbf{B}\right) = \left|\text{tr}\left(\mathbf{A}^{\text{H}}\mathbf{B}\right)\right|$. The CMD from (3) may be equivalently re-written as

$$\text{CMD}(\mathbf{A}, \mathbf{B}) = \frac{\left|\text{tr}\left(\mathbf{A}^{\text{H}}\mathbf{B}\right)\right|}{\|\mathbf{A}\|\,\|\mathbf{B}\|}. \quad (17)$$

With $\|\mathbf{A}\| = \sqrt{\text{tr}\left(\mathbf{A}^{\text{H}}\mathbf{A}\right)}$ and the Cauchy-Schwarz inequality, it follows $0 \leq \text{CMD}(\mathbf{A}, \mathbf{B}) \leq 1$.

## APPENDIX C
## SYSTEM MODEL AND ACHIEVABLE SPECTRAL EFFICIENCY

We consider a multi-user massive MIMO downlink scenario with $N$ transmit antennas at the BS. There are $U$ users, each with a single omni-directional antenna. The received signal of user $u$ is

$$y_u = \sum_{j=1}^{U} \mathbf{h}_u^{\text{H}}\mathbf{f}_j\sqrt{\rho_j}x_j + w_u. \quad (18)$$

where $w_u$ is additive withe Gaussian noise with $w_u \sim \mathcal{CN}\left(0, \sigma_w^2\right)$. The real positive power scaling factors are denoted by $\rho_u$ for users $u \in \{1, \ldots, U\}$. The vector $\mathbf{h}_u$ contains all channel coefficients from $N$ transmit antennas to user $u$. The independent random transmit symbol is denoted by $x_u$ and is of unit power, that is, $\mathbb{E}\{xx^*\} = 1$. The precoding vector of user $u$ is denoted by $\mathbf{f}_u$. A power constraint $\mathbb{E}\left\{\|\sum_{u=1}^{U}\mathbf{f}_u\sqrt{\rho_u}x_u\|_2^2\right\} \leq P_T$ is considered, which leads to $\|\mathbf{f}_u\|_2^2 = 1$ and $\sum_{u=1}^{U}\rho_u = P_T$ with the sum transmit power $P_T$. The precoding matrix $\mathbf{F} = (\mathbf{f}_1, \mathbf{f}_2, \ldots, \mathbf{f}_U) \in \mathbb{C}^{N\times U}$ is normalized per-user such that $\|\mathbf{f}_u\|_2 = 1$, $\forall u \in \{1, \ldots, U\}$. The signal to interference and noise ratio (SINR) of user $u$ is given by

$$\text{SINR}_u = \frac{\rho_u\left|\mathbf{h}_u^{\text{H}}\mathbf{f}_u\right|^2}{\sum_{\substack{j=1\\ j\neq u}}^{U}\rho_j\left|\mathbf{h}_u^{\text{H}}\mathbf{f}_j\right|^2 + \sigma_w^2}. \quad (19)$$

The achievable sum SE in bits/ s/ Hz is

$$\text{SE} = \sum_{u=1}^{U}\log_2\left(1 + \text{SINR}_u\right). \quad (20)$$

In this work, we consider MMSE precoding, with a precoding matrix calculated as

$$\widetilde{\mathbf{F}}^{\text{MMSE}} = \mathbf{H}\left(\mathbf{H}^{\text{H}}\mathbf{H} + \frac{U\sigma_w^2}{P_T}\mathbf{I}_U\right)^{-1}, \quad (21)$$

with the channel matrix $\mathbf{H} = (\mathbf{h}_1, \ldots, \mathbf{h}_U)$ and the precoding matrix $\widetilde{\mathbf{F}} = (\widetilde{\mathbf{f}}_1, \ldots, \widetilde{\mathbf{f}}_U)$. According to the sum transmit power constraint, the precoding matrix is normalized as

$$\mathbf{f}_u = \frac{\widetilde{\mathbf{f}}_u}{\|\widetilde{\mathbf{f}}_u\|_2} \quad \forall u \in \{1, \ldots, U\}. \tag{22}$$

Further, we apply equal power to all users, that is, we choose $\rho_u = \frac{P_T}{U}$ $\forall u \in \{1, \ldots, u\}$.

## REFERENCES


[1] E. Björnson, E. G. Larsson, and T. L. Marzetta, "Massive MIMO: Ten myths and one critical question," *IEEE Commun. Mag.*, vol. 54, no. 2, pp. 114–123, Feb. 2016.

[2] X. Gao, F. Tufvesson, and O. Edfors, "Massive MIMO channels—Measurements and models," in *Proc. Asilomar Conf. Signals, Syst. Comput.*, Pacific Grove, CA, USA, Nov. 2013, pp. 280–284.

[3] H. Quoc Ngo, E. G. Larsson, and T. L. Marzetta, "Energy and spectral efficiency of very large multiuser MIMO systems," *IEEE Trans. Commun.*, vol. 61, no. 4, pp. 1436–1449, Apr. 2013.

[4] L. Lu, G. Y. Li, A. L. Swindlehurst, A. Ashikhmin, and R. Zhang, "An overview of massive MIMO: Benefits and challenges," *IEEE J. Sel. Topics Signal Process.*, vol. 8, no. 5, pp. 742–758, Oct. 2014.

[5] E. Björnson, J. Hoydis, and L. Sanguinetti, "Massive MIMO networks: Spectral, energy, and hardware efficiency," *Found. Trends Signal Process.*, vol. 11, nos. 3–4, pp. 154–655, 2017.

[6] A.-S. Bana, E. de Carvalho, B. Soret, T. Abrão, J. C. Marinello, E. G. Larsson, and P. Popovski, "Massive MIMO for Internet of things (IoT) connectivity," *Phys. Commun.*, vol. 37, Dec. 2019, Art. no. 100859.

[7] D.-S. Shiu, G. J. Foschini, M. J. Gans, and J. M. Kahn, "Fading correlation and its effect on the capacity of multielement antenna systems," *IEEE Trans. Commun.*, vol. 48, no. 3, pp. 502–513, Mar. 2000.

[8] X. Gao, F. Tufvesson, O. Edfors, and F. Rusek, "Measured propagation characteristics for very-large MIMO at 2.6 GHz," in *Proc. Conf. Rec. Forty 6th Asilomar Conf. Signals, Syst. Comput. (ASILOMAR)*, Pacific Grove, CA, USA, Nov. 2012, pp. 295–299.

[9] J. Flordelis, X. Gao, G. Dahman, F. Rusek, O. Edfors, and F. Tufvesson, "Spatial separation of closely-spaced users in measured massive multi-user MIMO channels," in *Proc. IEEE Int. Conf. Commun. (ICC)*, London, U.K., Jun. 2015, pp. 1441–1446.

[10] C.-M. Chen, V. Volskiy, A. Chiumento, L. Van der Perre, G. A. E. Vandenbosch, and S. Pollin, "Exploration of user separation capabilities by distributed large antenna arrays," in *Proc. IEEE Globecom Workshops (GC Wkshps)*, Washington, DC, USA, Dec. 2016, pp. 1–6.

[11] S. Caban, C. Mehlfuhrer, L. W. Mayer, and M. Rupp, "2×2 MIMO at variable antenna distances," in *Proc. VTC Spring - IEEE Veh. Technol. Conf.*, Singapore, May 2008, pp. 1311–1315.

[12] J. Flordelis, F. Rusek, X. Gao, G. Dahman, O. Edfors, and F. Tufvesson, "Spatial separation of closely-located users in measured massive MIMO channels," *IEEE Access*, vol. 6, pp. 40253–40266, 2018.

[13] M. Z. Aslam, Y. Corre, E. Bjoernson, and Y. Lostanlen, "Massive MIMO channel performance analysis considering separation of simultaneous users," in *Proc. 22nd Int. ITG Workshop Smart Antennas*, Bochum, Germany, Mar. 2018, pp. 1–6.

[14] S. Pratschner, E. Zochmann, H. Groll, S. Caban, S. Schwarz, and M. Rupp, "Does a large array aperture pay off in Line-Of-Sight massive MIMO?" in *Proc. IEEE 20th Int. Workshop Signal Process. Adv. Wireless Commun. (SPAWC)*, Cannes, France, Jul. 2019, pp. 1–5.

[15] S. Pratschner, T. Blazek, E. Zochmann, F. Ademaj, S. Caban, S. Schwarz, and M. Rupp, "A spatially consistent MIMO channel model with adjustable k factor," *IEEE Access*, vol. 7, pp. 110174–110186, 2019.

[16] A. M. Pessoa, I. M. Guerreiro, C. F. Silva, T. F. Maciel, D. A. Sousa, D. C. Moreira, and F. R. Cavalcanti, "A stochastic channel model with dual mobility for 5G massive networks," *IEEE Access*, vol. 7, pp. 149971–149987, 2019.

[17] F. Ademaj, S. Schwarz, K. Guan, and M. Rupp, "Ray-tracing based validation of spatial consistency for geometry-based stochastic channels," in *Proc. IEEE 88th Veh. Technol. Conf. (VTC-Fall)*, Chicago, IL, USA, Aug. 2018.

[18] S. Jaeckel, L. Raschkowski, K. Borner, and L. Thiele, "QuaDRiGa: A 3-D multi-cell channel model with time evolution for enabling virtual field trials," *IEEE Trans. Antennas Propag.*, vol. 62, no. 6, pp. 3242–3256, Jun. 2014.

[19] L. Liu, C. Oestges, J. Poutanen, K. Haneda, P. Vainikainen, F. Quitin, F. Tufvesson, and P. Doncker, "The COST 2100 MIMO channel model," *IEEE Wireless Commun.*, vol. 19, no. 6, pp. 92–99, Dec. 2012.

[20] F. Ademaj, S. Schwarz, T. Berisha, and M. Rupp, "A spatial consistency model for geometry-based stochastic channels," *IEEE Access*, vol. 7, pp. 183414–183427, 2019.

[21] S. Payami and F. Tufvesson, "Channel measurements and analysis for very large array systems at 2.6 GHz," in *Proc. 6th Eur. Conf. Antennas Propag. (EUCAP)*, Prague, Czech Republic, Mar. 2012, pp. 433–437.

[22] L. Hao, X. Yi, J. Rodríguez-Piñeiro, B. Ai, and Z. Zhong, "Measurement-based massive-MIMO channel characterization for outdoor LoS scenarios," in *Proc. IEEE 29th Annu. Int. Symp. Pers., Indoor Mobile Radio Commun. (PIMRC)*, Bologna, Italy, Sep. 2018, pp. 1–6.

[23] X. Gao, O. Edfors, F. Rusek, and F. Tufvesson, "Massive MIMO performance evaluation based on measured propagation data," *IEEE Trans. Wireless Commun.*, vol. 14, no. 7, pp. 3899–3911, Jul. 2015.

[24] B. Ai, K. Guan, R. He, J. Li, G. Li, and D. He, "On indoor millimeter wave massive MIMO channels: Measurement and simulation," *IEEE J. Sel. Areas Commun.*, vol. 35, no. 7, pp. 1678–1690, Jul. 2017.

[25] A. O. Martinez, E. De Carvalho, and J. O. Nielsen, "Towards very large aperture massive MIMO: A measurement based study," in *Proc. IEEE Globecom Workshops (GC Wkshps)*, Austin, TX, USA, Dec. 2014, pp. 281–286.

[26] Q. Wang, B. Ai, D. W. Matolak, R. He, K. Guan, Z. Zhong, and D. Li, "Spatial variation analysis for measured indoor massive MIMO channels," *IEEE Access*, vol. 5, pp. 20828–20840, 2017.

[27] B. Zhang, Z. Zhong, R. He, B. Ai, G. Dahman, M. Yang, and J. Li, "Multi-user channels with large-scale antenna arrays in a subway environment: Characterization and modeling," *IEEE Access*, vol. 5, pp. 23613–23625, 2017.

[28] X. Gao, O. Edfors, F. Rusek, and F. Tufvesson, "Linear pre-coding performance in measured very-large MIMO channels," in *Proc. IEEE Veh. Technol. Conf. (VTC Fall)*, San Francisco, CA, USA, Sep. 2011, pp. 1–5.

[29] *Stadt Wien–ViennaGIS*. Accessed: Apr. 4, 2020. [Online]. Available: https://www.wien.gv.at/viennagis/

[30] S. Caban, J. A. García-Naya, and M. Rupp, "Measuring the physical layer performance of wireless communication systems," *IEEE Instrum. Meas. Mag.*, vol. 14, no. 5, pp. 8–17, May 2011.

[31] M. Lerch, S. Caban, M. Mayer, and M. Rupp, "The Vienna MIMO testbed: Evaluation of future mobile communication techniques," *Intel Technol. J.*, vol. 18, no. 3, pp. 58–69, 2014.

[32] M. Lerch, S. Caban, E. Zöchmann, and M. Rupp, "Quantifying the repeatability of wireless channels by quantized channel state information," in *Proc. IEEE Sensor Array Multichannel Signal Process. Workshop (SAM)*, Rio de Janeiro, Brazil, Jul. 2016, pp. 1–5.

[33] E. Zöchmann, C. F. Mecklenbräuker, M. Lerch, S. Pratschner, M. Hofer, D. Löschenbrand, J. Blumenstein, S. Sangodoyin, G. Artner, S. Caban, T. Zemen, A. Prokes, M. Rupp, and A. Molisch, "Measured delay and Doppler profiles of overtaking vehicles at 60 GHz," in *Proc. 12th Eur. Conf. Antennas Propag. (EuCAP)*, London, U.K., Apr. 2018, pp. 1–5.

[34] E. Zöchmann, S. Pratschner, S. Schwarz, and M. Rupp, "MIMO transmission over high delay spread channels with reduced cyclic prefix length," in *Proc. 19th Int. ITG Workshop Smart Antennas*, Ilmenau, Germany, Mar. 2015, pp. 1–8.

[35] M. Herdin, N. Czink, H. Ozcelik, and E. Bonek, "Correlation matrix distance, a meaningful measure for evaluation of non-stationary MIMO channels," in *Proc. IEEE 61st Veh. Technol. Conf.*, Stockholm, Sweden, 2005, pp. 136–140.

[36] E. D. Carvalho, A. Ali, A. Amiri, M. Angjelichinoski, and R. W. Heath, "Non-stationarities in Extra-Large-Scale massive MIMO," *IEEE Wireless Commun.*, vol. 27, no. 4, pp. 74–80, Aug. 2020.

[37] Y. Tan, C.-X. Wang, J. Ø. Nielsen, and G. F. Pedersen, "Comparison of stationarity regions for wireless channels from 2 GHz to 30 GHz," in *Proc. 13th Int. Wireless Commun. Mobile Comput. Conf. (IWCMC)*, Valencia, Spain, Jun. 2017, pp. 647–652.

[38] A. Gehring, M. Steinbauer, I. Gaspard, and M. Grigat, "Empirical channel stationarity in urban environments," in *Proc. Eur. Pers. Mobile Commun. Conf. (EMPCC)*, Vienna, Austria, 2001.

[39] M. Herdin and E. Bonek, "A MIMO correlation matrix based metric for characterizing non-stationarity," in *Proc. Mobile Wireless Commun. Summit*, Lyon, France, 2004.
[40] A. Goldsmith, *Wireless Communications*. Cambridge, U.K.: Cambridge Univ. Press, 2005.
[41] B. Clerckx and C. Oestges, *MIMO Wireless Networks: Channels, Techniques and Standards for Multi-Antenna, Multi-User and Multi-Cell Systems*. New York, NY, USA: Academic, 2013.
[42] N. Czink, B. Bandemer, G. Vazquez-Vilar, L. Jalloul, C. Oestges, and A. Paulraj, "Spatial separation of multi-user MIMO channels," in *Proc. IEEE 20th Int. Symp. Pers., Indoor Mobile Radio Commun.*, Tokyo, Japan, Sep. 2009, pp. 1059–1063.
[43] G. Dahman, J. Flordelis, and F. Tufvesson, "Experimental evaluation of the effect of BS antenna inter-element spacing on MU-MIMO separation," in *Proc. IEEE Int. Conf. Commun. (ICC)*, London, U.K., Jun. 2015, pp. 1685–1690.
[44] G. H. Golub and C. F. Van Loan, *Matrix Computations*, vol. 3. Baltimore, MD, USA: JHU Press, 2012.
[45] M. Franceschetti, J. Bruck, and L. J. Schulman, "A random walk model of wave propagation," *IEEE Trans. Antennas Propag.*, vol. 52, no. 5, pp. 1304–1317, May 2004.
[46] T. L. Marzetta, E. G. Larsson, H. Yang, and H. Q. Ngo, *Fundamentals Massive MIMO*. Cambridge, U.K.: Cambridge Univ. Press, 2016.
[47] C. Mehlführer, S. Caban, and M. Rupp, "Cellular system physical layer throughput: How far off are we from the Shannon bound?" *IEEE Wireless Commun.*, vol. 18, no. 6, pp. 54–63, Dec. 2011.
[48] J. Hoydis, C. Hoek, T. Wild, and S. ten Brink, "Channel measurements for large antenna arrays," in *Proc. Int. Symp. Wireless Commun. Syst. (ISWCS)*, Paris, France, Aug. 2012, pp. 811–815.
[49] C. Hermosilla, R. Feick, R. A. Valenzuela, and L. Ahumada, "Improving MIMO capacity with directive antennas for outdoor-indoor scenarios," in *Proc. EEE Veh. Technol. Conf. (VTC Spring)*, Singapore, May 2008, pp. 414–418.
[50] S. Pratschner, S. Caban, D. Schützenhöfer, M. Lerch, E. Zöchmann, and M. Rupp, "A fair comparison of virtual to full antenna array measurements," in *Proc. IEEE 19th Int. Workshop Signal Process. Adv. Wireless Commun. (SPAWC)*, Kalamata, Greece, Jun. 2018, pp. 1–5.
[51] S. Caban, A. Disslbacher-Fink, J. A. García Naya, and M. Rupp, "Synchronization of wireless radio testbed measurements," in *Proc. IEEE Int. Instrum. Meas. Technol. Conf.*, Binjiang, Hangzhou, China, May 2011, pp. 1–4.
[52] M. Laner, S. Caban, P. Svoboda, and M. Rupp, "Time synchronization performance of desktop computers," in *Proc. IEEE Int. Symp. Precis. Clock Synchronization Meas., Control Commun.*, Munich, Germany, Sep. 2011.

**STEFAN PRATSCHNER** (Member, IEEE) received the B.Sc. degree in electrical engineering and the M.Sc. degree in telecommunications from the Technical University of Vienna (TU Wien), Austria, in 2014 and 2016, respectively, where he is currently pursuing the Ph.D. degree. He has been a Project Assistant with the Institute of Telecommunications, TU Wien, since 2013. His current research interests include massive MIMO technologies for mobile communications, array processing, and testbed measurements.

**THOMAS BLAZEK** (Member, IEEE) received the B.Sc. degree in electrical engineering, the Dipl.Ing. degree (M.Sc. equivalent) in telecommunications, and the Dr.Tech. (Ph.D. equivalent) degree in telecommunications from the Technical University of Vienna (TU Wien), Vienna, Austria, in 2013, 2015, and 2019, respectively. His Dr.Tech. dissertation was on the essential aspects of reliable vehicular communications. He is employed at Silicon Austria Labs. His research interests include vehicular network topologies and radiofrequency machine learning solutions.

**HERBERT GROLL** (Graduate Student Member, IEEE) received the B.Sc. and Dipl.Ing. (M.Sc.) degrees in electrical engineering from Technische Universität Wien, in 2014 and 2017, respectively. He is currently pursuing the Ph.D. degree with the Technical University of Vienna (TU Wien), under supervision of Prof. C. Mecklenbräuker. His focus is on vehicular wireless communication with an emphasis on millimeter wave propagation for future wireless systems.

**SEBASTIAN CABAN** (Member, IEEE) received the master's degree in business administration, and the master's and Ph.D. degrees in telecommunications from the Technical University of Vienna (TU Wien), Vienna, Austria. His current research interests include measurements in wireless communications.

**STEFAN SCHWARZ** (Senior Member, IEEE) received the Ph.D. degree in telecommunications engineering from the Technical University of Vienna (TU Wien), Austria, in 2013. He currently holds a tenure track position as an Assistant Professor with the Institute of Telecommunications, TU Wien, where he heads the Christian Doppler Laboratory for Dependable Wireless Connectivity for the Society in Motion. His research interests include wireless communications, signal processing, and channel modeling. He is an Associate Editor of IEEE Access and *EURASIP JWCN*.

**MARKUS RUPP** (Fellow, IEEE) received the Dipl.Ing. degree from the University of Saarbrücken, Germany, in 1988, and the Dr.Ing. degree from the Technische Universität Darmstadt, Germany, in 1993. Until 1995, he held a postdoctoral position at the University of California at Santa Barbara, Santa Barbara, CA, USA. From 1995 to 2001, he was with the Department of Wireless Technology Research, Bell Labs, Holmdel, NJ, USA. Since 2001, he has been a Full Professor of digital signal processing in mobile communications with the Technical University of Vienna (TU Wien).

IEEE Access
Multidisciplinary | Rapid Review | Open Access Journal

SPECIAL SECTION ON ADVANCES IN STATISTICAL CHANNEL MODELING FOR FUTURE WIRELESS COMMUNICATIONS NETWORKS

Received July 19, 2019, accepted August 5, 2019, date of publication August 12, 2019, date of current version August 22, 2019.

*Digital Object Identifier 10.1109/ACCESS.2019.2934635*

# A Spatially Consistent MIMO Channel Model With Adjustable K Factor

**STEFAN PRATSCHNER[1,2], (Student Member, IEEE), THOMAS BLAZEK[2], (Student Member, IEEE), ERICH ZÖCHMANN[1,2], (Member, IEEE), FJOLLA ADEMAJ[1,2], SEBASTIAN CABAN[2], STEFAN SCHWARZ[1,2], (Member, IEEE), AND MARKUS RUPP[2], (Fellow, IEEE)**

[1]Christian Doppler Laboratory for Dependable Wireless Connectivity for the Society in Motion, TU Wien, Vienna 1040, Austria
[2]Institute of Telecommunications, TU Wien, Vienna, Austria

Corresponding author: Stefan Pratschner (stefan.pratschner@tuwien.ac.at)

This work was supported in part by the Christian Doppler Laboratory for Dependable Wireless Connectivity for the Society in Motion, in part by the Austrian Federal Ministry for Digital and Economic Affairs, in part by the National Foundation for Research, Technology, and Development, and in part by the TU Wien University Library through its Open Access Funding Program.

**ABSTRACT** In the area of research on massive multiple-input multiple-output (MIMO), two assumptions on the wireless channel dominate channel modeling. Either, a rich scattering environment is assumed and the channel is modeled as i.i.d. Rayleigh fading, or, a line of sight (LOS) channel is assumed, enabling geometric channel modeling under a farfield assumption. However, either of these assumptions represents an extreme case that is unlikely to be observed in practice. While there is a variety of MIMO channel models in literature, most of them, and even very popular geometry based stochastic channel models, are not spatially consistent. This is especially problematic for technologies in which channel correlation of adjacent users is an important factor, such as massive MIMO. In this work, we introduce a simple but spatially consistent MIMO channel model based on multiple scattering theory. Our proposed channel model allows to adjust the Rician $K$ factor by controlling the number and strength of scattering elements. This allows to perform spatially consistent simulations of wireless communications systems for a large range of scattering environments in between an i.i.d. Rayleigh fading assumption and pure LOS channels. A statistical analysis in terms of the Rician $K$ factor for the introduced model is provided and verified by simulations. By comparison to other channel models, we show that non spatially consistent channel models lead to an underestimation of inter-user correlation and therefore to an overestimation of achievable sum rate.

**INDEX TERMS** Channel models, MIMO communications, massive MIMO.

## I. INTRODUCTION

Massive MIMO promises to attain channel capacity in a multi-user MIMO scenario with simple linear precoding schemes. This optimal performance is attained under asymptotically favorable propagation conditions if the number of antennas at the base station (BS) tends to infinity [1]. The term *favorable propagation conditions* means that channel vectors are mutually orthogonal, that is, that the inter-user interference vanishes [2]. Massive MIMO supports dense scattering environments, that is, i.i.d. Rayleigh fading channels, as well as pure LOS scenarios [3]. While in the former case, channels become asymptotically orthogonal due to the law of large numbers, the latter case allows for the interpretation of forming increasingly sharp beams towards users [4].

For either of those extreme scenarios, simple channel models are at hand. Often, dense scattering environments are modeled by i.i.d. Rayleigh distributed channel coefficients. For pure LOS propagation, without any scattering objects within the propagation environment, channel coefficients are obtained by geometric models assuming planar wavefronts in a far field approximation. While in the former case, users are uncorrelated due to the independent generation of channel coefficients, in the latter case, channel correlation is implicitly given via geometry. Since massive MIMO is considered to be a multi-user MIMO system, the correlation of channels is critical for the communications system's performance [5]. There are several recent works considering the problem of

The associate editor coordinating the review of this article and approving it for publication was Kostas P. Peppas.

separating closely located users [6]–[8]. In order to investigate the impact of spatial correlation of co-located users, spatially consistent channel models are required. The property of spatial consistency in this context means that users in close proximity experience a higher correlation than well separated users on average.

In [9], the authors control the correlation between MIMO channels by varying the number and the angular spread of multi path components (MPCs) but do not employ a spatially consistent channel model. A user's channel correlation matrix is obtained by an exponential correlation model while there is no correlation assumed among users in [10]. Similarly in [11], a correlated MIMO channel is obtained by a matrix based correlation model. In [12], the LOS component is determined by geometry while the inter-user channel correlation matrix is obtained by the Gaussian local scattering model from [4].

Several channel models enable the analysis of MIMO wireless communications systems through link and system level simulations. The most popular models follow a geometric stochastic approach and consider clusters of scattering objects. MPCs within these clusters are then randomly generated according to specific large scale parameters (LSPs). Usually, LSPs are randomly drawn from a given distribution and the MPCs are then generated accordingly. This method is commonly applied within the Wireless World Initiative for New Radio (WINNER) channel models [13], [14], the 3rd Generation Partnership Project (3GPP) spatial channel model [15], [16], the 3GPP 3D channel model [17], [18] and the Quasi Deterministic Radio Channel Generator (QuaDRiGa) channel model [19]. Thereby, these models generate spatially correlated MIMO channels in terms of large scale fading. Even if the LSPs are generated spatially correlated, for example by 2D filtering as proposed in the QuaDRiGa channel model and the 3GPP 3D channel model, the resulting small scale fading is not spatially consistent for different users (users). In [20] and [21], authors put great effort into a modification of the 3GPP 3D model, in order to make it spatially consistent.

A different strategy is to generate a large number of MPCs first, and then to synthesize the LSPs from them. This method is adopted within the European Cooperation in Science and Technology (COST) 2100 channel model by introducing the concept of visibility regions for clusters [22]. The concept of visibility regions enables spatially consistent modeling of fading. However, this approach requires a proper choice of link cluster commonness in order to obtain a consistent model with multiple links [22]. In [23], for example, authors propose to augment the concept of visibility regions in the context of massive MIMO. As the COST 2100 channel model aims to reassemble specific scenarios that were observed in measurements, the set of supported scenarios is limited and the model does not allow to adjust the Rician $K$ factor. For example, the implementation available in [24] offers an indoor hall scenario at 5 GHz and a semi-urban scenario at 300 MHz.

We propose a channel model that overcomes spatial consistency issues of stochastic geometric channel models, by considering geometric positions of scattering objects. This way, the introduced channel model becomes inherently spatially consistent. While this approach leads to a channel model that is spatially consistent on a large scale and on a small scale, we focus on small scale fading effects in our contribution. To develop an analytic statistical description of the channel model, based on positions of scattering objects distributed in space, we consider multiple scattering theory. This theory follows the simple idea that a radiated electromagnetic wave is re-radiated by each scattering element. We do not aim to restrict our model to certain specific scenarios but maintain flexibility to choose the density of the scattering environment to adjust the Rician $K$ factor.

Multiple scattering theory was first employed in [25] and [26] to describe radio wave propagation through a random scattering environment. An extensive statistical analysis of multiple scattering propagation is provided in [27]. Based on this idea, a channel model based on stochastic propagation graphs is introduced in [28] and [29]. In these works, the authors consider multiple scattering events and derive closed form solutions for the case of an infinite number of scattering events [30].

### A. CONTRIBUTION

We adopt the idea of multiple scattering theory from [25]. We assume a discrete set of scattering elements with isotropic re-radiation of electromagnetic waves. We furthermore consider a single scattering event for non-line of sight (NLOS) paths. By explicitly assigning spatial positions to scattering elements, transmit antennas and receive antennas, we obtain a spatially consistent MIMO channel model. The proposed channel model allows for adjustment of the Rician $K$ factor, which enables investigation of wireless channels in between an i.i.d. Rayleigh fading channel and a pure LOS channel. We provide an analytic statistical analysis of our model in terms of the Rician $K$ factor and verify the analysis by simulations. We show that non spatially consistent channel models overestimate the achievable sum rate as they underestimate the inter-user interference compared to the proposed spatially consistent model. As the complexity of the model scales only linearly with the number of antennas, the model is especially suited for simulation of massive MIMO systems with a large number of antennas.

### B. NOTATION

We denote vectors by lowercase boldface symbols, such as $\mathbf{x}$, and matrices by uppercase boldface symbols, such as $\mathbf{X}$. The entry from the $n^{\text{th}}$ row and the $k^{\text{th}}$ column of matrix $\mathbf{X}$ is denoted by $[\mathbf{X}]_{n,k}$. We denote the Euclidean norm of vectors by $\|\cdot\|$ and the Frobenius norm by $\|\cdot\|_{\text{F}}$. The absolute value of a scalar as well as the cardinality of a set are denoted by $|\cdot|$. The transpose of a vector or matrix is denoted by $(\cdot)^{\text{T}}$ while the conjugate transpose of a vector or matrix is denoted by $(\cdot)^{\text{H}}$. The expectation of a random variable $X$ is denoted

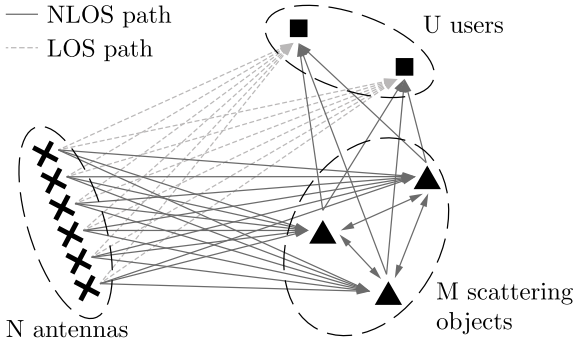


**FIGURE 1.** Nodes and propagation paths within the multiple scattering channel model. For this illustration, we chose $N = 6$, $M = 3$ and $U = 2$.

by $\mathbb{E}\{X\}$ while the variance of $X$ is denoted by $\mathrm{var}\{X\}$. The trace of a matrix is denoted by $\mathrm{tr}(\cdot)$.

## II. SPATIALLY CONSISTENT MIMO CHANNEL MODEL

In order to obtain a spatially consistent channel model, we consider a discrete set of scattering elements in free space. Assuming that a scattering event is described by an isotropic re-radiation of a wave corresponds to the idea of multiple scattering theory from [25] with an isotropic scattering kernel. As a simplification, we further assume that a scattering object cannot block propagation of electromagnetic waves. In line with this simplification, there is no self-scattering. This means that a scattering element re-radiates only a single wave rather than multiple ones. Applying a narrow band assumption, multiple rays that are scattered by a single scattering element cannot be distinguished. We cluster multiple scattered waves originating from one (or more than one) scattering element(s) and model them by a single scattering event. The cluster size is expressed via a clustering factor, describing the strength of the modeled scattering event. Therefore, a scattering element within the channel model may correspond to multiple scattering objects or scattered waves in a real-world scenario. The most important step to obtain a spatially consistent MIMO channel model is that each (transmit or receive) antenna, as well as each scattering object has an explicit location. While we employ a two dimensional space for all positions in this contribution, the proposed model is readily extended into three dimensions.

A complete statistical analysis of multiple scattering channel models is provided in [27]. There, the authors show that an $L$ Rayleigh distribution, being the distribution of a product of $L$ independent Rayleigh variables, is obtained for NLOS propagation with $L$ scattering events. Since this distribution is only obtained in few special cases, as also shown in [27], we assume MPCs with a single bounce to be dominant and consider only a single scattering event in this work.

We assume $N$ transmit antennas at positions $\mathbf{r}_n$ with $n \in \mathcal{T}$, where $\mathcal{T}$ denotes the set of transmit antenna indices with $|\mathcal{T}| = N$. There are $U$ users with single antennas at positions $\mathbf{r}_u$ with $u \in \mathcal{R}$, where $\mathcal{R}$ denotes the set of user indices with $|\mathcal{R}| = U$. One may also interpret $U$ as the number of receive antennas of a single user instead of a number of users with single antennas or any combination thereof. Further, we assume a discrete set of $M$ scattering objects, located at positions $\mathbf{r}_p$ with $p \in \mathcal{S}$, where $\mathcal{S}$ denotes the set of scattering object indices with $|\mathcal{S}| = M$. The sets of node indices are unique in the sense that each index belongs to exactly one set, that is, $\mathcal{T} \cap \mathcal{R} = \mathcal{T} \cap \mathcal{S} = \mathcal{R} \cap \mathcal{S} = \emptyset$.

The channel is described by a MIMO channel matrix $\mathbf{H} \in \mathbb{C}^{U \times N}$ from $N$ transmit antennas to $U$ receive antennas or users, with transmit antenna $n \in \mathcal{T}$ at position $\mathbf{r}_n$ and receive antenna $u \in \mathcal{R}$ at position $\mathbf{r}_u$. The channel coefficient from transmit antenna $n$ to receive antenna $u$ is given by

$$[\mathbf{H}]_{u,n} = \alpha_{u,n} + \sum_{p \in \mathcal{S}} \beta_{u,p} \alpha_{p,n} \,, \tag{1}$$

where $\alpha_{u,n}$ describes propagation without any scattering, that is, the LOS path, and the sum term describes all propagation paths that include a scattering event.

We obtain the path coefficients $\alpha$ and $\beta$ via simple wave propagation mechanisms assuming free space in between scattering objects. The path coefficients are given by

$$\alpha_{k,j} = \frac{\lambda}{4\pi \|\mathbf{r}_k - \mathbf{r}_j\|} e^{i\frac{2\pi}{\lambda}\|\mathbf{r}_k - \mathbf{r}_j\|} \,, \tag{2a}$$

$$\beta_{k,j} = \frac{\delta_j}{\sqrt{4\pi}\,\|\mathbf{r}_k - \mathbf{r}_j\|} e^{i\frac{2\pi}{\lambda}\|\mathbf{r}_k - \mathbf{r}_j\|} \,. \tag{2b}$$

Here, the coefficient $\alpha_{k,j}$ describes free space propagation from node $j$ to node $k$. Coefficient $\beta_{k,j}$ describes the propagation from node $j$ to node $k$, including a scattering event at node $j$ (a scattering element) with the scattering coefficient $\delta_j$. A scattering event at scattering object $j$ is described by the complex valued scattering coefficient $\delta_j = \gamma_j e^{\phi_j}$ with the random phase $\phi_j \sim \mathcal{U}[0, 2\pi)$ and the clustering factor $\gamma_j = |\delta_j|$. The scattering phase is randomly drawn once per channel realization, in order to obtain a spatially consistent phase between transmitters and receivers. The clustering factor represents the strength of the scattering event and, therefore, reflects the physical size of the scattering object. We assume a fixed deterministic clustering factor in the sequel, that is $\gamma_j = \gamma, \forall j \in \mathcal{S}$. A detailed derivation of the path factors is provided in Appendix A.

Due to the presented choice of factors, the channel model, consisting of (1) and (2), includes path loss as well as small scale fading. However, we focus on spatial consistency of small scale fading in our contribution and do not apply a large scale fading model on top of free space LOS propagation. The number of transmit antennas, receive antennas and scattering objects is arbitrary and only limited by computational complexity. As the position of transmitters and receivers is free to choose, the introduced model is capable of modeling multi-user MIMO systems in a spatially consistent way with large arrays as well as distributed antenna systems.

The computation time to obtain channel coefficients according to the proposed channel model may be split into two parts. First, the generation of random positions for users

and scattering objects and second, the calculation of all channel coefficients according to (1) and (2). The asymptotic complexity for the generation of random positions scales linearly with the number of users and the number of scattering elements. Therefore, the asymptotic computational complexity of the first task is $\mathcal{O}(U) + \mathcal{O}(M)$. Computing all channel coefficients, that is the complexity of the second task, asymptotically scales with the number of scattering elements $M$. Since the channel coefficients have to be calculated for each combination of transmit antenna and receive antenna (or user), the asymptotic complexity is $\mathcal{O}(NUM)$, that is, linear in the number of transmit antennas, number of users and number of scattering objects. Therefore, the overall computational complexity of the proposed channel model is dominated by the latter part of calculating all channel coefficients.

## III. STATISTICAL ANALYSIS

In this section, we investigate the distribution of channel coefficients for the proposed model and finally provide an expression for the $K$ factor, depending on the number of scattering objects $M$ and the clustering factor $\gamma$. Please note that although we define the $K$ factor analogously to the Rician $K$ factor, we do not make any assumption on the distribution of channel coefficients for the analysis provided in this section. We focus on the case of a fixed clustering factor $\gamma$ in this work.

Inserting the scattering coefficients (2) and $\delta_p = \gamma e^{i\phi_p}$ into the model (1), we obtain

$$[\mathbf{H}]_{u,n} = \frac{\lambda}{4\pi \|\mathbf{r}_u - \mathbf{r}_n\|} e^{i\frac{2\pi}{\lambda}\|\mathbf{r}_u - \mathbf{r}_n\|} + \frac{\lambda\gamma}{(4\pi)^{\frac{3}{2}}} \sum_{p\in\mathcal{S}} u(\mathbf{r}_p), \quad (3)$$

with the sum term

$$u(\mathbf{r}_p) = \left(\|\mathbf{r}_u - \mathbf{r}_p\|\|\mathbf{r}_p - \mathbf{r}_n\|\right)^{-1} \times e^{i\left(\phi_p + \frac{2\pi}{\lambda}\left(\|\mathbf{r}_u - \mathbf{r}_p\| + \|\mathbf{r}_p - \mathbf{r}_n\|\right)\right)} . \quad (4)$$

From this relation, we observe that the BS, user and scattering object placement, that is, the scenario geometry, determines the channel statistics. The behavior of the sum in (3) is determined by the range of possible values of its sum terms (4). The absolute value of the sum term (4), depends on the BS-to-scattering object and the scattering object-to-user distances. Given a certain number of scattering objects, this sum might be dominated by a single value of large magnitude. This corresponds to the situation of a scattering object that is closely located to a transmit antenna or receive antenna. To bound the sum term's absolute value, we consider a minimum distance $d_S > 0$ between any transmit and any receive antenna to any scattering object, that is

$$\|\mathbf{r}_k - \mathbf{r}_m\| \geq d_S \quad \forall k \in \mathcal{T} \cup \mathcal{R}, \ \forall m \in \mathcal{S} . \quad (5)$$

This condition is straight forward to fulfill in any simulation scenario, by introducing an empty region with radius $d_S$ around all BS and user antennas in which no scattering object is placed. The condition (5) guarantees the existance and boundedness of (3). Bounds on the magnitude of (4) are discussed in more detail in Appendix B.

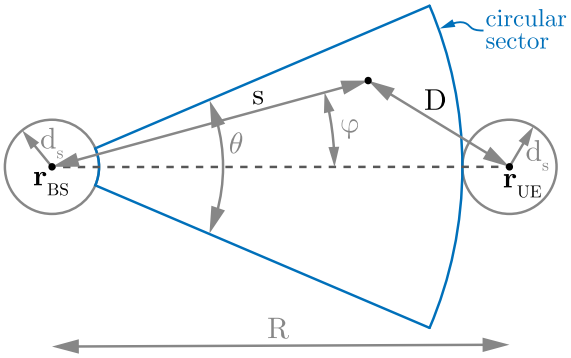


**FIGURE 2.** Circular sector geometry considered for calculation of the channel coefficient variance.

### A. PHASE DISTRIBUTION OF SUM TERMS

To investigate the phase of the sum terms $u(\mathbf{r}_p)$, we introduce the following lemma.

*Lemma 1 (Distribution of Modulo Sum):* Let $X$ be a random variable, uniformly distributed in the interval $[0, a)$ with $a > 0$ and $Y$ be a random variable independent of $X$. Then, $(X + Y) \bmod a$ is again uniformly distributed in $[0, a)$, independent of the distribution of $Y$.

Defining the argument of a complex number $z \in \mathbb{C}$ as $\text{Arg}\left(|z|e^{i\phi}\right) = \phi \bmod 2\pi$, the phase of the sum terms is given by

$$\text{Arg}\left(u(\mathbf{r}_p)\right) = \phi_p + \frac{2\pi}{\lambda}\left(\|\mathbf{r}_u - \mathbf{r}_p\| + \|\mathbf{r}_p - \mathbf{r}_n\|\right) \bmod 2\pi. \quad (6)$$

As the scattering phase $\phi_p$ is uniformly distributed within $[0, 2\pi)$ and independent of the scattering object and user placement, invoking Lemma 1 we obtain

$$\text{Arg}\left(u(\mathbf{r}_p)\right) \sim \mathcal{U}[0, 2\pi) . \quad (7)$$

Therefore, the sum term has a uniformly distributed phase, independent of the scattering object placement and scenario geometry.

### B. VARIANCE OF SUM TERMS

In order to find an expression for the Rician $K$ factor for the proposed channel model, the variance of the sum terms $u(\mathbf{r}_p)$ is required. As shown in the previous section, the phase of $u(\mathbf{r}_p)$ is uniformly distributed, if the scattering phase is uniformly distributed within $[0, 2\pi)$. Further, the magnitude distribution and the phase distribution of $u(\mathbf{r}_p)$ are independent. Therefore, $u(\mathbf{r}_p)$ is complex circularly distributed around zero and therefore has zero mean, that is, $\mathbb{E}\left\{u(\mathbf{r}_p)\right\} = 0$.

To find an expression for the variance $\omega^2 = \text{var}\left\{u(\mathbf{r}_p)\right\}$, we consider the geometry shown in Fig. 2. Here, we assume that the user is located at the middle of the sector, that is, at an angle of $\varphi = 0$. When considering a distribution of users with

a random angle, this is an approximation assuming that the maximum user angle is smaller than the sector angle.

Considering (4) in terms of the geometry shown in Fig. 2, we identify the transmitter-to-scattering object distance $\|\mathbf{r}_p - \mathbf{r}_n\|$ to be $s$ and the scattering object-to-receiver distance $\|\mathbf{r}_u - \mathbf{r}_p\|$ to be $D$.

We consider a random variable transformation to obtain an expression for the variance $\omega^2$. A two dimensional uniform distribution of scattering object positions within the circular sector is equivalent to a uniform distribution of the angle $\varphi$ and a triangular distribution of the distance to the BS $s$. Their probability density functions (PDFs) are given by

$$f_\varphi(\varphi) = \begin{cases} \frac{1}{\theta} & \text{for } -\frac{\theta}{2} \le \varphi \le \frac{\theta}{2} \\ 0 & \text{otherwise} \end{cases}, \tag{8}$$

and

$$f_s(s) = \begin{cases} \frac{2}{s_{\max}^2 - s_{\min}^2} s & \text{for } s_{\min} \le s \le s_{\max} \\ 0 & \text{otherwise} \end{cases}, \tag{9}$$

where the minimum value of $s$ is given by $s_{\min} = d_S$ and the maximum value of $s$ is given by $s_{\max} = R - d_S$. Since $\varphi$ and $s$ are independent, their joint PDF is given by $f_{s,\varphi}(s, \varphi) = f_s(s) f_\varphi(\varphi)$. Considering a scattering object location with distance $s$ from the transmitter at angle $\varphi$ and distance $D$ to the receiver and applying the law of cosines, a random variable transform of the form

$$|u|^2 = Y = g(s, \varphi) = \left(s^2 \left(R^2 + s^2 - 2Rs\cos(\varphi)\right)\right)^{-1} \tag{10}$$

is performed. Applying the random variable transform to calculate the variance of $u$, we obtain

$$\begin{aligned} \omega^2 &= \operatorname{var}\{u\} = \mathbb{E}\left\{|u|^2\right\} = \mathbb{E}\{Y\} \\ &= \int Y f_Y(Y) dY \\ &= \int_{-\frac{\theta}{2}}^{\frac{\theta}{2}} \int_{s_{\min}}^{s_{\max}} g(s, \varphi) f_{s,\varphi}(s, \varphi)\, ds\, d\varphi \\ &= \frac{8}{\theta\left(s_{\max}^2 - s_{\min}^2\right)} \\ &\quad \times \int_{s_{\min}}^{s_{\max}} \frac{1}{s(R-s)} \arctan\left(\frac{R+s}{R-s} \tan\left(\frac{\theta}{4}\right)\right) ds, \end{aligned} \tag{11}$$

where $\mathbb{E}\{u(\mathbf{r})\} = 0$ was employed.

### C. K FACTOR ANALYSIS

Assuming random and independent user positions as well as random and independent scattering object positions, the sum terms (4) from (3) have zero mean and are independent. Invoking the central limit theorem, the sum is approximately Gaussian distributed as long as $M$ is sufficiently large. We denote the resulting complex symmetric Gaussian random variable by $X$ and can therefore approximate the channel coefficient as

$$[\mathbf{H}]_{u,n} \approx \left[\widetilde{\mathbf{H}}\right]_{u,n} = \alpha_{u,n} + \frac{\lambda\gamma}{(4\pi)^{\frac{3}{2}}} X, \tag{12}$$

where $X \sim \mathcal{CN}\left(0, M\omega^2\right)$. Assuming a fixed but arbitrary position $\mathbf{r}_u$, corresponding to the BS antenna position, without loss of generality, $\alpha_{u,n}$ is deterministic for a given user to BS distance $R = \|\mathbf{r}_u - \mathbf{r}_n\|$, even if the user's antenna position $\mathbf{r}_n$ is random. Therefore, the approximated channel coefficients are distributed as $\left[\widetilde{\mathbf{H}}\right]_{u,n} \sim \mathcal{CN}\left(\alpha_{u,n}, M(\omega\gamma)^2 \frac{\lambda^2}{(4\pi)^3}\right)$. While the number of scattering elements $M$ required for a good approximation (12) depends on the minimum distance $d_S$, a few tens of scattering objects already lead to a good approximation for a few meters of $d_S$.

Let us consider the $K$ factor of the absolute value of the channel coefficients $\left|\left[\widetilde{\mathbf{H}}\right]_{u,n}\right|$ as the ratio of power in the specular (LOS) component to the power of the MPCs

$$K = \frac{|\nu|^2}{\sigma^2}, \tag{13}$$

analogous to the notion of a Rician $K$ factor. Here, $\nu = \mathbb{E}\left\{\left[\widetilde{\mathbf{H}}\right]_{u,n}\right\}$ is the mean, contributed through the LOS component, and $\sigma^2 = \operatorname{var}\left\{\left[\widetilde{\mathbf{H}}\right]_{u,n}\right\}$ is the variance .

Considering (12) we find

$$|\nu|^2 = |\alpha_{u,n}|^2 = \left(\frac{\lambda}{4\pi R}\right)^2, \tag{14}$$

$$\sigma^2 = M(\gamma\omega)^2 \frac{\lambda^2}{(4\pi)^3}, \tag{15}$$

which leads to a $K$ factor of

$$K = \frac{4\pi}{M(\gamma\omega R)^2}. \tag{16}$$

While it is not surprising that the $K$ factor depends on the user to BS distance via Friis' formula, (16) further reveals the dependence upon the number of scattering objects $M$ and the clustering factor $\gamma$. It is intuitive that the $K$ factor decreases with an increasing number of scattering objects as well as with an increasing clustering factor, as this renders scattered paths dominant compared to the LOS path. While the clustering factor $\gamma$ is a constant factor within the sum terms $u(\mathbf{r}_p)$, and therefore appears squared in their variance, the factor $\omega^2$ is dependent on the scenario geometry. As previously mentioned, the variance is increased for small antenna to scattering object and inter-scattering object distances $d_S$.

## IV. SIMULATION RESULTS

In this section we present and discuss simulation results obtained with the proposed channel model. Firstly, we demonstrate that the statistical model analysis from Section III is correct and the introduced approximation is valid. Secondly, to verify the introduced model, we compare simulation results in terms of spatial correlation to a simple *Rice* channel model and the 3GPP 3D channel model from [17]. The simulation scenario employed for the proposed channel model is as shown in Fig. 3. The scattering objects are uniformly distributed within a circular sector of 120° with an inner radius of 10 m and an outer radius of 50 m. The users have a single antenna each and are placed

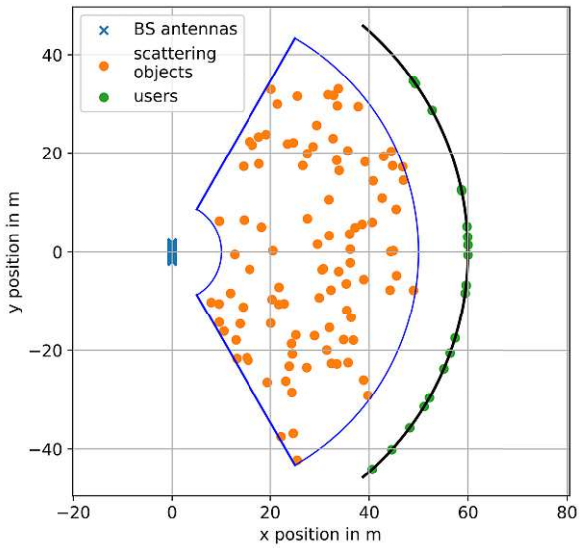


**FIGURE 3.** Simulation scenario geometry. The circular sector is outlined in blue. Possible user positions are indicated in black. User positions and scattering object positions in this figure are taken form a single realization. For the purpose of illustration we chose $M = 100$ scattering objects, $N = 64$ transmit antennas and $U = 20$ users.

at a constant distance of 60 m from the BS with a uniformly distributed polar angle of $[-50, 50]$ degrees. With this setup, a minimum distance between users and scattering objects as well as between BSs and scattering objects is automatically ensured. The BS is equipped with a uniform linear array (ULA) of $N = 64$ antennas along the y-axis with the array center at the origin. The elements of the ULA are spaced by $\lambda/2$ at a carrier frequency of 2.5 GHz. All antenna elements, user antennas and BS antennas, are omnidirectional.

### A. AMPLITUDE DISTRIBUTION

In order to verify the statistical description of the proposed channel model in terms of a $K$ factor, we perform simulations of channel amplitude distributions in this section. Simulations with 1 000 random realizations of user positions and scattering object positions are performed. We employ $M = 800$ scattering objects within the previously described simulation scenario. Results in terms of cumulative distribution functions of the channel coefficient magnitude are shown in Fig. 4 for different clustering factors $\gamma$. For this simulation result, the mean channel power was normalized to one. The maximum likelihood (ML) distribution fits for a Rice as well as for a Nakagami-$m$ distribution are provided. For the Rice distribution, the Rician $K$ factor $\hat{K}_{\mathrm{ML}}$ is obtained by ML estimation and for the Nakagami-$m$ distribution the shape factor $\hat{m}_{\mathrm{ML}}$ is ML estimated. The corresponding values for both parameters are provided in Fig. 4 as well. Both distributions, the Rician and the Nakagami-$m$, show a good match with the simulation data.

A Rician fading amplitude distribution of channel coefficients is obtained by assuming the presence of one

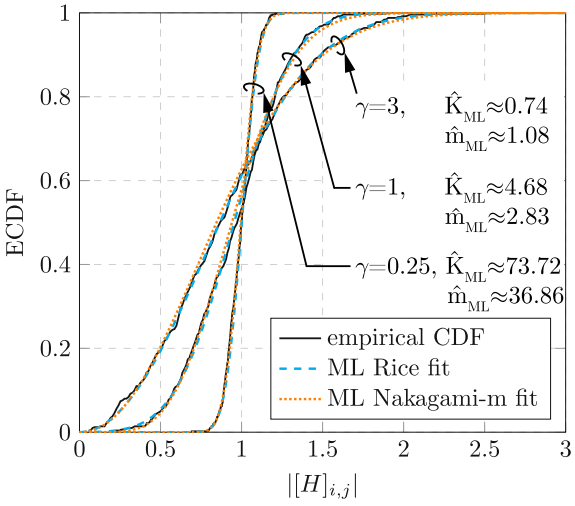


**FIGURE 4.** ML fit of Rice distribution to simulated channel coefficient's magnitude with $M = 800$ scattering objects.

specular component and many diffuse multipath components. A Nakagami-$m$ distribution [31] of amplitudes is obtained through maximum ratio combining of $m$ Rayleigh fading channel coefficients. While a Nakagami-$m$ distribution with $m = 1$ is equivalent to a Rayleigh distribution, a Rician distribution is approximated by the Nakagami-$m$ distribution when choosing the shape parameter according to [31]

$$m = \frac{(K+1)^2}{2K+1}. \tag{17}$$

Please note that the Rician $K$ factor and the Nakagami-$m$ shape parameter $m$ provided in Fig. 4, which are obtained independently by ML estimation, approximately fulfill relation (17).

From the results shown in Fig. 4 we observe that both, the Rician and the Nakagami-$m$ distribution, provide a good fit with the data obtained by simulation. Therefore, the statical analysis provided in Section III can also be performed in terms of the Nakagami-$m$ shape parameter

$$m = \frac{\left(\mathbb{E}\left\{\left|[\widetilde{\mathbf{H}}]_{u,n}\right|^2\right\}\right)^2}{\mathrm{var}\left\{\left|[\widetilde{\mathbf{H}}]_{u,n}\right|^2\right\}}. \tag{18}$$

However, due to the geometric interpretability of Rician fading, which suites our channel model very well, we performed the statistical description in terms of a $K$ factor in Section III. Since the amplitude distribution obtained through simulation fits a Rician one, we indeed identify the introduced $K$ factor to be the Rician $K$ factor.

Employing the same simulation setup, the derived relation for the Rician $K$ factor (16) is verified. Given the geometry, the variance $\omega^2$ is calculated through (11). Simulation results for $K$ over the number of scattering objects $M$ are shown in Fig. 5. Again, 1 000 random realizations were performed. In both cases, the calculated Rician $K$ factor is compared to its

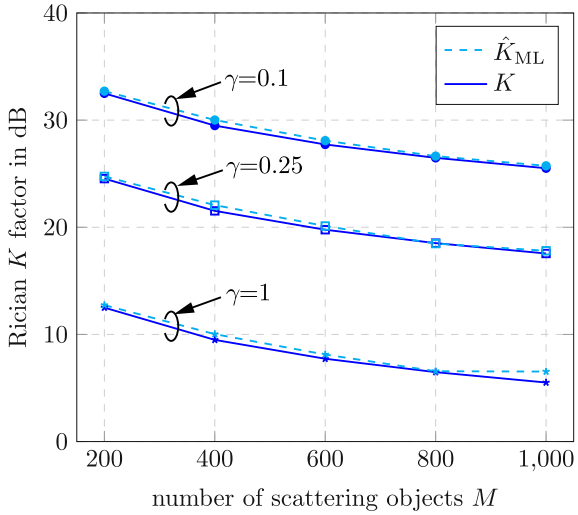


**FIGURE 5.** Comparison of the analytically predicted Rician *K* factor *K* and the ML estimated Rician *K* factor $\hat{K}_{\mathrm{ML}}$.

ML estimate, which is denoted by $\hat{K}_{\mathrm{ML}}$. Please recall that (11) is obtained as an approximation, where we assume to user to be located at the middle of the sector, that is, at $\varphi = 0$. Although simulations performed here employ a uniform user distribution within $[-50°, 50°]$, the predicted $K$ factor and the ML estimated $K$ factor show a good fit. This shows the validity of the approximation within the derivation of (16).

### B. SPATIAL CONSISTENCY

To demonstrate the key feature of our proposed channel model, which is spatial consistency, we perform simulations with the same sector geometry as shown in Fig. 3. To investigate the spatial correlation, we again consider a random placement of scattering objects but a deterministic placement of $U = 2$ users. While both users are at distance $R = 60\,\mathrm{m}$ from the BS, the first user is placed at an angle of $\varphi/2$ and the second user is placed at an angle of $-\varphi/2$, relative to the array broadside direction. In this setup, the MIMO channel matrix consists of the users' channel vectors $\mathbf{h}_u \in \mathbb{C}^{N\times 1}$ containing channel coefficients from $N$ antennas to user $u$, i.e., $\mathbf{H} = (\mathbf{h}_1, \mathbf{h}_2)^{\mathrm{T}}$.

As a comparison, we consider a *Rice* MIMO channel model of the form

$$\mathbf{H}_{\mathrm{Rice}} = \sqrt{\frac{K}{1+K}}\mathbf{H}_{\mathrm{LOS}} + \sqrt{\frac{1}{1+K}}\mathbf{H}_{\mathrm{iid}} \in \mathbb{C}^{U\times N} . \quad (19)$$

The i.i.d. Rayleigh fading channel matrix $\mathbf{H}_{\mathrm{iid}}$ contains Gaussian distributed channel coefficients, that is, $[\mathbf{H}_{\mathrm{iid}}]_{u,n} \sim \mathcal{CN}(0, 1)$. The columns of $\mathbf{H}_{\mathrm{LOS}}$ are given by the LOS far field channel vectors to all users. Assuming a ULA with antenna spacing $d$, the LOS channel vector for user $u$ is given by

$$\mathbf{h}_{\mathrm{LOS},u} = \left(e^{-i\frac{N}{2}\frac{2\pi}{\lambda}d\sin(\varphi_u)}, \ldots, e^{i\frac{N}{2}\frac{2\pi}{\lambda}d\sin(\varphi_u)}\right)^{\mathrm{T}} , \quad (20)$$

where $\varphi_u$ is the angular position of user $u$.

As a metric for spatial correlation of users' channel vectors, we consider the normalized inner product

$$\rho(\varphi) = \mathbb{E}\left\{\frac{|\mathbf{h}_1^{\mathrm{H}}\mathbf{h}_2|}{\|\mathbf{h}_1\|\|\mathbf{h}_2\|}\right\} , \quad (21)$$

similar as done in [32]. Considering maximum ratio transmission precoding in the case of two users, $\rho^2$ is the inter-user interference power. For two identical channel vectors $\rho = 1$, while two orthogonal channel vectors yield $\rho = 0$. We identify two criterions in terms of the spatial correlation metric $\rho(\varphi)$ for a spatially consistent channel model:

1) Users at the same position must experience the same channel and therefore a correlation of one:

$$\rho(0) = 1 . \quad (22a)$$

2) For a bounded variation in position $\varphi$, the change in correlation must be bounded as well, that is, the correlation function must be Lipschitz continuous:

$$\rho(\varphi_1) - \rho(\varphi_2) \leq L\,(\varphi_1 - \varphi_2) , \quad (22b)$$

for a Lipschitz constant $L \geq 0$ and two arbitrary user positions $\varphi_1, \varphi_2 \in [0, 2\pi)$.

Simulation results in terms of $\rho(\varphi)$ over the angle between the two users $\varphi$ are shown in Fig. 6. While results shown in Fig. 6a and Fig. 6b are obtained with the same parameters, the latter is considered as a detail view of the former with respect to small angles between users. Results for the normalized inner product $\rho$ are provided for four different Rician $K$ factors of $K = -6\,\mathrm{dB}, 0\,\mathrm{dB}, 6\,\mathrm{dB}, 17\,\mathrm{dB}$ for the proposed channel model and the *Rice* channel model. For our proposed channel model, these $K$ factor values are obtained with $M = 800$ scattering objects and clustering factors of $\gamma \approx 4.24, 2.14, 1.08, 0.28$. The two extreme cases, a pure *LOS* channel, that is, $K \to \infty$, and an i.i.d. Rayleigh fading channel, that is $K \to 0$, are provided as a reference.

From Fig. 6a we observe that the pure LOS channel and the proposed channel model are spatially consistent, as they fulfill criterion (22a). The proposed channel model achieves a very good fit with the *Rice* channel model (19) of the same Rician $K$ factor, except for the region around $\varphi = 0$. To investigate this region of small inter-user angles further, Fig. 6b is provided. Here, we observe that the spatial correlation of the proposed channel model is indeed spatially consistent, as its smooth behavior also fulfills criterion (22b).

All other compared channel models are not spatially consistent as they violate criterion (22a). Since we generate the i.i.d. Rayleigh fading channel by drawing channel coefficients from a complex Gaussian distribution without any dependence on the user position, two users at the same position experience different channels. However, even if the generation of channel coefficients was changed, such that two users at the same position are assigned identical channel coefficients, still does not render the channel model spatially consistent. While this leads to $\rho(0) = 1$ and therefore fulfills

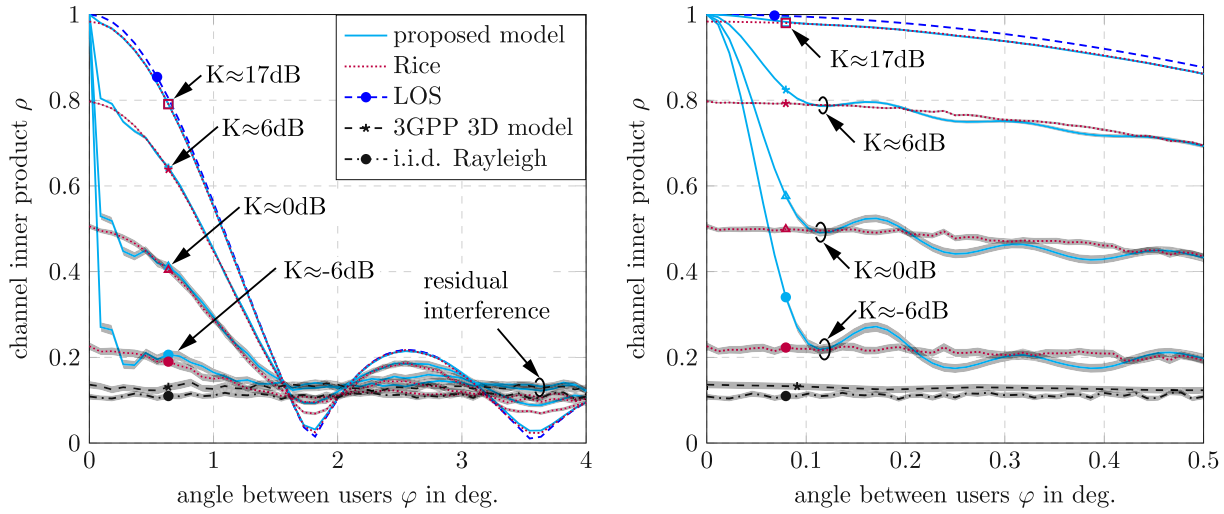


(a) Wide angular range. (b) Narrow angular range.

**FIGURE 6.** Normalized inner product over inter-user distance for (a) a wide angular range and (b) a narrow angular range. The proposed channel model as well as the pure LOS channel are spatially consistent. The 95% confidence regions obtained by bootstrapping are highlighted in gray.

the first criterion, this alternate generation of channel coefficients leads to a violation of criterion (22b) as the correlation suddenly drops for user distances larger than zero.

As a comparison, the spatial correlation obtained with the 3GPP 3D channel model with the same scenario geometry as previously described is also provided in Fig. 6. For this channel model, we assume an urban micro cell scenario with 12 clusters and 20 rays per cluster. To obtain a fair comparison, we exclude shadow fading effects of the 3GPP 3D channel model for our simulation. Since the small scale fading within this channel model is generated uncorrelated for different users, the obtained spatial correlation shows no spatial consistency.

Another important observation from these simulation results is the *residual interference* at comparably high inter-user angles, as indicated in Fig. 6a. The spatial correlation remains higher than the one obtained with an i.i.d. Rayleigh fading assumption, even for high values of $\varphi$. This residual correlation originates from the location of scattering objects on only one side of the user. The i.i.d. Rayleigh fading case is attained with a spatial channel model only, if there is a ring of scattering elements placed around the user. Although we assume a pure NLOS channel for the 3GPP 3D channel model, the spatial correlation is also higher than the i.i.d. Rayleigh fading channel. This again stresses that the i.i.d. Rayleigh fading assumption is only achieved by artificial scenario geometries with spatial channel models.

### C. ACHIEVABLE SPECTRAL EFFICIENCY

In this section we consider the effects of spatial consistency on the achievable rate of a massive MIMO communications system. We consider a multi-user MIMO downlink system. The vector of received signals for $U$ users is given by

$$\mathbf{y} = \mathbf{H}^{\mathrm{H}}\mathbf{F}\mathbf{x} + \mathbf{w} \in \mathbb{C}^{U\times 1}\,, \tag{23}$$

where $\mathbf{x} \in \mathbb{C}^{U\times 1}$ is the vector of random transmit symbols, $\mathbf{F}$ is the precoding matrix and $\mathbf{w}$ is additive white Gaussian noise, that is, $\mathbf{w} \sim \mathcal{CN}\left(\mathbf{0}, \sigma_w^2\mathbf{I}_U\right)$. We employ independent transmit symbols of unit power, that is, $\mathbb{E}\left\{\mathbf{x}\mathbf{x}^{\mathrm{H}}\right\} = \mathbf{I}_U$. The channel matrix $\mathbf{H}$ is given by $\mathbf{H} = (\mathbf{h}_1, \ldots, \mathbf{h}_U)$, where column vectors are the channel vectors for each user. A user's channel vector is given by $\mathbf{h}_k = \sqrt{\eta_k}\tilde{\mathbf{h}}_k$ for $k \in \{1, \ldots, U\}$ where $\eta_k > 0$ denotes the large scale fading coefficient of user $k$ and $\tilde{\mathbf{h}}_k$ describes the small scale fading with $\left\|\tilde{\mathbf{h}}_k\right\| = 1\ \forall k$. Since the transmit symbols are of unit power, a sum power constraint of the form $\mathbb{E}\left\{\|\mathbf{F}\mathbf{x}\|_2^2\right\} \leq P_T$ leads to the requirement $\|\mathbf{F}\|_{\mathrm{F}}^2 \leq P_T$. We consider a zero forcing (ZF) precoder given by

$$\mathbf{F}_{\mathrm{ZF}} = \frac{\sqrt{P_T}}{\sqrt{\mathrm{tr}\left(\left(\mathbf{H}^{\mathrm{H}}\mathbf{H}\right)^{-1}\right)}}\,\mathbf{H}\left(\mathbf{H}^{\mathrm{H}}\mathbf{H}\right)^{-1}\,, \tag{24}$$

fulfilling the power constraint. Therefore, the signal to noise ratio (SNR) of user $k$ is

$$\mathrm{SNR}_k = \frac{P_T}{\sigma_w^2\,\mathrm{tr}\left(\left(\mathbf{H}^{\mathrm{H}}\mathbf{H}\right)^{-1}\right)}\,. \tag{25}$$

The achievable downlink sum spectral efficiency (SE) is obtained as

$$R_{\mathrm{sum}} = \sum_{k=1}^{U}\log_2\left(1+\mathrm{SNR}_k\right)\,. \tag{26}$$

Again, we perform simulations with a scenario geometry as shown in Fig. 3 and previously described in Section IV.

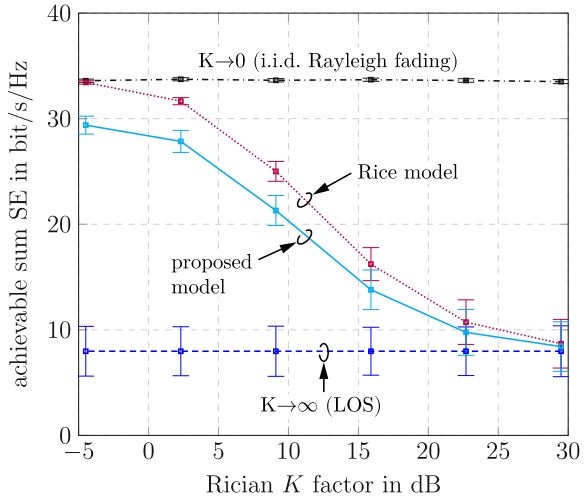


**FIGURE 7.** **Achievable sum SE with ZF precoding with 95% confidence intervals obtained by bootstrapping.**

We assume a downlink transmission to $U = 20$ users, which are placed at a distance of $R = 60$ m with uniformly distributed angles $\varphi_u$ within $[-50°, 50°]$. For a typical massive MIMO downlink scenario, we choose $\sigma_w^2 = 1$ and $P_T = 1/\eta$ to obtain an SNR of 0 dB in the interference free case. Please note that we assume $\eta_k = \eta \; \forall k$, which is automatically achieved in our simulation scenario due to the user placement. Simulation results for the achievable downlink sum SE over the Rician $K$ factor are shown in Fig. 7.

Together with the results for the *Rice* channel model according to (19) and the proposed channel model, we provide bounds for $K \to \infty$ (LOS) and $K \to 0$ (i.i.d. Rayleigh fading). Due to the ZF precoding, the achievable rate is significantly higher for an i.i.d. Rayleigh fading channel compared to the LOS channel assumption. This shows that there is a significant amount of inter-user correlation in the LOS case, since the randomly distributed users cannot be separated with the $N = 64$ antenna ULA. Therefore, a significant loss in signal power is experienced with ZF precoding in the high $K$ factor regime.

Necessarily, through the definition of the *Rice* channel model, its achievable rate converges to the same rate as the i.i.d. Rayleigh fading channel model for low $K$ factors and to the same rate as the LOS channel for high $K$ factors. While the proposed channel model has a similar trend over the Rician $K$ factor, it shows a gap to the *Rice* channel model for low $K$ factors. This behavior shows the importance of spatial consistency for multi-user MIMO applications. As explained in Section IV-B, the proposed model yields high correlation for very closely spaced users, c.f., Fig. 6, as well as correlation that is higher compared to the i.i.d. Rayleigh fading assumption also at larger inter-user distances. Although the difference in spatial correlation between the proposed and the *Rice* channel model seems to be limited, c.f. Fig. 6, the impact on the achievable SE is significant. To investigate the impact of user channel correlation on the SE, we derive an upper bound on the SNR in Appendix C, which is given by

$$\mathrm{SNR} \leq \frac{\eta P_T}{\sigma_w^2} \left( 1 - \max_{\substack{i,j \\ i \neq j}} \left| \tilde{\mathbf{h}}_i^{\mathrm{H}} \tilde{\mathbf{h}}_j \right| \right) . \tag{27}$$

Since the users are placed with equal distance to the BS, we assumed the same large scale fading coefficient $\eta$, that is path loss, for all users for the derivation of this bound. Please note that since the vectors $\tilde{\mathbf{h}}_k$ are normalized $0 \leq \left| \tilde{\mathbf{h}}_i^{\mathrm{H}} \tilde{\mathbf{h}}_j \right| \leq 1$ for $i \neq j$ and $i, j \in \{1, \ldots, U\}$. From (27) we observe that the SNR depends on the inner product of channel vectors, such as the previously introduced correlation measure (21). The upper bound on the SNR is decreasing with increasing correlation, showing the negative impact of user correlation on the achievable SE with ZF precoding. Moreover, the bound is given by the maximum magnitude of channel vectors between any two users. This shows that the sum SE is decreased if any two users are highly correlated. In the limit, we obtain $\mathrm{SNR} \to 0$ if there are any two users $i$ and $j$ with $\left| \tilde{\mathbf{h}}_i^{\mathrm{H}} \tilde{\mathbf{h}}_j \right| \to 1$.

Since for increasing Rician $K$ factors, the proposed model and the *Rice* channel model both converge to the spatially consistent LOS channel, the gap in achievable rate is decreasing with increasing $K$ factor. The gap in achievable rate occurs, since the not spatially consistent i.i.d. Rayleigh fading model underestimates the amount of spatial correlation between users. Please note that the LOS is always present in our proposed channel model and does not vanish for very low values of $K$.

## V. CONCLUSION

In this work, we introduce a channel model based on multiple scattering theory. By employing simple propagation mechanisms, we obtain a low complexity MIMO channel model. We consider only single scattering events for NLOS paths. Adjusting the number and strength of scattering events allows to adjust the Rician $K$ factor of the model. This allows to simulate propagation environments in between rich scattering and pure LOS channels. We provide a statistical description for the Rician $K$ factor of the proposed model and verify it by simulation. Investigating the model's spatial correlation properties, we show that the proposed channel model is indeed spatially consistent while the simplified assumption of i.i.d. Rayleigh fading and the 3GPP 3D channel model are not. Non spatially consistent channel models lead to an underestimation of spatial correlation among users and therefore to an overestimation of achievable sum rate. This underlines the importance of spatially consistent channel models for investigation of multi-user MIMO systems such as massive MIMO.

## APPENDIX A
## DERIVATION OF SCATTERING COEFFICIENTS

In the channel model (1), $\alpha_{k,j}$ describes propagation on a direct path from transmit antenna position $\mathbf{r}_j$ to positions $\mathbf{r}_k$,

where either a receive antenna or a scattering object is located at $\mathbf{r}_k$. Further, $\beta_{k,j}$ describes the propagation from position $\mathbf{r}_j$ to positions $\mathbf{r}_k$ including a scattering event at position $\mathbf{r}_j$ where either a receive antenna or an other scattering object is located at $\mathbf{r}_k$. In order to find physically meaningful expressions for the factors $\alpha$ and $\beta$, we consider a bi-static radar. In this setup, a transmitter emits a wave that is scattered at a target and received by a receiver, which is not co-located with the transmitter. The bi-static radar equation [33] is given by

$$\frac{P_r}{P_t} = \frac{G_t}{4\pi d_1^2}\,\gamma^2\,\frac{A_{\mathrm{r,eff}}}{4\pi d_2^2}\,, \tag{28}$$

with the distance $d_1$ between the transmitter and the target and the distance $d_2$ between the target and the receiver. Equation (28) describes the ratio between the received power $P_r$ by an antenna with effective area $A_{\mathrm{eff}}$ and the transmitted power $P_t$ from a transmit antenna with gain $G_t$. Here, $\gamma^2$ is the radar cross section of the target. Next, we insert the relation between the effective antenna aperture and antenna gain

$$A_{\mathrm{r,eff}} = \frac{\lambda^2}{4\pi} G_r\,, \tag{29}$$

and assume $G_r = G_t = 1$. Since the power is proportional to the square of the electrical field strength $E$, we obtain a ratio between the received and the transmitted field strength, including one scattering event as

$$\frac{E_r}{E_t} = \underbrace{\frac{1}{\sqrt{4\pi}d_1}e^{\frac{2\pi}{\lambda}d_1}}_{\text{transmitter to scatt.}}\ \underbrace{\gamma e^{i\phi_p}}_{\substack{\text{scattering}\\ \text{event}}}\ \underbrace{\frac{\lambda}{4\pi d_2}e^{\frac{2\pi}{\lambda}d_2}}_{\text{scatt. to receiver}}\,. \tag{30}$$

The phase of (30) is determined by free space propagation from the transmitter to the scattering object, free space propagation from the target to the receiver and a random scattering phase $\phi_p$.

Taking this idea further, to the case of multiple scattering events and considering the structure of the model (1), we obtain the path coefficients

$$\alpha_{k,j} = \frac{\lambda}{4\pi\|\mathbf{r}_k - \mathbf{r}_j\|}e^{i\frac{2\pi}{\lambda}\|\mathbf{r}_k-\mathbf{r}_j\|}\,, \tag{31a}$$

$$\beta_{k,j} = \frac{\delta_j}{\sqrt{4\pi}\|\mathbf{r}_k - \mathbf{r}_j\|}e^{i\frac{2\pi}{\lambda}\|\mathbf{r}_k-\mathbf{r}_j\|}\,. \tag{31b}$$

The magnitude of parameter $\alpha_{k,j}$ corresponds to Friis' formula for free space propagation between positions $\mathbf{r}_j$ and $\mathbf{r}_k$. The factor $\beta_{k,j}$ includes a scattering event at scattering object $j$ via the scattering coefficient $\delta_j = \gamma_j e^{\phi_j}$ with clustering factor $\gamma_j$ and the random phase $\phi_j$.

## APPENDIX B
## BOUNDS ON THE MAGNITUDE OF SUM TERMS

In this section we consider bounds on the magnitude of the sum term (4) and provide bounds for a circular sector geometry. For readability, we consider a single transmit antenna and a single receive antenna and denote $\mathbf{r}_n$ as the BS position $\mathbf{r}_{\mathrm{BS}}$, $\mathbf{r}_u$ as the user position $\mathbf{r}_{\mathrm{UE}}$ and $\mathbf{r}_p$ as the scattering object position $\mathbf{r}_{\mathrm{S}}$ in the sequel. In order to bound $|u(\mathbf{r}_{\mathrm{S}})|$ from above and therefore guarantee boundedness of channel coefficients, the distances $\|\mathbf{r}_{\mathrm{BS}} - \mathbf{r}_{\mathrm{S}}\|$ and $\|\mathbf{r}_{\mathrm{S}} - \mathbf{r}_{\mathrm{UE}}\|$ must not become arbitrarily small. We consider a minimum distance between a scattering object and any antenna, belonging to either a user or the BS, as $d_{\mathrm{S}}$. To bound the sum terms, the minimum and maximum product of user-to-scattering object and scattering object-to-BS distance is decisive. We obtain the following problem to determine the minimum product of distances as

$$\begin{aligned}\xi_{\min} = \min_{\mathbf{r}_{\mathrm{S}}}\ & \|\mathbf{r}_{\mathrm{BS}} - \mathbf{r}_{\mathrm{S}}\|\,\|\mathbf{r}_{\mathrm{UE}} - \mathbf{r}_{\mathrm{S}}\| \\ \text{subject to}\ & \|\mathbf{r}_{\mathrm{BS}} - \mathbf{r}_{\mathrm{S}}\| \geq d_{\mathrm{S}} \\ & \|\mathbf{r}_{\mathrm{UE}} - \mathbf{r}_{\mathrm{S}}\| \geq d_{\mathrm{S}}\end{aligned} \tag{32}$$

where the constraints correspond to the minimum distance between BS and scattering object and between user and scattering object. Similarly, changing (32) to a maximization problem with the same cost function and constraints leads to the solution $\xi_{\max}$. These extrema allow us to state lower and upper bounds on the absolute value of the sum terms $u(\mathbf{r}_{\mathrm{S}})$ as

$$\frac{1}{\xi_{\max}} \leq |u(\mathbf{r}_{\mathrm{S}})| \leq \frac{1}{\xi_{\min}}\,. \tag{33}$$

From the upper bound, we conclude that it is necessary and sufficient for boundedness of (3) that there exists a minimum distance $d_{\mathrm{S}} > 0$ between any transmit and any receive antenna to any scattering object, that is

$$\|\mathbf{r}_k - \mathbf{r}_m\| \geq d_{\mathrm{S}} \quad \forall k \in \mathcal{T} \cup \mathcal{R},\ \forall m \in \mathcal{S}\,, \tag{34}$$

with a bounded clustering factor, that is, $\gamma < \infty$, and a finite number of scattering objects, that is, $M = |\mathcal{S}| < \infty$. This condition is straight forward to fulfill in any simulation scenario, by introducing an empty region with radius $d_{\mathrm{S}}$ around all BS and user antennas in which no scattering object is placed.

While the optimization problem (32) does not assume a specific geometry, we now specialize upper and lower bounds on $|u(\mathbf{r}_{\mathrm{S}})|$ for the case of a circular sector with opening angle $\theta$, as shown in Fig. 8. The user is placed at a distance $R$ from the BS at an angle of $\zeta/2$ from the sector center where we assume $\zeta < \theta$.

The two distances, from the BS to the scattering object and from the scattering object to the user, have to add up to at least $R$ according to the triangle inequality. Therefore, the minimum product of these two distances is obtained, when either of these numbers attains its minimum value $d_{\mathrm{S}}$. As the distances have to add up to $R$, the other distance is $R - d_{\mathrm{S}}$. This corresponds to the case when the scattering object is located directly at the border of the empty region with radius $d_{\mathrm{S}}$, see positions $\mathbf{r}_{\min}^{(1)}$ and $\mathbf{r}_{\min}^{(2)}$ in Fig. 8. Therefore the solution to the minimization is given by

$$\xi_{\min} = d_{\mathrm{S}}\,(R - d_{\mathrm{S}})\,. \tag{35}$$

Changing (32) to a maximization problem, the product of the distances, from the BS to the scattering object and from the scattering object to the user, is at its maximum, if they both

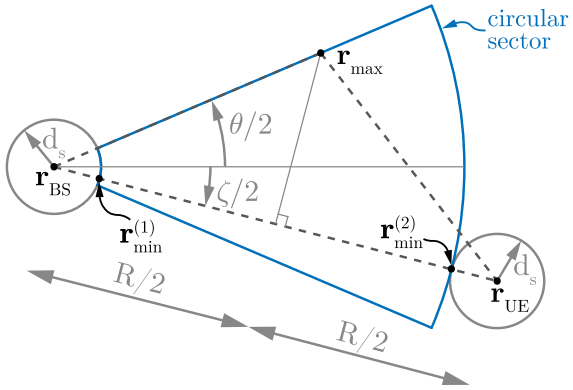


**FIGURE 8.** Geometry for a circular sector scenario. The scattering object positions $\mathbf{r}^{(1)}_{\min}$ and $\mathbf{r}^{(2)}_{\min}$ lead to a minimum product of distances while a scattering object position $\mathbf{r}_{\max}$ leads to a maximum product of distances.

attain the same maximal value within their possible range. In the case of a circular sector, this corresponds to the case when the scattering object is located at the border of the sector, such that the distances $\|\mathbf{r}_{BS} - \mathbf{r}_S\|$ and $\|\mathbf{r}_{UE} - \mathbf{r}_S\|$ are equal and maximal, see position $\mathbf{r}_{\max}$ in Fig. 8. Via elementary geometry, we obtain the solution to the maximization problem as

$$\xi_{\max} = \frac{R^2}{4\cos(\frac{\zeta+\theta}{2})^2}$$
$$\text{for } 0 < \zeta + \theta \leq 2\arccos\left(\frac{R}{2(R-d_S)}\right). \quad (36)$$

This leads to the upper and lower bounds on the absolute value of the sum terms:

$$\frac{4\cos(\frac{\theta}{2})^2}{R^2} \leq |u(\mathbf{r}_S)| \leq \frac{1}{d_S(R-d_S)}. \quad (37)$$

Equation (32) can be solved straight forward for other geometries. We focus on a circular sector geometry in this work.

## APPENDIX C
## UPPER BOUND ON THE SNR WITH ZF PRECODING

In this section, we provide an upper bound on the SNR (25), obtained by ZF precoding. Due to the similarity invariance of the tr $(\cdot)$ operator, we obtain

$$\text{SNR} = \frac{P_T}{\sigma_w^2}\frac{1}{\text{tr}\left(\left(\mathbf{H}^{\text{H}}\mathbf{H}\right)^{-1}\right)} = \frac{P_T}{\sigma_w^2}\frac{1}{\sum_{k=1}^{U}\frac{1}{\lambda_k}}, \quad (38)$$

where $\lambda_k$ for $k \in \{1,\ldots,U\}$ denote the eigenvalues of the non-singular matrix $\mathbf{H}^{\text{H}}\mathbf{H}$. Let $\lambda_1$ denote the smallest eigenvalue of $\mathbf{H}^{\text{H}}\mathbf{H}$. The channel matrix $\mathbf{H}$ consists of users' channel vectors, that is, $\mathbf{H} = (\mathbf{h}_1,\ldots,\mathbf{h}_U)$. A user's channel vector is given by $\mathbf{h}_k = \sqrt{\eta_k}\tilde{\mathbf{h}}_k$ for $k \in \{1,\ldots,U\}$ where $\eta_k > 0$ denotes the large scale fading coefficient of user $k$ and $\tilde{\mathbf{h}}_k$ describes the small scale fading with $\|\tilde{\mathbf{h}}_k\| = 1\ \forall k$. Through the Min-max Theorem by Courant and Fischer [34] we know

$$\lambda_1 = \min_{\|\mathbf{x}\|=1} \mathbf{x}^{\text{H}}\mathbf{H}^{\text{H}}\mathbf{H}\mathbf{x}. \quad (39)$$

Choosing a vector $\mathbf{v} = \frac{1}{\sqrt{2}}\left(\mathbf{e}_i + e^{i\varphi}\mathbf{e}_j\right)$ where $\mathbf{e}_i$ is a vector with a 1 in the i$^{\text{th}}$ entry and 0s elsewhere, we find an upper bound on the smallest eigenvector as

$$\begin{aligned}\lambda_1 &\leq \min_{\mathbf{v}} \mathbf{v}^{\text{H}}\mathbf{H}^{\text{H}}\mathbf{H}\mathbf{v}\\ &= \min_{i,j,\varphi}\frac{1}{2}\big(\eta_i\tilde{\mathbf{h}}_i^{\text{H}}\tilde{\mathbf{h}}_i + \eta_j\tilde{\mathbf{h}}_j^{\text{H}}\tilde{\mathbf{h}}_j\\ &\quad + \sqrt{\eta_i\eta_j}e^{i\varphi}\tilde{\mathbf{h}}_i^{\text{H}}\tilde{\mathbf{h}}_j + \sqrt{\eta_i\eta_j}e^{-i\varphi}\tilde{\mathbf{h}}_j^{\text{H}}\tilde{\mathbf{h}}_i\big)\\ &= \min_{\substack{i,j\\ i\neq j}}\frac{\eta_i+\eta_j}{2} - \sqrt{\eta_i\eta_j}\left|\tilde{\mathbf{h}}_i^{\text{H}}\tilde{\mathbf{h}}_j\right|,\end{aligned}$$

with $\varphi = \pi - \text{Arg}\left(\tilde{\mathbf{h}}_i^{\text{H}}\tilde{\mathbf{h}}_j\right)$. In the case of equal large scale fading for all users, that is, for $\eta_k = \eta\ \forall k$, we obtain

$$\lambda_1 \leq \eta\left(1 - \max_{\substack{i,j\\ i\neq j}}\left|\tilde{\mathbf{h}}_i^{\text{H}}\tilde{\mathbf{h}}_j\right|\right). \quad (40)$$

Since $\sum_{k=1}^{U}\frac{1}{\lambda_k} > \frac{1}{\lambda_1}$, we obtain an upper bound on the SNR as

$$\text{SNR} \leq \frac{\eta P_T}{\sigma_w^2}\left(1 - \max_{\substack{i,j\\ i\neq j}}\left|\tilde{\mathbf{h}}_i^{\text{H}}\tilde{\mathbf{h}}_j\right|\right). \quad (41)$$

## REFERENCES

[1] F. Rusek, D. Persson, B. K. Lau, E. G. Larsson, T. L. Marzetta, O. Edfors, and F. Tufvesson, "Scaling up MIMO: Opportunities and challenges with very large arrays," *IEEE Signal Process. Mag.*, vol. 30, no. 1, pp. 40–60, Jan. 2013.

[2] H. Q. Ngo, E. G. Larsson, and T. L. Marzetta, "Aspects of favorable propagation in massive MIMO," in *Proc. EUSIPCO*, Lisbon, Portugal, Sep. 2014, pp. 76–80.

[3] E. Björnson, E. G. Larsson, and T. L. Marzetta, "Massive MIMO: Ten myths and one critical question," *IEEE Commun. Mag.*, vol. 54, no. 2, pp. 114–123, Feb. 2016.

[4] E. Björnson, J. Hoydis, and L. Sanguinetti, "Massive MIMO networks: Spectral, energy, and hardware efficiency," *Found. Trends Signal Process.*, vol. 11, nos. 3–4, pp. 154–655, 2017.

[5] D.-S. Shiu, G. J. Foschini, M. J. Gans, and J. M. Kahn, "Fading correlation and its effect on the capacity of multielement antenna systems," *IEEE Trans. Commun.*, vol. 48, no. 3, pp. 502–513, Mar. 2000.

[6] C.-M. Chen, V. Volskiy, A. Chiumento, L. Van der Perre, G. A. E. Vandenbosch, and S. Pollin, "Exploration of user separation capabilities by distributed large antenna arrays," in *Proc. IEEE Globecom Workshops*, Washington, DC, USA, Dec. 2016, pp. 1–6.

[7] M. Z. Aslam, Y. Corre, E. Bjoernson, and Y. Lostanlen, "Massive MIMO channel performance analysis considering separation of simultaneous users," in *Proc. ITG WSA*, Bochum, Germany, Mar. 2018, pp. 1–6.

[8] J. Flordelis, F. Rusek, X. Gao, G. Dahman, O. Edfors, and F. Tufvesson, "Spatial separation of closely-located users in measured massive MIMO channels," *IEEE Access*, vol. 6, pp. 40253–40266, 2018.

[9] C. Wang and R. D. Murch, "Adaptive downlink multi-user MIMO wireless systems for correlated channels with imperfect CSI," *IEEE Trans. Wireless Commun.*, vol. 5, no. 9, pp. 2435–2446, Sep. 2006.

[10] T. Van Chien, C. Mollén, and E. Björnson, "Large-scale-fading decoding in cellular massive MIMO systems with spatially correlated channels," 2018, *arXiv:1807.08071*. [Online]. Available: https://arxiv.org/abs/1807.08071

[11] X. Q. Gao, B. Jiang, X. Li, A. B. Gershman, and M. R. McKay, "Statistical eigenmode transmission over jointly correlated MIMO channels," *IEEE Trans. Inf. Theory*, vol. 55, no. 8, pp. 3735–3750, Aug. 2009.
[12] Ö. Özdogan, E. Björnson, and E. G. Larsson, "Uplink spectral efficiency of massive MIMO with spatially correlated Rician fading," in *Proc. SPAWC*, Kalamata, Greece, Jun. 2018, pp. 216–220.
[13] P. Kyösti, J. Meinilä, L. Hentilä, X. Zhao, T. Jämsä, C. Schneider, M. Narandžić, M. Milojević, A. Hong, J. Ylitalo, V.-M. Holappa, M. Alatossava, R. Bultitude, Y. de Jong, and T. Rautiainen, "WINNER II channel models," WINNER, Tech. Rep. IST-4-027756 WINNER II, Deliverable D1.1.2 V1.2, Sep. 2007.
[14] J. Meinilä, P. Kyösti, L. Hentilä, T. Jämsä, E. Suikkanen, E. Kunnari, and M. Narandžić, "WINNER+ final channel models," WINNER, Tech. Rep. CELTIC/CP5-026, Deliverable D5.3, Jun. 2010.
[15] *Technical Specification Group Radio Access Network; Technical Specification Group Radio Access Network: Spatial Channel Model for Multiple Input Multiple Output (MIMO) Simulations*, document TR 25.996, 3GPP, Jun. 2018.
[16] C.-X. Wang, X. Hong, H. Wu, and W. Xu, "Spatial-temporal correlation properties of the 3GPP spatial channel model and the Kronecker MIMO channel model," *EURASIP J. Wireless Commun. Netw.*, vol. 2007, Feb. 2007, Art. no. 039871.
[17] *Study on 3D Channel Model for LTE*, document TR 36.873, 3GPP, May 2018.
[18] F. Ademaj, M. Taranetz, and M. Rupp, "Implementation, validation and application of the 3GPP 3D MIMO channel model in open source simulation tools," in *Proc. Int. Symp. Wireless Commun. Syst. (ISWCS)*, Brussels, Belgium, Aug. 2015, pp. 721–725.
[19] S. Jaeckel, L. Raschkowski, K. Börner, and L. Thiele, "QuaDRiGa: A 3-D multi-cell channel model with time evolution for enabling virtual field trials," *IEEE Trans. Antennas Propag.*, vol. 62, no. 6, pp. 3242–3256, Jun. 2014.
[20] F. Ademaj, M. Müller, S. Schwarz, and M. Rupp, "Modeling of spatially correlated geometry-based stochastic channels," in *Proc. IEEE 86th Veh. Technol. Conf. (VTC-Fall)*, Toronto, ON, Canada, Sep. 2017, pp. 1–6.
[21] F. Ademaj, S. Schwarz, K. Guan, and M. Rupp, "Ray-tracing based validation of spatial consistency for geometry-based stochastic channels," in *Proc. IEEE 88th Veh. Technol. Conf. (VTC-Fall)*, Chicago, IL, USA, Aug. 2018, pp. 1–5.
[22] L. Lium, C. Oestges, J. Poutanen, K. Haneda, P. Vainikainen, F. Quitin, F. Tufvesson, and P. De Doncker , "The COST 2100 MIMO channel model," *IEEE Wireless Commun.*, vol. 19, no. 6, pp. 92–99, Dec. 2012.
[23] X. Gao, F. Tufvesson, and O. Edfors, "Massive MIMO channels—Measurements and models," in *Proc. Asilomar Conf. Signals, Syst. Comput.*, Pacific Grove, CA, USA, Nov. 2013, pp. 280–284.
[24] M. Zhu. *A Public COST 2100 Channel Model MATLAB Source Code*. Accessed: Feb. 5, 2019. [Online]. Available: https://code.google.com/archive/p/cost2100model/downloads
[25] M. Franceschetti, "Stochastic rays pulse propagation," *IEEE Trans. Antennas Propag.*, vol. 52, no. 10, pp. 2742–2752, Oct. 2004.
[26] M. Franceschetti, J. Bruck, and L. J. Schulman, "A random walk model of wave propagation," *IEEE Trans. Antennas Propag.*, vol. 52, no. 5, pp. 1304–1317, May 2004.
[27] J. Salo, H. M. El-Sallabi, and P. Vainikainen, "Statistical analysis of the multiple scattering radio channel," *IEEE Trans. Antennas Propag.*, vol. 54, no. 11, pp. 3114–3124, Nov. 2006.
[28] T. Pedersen and B. H. Fleury, "A realistic radio channel model based in stochastic propagation graphs," in *Proc. MATHMOD*, Vienna, Austria, 2006, pp. 324–331.
[29] T. Pedersen and B. H. Fleury, "Radio channel modelling using stochastic propagation graphs," in *Proc. ICC*, Glasgow, U.K., Jun. 2007, pp. 2733–2738.
[30] T. Pedersen, G. Steinböck, and B. H. Fleury, "Modeling of reverberant radio channels using propagation graphs," *IEEE Trans. Antennas Propag.*, vol. 60, no. 12, pp. 5978–5988, Dec. 2012.
[31] M. Nakagami, "The *m*-distribution—A general formula of intensity distribution of rapid fading," in *Statistical Methods in Radio Wave Propagation*. Amsterdam, The Netherlands: Elsevier, 1960, pp. 3–36.
[32] N. Czink, B. Bandemer, G. Vazquez-Vilar, L. Jalloul, C. Oestges, and A. Paulraj, "Spatial separation of multi-user MIMO channels," in *Proc. PIMRC*, Tokyo, Japan, Sep. 2009, pp. 1059–1063.
[33] M. Skolnik, *Introduction to Radar Systems*, 2nd ed. New York, NY, USA: McGraw-Hill, 1981.
[34] G. H. Golub and C. F. Van Loan, *Matrix Computations*, vol. 3. Baltimore, MD, USA: JHU Press, 2012.

**STEFAN PRATSCHNER** received the B.Sc. degree in electrical engineering and the M.Sc. degree (Hons.) in telecommunications from TU Wien, Austria, in 2014 and 2016, respectively, where he is currently pursuing the Ph.D. degree with the Institute of Telecommunications and has been a Project Assistant, since 2013. His current research interests include massive MIMO technologies for mobile communications, array processing, and testbed measurements.

**THOMAS BLAZEK** received the B.Sc. degree in electrical engineering and Dipl.Ing. degree (M.Sc. equivalent) in telecommunications from TU Wien, Vienna, Austria, in 2013 and 2015, respectively, where he is currently pursuing the Ph.D. degree in telecommunications engineering and also a University Assistant with the Institute of Telecommunications. From 2013 to 2014, he was a member of the Mobile Communications Group, TU Wien, where he was involved in system level LTE simulations. His current research interests include modeling and analysis of vehicular channels and measurement testbed design.

**ERICH ZÖCHMANN** received the B.Sc., Dipl.Ing. (M.Sc.), and Dr.Techn. degrees (Hons.) in electrical engineering from TU Wien, in 2013, 2015, and 2019, respectively. From 2013 to 2015, he was a Project Assistant with the Institute of Telecommunications, where he co-developed the Vienna LTE-A uplink link level simulator and conducted research on physical layer signal processing for 4G mobile communication systems. From 2017 to 2018, he was a Visiting Scholar with The University of Texas at Austin. His current research interests include experimental characterization and modeling of millimeter-wave propagation, physical layer signal processing, array signal processing, compressed sensing, and convex optimization.

**FJOLLA ADEMAJ** received the M.Sc. degree (Hons.) in telecommunications from the Faculty of Electrical and Computer Engineering, Kosovo, University of Prishtina, in 2014. She is currently pursuing the Ph.D. degree in telecommunications engineering with the Institute of Telecommunications, TU Wien. Her research interests include system level modeling, channel modeling in three dimensions, and evaluation of full-dimension MIMO.

**SEBASTIAN CABAN** received the master's degree in business administration from the University of Vienna, Vienna, Austria, and the master's and Ph.D. degrees in telecommunications from TU Wien. His current research interest includes measurements in wireless communications.

**STEFAN SCHWARZ** received the Dipl.-Ing. degree in electrical engineering, the Dr. Techn. degree in telecommunications engineering, and the Habilitation degree in mobile communications from the Vienna University of Technology (TU Wien), in 2009, 2013, and 2019, respectively, where he currently holds a tenure track position at the Institute of Telecommunications and is the Head of the Christian Doppler Laboratory for Dependable Wireless Connectivity for the Society in Motion. His research interests include wireless communications channel modeling, signal processing, and optimization.

**MARKUS RUPP** received the Dipl.-Ing. degree from the University of Saarbräcken, Germany, in 1988, and the Dr. Ing. degree from the Technische Universität Darmstadt, Germany, in 1993. Until 1995, he held a Postdoctoral position at the University of California at Santa Barbara, Santa Barbara, CA, USA. From 1995 to 2001, he was with the Wireless Technology Research Department, Nokia Bell Labs, Holmdel, NJ, USA. Since 2001, he has been a Full Professor of digital signal processing in mobile communications with TU Wien.

Zöchmann *et al. EURASIP Journal on Wireless Communications and Networking* (2019) 2019:21
https://doi.org/10.1186/s13638-018-1336-6

EURASIP Journal on Wireless Communications and Networking

RESEARCH Open Access

# Better than Rician: modelling millimetre wave channels as two-wave with diffuse power

Erich Zöchmann[1,2,3*], Sebastian Caban[1,2], Christoph F. Mecklenbräuker[2], Stefan Pratschner[1,2], Martin Lerch[2], Stefan Schwarz[1,2] and Markus Rupp[2]

**Abstract**

This contribution provides experimental evidence for the two-wave with diffuse power (TWDP) fading model. We have conducted two indoor millimetre wave measurement campaigns with directive horn antennas at both link ends. One horn antenna is mounted in a corner of our laboratory, while the other is steerable and scans azimuth and elevation. Our first measurement campaign is based on scalar network analysis with 7 GHz of bandwidth. Our second measurement campaign obtains magnitude and phase information; it is additionally sampled directionally at several positions in space. We apply Akaike's information criterion to decide whether Rician fading sufficiently explains the data or the generalised TWDP fading model is necessary. Our results indicate that the TWDP fading hypothesis is favoured over Rician fading in situations where the steerable antenna is pointing towards reflecting objects or is slightly misaligned at line-of-sight. We demonstrate TWDP fading in several different domains, namely, frequency, space, and time.

**Keywords:** Millimetre wave, 60 GHz, Measurements, Fading, Hypothesis testing, Rician fading, TWDP fading

## 1 Introduction

Accurate modelling of wireless propagation effects is a fundamental prerequisite for a proper communication system design. After the introduction of the double-directional radio channel model [1], wireless propagation research ($< 6$ GHz) started to model the wireless channel agnostic to the antennas used. More than a decade later, propagation research focusses now on millimetre wave bands to unlock the large bandwidths available in this regime [2–5]. At millimetre waves (mmWaves), omni-directional antennas have small effective antenna areas, resulting in a high path loss [6–10]. To overcome this high path loss, researchers have proposed to apply highly directive antennas on both link ends [11–14]. Most researchers aim to achieve high directivity with antenna arrays [15–20] and a few with dielectric lenses [21–23]. When the link quality depends so much on the achieved beamforming gain, antennas must be considered as part of the wireless channel again. Small-scale fading is then influenced by the antenna.

According to Durgin [24, p. 137], "The use of directive antennas or arrays at a receiver, for example, amplifies several of the strongest multipath waves that arrive in one particular direction while attenuating the remaining waves. This effectively increases the ratio of specular to nonspecular received power, turning a Rayleigh or Rician fading channel into a TWDP fading channel." The mentioned two-wave with diffuse power (TWDP) fading channel describes this spatial filtering effect by two non-fluctuating receive signals together with many smaller diffuse components.

### 1.1 Related work

The authors of [25] investigated a simple wall scattering scenario and analysed how fading scales with various antenna directivities and different bandwidths. Increasing directivity [25], as well as increasing bandwidth [25, 26], results in an increased Rician K-factor. The authors of [27] analysed fading at 28 GHz with high gain horn antennas on both link ends. They observe high Rician K-factors even at non-line-of-sight (NLOS). This effect is explained by spatial filtering of directive antennas,

*Correspondence: ezoechma@nt.tuwien.ac.at
[1]Christian Doppler Laboratory for Dependable Wireless Connectivity for the Society in Motion, TU Wien, Gußhaustraße 25, 1040 Vienna, Austria
[2]Institute of Telecommunications, TU Wien, Gußhaustraße 25, 1040 Vienna, Austria
Full list of author information is available at the end of the article

as they suppress many multipath components [25]. Outdoor measurements in [28, 29], show a graphical agreement with the Rice fit, but especially Fig. 10 in [29] might be better explained as TWDP fading.

TWDP fading has already successfully been applied to describe 60 GHz near body shadowing [30]. Furthermore, as quoted above, TWDP must be considered for arrays, as they act as spatial filters [24, 31]. While theoretical work on TWDP fading is already advanced [32–37], experimental evidence, especially at millimetre waves, is still limited. For enclosed structures, such as aircraft cabins and buses, the applicability of the TWDP model is demonstrated by Frolik [38–42]. A deterministic two ray behaviour in ray tracing data of mmWave train-to-infrastructure communications is shown in [43]. A further extension of the TWDP-fading model, the so-called fluctuating two-ray fading model, was also successfully applied to fit mmWave measurement data [44–46]. This model brings in another degree of freedom and allows for common shadowing of both specular waves. The wireless channels in this present study are unblocked; thus, this model is not considered here.

Our group has conducted two measurement campaigns [47, 48] to directionally analyse receive power and small-scale fading parameters for mmWaves. This contribution is based on the measurement data gathered in [47, 48].

### 1.2 Outline and contributions

With this contribution, we aim to bring scientific rigour to the small-scale fading analysis of millimetre wave indoor channels. We show in Section 2 —by means of an information-theoretic approach [49] and null hypothesis testing [50]—that the TWDP model has evidence in mmWave communications.

We have conducted two measurement campaigns within the same laboratory with different channel sounding concepts. Our measurements are carried out in the V-band; the applied centre frequency is 60 GHz. For both measurement campaigns, 20 dBi horn antennas are used at the transmitter and at the receiver. The first measurement campaign (MC1) samples the channel in azimuth ($\varphi$) and elevation ($\theta$), keeping the antenna's (apparent) phase centre ([51, pp. 799] ) at a fixed $(x, y)$ coordinate. The transmitter is mounted in a corner of our laboratory. The sounded environment as well as the mechanical set-ups are explained in Section 3. For MC1, we sounded the channel in the frequency domain by aid of scalar network analysis, described in Section 4. These channel measurements span over 7 GHz bandwidth, supporting us to analyse fading in the *frequency domain*.

For the second measurement campaign (MC2), described in Section 5, we improved the set-up mechanically and radio frequency (RF) wise. By adding another linear guide along the $z$-axis, we keep the antenna's phase centre constant in $(x, y, z)$ coordinate, irrespective of the antenna's elevation. Furthermore, we changed the sounding concept to time-domain channel sounding. This approach allows us to utilise the *time domain* and to show channel impulse responses in Section 7. Additionally, by adjusting $(x, y, z, \varphi, \theta)$, we sample the channel in the *spatial domain* at all directions $(\varphi, \theta)$. These improvements enable us to show spatial correlations in Section 6, a further analysis tool to support the claims from MC1.

In summary, we demonstrate *TWDP fading* for directional mmWave indoor channels in the *frequency-domain*, in the *spatial-domain*, and in the *time-domain*.

## 2 Methodology—fading model identification

TWDP fading captures the effect of interference of two non-fluctuating radio signals and many smaller so-called diffuse signals [31]. The TWDP distribution degenerates to Rice if one of the two non-fluctuating radio signals vanishes. This is analogous to the well-known Rice degeneration to the Rayleigh distribution with decreasing K-factor. In the framework of model selection, TWDP fading, Rician fading, and Rayleigh fading are hence nested hypotheses [49]. Therefore, it is also obvious that among these alternatives, TWDP always allows the best possible fit of measurement data. Occam's razor [52] asks to select, among competing hypothetical distributions, the hypothesis that makes the fewest assumptions. Different distribution functions are often compared via a goodness-of-fit test [53]. Nevertheless, the authors of [54] argue that Akaike's information criterion (AIC) [49, 55–57] is better suited for the purpose of choosing among fading distributions. Later on, the AIC was also used in [58–62]. The AIC can be seen as a form of Occam's razor as it penalises the number of estimable parameters in the approximating model [49] and hence aims for parsimony.

### 2.1 Mathematical description of TWDP fading

An early form of TWDP fading was analysed in [32]. Durgin et al. [31] introduced a random phase superposition formalism. Later, Rao et al. [35] achieved a major breakthrough and found a description of TWDP fading as conditional Rician fading. For the benefit of the reader, we will briefly repeat some important steps of [35].

The TWDP fading model in the complex-valued baseband is given as:

$$r_{\text{complex}} = V_1 e^{j\phi_1} + V_2 e^{j\phi_2} + X + jY\,, \tag{1}$$

where $V_1 \geq 0$ and $V_2 \geq 0$ are the deterministic amplitudes of the non-fluctuating specular components. The phases $\phi_1$ and $\phi_2$ are independent and uniformly distributed in $(0, 2\pi)$. The diffuse components are modelled via the law of large numbers as $X + jY$, where $X, Y \sim \mathcal{N}\left(0, \sigma^2\right)$. The $K$-factor is the power ratio of the specular components to the diffuse components:

$$K = \frac{V_1^2 + V_2^2}{2\sigma^2}\,. \tag{2}$$

The parameter $\Delta$ describes the amplitude relationship among the specular components:

$$\Delta = \frac{2V_1V_2}{V_1^2 + V_2^2}\,. \tag{3}$$

The $\Delta$-parameter is bounded between 0 and 1 and equals 1 iff and only if both amplitudes are equal. The second moment of the envelope $r = |r_{\text{complex}}|$ of TWDP fading is given as:

$$\mathbb{E}\left[r^2\right] = \Omega = V_1^2 + V_2^2 + 2\sigma^2\,. \tag{4}$$

Expectation is denoted by $\mathbb{E}$. For bounded amplitudes $V_1$ and $V_2$, a clever choice of $\sigma^2$ normalises $\Omega$, that is $\Omega \equiv 1$. Starting from (4), by using (2) we arrive at:

$$\sigma^2 = \frac{1}{2(1+K)}\,. \tag{5}$$

Given $(K, \Delta, \Omega \equiv 1)$, the authors of [63] provide a formula for the amplitudes of both specular components:

$$V_{1,2} = \frac{1}{2}\sqrt{\frac{K}{K+1}}\left(\sqrt{1+\Delta} \pm \sqrt{1-\Delta}\right). \tag{6}$$

Real-world measurement data have $\Omega \neq 1$. To work with the formalism introduced above, we normalise the measurement data through estimating $\hat{\Omega}$ by the method of moments. The second moment $\Omega$ of Rician fading and TWDP fading is merely a scale factor [64, 65]. Notably, we are more concerned with a proper fit of $K$ and $\Delta$. Generally, estimation errors on $\Omega$ propagate to $K$ and $\Delta$ estimates. However, Lopez-Fernandez et al. [64] achieved an almost asymptotically efficient estimator with a moment-based estimation of $\Omega$.

Our envelope measurements are partitioned into 2 sets. We take the first set $(r_1, \ldots, r_n, \ldots r_N)$ for parameter estimation of the tuple $(K, \Delta)$ as described in Section 2.2, and hypothesis testing as described in Section 2.3. The first set is carefully selected to obtain envelopes samples that are as independent as possible. The second set $(r_1, \ldots, r_m, \ldots r_M)$ is the complement of the first set. We use the elements of the second set to estimate the second moment via:

$$\hat{\Omega} = \frac{1}{M}\sum_{m=1}^{M} r_m^2\,, \tag{7}$$

where $m$ is the sample index and $M$ is the size of the second set. Partitioning is necessary to avoid biases through noise correlations of $\hat{\Omega}$ and $\left(\hat{K}, \hat{\Delta}\right)$ [66].

By considering the estimate (7) as true parameter $\Omega$, all distributions are parametrised by the tuple $(K, \Delta)$, solely. Example distributions are shown in Fig. 1. The cumulative distribution function (CDF) of the envelope of (1) is given in [35] as:

$$F_{\text{TWDP}}(r; K, \Delta) = 1 - \frac{1}{2\pi}\int_0^{2\pi} Q_1\left(\sqrt{2K\left[1 + \Delta\cos(\alpha)\right]}, \frac{r}{\sigma}\right) \mathrm{d}\alpha\,. \tag{8}$$

The Marcum Q-function is denoted by $Q_1(\cdot,\cdot)$. For $\Delta \to 0$, Eq. (8) reduces to the well-known Rice CDF:

$$F_{\text{Rice}}(r; K) = 1 - Q_1\left(\sqrt{2K}, \frac{r}{\sigma}\right)\,. \tag{9}$$

It might sound tempting to have a second strong radio signal present; in fact, however, two waves can either superpose constructively or destructively and eventually lead to fading that is more severe than Rayleigh [38–42]. We observe the highest probability for deep fades for TWDP fading in Fig. 1.

### 2.2 Parameter estimation and model selection

Note that our model of TWDP fading (1) does not contain noise. Over our wide frequency range (in MC1, we have 7 GHz bandwidth), the receive noise power spectral density is not equal. A statistical noise description that is valid over our wide frequency range is frequency-dependent. To avoid the burden of frequency-dependent noise modelling, we only take measurement samples which lie at least 10 dB above the noise power and ignore noise in our estimation.

Having the envelope measurement data set $(r_1, \ldots, r_n, \ldots r_N)$ at hand, we are seeking a distribution of which the observed realisations $r_n$ appear most likely. To do so, we estimate the parameter tuple $(K, \Delta)$ via the maximum likelihood procedure:

$$\begin{aligned}\left(\hat{K}, \hat{\Delta}\right) &= \text{argmax}_{K,\Delta}\sum_{n=1}^{N} \ln\frac{\partial F_{\text{TWDP}}(r_n; K, \Delta)}{\partial r} \\ &= \text{argmax}_{K,\Delta}\sum_{n=1}^{N} \ln f_{\text{TWDP}}(r_n; K, \Delta) \\ &= \text{argmax}_{K,\Delta}\sum_{n=1}^{N} \ln \mathcal{L}(K, \Delta | r_n)\,.\end{aligned} \tag{10}$$

We denote the probability density function (PDF) by $f(\cdot)$, $n$ denotes the sample index, and $N$ the size of the set. To solve (10), we first discretise $K$ and $\Delta$ in steps of 0.05. Next, we calculate $\frac{\partial F_{\text{TWDP}}(r;K,\Delta)}{\partial r}$ for all parameters via numerical differentiation. Within this family of distributions, we search for the parameter vector maximising the log-likelihood function (10). For the optimal Rice fit, the maximum is searched within the parameter slice $(K, \Delta \equiv 0)$. An exemplary fit of Rician and TWDP fading is shown in Fig. 2. As a reference, Rayleigh fading $(K \equiv 0,\ \Delta \equiv 0)$ is shown as well.

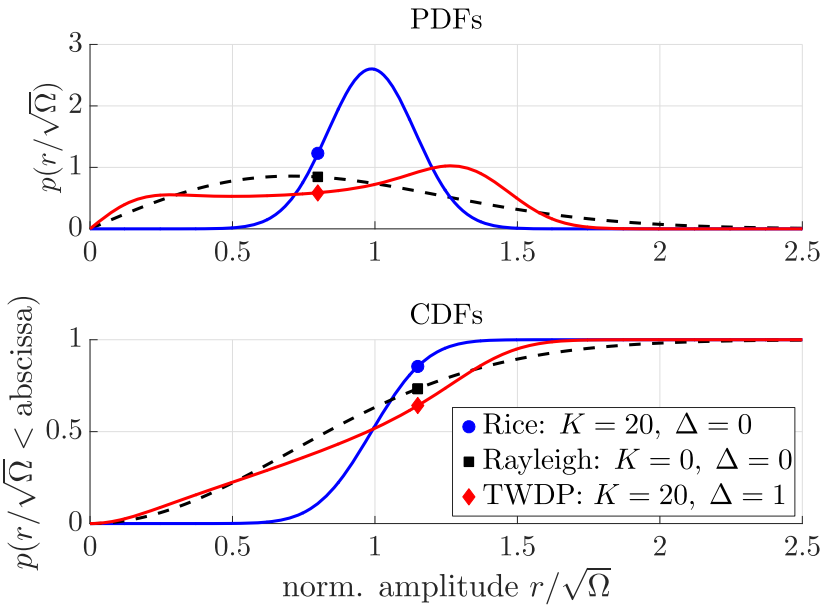


**Fig. 1** Comparison of Rayleigh, Rician, and TWDP fading. The TWDP distribution with $\Delta = 1$ deviates from the Rice distribution. TWDP fading's probability for deep fades is higher than for a Rayleigh distribution

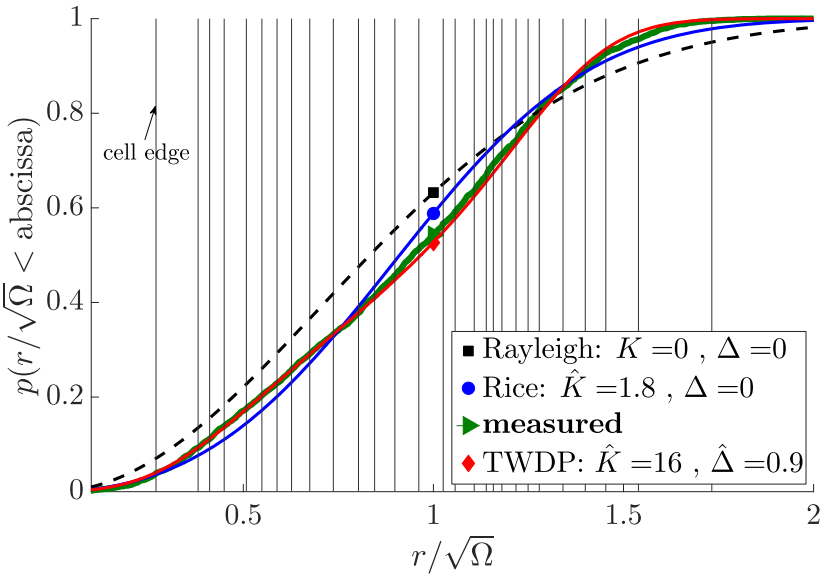


**Fig. 2** CDFs: Distribution fitting for exemplary frequency domain measurement data. Illustration of the maximum likelihood fitted Rice distribution and the maximum likelihood fitted TWDP fading distribution. The Rician *K*-factor and the TWDP *K*-factor deviate significantly. Rayleigh fading is plotted as reference

To select between Rician fading and TWDP fading, we employ Akaike's information criterion (AIC). The AIC is a rigourous way to estimate the Kullback-Leibler divergence, that is, the relative entropy based on the maximum-likelihood estimate [49]. Given the maximum-likelihood fitted parameter tuple $(\hat{K}, \hat{\Delta})$ of TWDP fading and Rician fading, we calculate the sample size-corrected AIC [49, p. 66] for Rician fading ($\mathrm{AIC_R}$) or TWDP fading ($\mathrm{AIC_T}$):

$$\mathrm{AIC_{R/T}} = -2\sum_{n=1}^{N} \ln \mathcal{L}_{\mathrm{R/T}}\left(\hat{K}, \hat{\Delta} | r\right) + 2U_{\mathrm{R/T}} + \frac{2U_{\mathrm{R/T}}(U_{\mathrm{R/T}}+1)}{N - U_{\mathrm{R/T}} - 1}, \tag{11}$$

where $U$ is the model order. For Rician fading, the model order is $U_{\mathrm{R}} = 1$, since we estimate the $K$-factor, only. For TWDP fading $U_{\mathrm{T}} = 2$, as $\Delta$ is estimated additionally. The second moment $\Omega$ (estimated already with a different data set before the parameter estimation) is not part of the ML estimation (10) and therefore not accounted in the model order $U$. We choose between Rician fading and TWDP fading based on the lower AIC.

### 2.3 Validation of the chosen model

Based on (11), one of the two distributions, Rice or TWDP, will always yield a better fit. To validate whether the chosen distributions really explains the data, we state the following statistical hypothesis testing problem:

$$\mathcal{H}_0 : \begin{cases} F_{\mathrm{Rice}}\left(r; \hat{K}\right), & \text{if } \mathrm{AIC_R} \leq \mathrm{AIC_T} \\ F_{\mathrm{TWDP}}\left(r; \hat{K}, \hat{\Delta}\right), & \text{else} \end{cases}$$

$$\mathcal{H}_1 : \begin{cases} \neg F_{\mathrm{Rice}}\left(r; \hat{K}\right), & \text{if } \mathrm{AIC_R} \leq \mathrm{AIC_T} \\ \neg F_{\mathrm{TWDP}}\left(r; \hat{K}, \hat{\Delta}\right), & \text{else} \end{cases} \tag{12}$$

The Boolean negation is denoted by $\neg$. Our statistical tool is the $g$-test [67, 68][1]. At a significance level $\alpha$, a null hypothesis is rejected if:

$$G = 2\sum_{i=1}^{m} O_i \ln\left(\frac{O_i}{E_i}\right) \overset{?}{>} \chi^2_{(1-\alpha, m-e)}, \tag{13}$$

where $O_i$ is the observed bin count in cell $i$ and $E_i$ is the expected bin count in cell $i$ under the null hypothesis $\mathcal{H}_0$. The cell edges are illustrated with vertical lines in Fig. 2. The cell edges are chosen, such that 10 observed bin counts fall into one cell. The estimated parameters of the model are denoted by $e$. For Rician fading, we estimate $e = 2$ $(\Omega, K)$ parameters, and for TWDP fading, we estimate $e = 3$ $(\Omega, K, \Delta)$ parameters in total. The $(1-\alpha)$ quantile of the chi-square distribution with $m - e$ degrees of freedom is denoted by $\chi^2_{(1-\alpha,m-e)}$. The prescribed confidence level is $1 - \alpha = 0.01$ .

## 3 Floor plan and set-ups for MC1 and MC2

Our measured environment is a mixed office and laboratory room. There are office desks in the middle of the room, and at the window side, there are laboratory desks

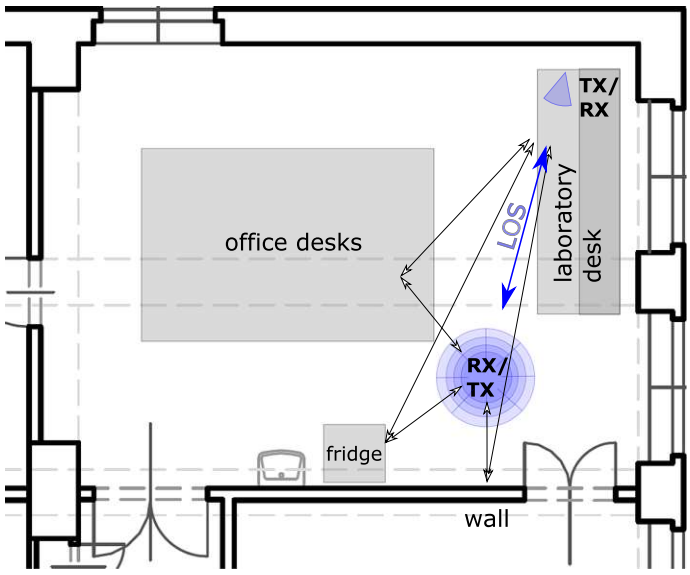


**Fig. 3** Floor plan of the measured environment. The floorplan indicates the multipath components that are visible in the measurement results. TX and RX switch roles for MC2. TX/RX in the right upper corner of the room is always static. RX/TX in the middle of the room is steerable, indicated by the spider's web

(see Fig 3.). The main interacting objects in our channel are office desks, a metallic fridge, a wall, and the surface of the laboratory desk. These objects are all marked in Fig. 3.

Our directional measurements are carried out by using the traditional approach of mechanically steered directional antennas [69, 70]. As directional antennas, 20 dBi conical horn antennas with an 18° 3 dB opening angle are used. Our polarisation is determined by the LOS polarisation. When TX and RX are facing each other at LOS, the polarisation is co-polarised and the E-field is orthogonal to the floor. In MC1, the essential mechanical adaptation to the state-of-the-art directional channel sounding set-up [71, 72] is that the elevation-over-azimuth positioner is mounted on an xy-positioning stage. Thereby, we compensate for all linear translations caused by rotations and keep the phase centre of the horn antenna always at the same $(x, y)$ coordinate, see Fig. 4. The $z$ coordinate is roughly 70 cm above ground but varies 13 cm for different elevation angles.

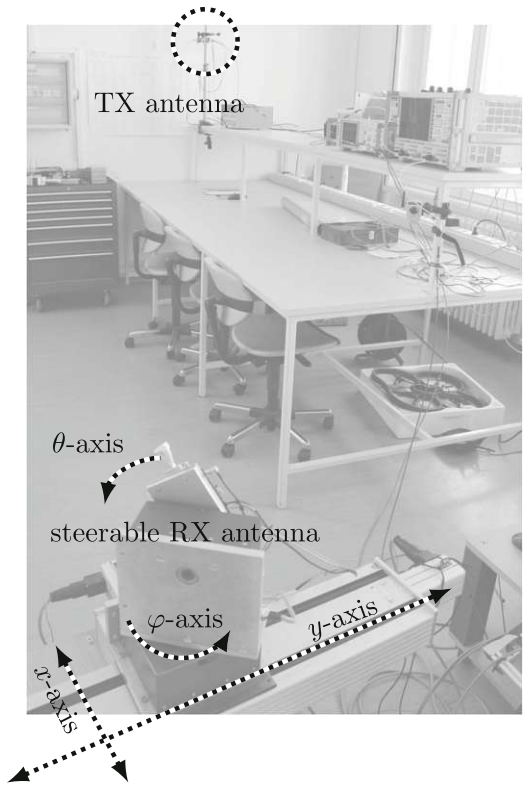


**Fig. 4** Photograph of the mechanical set-up for MC1 from the receiver point of view. The receive antenna, a conical 20 dBi horn, is mounted on a multi-axis positioning and rotating system. The azimuthal and elevation angle are controlled to scan the whole upper hemisphere. The multi-axis system moves and rotates the horn antenna such that its phase centre stays at the same $(x, y)$ coordinate during the directional scan

For MC2, we add another linear guide along the $z$-axis to compensate for all introduced offsets. The horn antenna's phase centre is thereby lifted upwards by 1 m. Now, we are able to fix the phase centre of the horn antenna at a specific $(x, y, z)$ coordinate in space. The whole mechanical set-up and the fixed phase centre is illustrated in Fig. 5.

## 4 MC1: Scalar-valued wideband measurements

A wireless channel is said to be small-scale fading, if the receiver (RX) cannot distinguish between different multipath components (MPCs). Depending on the position of the transmitter (TX), the position of the RX and the position of the interacting components, the MPCs interfere constructively or destructively [73, pp. 27]. The fading concept only asks for a single carrier frequency, whose MPCs arrive with different phases at the RX. By spatial sampling, a statistical description of the fading process is found.

In MC1, the spatial $(x, y)$ coordinate (of TX and RX) is kept constant. Different phases of the impinging MPCs are realised by changing the TX frequency over a bandwidth of 7 GHz. Thereby, we implicitly rely on frequency translations to estimate the parameters of the spatial fading process.

### 4.1 Measurement set-up

We measure the forward transfer function with an Rohde and Schwarz R&S ZVA24 vector network analyser (VNA). The VNA can measure directly up to 24 GHz. For mmWave up-conversion and down-conversion, we employ modules from Pasternack [74]. They are based on radio frequency integrated circuits described in [75]. The up-converter module and the down-converter module are operating built-in synthesiser phase-locked loops (PLLs), where the local oscillator (LO) frequency is calculated as:

$$f_{\mathrm{LO}} = 7/4 \cdot s_{\mathrm{PLL}} \cdot 285.714\,\mathrm{MHz} \approx s_{\mathrm{PLL}} \cdot 500\,\mathrm{MHz}\,. \quad (14)$$

The scaling factor of the synthesiser PLL counters is denoted by $s_{\mathrm{PLL}}$. For $f_{\mathrm{LO}} \approx 60\,\mathrm{GHz}$, the scaling factor is $s_{\mathrm{PLL}} = 120$. To avoid crosstalk, we measure the transfer function via the conversion gain (mixer) measurement option of our VNA and operate the transmitter and receiver at different baseband frequencies: 601 to 1100 MHz and 101 to 600 MHz. The set-up is shown in Fig. 6.

### 4.2 Receive power and fading distributions

In Fig. 7, we show the estimated received mean power of 7 GHz bandwidth, normalised to the maximum RX power, that is

$$P_{\mathrm{RX,norm.}}(\varphi, \theta) = \frac{\hat{\Omega}(\varphi, \theta)}{\max_{\varphi', \theta'} \left( \hat{\Omega}(\varphi', \theta') \right)}\,. \quad (15)$$

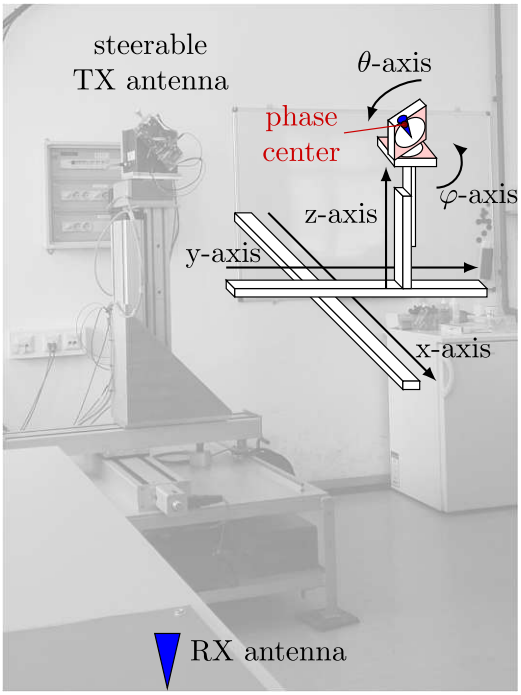


**Fig. 5** Photograph of the improved mechanical set-up for MC2 from the receiver point of view. Our mechanical set-up consists now of five independent axes to fully compensate all offsets introduced by rotation. A schematic sketch is superimposed. All five axes are necessary to rotate the horn antenna around the phase centre at a fixed $(x, y, z)$ coordinate. Notice that TX and RX switch roles as compared to Fig. 4

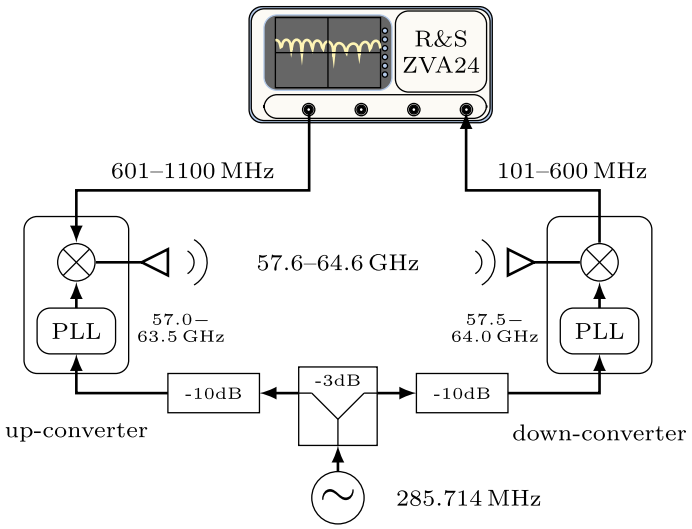


**Fig. 6** RF set-up for MC1. The combination of different PLL scaling factors allows for a measurement bandwidth of 7 GHz. The reference clock for the up-converter and the down-converter is shared. The power splitter has an isolation of 30 dB. To avoid possible leakage on the clock distribution network, attenuators additionally decouple both converters. The transfer function is measured applying the conversion gain (mixer) measurement option of the R&S VNA

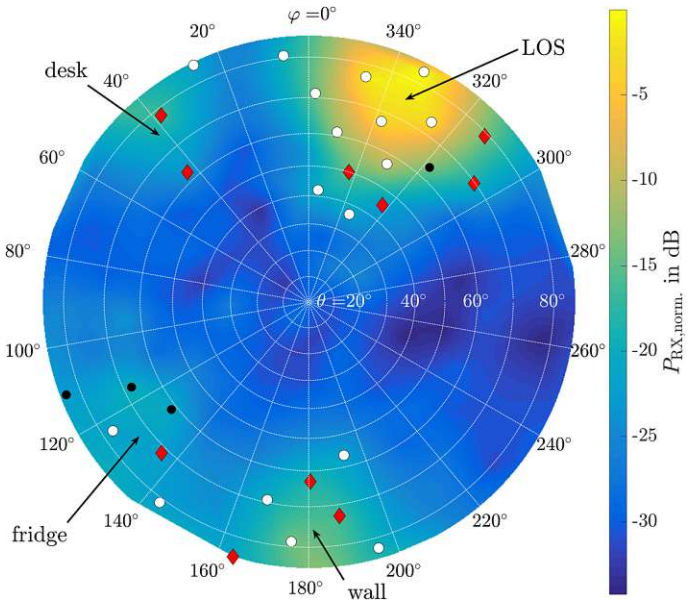


**Fig. 7** Estimated directional receive power of MC1. There are four main interacting objects leading to stronger receive power (marked in the figure). TWDP fading occurs whenever the LOS-link is not perfectly aligned or the reflecting structure is not perfectly plain. Red diamonds mark TWDP fading, and white circles mark Rician fading. Black markers show points where both distributions are rejected by the hypothesis test. Directions less than 10 dB above the noise level are not evaluated

As already mentioned in Section 2, we partition the frequency measurements into two sets. The normalised receive power is calculated according to (7), with frequency samples spaced by 2.5 MHz. Every tenth sample is left out as these samples are used for fitting of $(K, \Delta)$ and hypothesis testing. We display the results via a stereographic projection from the south pole and use $\tan(\theta/2)$ as azimuthal projection. All sampling points, lying at least 10 dB above the noise level, are subject of our study. They are displayed with red, white, or black markers. Sampling points where we decided for TWDP fading, following the procedure described in Section 2, are marked with red diamonds. White circles mark points for which AIC favours Rician fading. Four points are marked black. These points failed the null hypothesis test, and we neither argue for Rician fading nor for TWDP fading. TWDP fading occurs whenever the line-of-sight (LOS)-link is not perfectly aligned or if the interacting object cannot be described by a pure reflection.

In Fig. 8, the $K$-parameter of the selected hypothesis is illustrated. Figure 8 shows either the Rician K-factor or the TWDP K-factor, depending on the selected hypothesis. Note that their definitions are fully equivalent. For Rician fading, the amplitude $V_2$ in (1) is zero by definition. Whenever the RX power is high, the $K$-factor is high. Below the $K$-estimate, the estimate of $\Delta$ is shown. Here again, by definition, $\Delta \equiv 0$ whenever we decide for Rician fading. For interacting objects, the parameter $\Delta$ tends to be close to one. Note, that decisions based on AIC select TWDP fading mostly when $\Delta$ is above 0.3. Smaller $\Delta$ values do not change the distribution function sufficiently to justify a higher model order.

## 5 MC2: Vector-valued spatial measurements

In contrast to MC1, we no longer rely on frequency translations and are indeed sampling the channel in space. The fading results we present in Section 5.3 are evaluated at a single frequency. Fading is hence determined by the obtained spatial samples, exclusively.

### 5.1 Measurement set-up

At the transmitter side, a 2-GHz wide waveform is produced by an arbitrary waveform generator (AWG). A multi-tone waveform (OFDM) with Newman phases [76–78] is applied as sounding signal. The signal has 401 tones (sub-carriers) with a spacing of 5 MHz. This large spacing assures that our system is not limited by phase noise [79]. The TX sequence is repeated 2 000 times to obtain a coherent processing gain of 33 dB for i.i.d. noise. The Pasternack up-converter (the same as in MC1) shifts the baseband sequence to 60 GHz. The 20 dBi conical horn antenna, together with the up-converter is mounted

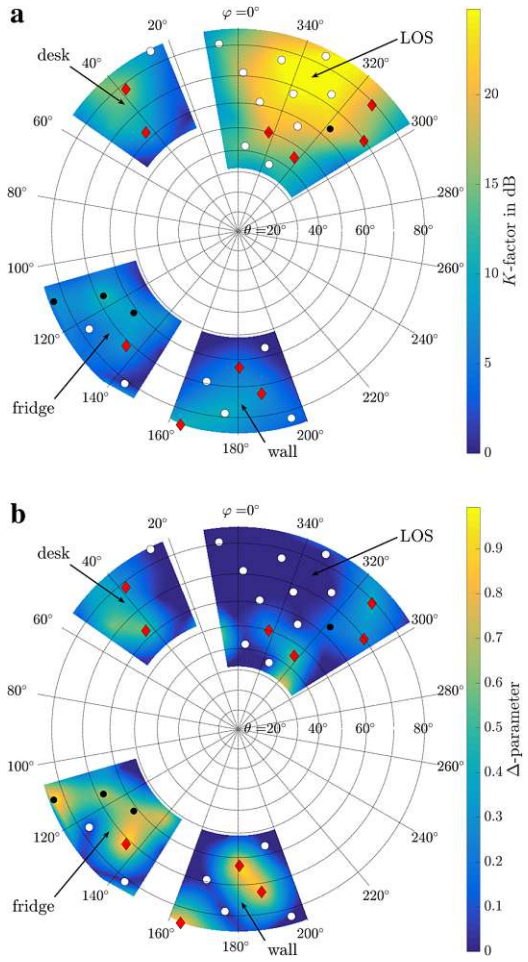


**Fig. 8** Estimated *K*-factor (**a**) and Delta-parameter (**b**) of MC1. We plot the *K*-factor estimate of the selected hypothesis. The *K*-factor behaves analogously to the RX power. At LOS, the *K*-factor is far above 20 dB. The desk reflection has a surprisingly high *K*-factor of about 15 dB. Other reflections have *K*-factors of approximately 10 dB. The Δ-parameter for reflections tends to be close to 1. Markers have the same meaning as in Fig. 7

on a five axis positioner to directionally steer them. As receiver, a signal analyser (SA) (R&S FSW67) with a 2-GHz analysis bandwidth is used. The received in-phase and quadrature (IQ) baseband samples are obtained from the SA. The whole system is sketched in Fig. 9.

In MC2, for feasibility reasons, TX and RX switch places compared to MC1. The RX in form of the SA is put onto the laboratory table. The RX 20 dBi conical horn antenna is directly mounted at the RF input of the SA. The SA is located on a table close to a corner of the room; the RX antenna is not steered.

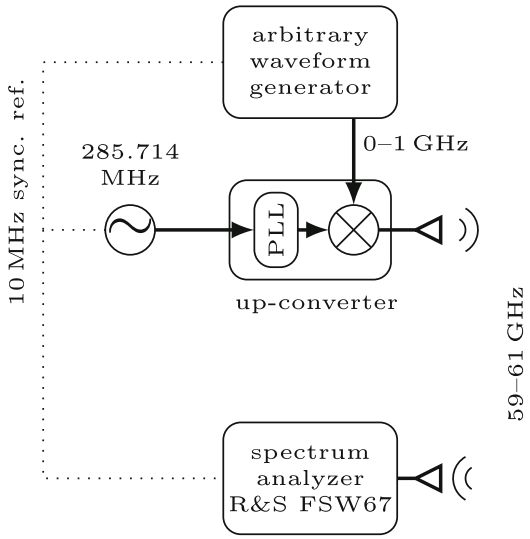


**Fig. 9** RF set-up for MC2. The VNA from Fig. 6 is replaced with an AWG and an SA. This leads to a set-up where we obtain phase information as well. An option of the SA gives us direct access to the baseband IQ samples

Similar to the set-ups of [80–83], proper triggering between the arbitrary waveform generator and the SA ensures a stable phase between subsequent measurements.

### 5.2 Receive power

For the calculation of the RX power, averaged over 2 GHz bandwidth, we perform a sweep through azimuth and elevation at a single coordinate. The LOS and wall reflection from MC1 are still visible in Fig. 10. Fading is evaluated at a single frequency in the subsection below. Nevertheless, we already indicate fading distributions by markers in Fig. 10 in order to better orient ourselves later on.

As the steerable horn antenna is above the office desks and the fridge level, these interacting objects do not become apparent. In case the steerable TX does not hit the RX at LOS accurately, the table surface acts as reflector and a TWDP model explains the data. For wall reflections, with non-ideal alignment, TWDP also explains the data best.

### 5.3 Fading distributions

To obtain different spatial realisations, with the horn antenna pointing into the same direction, the coordinate of the apparent phase centre is moved to $(x, y, z)$ positions uniformly distributed within a cube of side length $2.8\lambda$ (see Fig. 11). We realise a set of $9 \times 9 \times 9 = 729$ directional measurements. This results in a spacing between

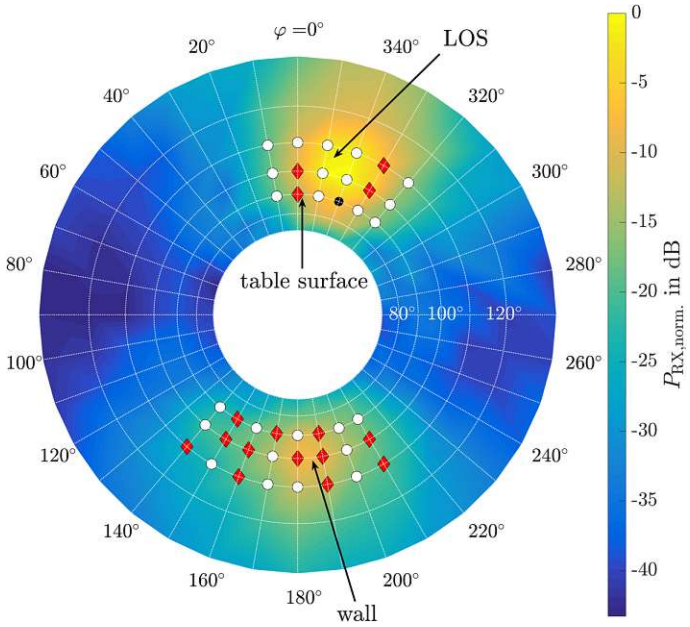


**Fig. 10** Estimated directional receive power of MC2. Due to the elevated position of the steerable horn antenna, two interacting objects from Fig. 7, namely the desk and the fridge, are no longer visible. LOS and the wall reflection are still present. These regions are the only ones which are spatially sampled. Markers have the same meaning as in Fig. 7

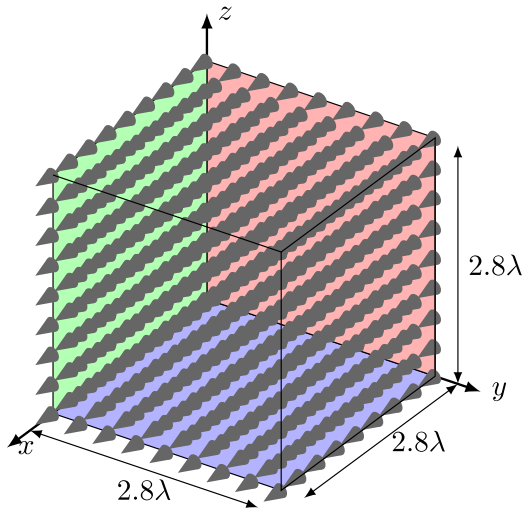


**Fig. 11** Spatial sampling grid. For one specific direction, we draw $9 \times 9 \times 9 = 729$ samples uniformly from a cube of side length $2.8\lambda$. The distance between samples is $0.35\lambda$ with a repeat accuracy of $\pm 0.004\lambda$. The orientation of the horn antenna is indicated via the cone shape at the sampling points

spatial samples of $0.35\lambda$ in each direction. Although $\lambda/2$ sampling is quite common [25, 27], we choose the sampling frequency to be co-prime with the wavelength, to circumvent periodic effects [84]. We restrict our spatial extend to avoid changes in large-scale fading. Only at directions with strong reception levels spatial sampling is performed[2]. Similar as in the previous section, we partition the measurements into 2 sets. The partitioning is made according to a 3D chequerboard pattern. The first set is used for the estimation of the second moment $\hat{\Omega}$, and the second set is used for the parameter tuple $(K, \Delta)$.

The best fitting $K$-factors, in both regions with strong reception, are illustrated in Fig. 12, top part. Below the $\Delta$-parameters are provided. Remember, the RX in form of an SA is put on the laboratory table. In case the TX is not perfectly aligned, a reflection from the table surface yields a fading statistic captured by the TWDP model. The interaction with the wall, similar to Fig. 8, has again regions best modelled via TWDP fading.

## 6 MC2: Efficient computation of the spatial correlation

The wall reflection from the previous section is now subject to a more detailed study. Our spatial samples are used to show spatial correlations among the drawn samples.

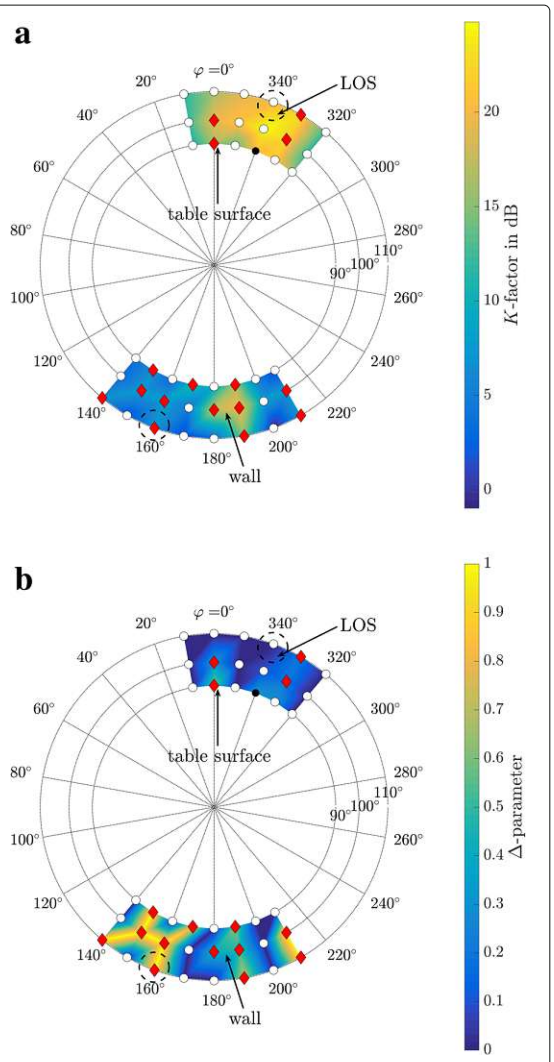


**Fig. 12** Estimated *K*-factor (**a**) and Delta-parameter (**b**) of MC2. Due to the elevated position, the wall reflection has a 6 dB increased *K*-factor as compared to MC1; see top part of Fig. 8. If the beam is not perfectly aligned, Rician fading turns again into TWDP fading. Wall reflections described by TWDP fading have a Δ-parameter of close to one. The table surface reflection leads to a significantly smaller reflected component ($\Delta \ll 1$). The encircled sampling points are subject of further study in Sections 6 and 7. Markers have the same meaning as in Fig. 7

Our three-dimensional sampling problem, see again Fig. 11, is treated via two-dimensional slicing. For the calculation of the spatial (2D) autocorrelation function, we apply the Wiener–Khintchine–Einstein theorem that relates the autocorrelation function of a wide-sense-stationary random process to its power spectrum [85]. In two dimensions, this theorem reads [86, 87]:

$$\mathcal{F}_{2D}\left\{\boldsymbol{C}(x,y)\right\} = \boldsymbol{S}\left(x',y'\right)\,, \tag{16}$$

where $\boldsymbol{C}$ is the 2D-autocorrelation and $\boldsymbol{S}$ is the power spectral density of a 2D signal. The operator $\mathcal{F}_{2D}$ denotes the 2D Fourier transform. We calculate all 2D autocorrelation functions $\boldsymbol{C}^{(z,f)}$ of one $x-y$ slice at height $z$ at a single frequency $f$ through

$$\mathcal{F}_{2D}\left\{\boldsymbol{C}^{(z,f)}(x,y)\right\} = \mathcal{F}_{2D}\left\{\Re\left\{\boldsymbol{H}^{(z,f)}\left(x',y'\right)\right\}\right\} \odot \operatorname{conj}\left\{\mathcal{F}_{2D}\left\{\Re\left\{\boldsymbol{H}^{(z,f)}\left(x',y'\right)\right\}\right\}\right\}\,. \tag{17}$$

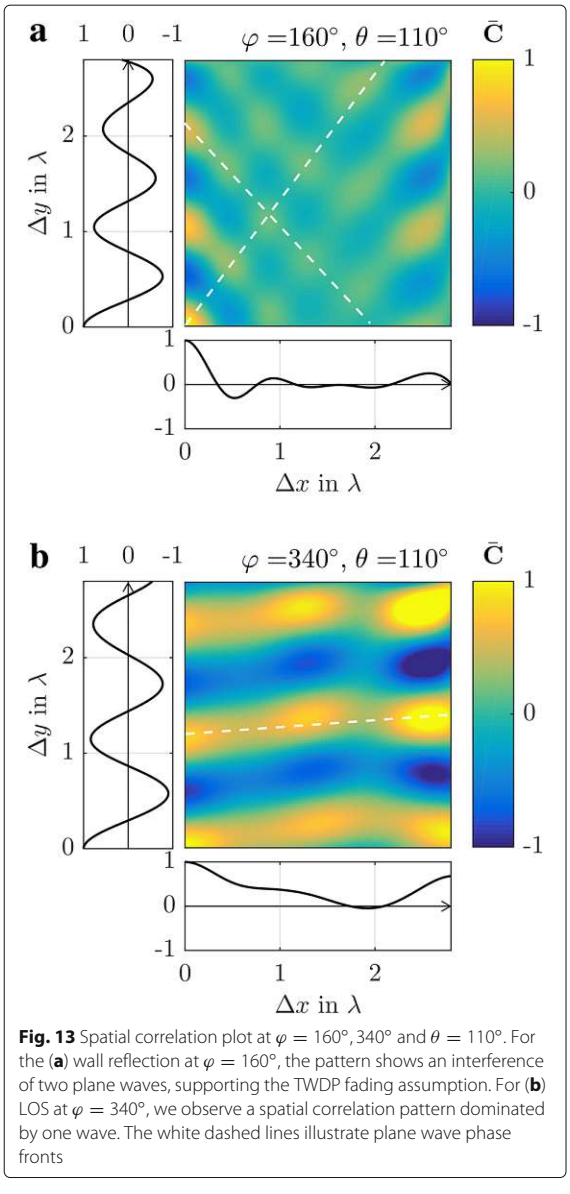


**Fig. 13** Spatial correlation plot at $\varphi = 160°, 340°$ and $\theta = 110°$. For the (**a**) wall reflection at $\varphi = 160°$, the pattern shows an interference of two plane waves, supporting the TWDP fading assumption. For (**b**) LOS at $\varphi = 340°$, we observe a spatial correlation pattern dominated by one wave. The white dashed lines illustrate plane wave phase fronts

The symbols $\odot$ denotes the Hadamard multiplication. The operator conj{·} denotes complex conjugation. To ensure a real-valued autocorrelation matrix (instead of a generally complex representation [87]), from the complex-valued channel samples, only the real parts $\Re\{\cdot\}$ are taken. The spatial autocorrelation of the imaginary parts are identical. One could also analyse the magnitude and phase individually. While the correlation of the magnitude stays almost at 1, the phase correlation patterns are similar to those of the real part.

The 2D Fourier transform $\mathcal{F}_{2D}$ is realised via a 2D discrete Fourier transform (DFT). The 2D DFT is calculated via a multiplication with the DFT matrix $\boldsymbol{D}$ from the left and the right. To mimic a linear convolution with the DFT, zero padding is necessary. We hence take the matrix $\widetilde{\boldsymbol{H}}^{(z,f)}$

$$\widetilde{\boldsymbol{H}}^{(z,f)} = \begin{pmatrix} \Re\left\{\boldsymbol{H}^{(z,f)}\right\} & \mathbf{0} \\ \mathbf{0} & \mathbf{0} \end{pmatrix}. \tag{18}$$

Furthermore, the finite spatial extend of our samples acts as rectangular window. The rectangular window leads to a triangular envelope of the the autocorrelation function. This windowed spatial correlation is denoted by:

$$\mathbf{C}^{(z,f)}_{\text{windowed}} = \boldsymbol{D}^H \left( \left( \boldsymbol{D}\widetilde{\boldsymbol{H}}^{(z,f)}\boldsymbol{D} \right) \odot \text{conj}\left\{ \boldsymbol{D}\widetilde{\boldsymbol{H}}^{(z,f)}\boldsymbol{D} \right\} \right) \mathbf{D}^H. \tag{19}$$

To compensate the windowing effect, we calculate the spatial correlation of the rectangular window, constructed in accordance to (18):

$$\boldsymbol{S} = \boldsymbol{D}^H \left( \left( \boldsymbol{D} \begin{pmatrix} \mathbb{1} & \mathbf{0} \\ \mathbf{0} & \mathbf{0} \end{pmatrix} \mathbf{D} \right) \odot \text{conj}\left\{ \boldsymbol{D} \begin{pmatrix} \mathbb{1} & \mathbf{0} \\ \mathbf{0} & \mathbf{0} \end{pmatrix} \boldsymbol{D} \right\} \right) \boldsymbol{D}^H.$$

The matrix $\mathbb{1}$ denotes the all-ones matrix. Matrix $\boldsymbol{S}$ compensates the truncation effect of the autocorrelation

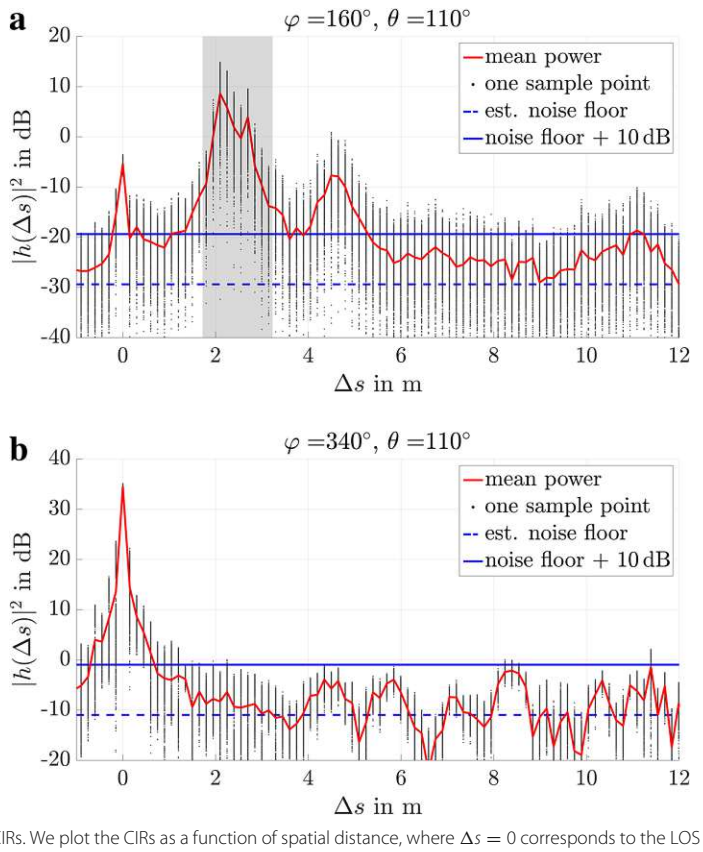


**Fig. 14** Scatter-plot of the CIRs. We plot the CIRs as a function of spatial distance, where $\Delta s = 0$ corresponds to the LOS distance. Our spatial resolution (a channel tap) is 15 cm. The spatial extend of our sampled cube (729 samples) is $2.8\lambda = 1.4$ cm, a magnitude smaller than the spatial resolution. The scatter-plot is evaluated at a (**a**) wall reflection ($\varphi = 160°$) and at (**b**) LOS ($\varphi = 340°$). The mean power is plotted with a continous red line. We observe that the arrival cluster centred at 2.5 m fades very deeply. The gray highlighted region around 2.5 m is further analysed in Fig. 15

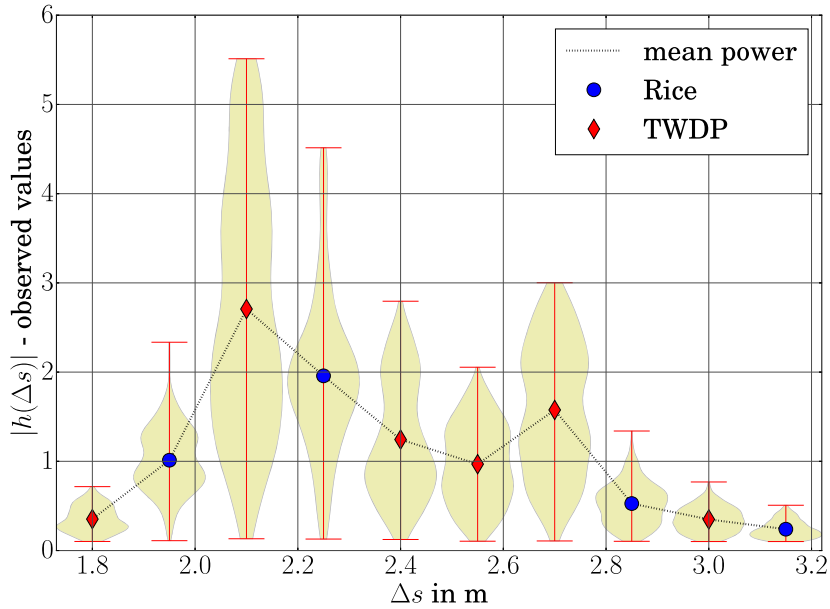


**Fig. 15** Violin-plot of the CIR time-gated for the wall reflection. This figure shows a zoom-in of the gray-highlighted region in Fig. 14. In contrast to Fig. 14, the *y*-axis is in linear scale. Thereby, the violin plot indicates the distribution at each tap. The marker shows the mean value. The marker style codes best fitting distributions

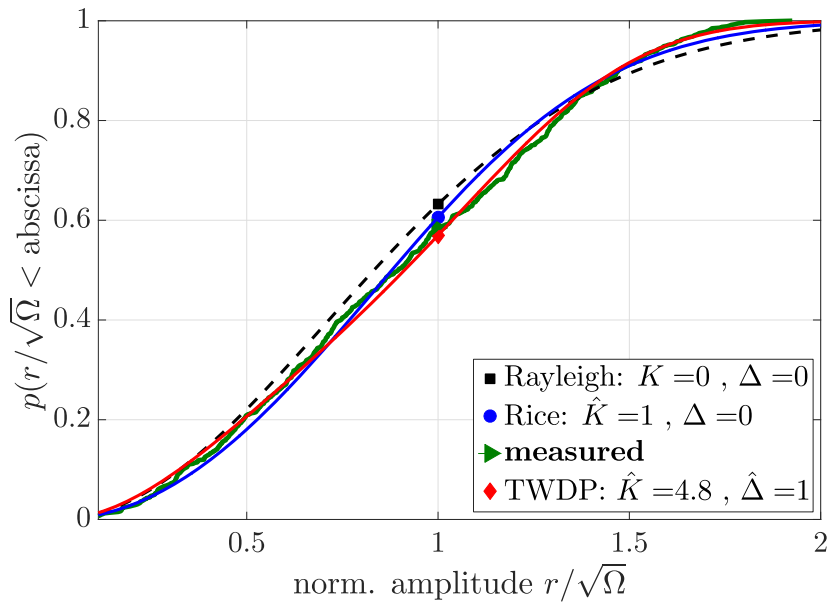


**Fig. 16** CDF: Distribution fitting for spatial measurement data, time gated by the channel tap at 2.5 m, $\varphi = 160°$, and $\theta = 110°$. Note that, similar to the fitting result in Fig. 2, the estimated Rician K-factor is again much smaller than the TWDP K-factor

through element-wise (Hadamard) division, denoted by $\oslash$. Finally, the efficient computation of the spatial correlation (17) reads:

$$\boldsymbol{C}^{(z,f)} = \boldsymbol{C}^{(z,f)}_{\text{windowed}} \oslash \boldsymbol{S} \,. \tag{20}$$

At a distance of $0.35\lambda$, the measurement data is still correlated; therefore, we are able to view our correlation results on the finer, interpolated grid. The interpolation factor is 20. That means that our spatial correlations are shown on a grid of $^{0.35\lambda}/_{20} = 0.0175\lambda$ distance. The very efficient implementation of (20) is applied to all (parallel) 2D slices and to all frequencies. All realisations in $z$ and $f$ are averaged:

$$\bar{\boldsymbol{C}} = \frac{1}{9}\frac{1}{401}\sum_{z=1}^{9}\sum_{f=1}^{401}\boldsymbol{C}^{(z,f)} \,. \tag{21}$$

Furthermore, we plot one-dimensional autocorrelation functions, evaluated along $x$ and $y$, together with their two-dimensional representations. We provide two spatial correlation plots evaluated at an azimuth angle of $\varphi = 340°$ and $\varphi = 160°$ in Fig. 13, both at an elevation angle of $\theta = 110°$. The bottom part of Fig. 13 shows a correlation pattern dominated by a single wave. The spatial correlation above shows an interference pattern, which is intuitively explained by a superposition of two plane waves. The one dimensional correlations, evaluated either at the $x$-axis or at the $y$-axis, show this oscillatory behaviour as well.

## 7 MC2: Time-gated fading results

To confirm that our observations are not artefacts of our measurement set-up, for example back-lobes of the horn antenna, we now study the wireless channel in the time domain. Our 2-GHz wide measurements from MC2 allow for a time resolution of approximately 0.5 ns. This corresponds to a spatial resolution of 15 cm. We plot the channel impulse responses (CIRs) as a function of distance, namely the LOS excess length $\Delta s$, that is:

$$h(\Delta s) = h((\tau - \tau_{\text{LOS}})c_0) \,. \tag{22}$$

The scatter-plot of the CIRs for $\varphi = 160°$ is shown in Fig. 14. The LOS CIR at $\varphi = 340°$ is displayed as reference as well. The steerable TX is positioned more than a metre apart from the wall. This amounts in an excess distance of approximately two to three metres. At this excess distance, a cluster of multipath components is present. Note, if the horn antenna points towards the wall, the wave emitted by the back-lobe of the horn antenna is received at zero excess distance. Still, the receive power of the back-lobe is far below the components arriving from the wall reflection. Fading is hence determined by the wall scattering behaviour.

The gray-highlighted region of Fig. 14 (top part) shows a reflection cluster that corresponds to the excess distance of the wall reflection. The distributions of each channel tap are represented by a violin plot in Fig. 15. A violin plot illustrates the distribution estimated via Gaussian kernels [88]. Figure 15 clearly demonstrates that the TWDP-decided distributions have multiple modes. The AIC decisions are plotted as markers at the mean power levels.

We evaluated the fading statistic in space for $\varphi = 160°$ at the channel tap corresponding to approximately 2.5 m excess distance. This channel tap is mid in the cluster belonging to the wall reflection. Fig. 16 clearly shows a TWDP fading behaviour, confirmed by AIC.

## 8 Conclusion

We demonstrate, by means of model selection and hypothesis testing, that TWDP fading explains observed indoor millimetre wave channels. Rician fits of reported studies must be considered with caution. As two exemplary fits, in Figs. 2 and 16, show Rician K-factors tend to be much smaller than their TWDP companions. There is more power in the specular components than is predicted by the Rician fit. The TWDP fading fit accounts for a possible cancellation of two specular waves. Our results are verified through two independent measurement campaigns. For MC1 and MC2 we even used different RF hardware. While MC1 was limited to results in the frequency domain, MC2 allowed a careful study in the spatial-domain and the time-domain.

Having this strong evidence at hand, we claim that the TWDP fading model is more accurate to describe mmWave indoor channels. The flexibility of this model allows furthermore to obtain Rician fading ($\Delta \equiv 0$) and Rayleigh fading ($K \equiv 0$) results with the same channel model.

## Endnotes

[1] The well-known chi-squared test approximates the $g$-test via a local linearisation [89].

[2] Spatial sampling for all directions takes more than 3 days.

### Abbreviations

AIC: Akaike's information criterion; AWG: Arbitrary waveform generator; BER: Bit error ratio; CDF: Cumulative distribution function; CIR: Channel impulse response; DFT: Discrete Fourier transform; IQ: In-phase and quadrature; LO: Local oscillator; LOS: Line-of-sight; MC1: First measurement campaign; MC2: Second measurement campaign; mmWave: Millimetre wave; MPC: Multipath component; NLOS: Non-line-of-sight; PDF: Probability density function; PLL: Phase-locked loop; RX: Receiver; SA: Signal analyser; RF: Radio frequency; SNR: Signal-to-noise ratio; TWDP: Two-wave with diffuse power; TX: Transmitter; VNA: Vector network analyser

**Acknowledgements**
The financial support by the Austrian Federal Ministry for Digital and Economic Affairs and the National Foundation for Research, Technology and Development is gratefully acknowledged. The research has been co-financed by the Czech Science Foundation, Project No. 17-18675S "Future transceiver techniques for the society in motion", and by the Czech Ministry of Education in the frame of the National Sustainability Program under grant LO1401. The authors would like to thank Ronald Brunner from Rohde & Schwarz Austria for his great support during the measurement campaign. The authors acknowledge the TU Wien University Library for financial support through its Open Access Funding Program.

**Authors' contributions**
EZ conducted the measurements, fitted the data. EZ and SC were writing the article. CFM brought in the idea of hypothesis testing. SC, SP, and ML were co-developing the measurement set-ups. SS was introducing the TWDP model to the group. MR was connecting the dots between previous two-ray model contributions and TWDP fading. All authors were proof-reading and reviewing the manuscript. All authors read and approved the final manuscript.

**Competing interests**
The authors declare that they have no competing interests.

## Publisher's Note

Springer Nature remains neutral with regard to jurisdictional claims in published maps and institutional affiliations.

**Author details**
[1]Christian Doppler Laboratory for Dependable Wireless Connectivity for the Society in Motion, TU Wien, Gußhaustraße 25, 1040 Vienna, Austria. [2]Institute of Telecommunications, TU Wien, Gußhaustraße 25, 1040 Vienna, Austria. [3]Department of Radio Electronics, TU Brno, Technicka 3082, 616 00 Brno, Czech Republic.

Received: 21 March 2018 Accepted: 21 December 2018
Published online: 24 January 2019

**References**

1. M. Steinbauer, A. F. Molisch, E. Bonek, The double-directional radio channel. IEEE Antennas Propag. Mag. **43**(4), 51–63 (2001)
2. C. R. Anderson, T. S. Rappaport, In-building wideband partition loss measurements at 2.5 and 60 GHz. IEEE Trans. Wirel. Commun. **3**(3), 922–928 (2004)
3. N. Moraitis, P. Constantinou, Measurements and characterization of wideband indoor radio channel at 60 GHz. IEEE Trans. Wirel. Commun. **5**(4), 880–889 (2006)
4. S. Geng, J. Kivinen, X. Zhao, P. Vainikainen, Millimeter-wave propagation channel characterization for short-range wireless communications. IEEE Trans. Veh. Technol. **58**(1), 3–13 (2009)
5. K. Wangchuk, K. Umeki, T. Iwata, P. Hanpinitsak, M. Kim, K. Saito, J.-i. Takada, Double directional millimeter wave propagation channel measurement and polarimetric cluster properties in outdoor urban pico-cell environment. IEICE Trans. Commun. **100**(7), 1133–1144 (2017)
6. M. Peter, W. Keusgen, R. J. Weiler, in *Proc. of 9th European Conference on Antennas and Propagation (EuCAP)*. On path loss measurement and modeling for millimeter-wave 5G (IEEE, Lisbon, 2015), pp. 1–5
7. M. Peter, R. J. Weiler, B. Göktepe, W. Keusgen, K. Sakaguchi, Channel measurement and modeling for 5G urban microcellular scenarios. Sensors. **16**(8), 1330 (2016)
8. M. K. Samimi, T. S. Rappaport, G. R. MacCartney, Probabilistic omnidirectional path loss models for millimeter-wave outdoor communications. IEEE Wirel. Commun. Lett. **4**(4), 357–360 (2015)
9. S. Deng, M. K. Samimi, T. S. Rappaport, in *Proc. of IEEE International Conference on Communication Workshop (ICCW)*. 28 GHz and 73 GHz millimeter-wave indoor propagation measurements and path loss models (IEEE, London, 2015), pp. 1244–1250
10. G. R. MacCartney, T. S. Rappaport, M. K. Samimi, S. Sun, Millimeter-wave omnidirectional path loss data for small cell 5G channel modeling. IEEE Access. **3**, 1573–1580 (2015)
11. W. Roh, J.-Y. Seol, J. Park, B. Lee, J. Lee, Y. Kim, J. Cho, K. Cheun, F. Aryanfar, Millimeter-wave beamforming as an enabling technology for 5G cellular communications: Theoretical feasibility and prototype results. IEEE Commun. Mag. **52**(2), 106–113 (2014)
12. S. Hur, T. Kim, D. J. Love, J. V. Krogmeier, T. A. Thomas, A. Ghosh, Millimeter wave beamforming for wireless backhaul and access in small cell networks. IEEE Trans. Commun. **61**(10), 4391–4403 (2013)
13. S. Sun, T. S. Rappaport, R. W. Heath, A. Nix, S. Rangan, MIMO for millimeter-wave wireless communications: Beamforming, spatial multiplexing, or both? IEEE Commun. Mag. **52**(12), 110–121 (2014)
14. Z. Pi, F. Khan, An introduction to millimeter-wave mobile broadband systems. IEEE Commun. Mag. **49**(6), 101–107 (2011)
15. R. W. Heath, N. Gonzalez-Prelcic, S. Rangan, W. Roh, A. M. Sayeed, An overview of signal processing techniques for millimeter wave MIMO systems. IEEE J. Sel. Top. Sign. Process. **10**(3), 436–453 (2016)
16. J. G. Andrews, T. Bai, M. N. Kulkarni, A. Alkhateeb, A. K. Gupta, R. W. Heath, Modeling and analyzing millimeter wave cellular systems. IEEE Trans. Commun. **65**(1), 403–430 (2017)
17. A. Alkhateeb, O. El Ayach, G. Leus, R. W. Heath, Channel estimation and hybrid precoding for millimeter wave cellular systems. IEEE J. Sel. Top. Sign. Process. **8**(5), 831–846 (2014)
18. M. N. Kulkarni, A. Ghosh, J. G. Andrews, A comparison of MIMO techniques in downlink millimeter wave cellular networks with hybrid beamforming. IEEE Trans. Commun. **64**(5), 1952–1967 (2016)
19. E. Zöchmann, S. Schwarz, M. Rupp, in *Proc. of IEEE Sensor Array and Multichannel Signal Processing Workshop (SAM)*. Comparing antenna selection and hybrid precoding for millimeter wave wireless communications (IEEE, Rio de Janerio, 2016), pp. 1–5
20. S. Pratschner, S. Caban, S. Schwarz, M. Rupp, in *Proc. of 25th European Signal Processing Conference (EUSIPCO)*. A mutual coupling model for massive MIMO applied to the 3GPP 3D channel model (IEEE, Kos, 2017), pp. 623–627
21. J. Brady, N. Behdad, A. M. Sayeed, Beamspace MIMO for millimeter-wave communications: System architecture, modeling, analysis, and measurements. IEEE Trans. Antennas Propag. **61**(7), 3814–3827 (2013)
22. Y. Zeng, R. Zhang, Millimeter wave MIMO with lens antenna array: A new path division multiplexing paradigm. IEEE Trans. Commun. **64**(4), 1557–1571 (2016)
23. Y. Zeng, R. Zhang, Cost-effective millimeter-wave communications with lens antenna array. IEEE Wirel. Commun. **24**(4), 81–87 (2017)
24. G. D. Durgin, *Space-time Wireless Channels*. (Prentice Hall Professional, Upper Saddle River, 2003)
25. D. Dupleich, N. Iqbal, C. Schneider, S. Haefner, R. Müller, S. Skoblikov, J. Luo, R. Thomä, in *Proc. of 11th European Conference on Antennas and Propagation (EUCAP)*. Investigations on fading scaling with bandwidth and directivity at 60 GHz (IEEE, Paris, 2017), pp. 3375–3379
26. N. Iqbal, C. Schneider, J. Luo, D. Dupleich, R. Müller, S. Haefner, R. S. Thomä, in *Proc. of 11th European Conference on Antennas and Propagation (EUCAP)*. On the stochastic and deterministic behavior of mmWave channels (IEEE, Paris, 2017), pp. 1813–1817
27. M. K. Samimi, G. R. MacCartney, S. Sun, T. S. Rappaport, in *Proc. of Vehicular Technology Conference (VTC Spring)*. 28 GHz millimeter-wave ultrawideband small-scale fading models in wireless channels (IEEE, Nanjing, 2016), pp. 1–6
28. S. Sun, H. Yan, G. R. MacCartney, T. S. Rappaport, in *Proc. of IEEE International Conference on Communications (ICC)*. Millimeter wave small-scale spatial statistics in an urban microcell scenario (IEEE, Paris, 2017), pp. 1–7
29. T. S. Rappaport, G. R. MacCartney, S. Sun, H. Yan, S. Deng, Small-scale, local area, and transitional millimeter wave propagation for 5G communications. IEEE Trans. Antennas Propag. **65**(12), 6474–6490 (2017)
30. T. Mavridis, L. Petrillo, J. Sarrazin, A. Benlarbi-Delai, P. De Doncker, Near-body shadowing analysis at 60 GHz. IEEE Trans. Antennas Propag. **63**(10), 4505–4511 (2015)
31. G. D. Durgin, T. S. Rappaport, D. A. De Wolf, New analytical models and probability density functions for fading in wireless communications. IEEE Trans. Commun. **50**(6), 1005–1015 (2002)
32. R. Esposito, L. Wilson, Statistical properties of two sine waves in Gaussian noise. IEEE Trans. Inf. Theory. **19**(2), 176–183 (1973)
33. S. H. Oh, K. H. Li, BER performance of BPSK receivers over two-wave with diffuse power fading channels. IEEE Trans. Wirel. Commun. **4**(4), 1448–1454 (2005)
34. S. A. Saberali, N. C. Beaulieu, New expressions for TWDP fading statistics. IEEE Wirel. Commun. Lett. **2**(6), 643–646 (2013)

35. M. Rao, F. J. Lopez-Martinez, M.-S. Alouini, A. Goldsmith, MGF approach to the analysis of generalized two-ray fading models. IEEE Trans. Wirel. Commun. **14**(5), 2548–2561 (2015)
36. S. Schwarz, Outage investigation of beamforming over random-phase finite-scatterer MISO channels. IEEE Signal Proc. Lett. **24**(7), 1029–1033 (2017)
37. S. Schwarz, in *Proc. of IEEE Vehicular Technology Conference (VTC-Fall)*. Outage-based multi-user admission control for random-phase finite-scatterer MISO channels (Montreal, 2017), pp. 1–5
38. J. Frolik, A case for considering hyper-Rayleigh fading channels. IEEE Trans. Wirel. Commun. **6**(4), 1235–1239 (2007)
39. J. Frolik, On appropriate models for characterizing hyper-Rayleigh fading. IEEE Trans. Wirel. Commun. **7**(12), 5202–5207 (2008)
40. J. Frolik, T. M. Weller, S. DiStasi, J. Cooper, A compact reverberation chamber for hyper-Rayleigh channel emulation. IEEE Trans. Antennas Propag. **57**(12), 3962–3968 (2009)
41. D. W. Matolak, J. Frolik, Worse-than-Rayleigh fading: Experimental results and theoretical models. IEEE Commun. Mag. **49**(4), 140–146 (2011)
42. L. Bakir, J. Frolik, Diversity gains in two-ray fading channels. IEEE Trans. Wirel. Commun. **8**(2), 968–977 (2009)
43. E. Zöchmann, K. Guan, M. Rupp, in *Proc. of Workshop on Signal Processing Advances in Wireless Communications (SPAWC)*. Two-ray models in mmWave communications, (2017), pp. 1–5
44. J. M. Romero-Jerez, F. J. Lopez-Martinez, J. F. Paris, A. J. Goldsmith, The fluctuating two-ray fading model: Statistical characterization and performance analysis. IEEE Trans. Wirel. Commun. **16**(7), 4420–4432 (2017)
45. J. Zhang, W. Zeng, X. Li, Q. Sun, K. P. Peppas, New results on the fluctuating two-ray model with arbitrary fading parameters and its applications. IEEE Trans. Veh. Technol. **67**(3), 2766–2770 (2018)
46. W. Zeng, J. Zhang, S. Chen, K. P. Peppas, B. Ai, Physical layer security over fluctuating two-ray fading channels. IEEE Trans. Veh. Technol. **67**(9), 8949–8953 (2018)
47. E. Zöchmann, M. Lerch, S. Caban, R. Langwieser, C. Mecklenbräuker, M. Rupp, in *Proc. of IEEE Topical Conference on Antennas and Propagation in Wireless Communications (APWC)*. Directional evaluation of receive power, Rician K-factor and RMS delay spread obtained from power measurements of 60 GHz indoor channels, (2016), pp. 1–4
48. E. Zöchmann, M. Lerch, S. Pratschner, R. Nissel, S. Caban, M. Rupp, in *Proc. of IEEE Vehicular Technology Conference (VTC-Fall)*. Associating spatial information to directional millimeter wave channel measurements, (2017), pp. 1–5
49. K. P. Burnham, D. R. Anderson, *Model Selection and Multimodel Inference: a Practical Information-theoretic Approach*. (Springer, New York, 2003)
50. R. W. Frick, The appropriate use of null hypothesis testing. Psychol. Methods. **1**(4), 379 (1996)
51. C. A. Balanis, *Antenna Theory: Analysis and Design*. (Wiley, Hoboken, 2005)
52. J. O. Berger, W. H. Jefferys, The application of robust Bayesian analysis to hypothesis testing and Occam's razor. J. Ital. Stat. Soc. **1**(1), 17–32 (1992)
53. A. Maydeu-Olivares, C. Garcia-Forero, Goodness-of-fit testing. Int. Encycl. Educ. **7**(1), 190–196 (2010)
54. U. G. Schuster, H. Bolcskei, Ultrawideband channel modeling on the basis of information-theoretic criteria. IEEE Trans. Wirel. Commun. **6**(7), 2464–2475 (2007)
55. H. Akaike, A new look at the statistical model identification. IEEE Trans. Autom. Control. **19**(6), 716–723 (1974)
56. T. M. Ludden, S. L. Beal, L. B. Sheiner, Comparison of the Akaike information criterion, the Schwarz criterion and the F test as guides to model selection. J. Pharmacokinet. Biopharm. **22**(5), 431–445 (1994)
57. K. P. Burnham, D. R. Anderson, Multimodel inference: understanding AIC and BIC in model selection. Sociol. Methods Res. **33**(2), 261–304 (2004)
58. R. He, A. F. Molisch, F. Tufvesson, Z. Zhong, B. Ai, T. Zhang, Vehicle-to-vehicle propagation models with large vehicle obstructions. IEEE Trans. Intell. Transp. Syst. **15**(5), 2237–2248 (2014)
59. T. Santos, F. Tufvesson, A. F. Molisch, Modeling the ultra-wideband outdoor channel: Model specification and validation. IEEE Trans. Wirel. Commun. **9**(6), 1987–1997 (2010)
60. R. He, Z. Zhong, B. Ai, G. Wang, J. Ding, A. F. Molisch, Measurements and analysis of propagation channels in high-speed railway viaducts. IEEE Trans. Wirel. Commun. **12**(2), 794–805 (2013)
61. K. Guan, Z. Zhong, B. Ai, T. Kürner, Propagation measurements and modeling of crossing bridges on high-speed railway at 930 MHz. IEEE Trans. Veh. Technol. **63**(2), 502–517 (2014)
62. R. He, Z. Zhong, B. Ai, J. Ding, Y. Yang, A. F. Molisch, Short-term fading behavior in high-speed railway cutting scenario: Measurements, analysis, and statistical models. IEEE Trans. Antennas Propag. **61**(4), 2209–2222 (2013)
63. D. Kim, H. Lee, J. Kang, Comments on "Near-body shadowing analysis at 60 GHz". IEEE Trans. Antennas Propag. **65**(6), 3314–3314 (2017)
64. J. Lopez-Fernandez, L. Moreno-Pozas, F. J. Lopez-Martinez, E. Martos-Naya, Joint parameter estimation for the two-wave with diffuse power fading model. Sensors. **16**(7), 1014 (2016)
65. J. Lopez-Fernandez, L. Moreno-Pozas, E. Martos-Naya, F. J. López-Martínez, in *Proc. of the 84th IEEE Vehicular Technology Conference (VTC-Fall)*. Moment-based parameter estimation for the two-wave with diffuse power fading model (IEEE, Montreal, 2016), pp. 1–5
66. A. S. Goldberger, *Econometric Theory*. (Wiley, New York, 1964)
67. J. H. McDonald, *Handbook of Biological Statistics vol. 2*. (Sparky House Publishing Baltimore, MD, Baltimore, 2009)
68. B. Woolf, The log likelihood ratio test (the g-test): Methods and tables for tests of heterogeneity in contingency tables. Ann. Hum. Genet. **21**(4), 397–409 (1957)
69. Q. H. Spencer, B. D. Jeffs, M. A. Jensen, A. L. Swindlehurst, Modeling the statistical time and angle of arrival characteristics of an indoor multipath channel. IEEE J. Sel. Areas Commun. **18**(3), 347–360 (2000)
70. G. D. Durgin, V. Kukshya, T. S. Rappaport, Wideband measurements of angle and delay dispersion for outdoor and indoor peer-to-peer radio channels at 1920 MHz. IEEE Trans. Antennas Propag. **51**(5), 936–944 (2003)
71. F. Fuschini, S. Häfner, M. Zoli, R. Müller, E. M. Vitucci, D. Dupleich, M. Barbiroli, J. Luo, E. Schulz, V. Degli-Esposti, R. S. Thomä, Analysis of in-room mm-Wave propagation: Directional channel measurements and ray tracing simulations. J. Infrared Millimeter Terahertz Waves. **38**(6), 727–744 (2017)
72. J. Vehmas, J. Jarvelainen, S. L. H. Nguyen, R. Naderpour, K. Haneda, in *Proc. of IEEE Vehicular Technology Conference (VTC-Fall)*. Millimeter-wave channel characterization at Helsinki airport in the 15, 28, and 60 GHz bands, (2016)
73. A. F. Molisch, *Wireless Communications vol. 34*. (Wiley, Chichester, 2012)
74. Pasternack 60 GHz Transmitter and 60 GHz Receiver Modules. https://www.pasternack.com/60-ghz-modules-category.aspx
75. P. Zetterberg, R. Fardi, Open source SDR frontend and measurements for 60-GHz wireless experimentation. IEEE Access. **3**, 445–456 (2015)
76. S. Sangodoyin, J. Salmi, S. Niranjayan, A. F. Molisch, in *Proc. of Antennas and Propagation Conference (EUCAP)*. Real-time ultrawideband MIMO channel sounding (IEEE, Prague, 2012)
77. M. Kim, H. K. Pham, Y. Chang, J.-i. Takada, in *Proc. of Global Symposium on Millimeter Wave (GSMM)*. Development of low-cost 60-GHz millimeter-wave channel sounding system, (2013)
78. E. Zöchmann, C. Mecklenbräuker, M. Lerch, S. Pratschner, M. Hofer, D. Löschenbrand, J. Blumenstein, S. Sangodoyin, G. Artner, S. Caban, T. Zemen, A. Prokes, M. Rupp, A. F. Molisch, in *Proc. of the 12th European Conference on Antennas and Propagation (EuCAP)*. Measured delay and Doppler profiles of overtaking vehicles at 60 GHz (IEEE, London, 2018), pp. 1–5
79. M. Lerch, E. Zöchmann, S. Caban, M. Rupp, in *Proc. of European Wireless*. Noise bounds in multicarrier mmWave Doppler measurements, (2017)
80. R. Nissel, E. Zöchmann, M. Lerch, S. Caban, M. Rupp, in *Proc. of IEEE International Microwave Symposium (IMS)*. Low latency MISO FBMC-OQAM: It works for millimeter waves! (2017)
81. M. Lerch, S. Caban, M. Mayer, M. Rupp, The Vienna MIMO testbed: Evaluation of future mobile communications techniques. Intel Technol. J. **18**(3), 58–69 (2014)
82. S. Caban, A. Disslbacher-Fink, J. A. García-Naya, M. Rupp, in *Proc. of IEEE Instrumentation and Measurement Technology Conference (I2MTC)*. Synchronization of wireless radio testbed measurements (IEEE, Binjiang, 2011), pp. 1–4
83. M. Laner, S. Caban, P. Svoboda, M. Rupp, in *Proc. of IEEE Symposium on Precision Clock Synchronization for Measurement Control and Communication (ISPCS)*. Time synchronization performance of desktop computers (IEEE, Munich, 2011), pp. 75–80
84. R. Haining, *Spatial Data Analysis in the Social and Environmental Sciences*. (Cambridge University Press, Cambridge, 1993)

85. A. Khintchine, Korrelationstheorie der stationären stochastischen Prozesse. Math. Ann. **109**(1), 604–615 (1934)
86. T. A. Ell, S. J. Sangwine, in *Proc. of International Conference on Image Processing*. Hypercomplex Wiener-Khintchine theorem with application to color image correlation, vol. 2 (IEEE, Vancouver, 2000), pp. 792–795
87. C. E. Moxey, S. J. Sangwine, T. A. Ell, Hypercomplex correlation techniques for vector images. IEEE Trans. Signal Process. **51**(7), 1941–1953 (2003)
88. J. L. Hintze, R. D. Nelson, Violin plots: a box plot-density trace synergism. Am. Stat. **52**(2), 181–184 (1998)
89. J. Hoey, The two-way likelihood ratio (G) test and comparison to two-way Chi squared test. arXiv preprint arXiv:1206.4881 (2012)

ACCEPTED FROM OPEN CALL

# CELLULAR SYSTEM PHYSICAL LAYER THROUGHPUT: HOW FAR OFF ARE WE FROM THE SHANNON BOUND?

CHRISTIAN MEHLFÜHRER, SEBASTIAN CABAN, AND MARKUS RUPP,
VIENNA UNIVERSITY OF TECHNOLOGY

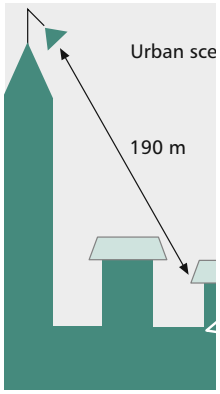


The authors take a closer look at WiMAX and HSDPA, two successful cellular systems that are being operated currently in many countries and check their truly achievable performance.

## ABSTRACT

Cellular wireless systems have made impressive progress over the past two decades. They currently connect more than five billion people worldwide. With the advent of turbo decoders in the 1990s, the design of optimal decoders very close to the Shannon bound became possible in AWGN channels. Nowadays many researchers believe that this is true for entire wireless systems and that therefore there is not much left to investigate. In this contribution, we take a closer look at WiMAX and HSDPA, two successful cellular systems being operated currently in many countries, and check their truly achievable performance. We have measured the physical layer throughput of WiMAX and HSDPA in various realistic environments (urban and mountainous) with high-quality equipment and different antenna configurations. We furthermore compared the throughput measured to the Shannon bound. Based on our measurements, we analyze the losses in design and implementation (e.g., pilots, guard carriers, coding, equalization, and channel estimation) and report our findings. Surprisingly, we are currently only utilizing 40 percent of the available channel capacity; or roughly equivalently, we are up to 10 dB off the Shannon bound at typical operational points, thus providing a lot of potential improvement for future 4G systems. In advanced four transmit antenna configurations of HSDPA, the losses are even more pronounced, showing that our current standards are not well suited to take advantage of the much higher capacity provided.

*This work has been funded by the Christian Doppler Laboratory for Wireless Technologies for Sustainable Mobility, the Institute of Communications and Radio Frequency Engineering, and KATHREIN-Werke KG as well as A1 Telekom Austria AG. The financial support of the Federal Ministry of Economy, Family and Youth and the National Foundation for Research, Technology and Development is gratefully acknowledged. We further thank Gottfried Lechner for designing the LDPC code for WiMAX and Christoph Mecklenbräuker for his profound leadership.*

## INTRODUCTION

In 1948, Claude Shannon provided us with a clear channel capacity bound for point-to-point connections [1]. This bound was extended independently in the mid-1990s by Gerry Foschini and Mike Gans [2] as well as by Emre Telatar [3] to the case of multiple transmit and receive antennas (multiple-input multiple-output, MIMO). It is this bound measured in small frequency bins over the utilized bandwidth (Eq. 1 ahead) to which we refer and compare our throughput results. It is this bound that coding experts compare to their turbo codes as well as their iterative receivers. Note, however, that this bound is a single user bound, even if it supports several transmit and receive antennas. Considering multiple users and/or interference is much more difficult. In many situations, the definition of capacity alone is still under discussion. Furthermore, the Shannon bound describes aspects of the physical layer system, not the scheduling techniques, network routing issues, or application layer facets. It is thus far from describing the entire third-generation (3G) system performance, but merely an important piece: the channel.

Nowadays, mathematical models are very common for predicting the performance of systems designed by either mankind or nature. We apply mathematical models to predict tomorrow's weather, our climate 100 years from now, and the performance of next-generation wireless systems. Clearly, models reflect the behavior of the system under investigation. Depending on how precisely we know such a modeled system or subsystem, our prediction models can be more or less accurate. Higher accuracy typically comes with the price of parameter and complexity increase, yet the beauty of a model lies in its simplicity. Once they contain hundreds of parameters and require many hours of simulation time for each new parameter setup, models become less and less treatable. Unfortunately, wireless 3G systems are very complex systems with hundreds of parameters. The channel, a significant part of wireless systems, is still a hot topic for


1536-1284/11/$25.00 © 2011 IEEE

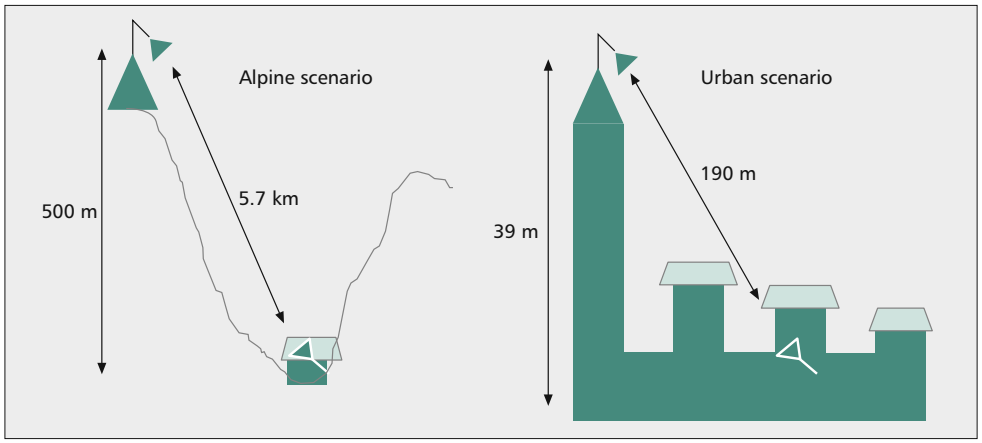


**Figure 1.** *Schematic view of the two measurement scenarios, left: alpine, right: urban.*

investigation. A recent channel model (e.g., Winner Phase 2+) may contain more than 100 parameters to support a multitude of situations with extreme flexibility. If not an expert in modeling, such complex channel models can easily be mistreated and wrong results generated. We therefore based our investigations on measurements.

Compared to simulations, measurements are tedious. On the other hand, each measurement scenario is a true, realistic, and physically correct scenario. With even more effort, measurements can be made repeatable, although not easily reproducible.[1] In order to minimize the effect of our measurement hardware on the results, we employed rather expensive self-built measurement equipment with high linearity, a large range of operation, and a very low noise figure. In the digital domain, we employed receiver structures with the highest performance still feasible for real-time implementation. Our linear minimum mean square error (LMMSE) equalizers are computed in 64-bit floating point MATLAB with a length of 60 taps, certainly in quality much higher than what we can expect in commercial low-cost fixed-point equipment. In high-speed downlink packet access (HSDPA) we also applied successive interference cancellation of the synchronization and pilot signals as well as eight iterations of the turbo channel decoder in order to obtain the best results. Due to cost limitations, however, such optimized receivers are unlikely to be employed in commercial 3G systems. Therefore, the measured implementation loss can be interpreted as a *truly lower bound for commercial systems*.

Eventually, measurements are more honest as they exclude assumptions in general. If you do not know, for example, the channel, the frequency offset, or the noise variance, this is natural for a measurement, but not so for a simulation. More severe, unknown impairments (of unknown sources) only occur in measurements, never in simulations.

This article is organized as follows. We briefly explain our measurement setup and methodology; the interested reader can find more details in the references provided. We provide a very brief introduction to MIMO WiMAX and HSDPA. We explain the transmit precoding as well as the receiver processing as it is important for understanding and interpreting the results. The major part of the article in which we present the performance losses observed for WiMAX and HSDPA in single-input single-output (SISO) as well as 2 × 2 MIMO scenarios. For HSDPA we also present some advanced studies employing up to four antennas. We conclude the article with some final comments.

## Measurement Methodology and Setup

Several scenarios have been measured by us over the past years; two of them are compared in this article: an alpine scenario and an urban one (Fig. 1). We picked those two scenarios as they both reflect existing cells in a Carinthian Alpine valley and in downtown Vienna, Austria.

In the alpine environment, the transmitter was placed 5.7 km from the receiver with an essentially strong line-of-sight (LOS) component and moderate scattering. The root mean square (RMS) delay spread of the channels was 260 ns (corresponding to roughly one chip duration of HSDPA). The other scenario was an urban measurement with only 190 m distance but without an LOS component. The scattering was much richer, the RMS delay spread 1.1 μs. Other scenarios, not presented in this article but measured for reference purposes, had a characteristic performance in between the alpine and urban scenarios.

Although many more situations were investigated, we present here only the results for SISO and 2 × 2 MIMO with cross-polarized transmit antennas. In addition, we present results of a four-transmit-antenna measurement of advanced HSDPA to provide a flavor of what more antennas can offer. We employed commercially available cross-polarized base station antennas (Kathrein 80010543), as they support the highest diversity at the smallest size, and are thus of great interest to providers. Measurements with equally polarized antennas typically provided much smaller capacity and correspondingly smaller throughput. Our receiver has a noise figure of 1.9 dB,

Eventually, measurements are more honest as they exclude assumptions in general. If you do not know, for example, the channel, the frequency offset, or the noise variance, this is natural for a measurement, but not so for a simulation.

[1] *For simulations this seems to be a very simple task; still, simulation code is rarely provided in the signal processing community, and reproducibility by others is hampered [4].*

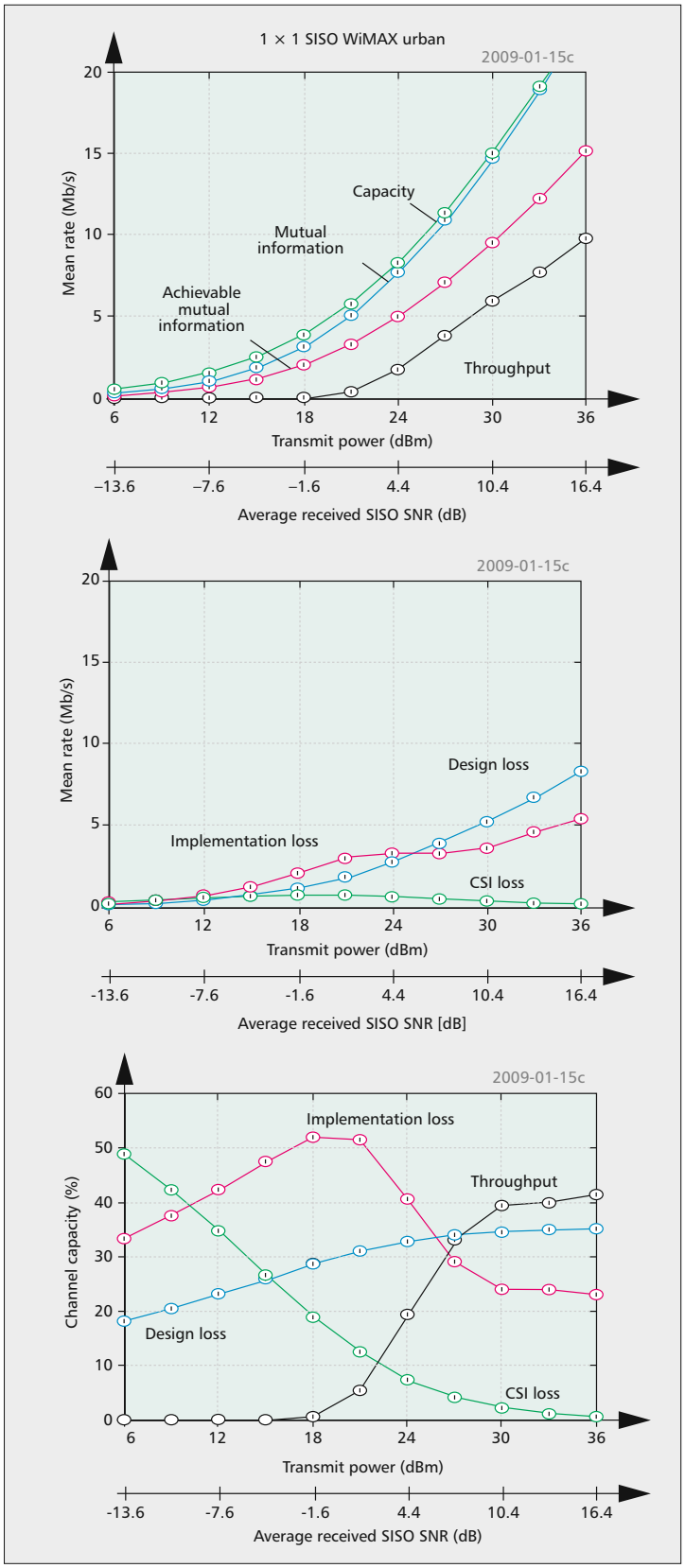


**Figure 2.** *Example of measured performance metrics (left) and derived throughput losses, absolute (middle) and relative (right).*

which increases by the attenuation of the feeder cable (1 dB/m cable length) to a total of approximately 4 dB. We operate our 5 MHz transmit signal in 6.25 MHz available spectrum to facilitate sharp spectral filtering. Our power amplifiers are capable of transmitting at a power of 30 W (per antenna) of which we use less than 15 percent to ensure high-linearity transmissions.

Typically, the performance of wireless systems is evaluated by drive tests (i.e., measuring the throughput in a vehicle continuously while driving along a road). Unfortunately, the same test repeated at another day can result in entirely different outcomes. In order to make our measurements repeatable we apply a measurement technique employing XY positioning tables on which we automatically change the antenna positions and measure many locations in an area of $3\lambda \times 3\lambda$. At each antenna position in the same scenario, we perform repeated measurements of all transmission schemes of interest. By such a setup we ensure that all schemes are measured under exactly the same conditions. The averaged *measurement results* over all antenna positions later reflect an estimated mean value for the throughput at a given transmit power $P_{Tx}$. Similarly, this is also the method by which the channel coefficients were evaluated. We measure a set of channels at highest transmit power $P_{Tx}$ (e.g., at 36 dBm; Fig. 2) and evaluate the channel coefficients by the best estimator we have available (LMMSE) utilizing all data (not just the pilots). This provides us with an estimate of the highest quality, certainly an order of magnitude higher in quality than the estimator later employed based on the pilots only. Taking these channel estimates, we then calculated the channel capacity according to Eq. 1 and averaged it to obtain the average channel capacity for a given signal-to-noise ratio (SNR), which is plotted in the figures. Similarly, we proceeded for mutual information[2] according to Eq. 2 and further constrained measures such as achievable mutual information according to Eq. 3. In addition, we calculated the 99 percent confidence intervals to gauge the precision of our estimates. Taking the measurement with highest SNR and all symbols for estimating the channel ensured that the level of uncertainty observed is small compared to the results obtained.

We compute for each measurement point the 99 percent confidence interval by bootstrapping methods and plot the point augmented on a small scale (e.g., Figs. 2 and 3) according to the size of the achieved confidence interval. Most of these only appear as points, indicating extremely high precision. See [8] for a more detailed description of the measurement procedure employed.

## Cellular Systems Investigated: WiMAX and HSDPA

### WiMAX and HSDPA

We implemented, measured, and analyzed two standardized 3G cellular systems:

- The WiMAX physical layer, as defined in IEEE 802.16-2004, Section 8.3: This standard

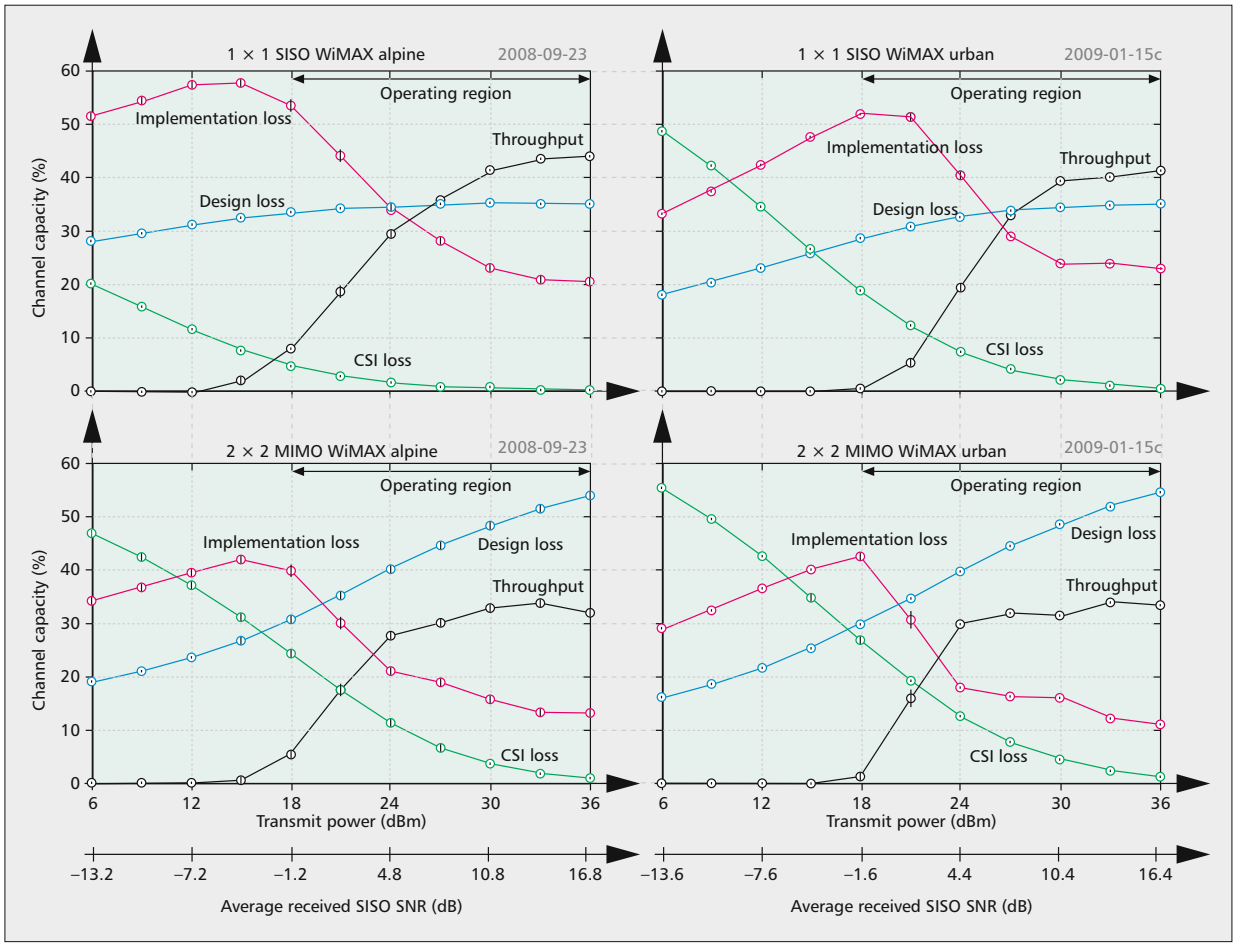


**Figure 3.** *Relative losses in WiMAX 1 × 1 and 2 × 2 transmissions: left, alpine; right, urban; upper, SISO; lower, MIMO.*

was developed to provide wireless Internet access to stationary and low-mobility users [9]. In our measurements, we employed an orthogonal frequency-division multiplexing (OFDM) physical layer with 256 narrowband subcarriers. By choosing one out of seven adaptive modulation and coding (AMC) schemes at the transmitter, the data rate is adjusted to the current channel conditions, thereby maximizing the data throughput. The standard defines various channel codes out of which we selected for our evaluations the mandatory Reed-Solomon convolutional code (RS-CC) and the optional convolutional turbo code (CTC). We furthermore implemented and measured a regular low-density parity check (LDPC) channel code, which is not defined in the standard. Unless stated otherwise, all our results refer to the CTC. In order to utilize transmit diversity, the standard furthermore foresees simultaneous transmission on two transmit antennas by Alamouti space-time coding.

• The HSDPA mode of the Universal Mobile Telecommunications System (UMTS) [10]: The first version of HSDPA was introduced in Release 5 of UMTS to provide high data rates to mobile users. This is achieved by several techniques such as fast link adaptation, fast hybrid automated repeat request, and fast scheduling. In contrast to the pure transmit power adaptation performed in UMTS, fast link adaptation in HSDPA adjusts the data rate and the number of spreading codes depending on so-called channel quality indicator (CQI) feedback. MIMO HSDPA, standardized in Release 7 of UMTS, further increases the maximum downlink data rate by spatially multiplexing two independently coded and modulated data streams. Additionally, channel-adaptive spatial precoding is implemented at the base station. This is achieved by a standardized set of precoding vectors from which one vector is chosen based on so-called precoding control indication (PCI) feedback obtained from the user equipment.

## Throughput Bounds and System Losses

In this section, we define several bounds for the data throughput. The differences between the bounds can be considered as system losses.

In 1998, Foschini and Gans [2] as well as Telatar [3] extended the Shannon capacity $C$ to MIMO systems. For a system working on discrete frequencies[3] $k = 1 \ldots K$, the capacity $C$ as a function of the transmit power $P_{\mathrm{Tx}}$, the channel matrix $\mathbf{H}_k \in \mathbb{C}^{N_{\mathrm{R}} \times N_{\mathrm{T}}}$ at the $k$th frequency bin with bandwidth $B/K$, the entire channel band-

[2] *Note that there are many different terms in literature describing a constrained capacity, the most prominent being non-coherent capacity [5], functional capacity [6], and simply capacity without CSI at the transmitter [7].*

[3] *We show the formulas in terms of discrete frequency bins* k = 1…K, *as this is very natural for OFDM systems. In HSDPA an equivalent discrete Fourier transform (DFT) on the channel impulse responses has been applied to calculate frequency domain channel coefficients, which in turn are required to compute capacity and mutual information. As the channels have approximately the same bandwidth, the resulting channel capacities match.*

For a MIMO receiver the situation is more complicated, as one antenna may consistently receive less energy than another; we average over all individual SISO channels, or four channels for a 2 × 2 MIMO system.

width $B$, the receiver noise variance $\sigma_n^2$, and the number of transmit antennas $N_T$ is given by

$$C(P_{Tx}) = \max_{\sum^{tr}\{\mathbf{R}_k\}\le K} \frac{B}{K}\sum_{k=1}^{K}\log_2\det\left(\mathbf{I}+\frac{P_{Tx}}{\sigma_n^2 N_T}\mathbf{H}_k\mathbf{R}_k\mathbf{H}_k^H\right) \quad (1)$$

A transmission system that is designed to achieve the channel capacity $C(P_{Tx})$ has to perform frequency-selective and spatial precoding according to the matrices $\mathbf{R}_k$. For specific channel realizations, solutions for $\mathbf{R}_k$ are found by the waterfilling algorithm. Such a precoding, of course, only works if a priori channel state information (CSI) is available at the transmitter. If this is not the case, the best strategy is to transmit with equal power over all transmit antennas and over all frequencies. The throughput of a system following this strategy is bounded by the mutual information (MI) $I(P_{Tx})$:

$$I(P_{Tx}) = \frac{B}{K}\sum_{k=1}^{K}\log_2\det\left(\mathbf{I}+\frac{P_{Tx}}{\sigma_n^2 N_T}\mathbf{H}_k\mathbf{H}_k^H\right) \quad (2)$$

Since the difference between the channel capacity $C(P_{Tx})$ and the mutual information $I(P_{Tx})$ is only caused by the absence of CSI at the transmitter side, we define the difference between them as the *absolute CSI loss* $L_{CSI}(P_{Tx})$ and the *relative CSI loss* $L_{CSI\%}(P_{Tx})$:

$$L_{CSI}(P_{Tx}) = C(P_{Tx}) - I(P_{Tx});$$
$$L_{CSI\%}(P_{Tx}) = 100\cdot\frac{C(P_{Tx}) - I(P_{Tx})}{C(P_{Tx})} \quad (3)$$

The definitions of capacity and mutual information do not take specific constraints of current cellular systems into account. For example, current systems cannot utilize the whole frequency band and/or the whole transmit power for transmitting information bits. Parts of the spectrum and/or parts of the transmit power have to be allocated to pilot, control, and synchronization information. This is reflected in the measure $I_a(P_{Tx})$, which we call the *achievable mutual information*:

$$I_a(P_{Tx}) = \max_{\mathbf{W}\in\mathcal{W}} \frac{\beta B}{K}\sum_{k=1}^{K}\log_2\det\left(\mathbf{I}+\frac{\alpha P_{Tx}}{\sigma_n^2 N_T}\mathbf{H}_k\mathbf{W}\mathbf{W}^H\mathbf{H}_k^H\right) \quad (4)$$

The parameter $\alpha \le 1$ accounts for transmit power losses, and the parameter $\beta \le 1$ accounts for spectrum and transmission time losses. In our setup, we find $\alpha = 1$ and $\beta \approx 0.65$ for WiMAX and $\alpha \approx 0.4$ and $\beta \approx 0.77$ for HSDPA. The matrix $\mathbf{W}$ accounts for non-optimal precoding/space-time coding. In the case of HSDPA, the precoding matrix $\mathbf{W}$ is strongly quantized and chosen adaptively out of a predefined codebook $\mathcal{W}$. Depending on the transmission mode, the inclusion of the precoding $\mathbf{W}$ in the calculation of the achievable mutual information may or may not (e.g., if the matrices $\mathbf{W}$ are chosen unitary) impact $I_a(P_{Tx})$. Note that in HSDPA only one precoding matrix $\mathbf{W}$ is chosen for the entire bandwidth; future standards, such as Long Term Evolution (LTE), allow for frequency-dependent precoding, thereby increasing the achievable mutual information. In the case of WiMAX, the transmitter employs Alamouti space-time coding, which can be rewritten as a constant precoding.[4] In contrast to the channel capacity and MI, the achievable MI is therefore a capacity constrained by the specific cellular standard.

We define the difference between the MI $I(P_{Tx})$ and the achievable MI $I_a(P_{Tx})$ as the *design loss*, as it quantifies the loss imposed by the system design:

$$L_d(P_{Tx}) = I(P_{Tx}) - I_a(P_{Tx});$$
$$L_{d\%}(P_{Tx}) = 100\cdot\frac{I(P_{Tx}) - I_a(P_{Tx})}{C(P_{Tx})} \quad (5)$$

The design loss accounts for the inherent system design losses caused by, for example, losses due to the transmission of pilot and synchronization symbols, quantized precoding, or suboptimal space-time coding. By alternating design parameters, which can partially also be achieved adaptively on the transmission scenario, the design loss can be reduced.

Finally, there is the throughput $D_m(P_{Tx})$ that can be measured in bits per second in a given link, allowing the so-called *implementation loss* to be defined,

$$L_i(P_{Tx}) = I_a(P_{Tx}) - D_m(P_{Tx});$$
$$L_{i\%}(P_{Tx}) = 100\cdot\frac{I_a(P_{Tx}) - D_m(P_{Tx})}{C(P_{Tx})} \quad (6)$$

as the difference between the achievable mutual information $I_a(P_{Tx})$ and the measured data throughput $D_m(P_{Tx})$. It accounts for losses caused by non-optimum receivers and channel codes. A more detailed discussion of the individual parts of the implementation loss in WiMAX or HSDPA is provided further ahead.

In order to complete the picture we also need to define the *relative throughput*,

$$D_{m\%}(P_{Tx}) = 100\cdot\frac{D_m(P_{Tx})}{C(P_{Tx})}. \quad (7)$$

Summing up the relative losses and relative throughput results in 100 percent. We display the relative losses together with the relative throughput.

In Fig. 2, all terms defined above are shown in their absolute and relative measures for a SISO WiMAX transmission. Comparing the CSI loss to the other two losses, it is almost negligible, especially at higher transmit powers and thus higher SNR [11]. Note that in the plot of relative losses, the CSI loss appears as a monotone decreasing function over transmit power with high values (50 percent) at the lower end. However, at very low transmit power (approximately –10 dB SNR) the capacity is extremely small, and losing 50 percent does not make a noticeable performance difference. The initial loss of 50 percent varies depending on the offered selectivity in frequency and spatial domain, as shown later. The more diversity offered, the larger the CSI loss.

In the literature, we find the measures defined above to be a function of the receive

[4] *This is to be seen in contrast to the option of including space-frequency Alamouti coding.*

SNR. Note, however, that in modern 3G systems such a definition is obsolete. There are three reasons, the first being that we measure in terms of transmit power $P_{Tx}$, and comparing two systems, we should compare them at equal transmit power and not at equal receive SNR. Once channel adaptive precoding is introduced, the receive power is systematically increased, also increasing the receive SNR without changing $P_{Tx}$, providing a second reason. Third, depending on the scenario and the construction, one receive antenna will generally receive a different amount of power than another. Such differences can be as large as 6 dB in the mean. The reason for such differences is the scattering environment not being symmetric in nature, as has been assumed in most earlier MIMO channel models. The Winner Phase 2+ model is the first to allow for defining such asymmetries. We thus have to plot over transmit power $P_{Tx}$ rather than SNR. Nevertheless, in order to facilitate comparisons to previous simulation results, we provide two scales in our plots, one being $P_{Tx}$ and the other a computed equivalent average SISO receiver SNR. In the case of a SISO receiver this is simply the average value obtained over the individual SISO channels. For a MIMO receiver the situation is more complicated, as one antenna may consistently receive less energy than another; we average over all individual SISO channels, or four channels for a 2 × 2 MIMO system.[5]

## Measurement Results

### WiMAX Results

Now that we have explained how we obtained the data, we present them decomposed into their various relative losses. Figure 3 shows our measurement results for the selected scenarios.

The reader may recognize the upper right subfigure of Fig. 3 being identical to the bottom subfigure of Fig. 2.

- The *relative CSI losses* are monotonically decreasing functions. For moderate to high transmit power values $P_{Tx}$, the impact of missing CSI at the transmitter can be neglected, questioning why channel information beyond the receiver SNR is useful for the transmitter.
- The *relative design losses* show a gradually increasing behavior with $P_{Tx}$. This behavior is more pronounced in MIMO scenarios, in which Alamouti space-time coding plays a crucial role. In the case of 2 × 2 MIMO transmission, the Alamouti space-time code is suboptimal; hence, the achievable mutual information is limited by the system design. Especially at large transmit power levels, the loss due to Alamouti space-time coding becomes dominant, wasting approximately 50 percent of the available channel capacity.
- For lower to moderate $P_{Tx}$, the *relative implementation losses* are severe. Only at high $P_{Tx}$ do they fall below the design losses. The reason for this is found in the measured throughput. As at low $P_{Tx}$ there is no AMC scheme supporting the transmission, the throughput is zero for SNR values lower than approximately –3 dB (equivalent to 15 dBm transmit power).

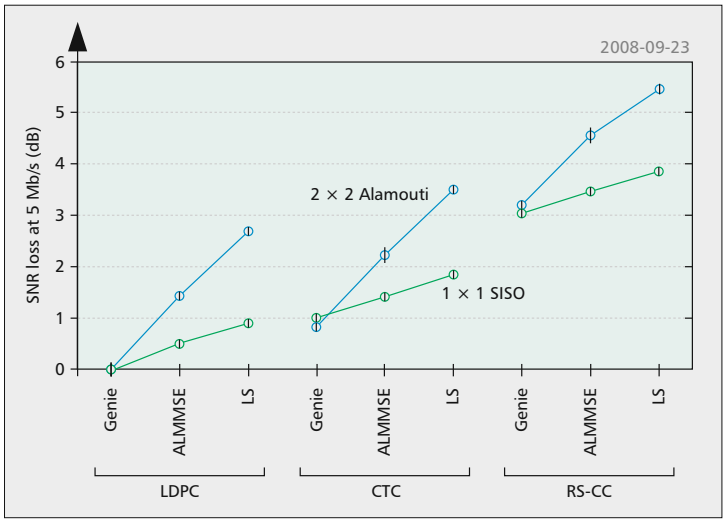


**Figure 4.** *SNR losses of different channel estimators and channel coding schemes with respect to genie-driven channel estimation and LDPC coding, measured in the alpine scenario.*

Until there, the implementation loss increases with the capacity. Once the throughput begins to rise, the relative implementation loss drops to 10–20 percent at high SNR and then remains roughly constant.

- The *relative throughput* appears to be a monotonically increasing function. However, at high $P_{Tx}$, the AMC schemes run out and no higher rate can be transmitted. Consequently, the relative throughput starts decreasing. As our maximum transmit power was 36 dBm, we hardly reached this area. Only in the alpine MIMO scenario with a strong LOS component can we observe such a decline at high $P_{Tx}$. Surprisingly, the relative throughput is lower in MIMO (30 percent) than in SISO (40 percent), even though the absolute values are much higher in MIMO, showing that this version of WiMAX is not capable of taking advantage of what MIMO offers.

In summary, we conclude that WiMAX behaves quite similar in alpine and urban environments as well as in SISO and MIMO. Comparing SISO with MIMO performance, we can only conclude that the various components show larger variations in SISO and less in MIMO.[6]

Let us now take a closer look at the implementation loss. In our displayed measurements we employed the CTC with an advanced channel estimation scheme (ALMMSE). Figure 4 depicts the SNR loss of various channel estimation and channel coding schemes at a throughput of 5 Mb/s when compared to a genie channel estimator and LDPC channel coding. The genie channel estimator knows not only the 200 pilot symbols, but all 9400 transmitted data symbols and uses them to achieve a very high channel estimation quality. Similarly, a regular LDPC code was designed to provide a high-quality channel code for a given SNR. Figure 4 reveals that between genie knowledge of the channel in combination with high-quality channel coding on one hand and poor LS channel estimation in combination

[5] *We have provided such "equivalent" SISO SNR to facilitate comparison by researchers working with receive SNR and simplified channel models.*

[6] *When compared to absolute loss values (not displayed here, see [12]), the results are also quite the same for all WiMAX scenarios. The largest loss is the design loss, monotonically increasing over* $P_{Tx}$*, followed by the implementation loss, which is dominant at low* $P_{Tx}$ *but only small at large* $P_{Tx}$*. In the regions of interest, the CSI loss is the smallest of the losses, only showing its existence in MIMO conditions at low to moderate* $P_{Tx}$*.*

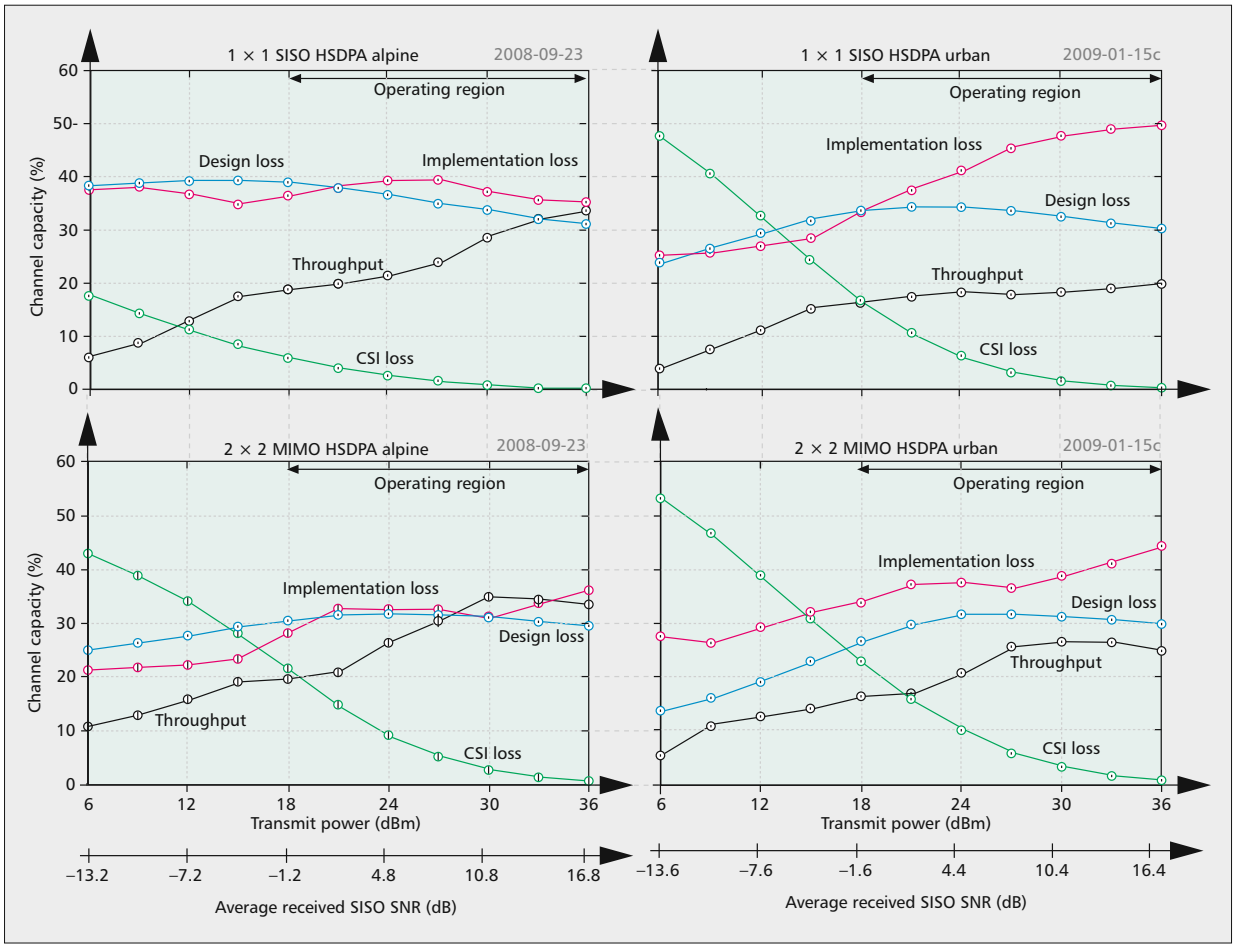


**Figure 5.** *Relative losses in HSDPA 1 × 1 and 2 × 2 transmissions: left, alpine; right, urban; upper, SISO; lower, MIMO.*

with the mandatory RS-CC channel coding of WiMAX on the other hand can be more than 6 dB distance. In the case of 2 × 2 transmissions, when Alamouti space-time coding is employed at the transmitter, we observe a much higher dependence on the type of channel estimator chosen. This can be explained by two facts:

- In the case of Alamouti space-time coded transmission, the available transmit power and thus also the training signal power are equally distributed on the two transmit antennas. Therefore, only half the training signal power is available per channel coefficient to be estimated. As a consequence, the channel estimation performance is poorer than in the one transmit antenna case.
- The comparison in Fig. 4 is carried out at a constant throughput value of 5 Mb/s. The Alamouti space-time coded transmission achieves this throughput at a much lower receive SNR than the SISO transmission. This lower SNR in turn causes poorer channel estimation quality and thus substantial SNR loss in comparison to the genie channel estimator.

In order to compensate for the above effects, one would have to apply a much better channel estimator for MIMO than in the case of SISO transmissions.

## HSDPA Results in Standard-Compliant Setting

All measurement results presented in this section are for a Category 16 HSDPA user equipment. In the MIMO case, D-TxAA with adaptive precoding is applied [13].

The various losses in HSDPA (Fig. 5) show a much less lively picture when compared to WiMAX.

- As before, the relative CSI loss is decreasing monotonically in exactly the same dimensions, as the CSI loss is independent of the transmission standard, proving that both measurements have experienced the same equipment as well as the same wireless conditions. Small differences when compared to the WiMAX results are due to a slightly different occupied bandwidth.
- The other losses are more or less constant functions or slightly increasing with $P_{Tx}$. The relative design loss with values between 30 and 40 percent is a particularly flat curve when compared to WiMAX. Only at low $P_{Tx}$ in the urban MIMO scenario the values can become as small as 15 percent .
- The *relative implementation loss* is either of same value than the design loss or larger. The distinct behavior in the urban scenario is of

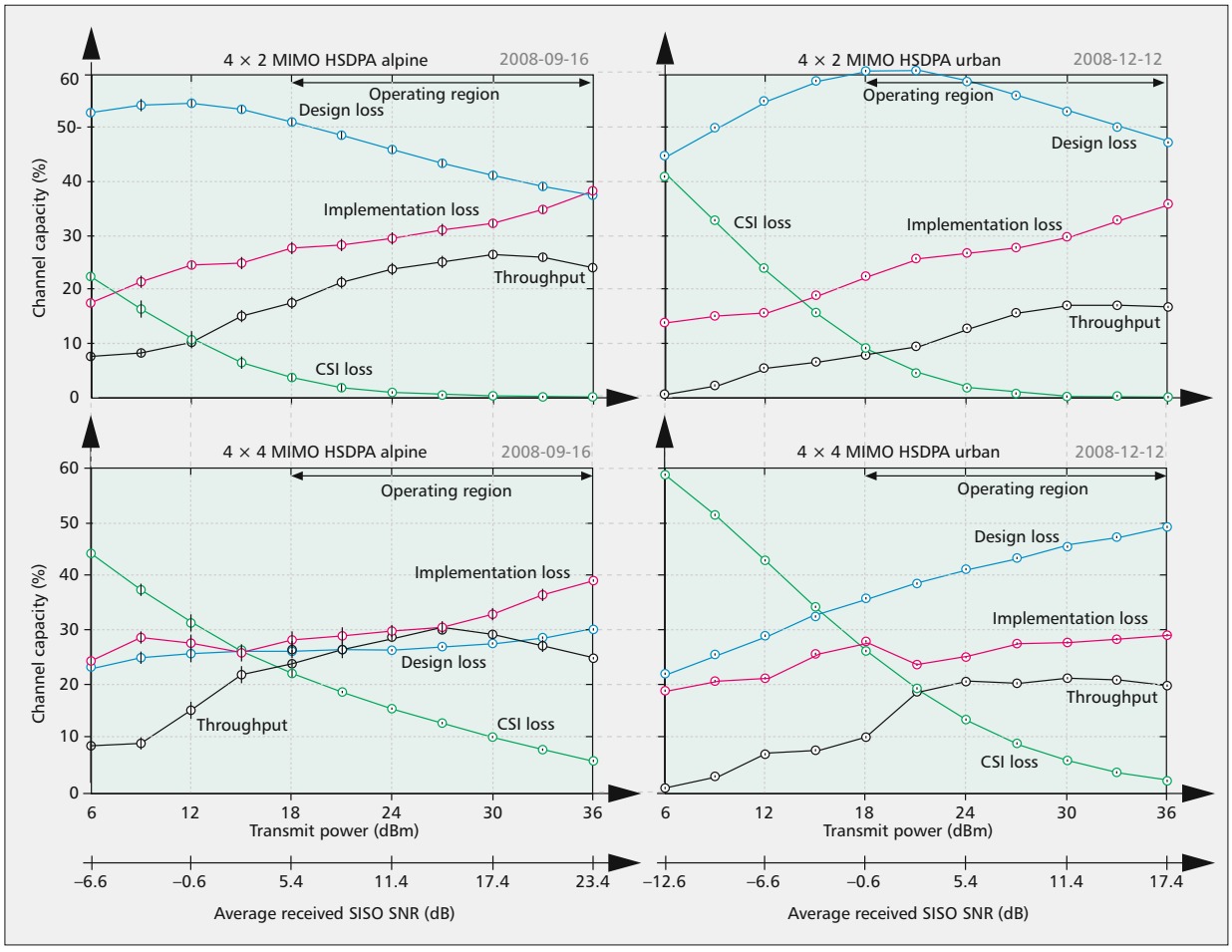


**Figure 6.** *Relative losses in HSDPA 4 Tx antenna transmissions: left, alpine; right, urban; upper, 4 × 2 MIMO; lower, 4 × 4 MIMO.*

interest. Due to the larger RMS delay spread in the urban scenario, the inter code interference is increased and becomes a dominant part at high $P_{Tx}$. Therefore, we recognize a higher implementation loss and a smaller design loss for high $P_{Tx}$.

- Similar to WiMAX, the *relative throughput* is an increasing function in SNR. For low values of $P_{Tx}$ the spreading functions of HSDPA improve the situation considerably, allowing a transmission even for very low receiver SNR at low bit rates. Furthermore, HSDPA has many more AMC schemes than WiMAX, especially at low SNR. At high $P_{Tx}$ we obtain in the alpine environment with its strong LOS the close to 40 percent values in relative throughput just as for WiMAX. However, in the urban scenario with high RMS delay spread the relative throughput is much lower as the transmitter is producing strong inter code interference in such channels, visible in SISO as well as in MIMO transmissions.

Although the results in absolute values [13] show a considerable performance increase of the different MIMO schemes when compared to the SISO transmission, all measured throughput curves are losing between 3 and 9 dB SNR compared to the achievable mutual information. The following effects contribute (next to maybe others) to this loss:

- The rate-matched turbo code utilized in HSDPA is good but not optimal. By carrying out a set of comparative additive white Gaussian noise (AWGN) simulations, we found that at higher code rates, the rate-matched turbo code loses up to 2 dB when decoded by a max-log-MAP decoder (approximately 2 dB).
- The LMMSE equalizer representing a low complexity and cost-effective solution is also not optimal. Better receivers such as the LMMSE-MAP have the potential to improve the performance by approximately 1 dB.
- In the urban scenario, a larger throughput loss was measured than in the alpine scenario because of the larger delay spread and, consequently, the larger inter-code interference. For example, in the alpine scenario the SISO system loses approximately 6 dB to the achievable MI, whereas the loss in the urban scenario is approximately 9 dB (3 dB *additional loss in the urban scenario compared to the alpine scenario*).
- In addition to the above mentioned losses, channel estimation errors and over-/underestimation of the post-equalization signal-to-interference-plus-noise ratio (SINR) degrade the measured throughput. Exactly quantifying the loss caused by these effects is difficult because

A system designer should equally take all losses into consideration, but note that the design loss imposed by the system design can never be reduced in the future by a clever receiver implementation.

neither perfect CSI nor perfect post-equalization SINR is available in measurements.

It should be noted that HSDPA supports hybrid automatic repeat request (HARQ) retransmissions, while the chosen WiMAX standard did not support this yet. We indeed implemented retransmissions in HSDPA, but the measurement plots shown here are not utilizing such retransmissions to keep the comparison to WiMAX fair. Note that including up to three retransmissions hardly changed the figures. We conclude that while HARQ offers some advantages in service quality (e.g., lower latency), it has no impact on the throughput performance. This may be due to the fact that in our measurements the block error rate (BLER) is kept at approximately 1 percent throughout the whole measurement range.

### HSDPA Results in an Advanced Setting

By employing a straightforward extension of the two transmit antenna precoding, we extended the HSDPA standard toward four antennas at the transmit side and utilized either two or four receive antennas [13]. The results obtained when employing 4 × 2 and 4 × 4 MIMO systems are very different from the ones shown above:

- The relative design loss is now clearly the major loss, dominating the implementation loss in every scenario, while above they were roughly of equal size. This indicates that precoding for four antennas should be implemented with much more sophistication than we did in our experiment.
- The relative throughput has reached 30 percent of the capacity at best. We can thus conclude that although advanced settings on HSDPA improve absolute values of throughput by up to 50 percent, relatively speaking they utilize less of the now much higher capacity.

## Conclusions

The measured throughput $D_m$ actually observed accounts for only 15–45 percent of the available channel capacity. In terms of the individual losses, our findings are summarized as:

- **The CSI loss** $L_{CSI}$: This loss is given by absence of full channel state information at the transmitter. The CSI loss is typically small, and for SISO and cross polarized 2 × 2 MIMO systems it can be neglected compared to the other losses. Only when the transmission system employs more than two antennas and is operating at low SNR is it worth combatting the CSI loss by employing detailed CSI feedback. A potential of 50 percent improvement in capacity may sound appealing; note, however, that the absolute values are rather small in the low SNR regime.
- **The design loss** $L_d$: Here the differences between HSDPA and WiMAX are not very pronounced. HSDPA is generally better designed as the design loss is roughly constant over the full SNR range, while in WiMAX the design loss is small for low SNRs and increases with SNR. In the case of 2 × 2 MIMO WiMAX this is caused by suboptimal Alamouti space-time coding. Precoding is not expected to have an impact on the design loss, as optimal precoding matrices are unitary, and so are the proposed precoding schemes in the HSDPA and LTE standards. The design loss is the vehicle of the future to achieve improvements at the design stage. Once the standard is released, the design loss is final.
- **The implementation loss** $L_i$: In environments with high RMS delay spread (urban environment with 1.1 μs), the implementation loss of HSDPA is extremely large due to self-interference, while in small RMS delay spread areas (alpine environment with 260 ns) the behavior is different. In WiMAX the different delay spread has no impact, as the cyclic prefix was selected sufficiently large. Both WiMAX and HSDPA suffer losses of several decibels due to channel estimation and non-optimal coding. The much higher number of AMC schemes in HSDPA does not show much of a benefit compared to WiMAX. A good strategy for standardization bodies could be to accept a rather large initial implementation loss, anticipating that manufacturers will figure out how to improve implementation quality by employing more digital signal processing complexity. However, some implementations are close to optimal, no longer offering much to be gained. Once manufacturers are offering close to optimal implementations, they cannot differentiate their products between each other.

What counts at the end of the day when designing a system is the throughput actually achieved. Therefore, a system designer should take *all* losses into consideration equally, but note that the design loss imposed by the system design can never be reduced in the future by a clever receiver implementation. Therefore, it may pay off to start with a smaller design loss and a larger implementation loss.

## References


[1] C. Shannon, "A Mathematical Theory of Communication," *Bell Sys. Tech. J.*, vol., July, Oct. 1948, http://cm.bell-labs.com/cm/ms/what/shannonday/shannon1948.pdf27, pp. 379–423, 623–56.

[2] G. J. Foschini and M. J. Gans, "On Limits of Wireless Communications in a Fading Environment When Using Multiple Antennas," *Wireless Pers. Commun.*, vol. 6, no. 3, Mar. 1998, http://www.springerlink.com/content/h1n7866218781520/fulltext.pdf, pp. 311–35.

[3] I. E. Telatar, "Capacity of Multi-Antenna Gaussian Channels," *Euro. Trans. Telecommun.*, 1999, tech. memo, Bell Labs, Lucent Technologies, vol. 10, no. 6, Oct. 1998, http://mars.bell-labs.com/papers/proof/proof.pdf, pp. 585–95.

[4] P. Vandewalle, J. Kovacevic, and M. Vetterli, "Reproducible Research in Signal Processing — What, Why, and How," *IEEE Sig. Proc. Mag.*, vol. 26, no. 3, 2009, pp. 37–47.

[5] G. Durisi *et al.*, "Noncoherent Capacity of Underspread Fading Channels," *IEEE Trans. Info. Theory*, vol. 56, no. 1, Jan. 2010, http://www.nari.ee.ethz.ch/commth/pubs/p/dsbsIT08, pp. 367–95.

[6] J. Andrews *et al.*, "Rethinking Information Theory for Mobile Ad Hoc Networks," *IEEE Commun. Mag.*, vol. 46, no. 12, 2008, pp. 94–101.

[7] A. Tulino, A. Lozano, and S. Verdu, "MIMO Capacity with Channel State Information at the Transmitter," *Proc. ISSSTA*, Sydney, Australia, Aug. 2004, pp. 22–26.

[8] S. Caban *et al.*, "Testbedding MIMO HSDPA and WiMAX," *Proc. VTC '09-Fall*, Anchorage, AK, Sept. 2009, http://publik.tuwien.ac.at/files/PubDat_176574.pdf

[9] A. Ghosh *et al.*, "Broadband Wireless Access with WiMax/802.16: Current Performance Benchmarks and Future Potential," *IEEE Commun. Mag.*, vol. 43, no. 2, 2005, http://ieeexplore.ieee.org/iel5/35/30297/01391513.pdf?tp=&arnumber=1391513, pp. 129–36.

[10] H. Holma *et al.*, "High-Speed Packet Access Evolution in 3GPP release 7," *IEEE Commun. Mag.*, vol. 45, no. 12, pp. 29–35, Dec. 2007, http://ieeexplore.ieee.org/stamp/stamp.jsp?arnumber=4395362
[11] M. Rupp *et al.*, "On Mutual Information and Capacity in Frequency Selective Wireless Channels," *Proc. IEEE ICC '10*, Cape Town, South Africa, May 2010, http://publik.tuwien.ac.at/files/PubDat_184660.pdf
[12] M. Rupp, C. Mehlführer, and S. Caban, "On Achieving the Shannon Bound in Cellular Systems," *Proc. 20th Int'l. Conf. Radioelektronika 2010*, Brno, Czech Republik, Apr. 2010, http://publik.tuwien.ac.at/files/PubDat_185403.pdf
[13] C. Mehlführer, S. Caban, and M. Rupp, "Measurement-Based Performance Evaluation of MIMO HSDPA," *IEEE Trans. Vehic. Tech.*, vol. 59, no. 9, Nov. 2010, http://publik.tuwien.ac.at/files/PubDat_187112.pdf, pp. 4354–67.

## Biographies

Christian Mehlführer [M'09] received his Dipl.-Ing. degree in electrical engineering from the Vienna University of Technology. Besides his diploma studies he worked part time at Siemens AG, where he performed integration tests of GSM carrier units. After finishing his diploma thesis on implementation and real-time testing of space-time block codes at the Institute of Communications and Radio Frequency Engineering, Vienna University of Technology, for which he received the Vodafone Förderpreis 2006 (together with Sebastian Caban), he started his doctoral thesis at the same institute. In 2009 he finished his Ph.D. about measurement-based performance evaluation of WiMAX and HSDPA with summa cum laude. His research interests include experimental investigation of MIMO systems, UMTS HSDPA, WLAN (802.11), WiMAX (802.16), and the upcoming 3GPP LTE system.

Sebastian Caban [M'09] went to a technical high school and received his Bachelor's degree in electrical and communication engineering from the Vienna University of Technology. He received his Master's degree in 2005 and his Ph.D. degree in 2009. In between, he spent a year with the University of Illinois at Urbana-Champaign. He received B.B.A. and M.B.A. degrees, with a major in economics, from the University of Vienna in 2010. He is currently with the Institute of Communications and Radio Frequency Engineering, Vienna University of Technology. His research interests include developing measurement methodologies and building testbeds to quantify the actual performance of wireless cellular communication systems (e.g., UMTS and LTE) in realistic scenarios. He received 12 national scholarships and prizes, and the Förderpreis 2006 from the German Vodafone Stiftung für Forschung for his research.

Markus Rupp [SM'06] received his Dipl.-Ing. degree from the University of Saarbrücken, Germany, in 1988 and his Dr.Ing. degree from Technische Universität Darmstadt, Germany, in 1993, where he worked with E. Hänsler on designing new algorithms for acoustical and electrical echo compensation. From November 1993 to July 1995 he held, with S. Mitra, a postdoctoral position with the University of California, Santa Barbara, where he worked with A. H. Sayed on a robustness description of adaptive filters with impact on neural networks and active noise control. From October 1995 to August 2001 he was a member of technical staff with the Wireless Technology Research Department, Bell Laboratories, Crawford Hill, New Jersey, where he worked on various topics related to adaptive equalization and rapid implementation for IS-136, 802.11, and UMTS. Since October 2001 he has been a full professor of digital signal processing in mobile communications with the Vienna University of Technology, where he founded the Christian Doppler Laboratory for Design Methodology of Signal Processing Algorithms at the Institute of Communications and Radio Frequency Engineering in 2002. He served as dean from 2005 to 2007. He is currently an Associate Editor for the EURASIP *Journal of Advances in Signal Processing* and EURASIP *Journal on Embedded Systems*. He is an author or coauthor of more than 350 papers and is the holder of 15 patents on adaptive filtering, wireless communications, and rapid prototyping, as well as automatic design methods. He was an Associate Editor for *IEEE Transactions on Signal Processing* from 2002 to 2005. He has been an Administrative Committee Member of EURASIP since 2004 and served as the President of EURASIP from 2009 to 2010.

# Low-Latency MISO FBMC-OQAM: It Works for Millimeter Waves!

Ronald Nissel, Erich Zöchmann, Martin Lerch, Sebastian Caban, and Markus Rupp

Christian Doppler Laboratory for Dependable Wireless Connectivity for the Society in Motion,
Institute of Telecommunications, TU Wien, Vienna, 1040, Austria

***Abstract*—A key enabler for high data rates in future wireless systems will be the usage of millimeter Waves (mmWaves). Furthermore, Filter Bank Multi-Carrier (FBMC) with its good spectral properties has also been considered as a possible future transmission technique. However, many authors claim that multiple antennas and low-latency transmissions, two of the key requirements in 5G, cannot be efficiently supported by FBMC. This is not true in general, as we will show in this paper. We investigate FBMC transmissions over real world channels at 60 GHz and show that Alamouti's space time block code works perfectly fine once we spread (code) symbols in time. Although it is true that spreading increases the transmission time, the overall transmission time is still very low due to the high subcarrier spacing employed in mmWaves. Therefore, coded FBMC in combination with mmWaves enables high spectral efficiency, low-latency and allows the straightforward usage of multiple antennas.**

***Index Terms*—5G mobile communication, Millimeter wave measurements, Space-time codes, Code division multiplexing**

## I. Introduction

Orthogonal Frequency Division Multiplexing (OFDM), currently employed in Long Term Evolution (LTE), applies a rectangular prototype filter, leading to high Out-Of-Band (OOB) emissions; not suitable for future wireless systems. There are methods to reduce the OOB emissions in OFDM, such as windowing or filtering, but they all have the disadvantage of reduced spectral efficiency. Filter Bank Multi-Carrier (FBMC) with Offset Quadrature Amplitude Modulation (OQAM), on the other hand, preserves high spectral efficiency at the expense of sacrificing the complex orthogonality condition with the less strict real orthogonality condition. This leads to additional challenges [1], especially for Multiple-Input Single-Output (MISO) [2] and channel estimation [3], [4]. Although it is true that many MISO methods cannot be directly employed in FBMC because the orthogonality condition is fulfilled in the real domain only, it is possible to recover complex orthogonality by precoding (spreading) symbols in time. This allows us to straightforwardly use all MISO methods known in OFDM. Such coding approach in the context of MISO was first proposed in [2] and later analyzed in more detail in [5]. The spreading process itself utilizes a fast Walsh-Hadamard transform so that the additional computational complexity is very low.

Besides new waveforms, millimeter Waves (mmWaves) will also be important in future wireless systems due to large available bandwidths in those frequency ranges [6]–[8]. Unfortunately, the propagation conditions of mmWaves are severely different compared to lower frequencies. Thus, extensive research is required to validate the applicability of mmWaves in practical systems. As proposed in [7] for mmWave transmissions, we also consider a high subcarrier spacing, inherently satisfying the low-latency condition.

The focus of this paper is the comparison of FBMC to OFDM in terms of Bit Error Ratio (BER). As we will show, FBMC and OFDM experience both the same BER and require approximately the same frame transmission time. Thus, utilizing OFDM, as currently done, for example, in IEEE 802.11ad, might not be optimal. Instead, FBMC might be a better solution because it offers a higher spectral efficiency.

**Novel contribution:** We present a 60 GHz measurement setup and show experimentally that, in contrast to common believe, low latency MISO works in FBMC.

## II. System Model

The basic idea of multi-carrier systems is to transmit data symbols, usually chosen from a Quadrature Amplitude Modulation (QAM) signal constellation, over a rectangular time-frequency grid, so that the transmitted signal $s(t)$ can be written as [9]:

$$s(t) = \sum_{k=1}^{K} \sum_{l=1}^{L} g_{l,k}(t)\, x_{l,k}. \tag{1}$$

Here, $x_{l,k}$ denotes the transmitted symbol (at subcarrier-position $l$ and time-position $k$) and $g_{l,k}(t)$ the corresponding basis pulse, essentially a time and frequency shifted prototype filter (we employ a Hermite prototype filter [10], [11]). The total number of subcarriers is given by $L$ and the total number of time-symbols (per frame) by $K$.

Unfortunately, maximum spectral efficiency, time-localization, frequency-localization and orthogonality cannot be fulfilled at the same time according to the Balian-Low theorem [12]. In OFDM, the underlying rectangular function violates frequency localization, leading to high OOB emissions. Conventional FBMC-OQAM, on the other hand, replaces the complex orthogonality condition with the less strict real orthogonality condition, making the application of MISO more challenging. However, by spreading symbols in time (or frequency), we can restore complex orthogonality in FBMC-OQAM, so that MISO becomes as straightforward as in OFDM. For more information on such a coding approach we refer to our work in [5], which also includes a downloadable MATLAB code. Our measurements show that the channel is highly correlated in time and frequency. Thus, the channel induced inter-carrier interference and

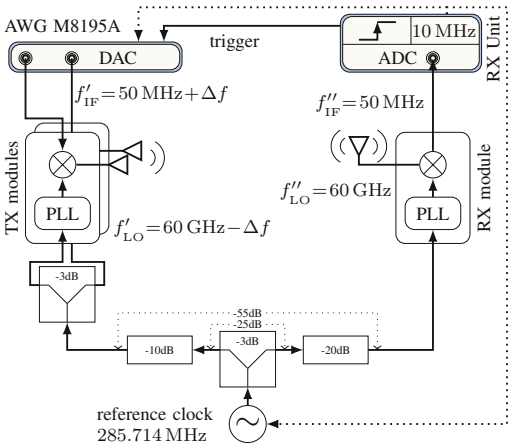


Fig. 1. Block diagram of our 60 GHz measurement setup. Fig. 2 shows pictures of our TX and RX modules. More information about our laboratory environment can be found in [13].

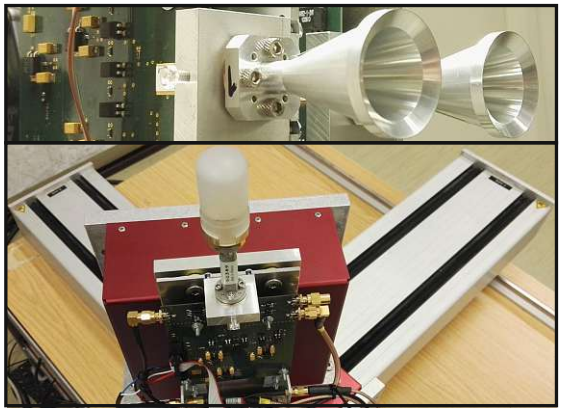

Fig. 2. Two 20 dBi conical horn TX antennas (top) and one omni-directional RX antenna (bottom) are located indoor, approximately 5 m apart. In order to obtain different channel realizations, we utilize an xy-table to relocate the RX antenna, resulting in Rician fading, see Fig. 3. In case of NLOS, we put an object between TX and RX, blocking most of the LOS components.

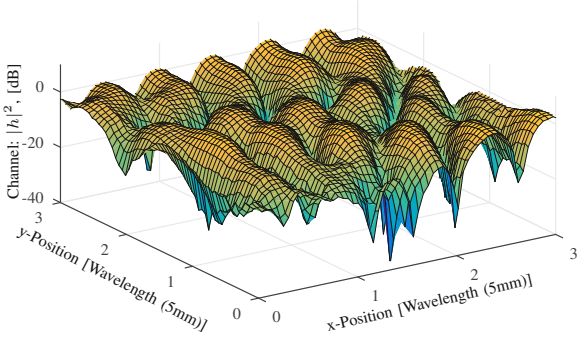


Fig. 3. The measured channel (averaged over 6 MHz and 300 $\mu$s, possible due to high correlation in time and frequency) shows large fading dips in case of NLOS (low Rician K factor). For LOS we observe smaller fluctuations due to a higher Rician K factor (not shown here).

inter-symbol interference can be neglected. This allows us to accurately model the received symbols $y_{l,m}$ by:

$$y_{l,m} = h^{(1)}_{l,m} x^{(1)}_{l,m} + h^{(2)}_{l,m} x^{(2)}_{l,m} + n_{l,m}. \quad (2)$$

In OFDM, the subscript $m$ describes the time index $m = k$ while in Coded-FBMC it describes the coding index. Furthermore, the superscript $(\cdot)^{(1)}$ indicates transmit antenna 1 and $(\cdot)^{(2)}$ transmit antenna 2. We consider Alamouti's space time block coding [2] as well as Single-Input Single-Output (SISO) transmissions, that is, $x^{(2)}_{l,m} = 0$. Our measurements show that the channel can be modeled by a Rician fading process, with $|h_{l,m}| \sim \text{Rice}\left(\sqrt{\frac{K}{K+1}}, \frac{1}{\sqrt{2(K+1)}}\right)$, where K is the Rician-K factor. The phase of $h_{l,m}$ is uniformly distributed and the channel between antenna 1 and antenna 2 is correlated, $\rho = \mathbb{E}\{|h^{(1)}_{l,m}||h^{(2)}_{l,m}|\}$. The variable $n_{l,m}$ describes the Gaussian distributed noise $n_{l,m} \sim \mathcal{CN}(0, P_n)$, with $P_n$ denoting the noise power. The signal power, on the other hand, is defined as $P_s = \mathbb{E}\{|h^{(1)}_{l,m} x^{(1)}_{l,m}|^2 + |h^{(2)}_{l,m} x^{(2)}_{l,m}|^2\}$. In order to validate our measurements, we compare them to simulations in case of Rician fading and to analytical expressions in case of an Additive White Gaussian Noise (AWGN) channel, $h_{l,m} = 1$.

## III. mmWave Testbed

We use a similar methodology as for our measurements at 2.5 GHz [14]–[16]. FBMC and OFDM waveforms are generated off-line in MATLAB, digitally up-converted to an Intermediate Frequency (IF) and converted to the analog domain by an Arbitrary Waveform Generator (AWG) (8-bit, 16 GSamples/s). Our mmWave modules [17], [18] then up-convert this IF signal to 60 GHz, see Fig. 1. The receiver works in a similar way, but in reversed order. The received samples (16-bit, 200 MSamples/s) are also evaluated off-line in MATLAB. To guarantee time-synchronization, we employ a trigger network. The built-in synthesizer Phase-Locked Loop (PLL) is locking on a reference clock of 285.714 MHz and capable of synthesizing a frequency grid of $\Delta f = 285.714\,\text{MHz} \cdot 7/4 \approx 500\,\text{MHz}$ distance. To avoid IF crosstalk, we operate the transmitters and the receiver at different IFs. Furthermore, the mirror frequencies are suppressed as the Local Oscillator (LO) at the receiver is $\Delta f$ higher than the LO at the transmitter.

A common reference clock is applied to all mmWave modules. To avoid any crosstalk on the common clock line, we increase the isolation by additional attenuators, see Fig. 1.

## IV. Measurement Results

Table I summarizes our measurement parameters. Note that in FBMC, pulses overlap in time (overlapping factor of 3), so that the transmission time in FBMC is 4 $\mu$s longer than in OFDM. However, the overall transmission time is still much lower than 100 $\mu$s, allowing low-latency transmissions [19]. For a fair comparison, OFDM and FBMC have the same transmit power $\mathbb{E}\{|s(t)|^2\}$, leading also to the same Signal-to-Noise Ratio (SNR) at the receiver. Furthermore, OFDM and

TABLE I
MEASUREMENT PARAMETERS

| | |
|---|---|
| Carrier frequency | 60 GHz |
| Subcarrier spacing, $F$ | 500 kHz |
| Number of subcarriers, $L$ | 48 |
| Transmission bandwidth (without guard), $FL$ | 24 MHz |
| Number of (complex) time-symbols per frame, $K$ | 16 |
| Frame transmission time for OFDM (with cyclic prefix) | 33 $\mu$s |
| Frame transmission time for FBMC (with guard+overlap) | 33 $\mu$s + 4 $\mu$s |
| Signal constellation | 4-QAM |
| Bit rate (ignoring pilots) | 46.5 MBit/s |
| Pilot spacing in frequency (diamond shaped) | 6 |
| Pilot spacing in time (diamond shaped) | 8 |
| Number of random RX positions (xy-table) | 1000 |
| RX positioning area in wavelengths (5mm) | $7 \times 6$ |

TABLE II
MEASURED CHANNEL PARAMETERS

| | Rician K Ant. 1 | Rician K Ant. 2 | Ant. correlation, $\rho$ |
|---|---|---|---|
| LOS | 24 | 42 | 0.2 |
| NLOS | 0.9 | 2.9 | 0.4 |

FBMC have the same bit rate, but FBMC has better spectral properties and therefore a higher spectral efficiency.

The interference plus noise power is estimated by evaluating the received symbols at subcarrier position 0 and $L+1$, that is, the first subcarrier below and above the transmission band. On the other hand, the noise power is estimated by setting all transmitted symbols to zero, $x_{l,m}^{(1)} = x_{l,m}^{(2)} = 0$. Our setup behaves linearly within the considered transmit power range. However, phase noise causes severe self interference, leading to a Signal-to-Interference Ratio (SIR) of approximately 17 dB.

We measure three different scenarios: Line-Of-Sight (LOS), Non-Line-Of-Sight (NLOS) and AWGN. For the NLOS case, we block the direct path by an object. This causes a loss in received signal power by approximately 10 dB that we compensate by increasing the transmit power. For the AWGN scenario (SISO), we connect the TX module and the RX module back-to-back with 60 dB attenuation.

Our measurements show that the channel is highly correlated in time and frequency. Indeed, the correlation coefficient in time is approximately one for all scenarios. The correlation coefficient in frequency is also approximately one, except for antenna 1 in case of NLOS, where we observe a correlation coefficient between the first and the last subcarrier (23.5 MHz) of 0.83.

As shown in Table I, our transmission bandwidth of $FL = 24$ MHz is relatively narrow (for mmWaves). This is due to the sampling rate of our analog-to-digital converter (a maximum of 100 MHz would be possible, but filters and robustness to crosstalk prevents us from doing that). Furthermore, a narrow bandwidth guarantees a sufficiently high SNR at the receiver (we currently do not employ a power amplifier). However, the bandwidth has no impact on the (averaged) uncoded BER.

Our measurement results also include a confidence interval obtained by bootstrapping [20]. For each RX position, we average the BER over one transmission block. On these measurement results we then apply the MATLAB built-in bootstrap function.

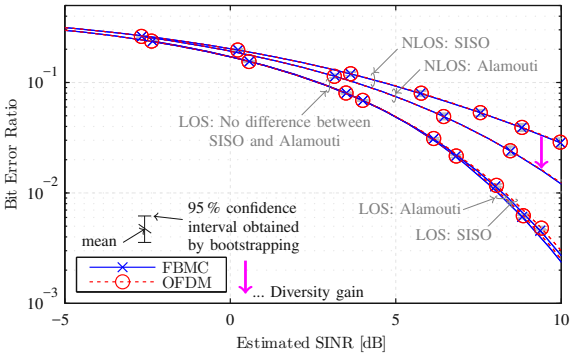


Fig. 4. FBMC performs as good as OFDM in terms of BER, but has the additional advantage of much lower out-of-band emissions. Alamouti's space time block code improves the performance in case of NLOS but not for LOS because there is almost no diversity to exploit.

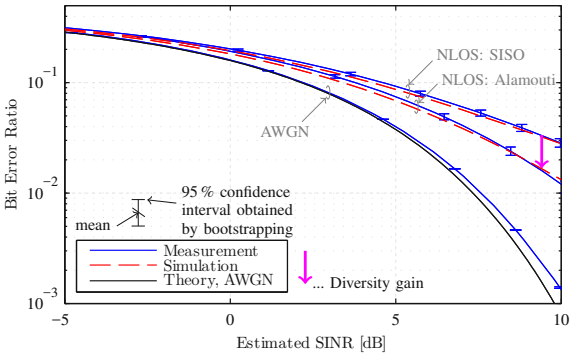


Fig. 5. The system model in (2) accurately describes our measurement results. The simulation parameters can be found in Table II while for AWGN we rely on theoretical expressions (complementary error function). In case of AWGN, the small deviation between theory and measurements can be explained by hardware effects.

Fig. 4 compares OFDM and FBMC in terms of BER over estimated Signal-to-Interference plus Noise Ratio (SINR) for the LOS and the NLOS scenario. In FBMC we observe the same BER as in OFDM, but FBMC has better spectral properties [5]. Thus, if high spectral efficiency is the primary goal, FBMC should be chosen over OFDM (which, however, has a slightly lower computational complexity). We further see that Alamouti's space time block code provides no diversity gain in case of LOS. Once the direct path is blocked, however, Alamouti's space time block code exploits spatial diversity, increasing the overall robustness of the system. Note that the BER is relatively high due to the random fading dips, see Fig. 3. In practice, we would include channel coding.

Fig. 5 shows the measurement results for FBMC and compares them to our system model in (2). Overall, we see a good match between theory and measurements. In case of AWGN, we observe small deviations starting at approximately 5 dB which can be explained by non-Gaussian interference.

## V. Conclusion

Spreading symbols in time allows us to restore complex orthogonality in FBMC-OQAM, so that all MISO methods known in OFDM can be straightforwardly applied. We showed through real world testbed measurements that for such coding scheme, FBMC has the same BER as OFDM but the additional advantage of lower OOB emissions. Furthermore, the high subcarrier spacing proposed for mmWaves [7] leads to a reduced transmission time, allowing low latency communications despite the increased frame duration due to spreading. Thus, the requirements of 5G can be perfectly met by Coded-FBMC in mmWave communications.

In case of LOS, Alamouti's space time block code shows no improvement compared to SISO. However, once the direct path is blocked, such spatial diversity scheme improves the performance. This is particularly useful in mmWave communications where the LOS path might easily be blocked.

## Acknowledgment

The financial support by the Austrian Federal Ministry of Science, Research and Economy, the National Foundation for Research, Technology and Development, and the TU Wien is gratefully acknowledged.

## References

[1] A. A. Zaidi, J. Luo, R. Gerzaguet, A. Wolfgang, R. J. Weiler, J. Vihriala, T. Svensson, Y. Qi, H. Halbauer, Z. Zhao *et al.*, "A preliminary study on waveform candidates for 5G mobile radio communications above 6 GHz," in *IEEE Vehicular Technology Conference (VTC Spring)*, 2016.

[2] C. Lélé, P. Siohan, and R. Legouable, "The Alamouti scheme with CDMA-OFDM/OQAM," *EURASIP Journal on Advances in Signal Processing*, 2010.

[3] R. Nissel and M. Rupp, "Bit error probability for pilot-symbol aided channel estimation in FBMC-OQAM," in *IEEE International Conference on Communications (ICC)*, 2016.

[4] R. Nissel, E. Zöchmann, and M. Rupp, "On the influence of doubly-selectivity in pilot-aided channel estimation for FBMC-OQAM," in *IEEE Vehicular Technology Conference (VTC Spring)*, 2017.

[5] R. Nissel and M. Rupp, "Enabling low-complexity MIMO in FBMC-OQAM," in *IEEE Globecom Workshops (GC Wkshps)*, 2016.

[6] T. S. Rappaport, S. Sun, R. Mayzus, H. Zhao, Y. Azar, K. Wang, G. N. Wong, J. K. Schulz, M. Samimi, and F. Gutierrez, "Millimeter wave mobile communications for 5G cellular: It will work!" *IEEE Access*, vol. 1, pp. 335–349, 2013.

[7] Z. Pi and F. Khan, "An introduction to millimeter-wave mobile broadband systems," *IEEE Communications Magazine*, vol. 49, no. 6, pp. 101–107, June 2011.

[8] E. Zöchmann, S. Schwarz, and M. Rupp, "Comparing antenna selection and hybrid precoding for millimeter wave wireless communications," in *IEEE Sensor Array and Multichannel Signal Processing Workshop (SAM)*, 2016.

[9] R. Nissel and M. Rupp, "OFDM and FBMC-OQAM in doubly-selective channels: Calculating the bit error probability," *IEEE Communications Letters*, 2017, accepted for publication.

[10] R. Haas and J.-C. Belfiore, "A time-frequency well-localized pulse for multiple carrier transmission," *Wireless Personal Communications*, vol. 5, no. 1, pp. 1–18, 1997.

[11] R. Nissel and M. Rupp, "On pilot-symbol aided channel estimation in FBMC-OQAM," in *IEEE International Conference on Acoustics, Speech and Signal Processing (ICASSP)*, 2016.

[12] H. G. Feichtinger and T. Strohmer, *Gabor analysis and algorithms: Theory and applications*. Springer Science & Business Media, 2012.

[13] E. Zöchmann, M. Lerch, S. Caban, R. Langwieser, C. Mecklenbräuker, and M. Rupp, "Directional evaluation of receive power, Rician K-factor and RMS delay spread obtained from power measurements of 60 GHz indoor channels," in *IEEE Topical Conference on Antennas and Propagation in Wireless Communications (APWC)*, 2016.

[14] R. Nissel, S. Caban, and M. Rupp, "Experimental evaluation of FBMC-OQAM channel estimation based on multiple auxiliary symbols," in *IEEE Sensor Array and Multichannel Signal Processing Workshop (SAM)*, 2016.

[15] S. Caban, J. A. García-Naya, and M. Rupp, "Measuring the physical layer performance of wireless communication systems," *IEEE Instrumentation & Measurement Magazine*, vol. 14, no. 5, pp. 8–17, 2011.

[16] R. Nissel, S. Caban, and M. Rupp, "Closed-Form capacity expression for low complexity BICM with uniform inputs," in *IEEE International Symposium on Personal, Indoor and Mobile Radio Communications (PIMRC)*, 2015.

[17] P. Zetterberg and R. Fardi, "Open source SDR frontend and measurements for 60-GHz wireless experimentation," *IEEE Access*, vol. 3, pp. 445–456, 2015.

[18] Pasternack: 60 GHz transmitter and 60 GHz receiver modules. [Online]. Available: https://www.pasternack.com/60-ghz-modules-category.aspx

[19] G. P. Fettweis, "The tactile internet: Applications and challenges," *IEEE Vehicular Technology Magazine*, vol. 9, no. 1, pp. 64–70, 2014.

[20] B. Efron and R. J. Tibshirani, *An introduction to the bootstrap*. CRC press, 1994.

## 5.3 Mobile Scenarios

[28] **S. Caban**, J. Rodas, and J. A. García-Naya. "A Methodology for Repeatable, Off-line, Closed-loop Wireless Communication System Measurements at Very High Velocities of up to 560 km/h". In: *Proc. International Instrumentation and Measurement Technology Conference (I2MTC 2011)*. Binjiang, Hangzhou, China, May 2011. DOI: 10.1109/IMTC.2011.5944019. → see Page 136

[33] J. Rodríguez-Piñeiro, M. Lerch, J. A. García-Naya, **S. Caban**, M. Rupp, and L. Castedo. "Emulating Extreme Velocities of Mobile LTE Receivers in the Downlink". In: *EURASIP Journal on Wireless Communications and Networking* 2015.106 (Apr. 2015), pp. 1–14. ISSN: 1687-1499. DOI: 10.1186/s13638-015-0343-0. → see Page 141

[36] M. Lerch, **S. Caban**, E. Zöchmann, P. Svoboda, and M. Rupp. "Scaled-Time OFDM Experiments for Channels Exceeding the Cyclic Prefix". In: *Electronics Letters* 55.25 (2019), pp. 1370–1373. DOI: 10.1049/el.2019.2857. → see Page 155

[38] E. Zöchmann, M. Hofer, M. Lerch, S. Pratschner, L. Bernadó, J. Blumenstein, **S. Caban**, S. Sangodoyin, H. Groll, T. Zemen, A. Prokes, M. Rupp, A. Molisch, and C. Mecklenbräuker. "Position-Specific Statistics of 60 GHz Vehicular Channels During Overtaking". In: *IEEE Access* 7 (2019), pp. 14216–14232. ISSN: 2169-3536. DOI: 10.1109/ACCESS.2019.2893136. → see Page 158

# A Methodology for Repeatable, Off-line, Closed-loop Wireless Communication System Measurements at Very High Velocities of up to 560 km/h

Sebastian Caban*, Javier Rodas‡, and José A. García-Naya‡
*Institute of Communications and Radio-Frequency Engineering, Vienna University of Technology, Vienna, Austria
‡Department of Electronics and Systems, University of A Coruña, A Coruña, Spain
Contact e-mail: scaban@nt.tuwien.ac.at

***Abstract*—The impact of high velocities on the physical layer downlink performance of mobile radio communication systems is generally measured by placing a receiver in a car, train, or similar vehicle. While these so-called drive test measurements produce valuable results, they lack the flexibility, repeatability, and controllability usually required for initial testing of ideas and algorithms.**

**In this paper, we present a methodology that allows for repeatable, closed-loop, off-line-processed measurements at velocities up to 560 km/h (350 mph). The proposed laboratory set-up allows for precise controlling of velocity and average signal-to-noise ratio. For increased convenience during initial testing, the apparatus can be even used indoors.**

## I. Introduction

Nowadays, there is an increasing demand for wireless services in high-speed vehicles, as for example in new generation trains. Implementing wireless applications suitable for high-speed conditions requires the adaptation of existing wireless protocols and applications to guarantee a reliable service. For example, in [1] the authors work with faster handover protocols than the ones currently used in GSM (250 km/h) and UMTS[1]. Additionally, fast IP handover improvements allowing for Internet services in high-speed trains are studied in [2] by means of a combination of a geo-satellite network and a terrestrial wireless local area network. In [3], a reliable communication-based train control to improve track utilization and enhance train safety is introduced. A system demonstrator is proposed in [4] with the objective of providing all available UMTS services to train passengers as well as allowing for control and signaling train applications.

On the other hand, [5] and [6] evaluate both, performance and propagation characteristics of wireless communications in high-speed trains, studying factors such as speed, waveguide effects in closed (narrow) environments, propagation loss affected by waves re-entering the car through train windows, and propagation loss among train cars. Finally, harmonic characteristics of Korean high-speed trains using power electronics equipment such as converter-driven motor drives, battery chargers, or auxiliary power supplies are analyzed in [7].

The aforementioned studies contribute to the inclusion of new wireless services in high-speed vehicles. In this sense, this paper proposes a methodology that allows for repeatable, closed-loop, off-line-processed measurements at very high velocities (up to 560 km/h), exceeding the speed limits of current wireless communication standards (500 km/h for GSM-R[2] [8] and for LTE[3] [9, p. 4]). Nonetheless, note that directly evaluating the performance of mobile wireless communication systems under the aforementioned conditions becomes extremely difficult in, for example, high-speed train environments.

## II. Testbed Measurements

*In principle*, measuring the physical layer downlink performance of a new wireless communication system at high velocities is simple. Figure 1 shows a possible set-up where a static transmitter is mounted on a roof, and a moving receiver is placed in a car or a train:

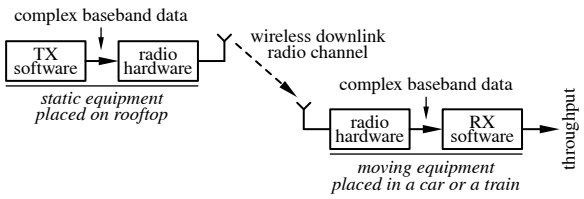


Fig. 1. Testbed measurement set-up.

Keeping things as simple as possible, the first step is to generate a representative transmit signal block (a representative statistical sample) in high-level programming environments as for example Matlab[4] or C++. The next step is to convert

This work has been funded by the Christian Doppler Laboratory for Wireless Technologies for Sustainable Mobility, the A1 Telekom Austria AG, and the KATHREIN-Werke KG. It has also been supported by the Xunta de Galicia, the Ministerio de Ciencia e Innovación of Spain, and the FEDER funds of the European Union under the grants 10TIC003CT, IPT-020000-2010-35, TEC2010-19545-C04-01, and CSD2008-00010. The financial support by the Federal Ministry of Economy, Family and Youth and the National Foundation for Research, Technology and Development is gratefully acknowledged.

[1]GSM, Global System for Mobile Communications and UMTS, Universal Mobile Telecommunications System... mobile communication standards.

[2]GSM-Railway... mobile communication standard for railway communication.

[3]LTE, 3GPP Long Term Evolution... mobile communication standard, successor of GSM/EDGE and UMTS/HSxPA.

[4]Mathworks™ Matlab®, a numerical computing environment often used in communication engineering.

this block into an analog, high-power signal to be transmitted over a wireless channel. Finally, at the receiver, this block is then converted back into a format that can be processed using high-level programming on a personal computer. The resulting throughput then represents the instantaneous physical layer downlink performance of the radio communication system under investigation. If the average downlink performance is of interest, one has to take a larger sample by repeating the measurement. The mean throughput performance of the scenario is then calculated by averaging all values obtained.

*However*, the following **difficulties** arise:

- **Code** has to be written to generate and receive standard-compliant blocks of data. Fortunately, for mobile communication standards such as LTE, free simulators exist [10]. Implementing the complete transmitter and receiver in dedicated real-time capable hardware would also be possible, yet usually too time-consuming. We therefore chose to implement all algorithms off-line in Matlab.
- The transmit and receive **radio hardware** has to be bought or built. When dealing with multiple base-stations employing multiple antennas at the transmitter site and multiple antennas at the receiver site this task is not trivial. Such endeavor consumes a lot of money as well as resources and, therefore, it is a challenge on its own (see [11]). In this paper, we utilize the Vienna MIMO Testbed developed by us from 2006 to 2009 [12].
- If carried out using a car, measurements are **neither controllable nor repeatable**. In other words, it is impossible to externally set a specific average signal to noise ratio or to drive exactly the same route twice, especially not several times a second as it may be preferred in certain measurement set-ups. We therefore refrain from measuring in a car and seek other possibilities.
- **High velocities**, as for example the 500 km/h considered for LTE [9, p. 4], present an additional challenge as trains (and other ground-based vehicles) usually fail to deliver such high speeds.
- Modern wireless communication systems employ channel adaptive modulation and coding techniques. For a measurement, this means that channel information gathered by the receiver —the so-called "**feedback** information"— has to be transmitted back to the transmitter in the uplink or via an external connection. This imposes a problem if the feedback chain consisting of receiver signal-processing, link back to the transmitter, and transmitter signal-processing is not implemented in dedicated hardware, thus does not operate in real-time.
  - A possible solution often employed (e.g., [12]) is to operate the measurement in a static environment. This is not feasible, as we want to measure while the receiver is moving at high velocities.
  - Another possible solution is to implement the feedback chain in dedicated real-time capable hardware. Such an endeavor is only feasible for large companies (e.g. [13]).

We therefore seek to employ a technique that allows for off-line signal processing, while still supporting feedback, repeatability, controllability, and measuring at high velocities.

## III. Issues When Measuring at High Velocities

### A. Feedback

Consider, for example, LTE (see Figure 2): An LTE sub-frame is 1 ms long (Block C) and may use the feedback from the sub-frame 6 ms ago (Block B) [9, p. 294] while the off-line processing for the feedback itself requires e.g. 56 ms, so Block A is the closest block that can be used to calculate the feedback.

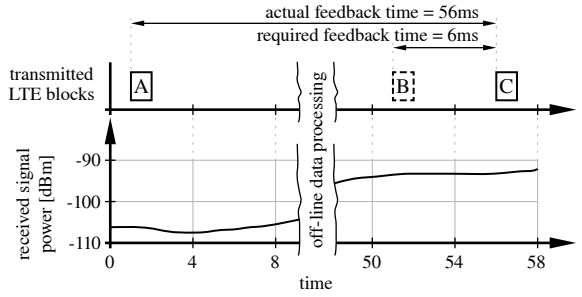


Fig. 2. Feedback in LTE.

If the channel were repeatable (equal in the left-hand and right-hand part of Figure 2) such that block A experiences the same channel as block B, off-line-processed feedback would be possible.

### B. Repeatability and Controllability

To make the channel repeatable, we propose to

1) keep the surroundings constant: By carefully choosing a scenario where no objects move, this is easily possible for time spans in the magnitude of 50 ms.
2) mount the receiver on, for example, a linear guide: Accelerated by a direct-drive linear motor, accelerations of 10 g can be easily reached (g=9,81m/s$^2$) such that a 2.5 m long guide is sufficient to accelerate to a speed of 14 m/s (50 km/h, 31 mph) and stop afterwards.

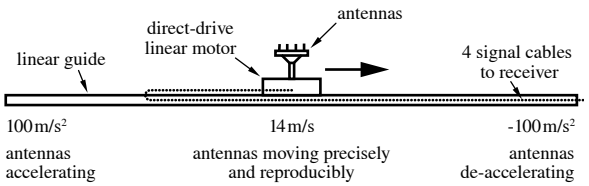


Fig. 3. Proposed set-up for low-velocity feedback measurements.

While direct-drive linear guides are precise enough to repeat a position with an accuracy of 100 µm and high accelerations can be handled by a careful mechanical design, reaching speeds greater than 20 m/s does not seem possible using off-the-shelf components. Furthermore, in the above example, it takes about half a second until the antennas are de-accelerated, moved

back to the left-hand side of the guide, and then accelerated again. This minimum possible time to measure with feedback increases quadratically with the speed to be reached.

### C. High Velocities

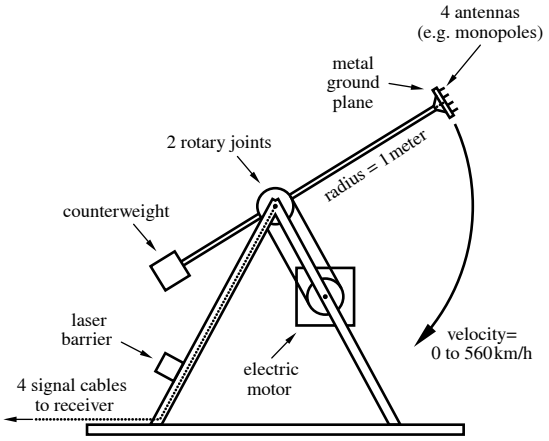


Fig. 4. Proposed set-up with fast-moving receive antennas.

At a greatly reduced price and mechanical effort, all aforementioned issues can be overcome by moving the antennas around a central pivot as shown in Figure 4. This design now allows for very high speeds while the same antenna position is still reached once per rotation.

## IV. Discussion of the Set-Up Proposed in Figure 4

### A. Applicability

While the proposed set-up can be placed at any location desired, closed-loop measurements, that is, measurements with feedback, can only be performed when the surroundings are static. In open-loop mode, measurements in any scenario are possible.

To measure the downlink of LTE at its maximum supported speed of $v_{\text{LTEmax}}$=139 m/s, we chose an arm length of 1 m and an electric motor that can rotate at up to 1500 revolutions per minute. At maximum speed ($v$=157 m/s), the antennas move about 16 cm during a 1 ms long LTE sub-frame, equivalent to 9 degrees of rotation.

Whether this set-up represents real-live situation is subject to discussion. In any case, we believe that it is useful for the initial testing of algorithms and devices in research and development as it allows for measurements that would otherwise require enormous efforts (for example measuring at 500 km/h).

### B. Mechanical Considerations

In mechanical terms, the design proposed in Figure 4 is best described as a centrifuge. Rotating around a central axis at 1500 rotations per minute ($f$=25 rotations per second) and an arm length of $r$=1 m, the antenna moves at a speed of $v$=157 m/s (= 560 km/h = 350 mph). Therefore, the centripetal acceleration of

$$a = \omega^2 r = (2\pi f)^2 r \approx 25000\, m/s^2 \approx 2500\, g$$

has to be exerted by the arm on the antenna. Even without an antenna, to withstand this acceleration, an aluminum alloy arm must exceed a yield strength of 70 N/mm$^2$. To be on the safe side, we therefore chose to use a carbon fiber-reinforced polymer pipe for the arm and design all other critical parts out of high-strength aluminum alloy. A printed circuit board will act as ground plane for the antennas, while the semi-rigid coaxial radio-frequency cables required to guide the received radio waves to the receiver are glued inside the arm using fiberglass glue. The bearings, as well as the engine, can be bought off-the-shelf.

### C. Electrical Considerations

Here, the critical parts are the two rotary joints that are required to connect the four rotating coaxial cables in the arm (we want our set-up to support four antennas, signal center frequency=2.5 GHz) to the static cables outside the arm. Fortunately, military-grade solutions do exist for this application. Except for the rotation, the cables itself are glued inside the arm and therefore static to not change their electrical properties due to bending. Furthermore, even while rotating, the properties of the cables can be easily checked by disconnecting the antennas and pairwise connecting the antenna ports at the end of the arm.

### D. Synchronization Considerations

In order to carry out precise, repeatable measurements, the time at which the antennas will reach a distinct position has to be precisely known beforehand. We therefore utilize a high-speed laser barrier and dedicated real-time capable hardware for the timing synchronization of the blocks transmitted.

### E. Validation

First, we disconnect the four antennas from the end of the arm. Then, we connect the antenna cables pairwise at the end of the arm using rigid cables. Next, we connect two antennas to the cables that come from the rotary unit. Summarizing, these two antennas are then connected to the radio frequency hardware through the proposed set-up without antennas, that is, through a looped-back “long cable” and two rotary joints.

Using this set-up, we then check whether the properties of the transmission change if the arm is rotating at different speeds.

### F. Repeatability

Using the Vienna MIMO Testbed, we can repeat a measurement in an outdoor-to-indoor scenario with a throughput-precision of approximately 2% [14, p.29]. Rotating the antennas between successive measurements by multiples of whole rounds should not affect this precision.

### G. Controllability

A major advantage of the proposed set-up is controllability. One can easily externally change and set the average signal to noise ratio (by changing the power of the transmitter) or the velocity (by changing the rotation speed using a frequency inverter).

### H. Measurement Repetition Rate

Another advantage of the set-up proposed is the ability to carry out many measurements in short time-spans at similar or even equal conditions. Measuring, for example, in a train at 300 km/h would only allow for a few measurements until the train has passed the transmitter, and only for one measurement at a specific position.

Using the proposed set-up, several measurements can be carried out during one rotation of the arm, and measurements at equal channel conditions can be carried out once per rotation. At 300 km/h, for example, a measurement can be repeated every 75 ms. (An increased repetition rate can be achieved by reducing the length of the arm rotated.)

### I. High Velocities

Future applications in high-speed trains may require algorithms to work at speeds up to 500 km/h. Unfortunately, trains or other ground-based vehicles currently do not support such high speeds. The set-up proposed in Figure 4 is designed to support velocities of up to 560 km/h.

## V. Exemplary Measurement Environment

To carry out repeatable, off-line testbed measurements we propose the measurement environment shown in Figure 5:

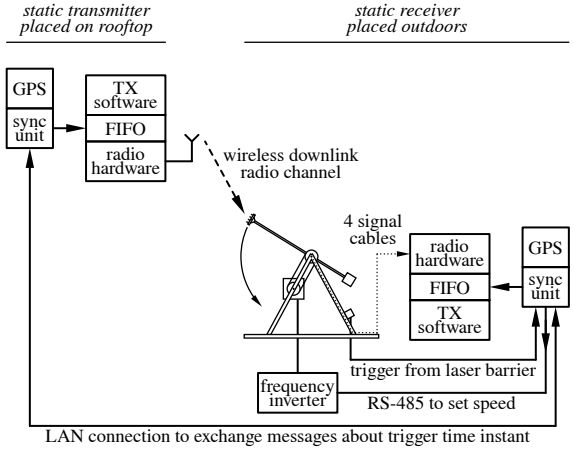


Fig. 5. Proposed testbed set-up for measuring at very high velocities.

In this measurement environment, a data block to be transmitted is first created off-line in software. Next, this block is loaded into a real-time capable transmit FIFO[5] that waits for a trigger pulse of a synchronization unit before forwarding the data samples to the radio hardware.

At the receiver, the incoming signals are captured by four antennas moving at very high-speed, next guided through coaxial cables inside the arm of the rotary unit to its axis, then guided through the rotary joints, then guided to the radio hardware and finally converted to the digital domain. In case the synchronization unit at the receiver issues a trigger, the digital data samples are stored in a FIFO buffers to be then evaluated off-line in software.

The speed of the rotary unit is controlled via RS-485 using an off-the-shelf frequency inverter. Once rotating, the arm passes once per rotation through a laser barrier that sends a pulse to the sync unit. The synchronization unit itself can use this information to exactly calculate the position of the arm. As the synchronization units of the transmitter and the receiver are locked to a GPS reference and connected to each other by a local area network connection, a synchronous trigger pulse can be issued at transmitter and receiver at always the same arm position (that is reached once per rotation). More details on how to build the therefore needed synchronization unit can be found in [15, 16].

## VI. Conclusions

In this paper we present a novel way to measure the performance of mobile radio transmissions at high speeds. In contrast to drive-test measurements, our set-up allows for repeatable, off-line, closed-loop measurements at velocities exceeding 500 km/h.

We see the applicability of the proposed set-up not in the final evaluation of mobile communication devices (namely cell phones) at high speeds, but in the initial testing of parts of them and algorithms under conditions, that would otherwise require way too high efforts.

[5] FIFO, First In First Out... a buffer that is filled from the input side slowly with data and then replays this data on the output side in real-time.

## References

[1] K. Kastell and R. Jakoby, "Implementation of fast handovers and additional authentication in GSM/UMTS for high-speed users," in *Proc. of IEEE International Symposium on Personal, Indoor and Mobile Radio Communications (PIMRC 2005)*, vol. 3, pp. 1753–1757, Sept. 2005, doi: 10.1109/PIMRC.2005.1651743.

[2] M. hee Han, K.-S. Han, and D.-J. Lee, "Fast IP handover performance improvements using performance enhancing proxys between satellite networks and wireless LAN networks for high-speed trains," in *Proc. of IEEE Vehicular Technology Conference (VTC 2008-Spring*, pp. 2341–2344, May 2008, doi: 10.1109/VETECS.2008.519.

[3] Y. Yang, Z. quan Huang, Z.-D. Zhong, and X. Fu, "A study of real-time data transmission model of train-to-ground control in high-speed railways," in *Proc. of IEEE 72nd Vehicular Technology Conference (VTC 2010-Fall)*, pp. 1–5, Sept. 2010, doi: 10.1109/VETECF.2010.5594434.

[4] J. Irvine, D. Robertson, and J. Dunlop, "The MOSTRAIN (mobile services for high speed trains) system demonstrator," in *Proc. of IEEE International Symposium on Personal, Indoor and Mobile Radio Communications (PIMRC 1998)*, vol. 2, pp. 1004–1008, Sept. 1998, doi: 10.1109/PIMRC.1998.734711.

[5] N. Kita, T. Ito, S. Yokoyama, M.-C. Tseng, Y. Sagawa, M. Ogasawara, and M. Nakatsugawa, "Experimental study of propagation characteristics for wireless communications in high-speed train cars," in *Proc. of 3rd European Conference on Antennas and Propagation (EuCAP 2009)*, pp. 897–901, Mar. 2009.

[6] M. Minea, I. Badescu, O. Dobre, and N. Wetzel, "Estimation of disturbative effects of electric traction on data transmission equipment for high-speed trains," in *Proc. of 4th International Conference on Telecommunications in Modern Satellite, Cable and Broadcasting Services*, vol. 1, pp. 106–109, 1999, doi: 10.1109/TELSKS.1999.804705.

[7] T. H. Lee, C. S. Park, S. H. Choi, and S. W. Kim, "A study of the harmonic characteristics of Korean high speed train on the Seoul-Pusan conventional line," in *Proc. of International Conference on Electrical Machines and Systems (ICEMS 2007)*, pp. 1899–1901, Oct. 2007.

[8] K. Kastell, S. Bug, A. Nazarov, and R. Jakoby, "Improvments in railway communication via GSM-R," in *Proc. of IEEE 63rd Vehicular Technology Conference (VTC 2006-Spring)*, vol. 6, pp. 3026–3030, May 2006, doi: 10.1109/VETECS.2006.1683424.

[9] Agilent Technologies, LTE and the Evolution to 4G Wireless: Design and Measurement Challenges. John Wiley & Sons, 2009. ISBN: 0470682612.

[10] C. Mehlführer, M. Wrulich, J. C. Ikuno, D. Bosanska, and M. Rupp, "Simulating the long term evolution physical layer," in *Proc. of the 17th European Signal Processing Conference (EUSIPCO 2009)*, Glasgow, Scotland, Aug. 2009. http://publik.tuwien.ac.at/files/PubDat_175708.pdf

[11] M. Rupp, S. Caban, and C. Mehlführer, "Challenges in building MIMO testbeds," in *Proc. of the 13th European Signal Processing Conference (EUSIPCO 2007)*, Poznan, Poland, Sept. 2007. http://publik.tuwien.ac.at/files/PubDat_112138.pdf

[12] S. Caban, C. Mehlführer, G. Lechner, and M. Rupp, "Testbedding MIMO HSDPA and WiMAX," in *Proc. 70th IEEE Vehicular Technology Conference (VTC2009-Fall)*, Anchorage, AK, USA, Sept. 2009, doi: 10.1109/VETECF.2009.5378995. http://publik.tuwien.ac.at/files/PubDat_176574.pdf

[13] J. Karlsson and M. Riback, "Initial field performance measurements of LTE," Available online from Ericsson, 2008. http://www.ericsson.com/ericsson/corpinfo/publications/review/2008_03/files/LTE.pdf

[14] S. Caban, "Testbed-based evaluation of mobile communication systems," Ph.D. dissertation, Technische Universität Wien, Institut für Nachrichtentechnik und Hochfrequenztechnik, Sept. 2009, supervisor: Markus Rupp.

[15] S. Caban, A. Disslbacher-Fink, and J. A. García-Naya, "Synchronization of wireless radio testbed measurements," in *Proc. IEEE Instrumentation and Measurement Technology Conference (I2MTC2011)*, accepted. Binjiang, Hangzhou, China, May 2011.

[16] A. Disslbacher-Fink, "Hardware-based timing synchronization," Master's thesis, Vienna, Austria, 2011. http://publik.tuwien.ac.at/files/PubDat_195758.pdf

Rodríguez-Piñeiro *et al. EURASIP Journal on Wireless Communications and Networking* (2015) 2015:106
DOI 10.1186/s13638-015-0343-0

EURASIP Journal on Wireless Communications and Networking
a SpringerOpen Journal

RESEARCH Open Access

# Emulating extreme velocities of mobile LTE receivers in the downlink

José Rodríguez-Piñeiro[1*], Martin Lerch[2], José A. García-Naya[1], Sebastian Caban[2], Markus Rupp[2] and Luis Castedo[1]

**Abstract**

Long-Term Evolution (LTE) is expected to substitute the Global System for Mobile (GSM) Communications as the radio access technology for railway communications. Recently, considerable attention has been devoted to high-speed trains since this particular environment poses challenging problems in terms of performance simulation and measurement. In order to considerably decrease the cost and complexity of high-speed measurement campaigns, we have proposed a technique to induce effects caused by highly time-varying channels on Orthogonal Frequency-Division Multiplexing (OFDM) signals while conducting measurements at low speeds. In this work, we illustrate the performance of this technique by comparing the results of LTE measurements at different velocities in a controlled measurement environment. Additionally, we validate this technique by means of simulations, considering one of the scenarios defined as part of the Winner Phase II Channel Models, specifically designed for high-speed train scenarios.

**Keywords:** LTE; OFDM; Measurement; High speed

## 1 Introduction

Over the last few years, broadband communication between nodes moving at high speeds has attracted special attention. One of the most relevant research topics in this field is the modeling of the High-Speed Train (HST) channel. Nowadays, the most widely used communication system between trains and the elements involved in operation, control, and intercommunication within the railway infrastructure is based on the Global System for Mobile (GSM) Communications. This technology, namely, the GSM for Railways (GSM-R), is not well-suited for supporting advanced services such as automatic pilot applications or provisioning broadband services to the train staff and passengers. Besides trains, the increasing number of broadband services available for mobile devices motivated the migration from third-generation mobile networks to fourth-generation ones, mainly Long-Term Evolution (LTE). Therefore, LTE seems to be a good candidate to substitute the GSM as the fundamental technology for railway communications.

Several radio channel models have been proposed for moving radio interfaces, such as the International Telecommunication Union (ITU) channel models [1]. The first channel modeling approach for high-speed train scenarios was proposed by Siemens in 2005 [2]. More recent proposals are the Winner Phase II Model (high-speed moving networks were included in [3]) and the radio channel models approved by the ITU Radiocommunication (ITU-R) Sector for the evaluation of IMT-Advanced Technologies (high-speed train scenarios were explicitly considered in [4]). However, only a few results based on empirically obtained data which can validate the aforementioned channel models are available. One example of high-speed train channel modeling contributions based on the results obtained by means of measurement campaigns is the propagation path-loss model proposed in [5]. The same experimental results were also used for the definition of the large-scale model proposed in [6]. An efficient channel sounding method for high-speed train scenarios using cellular communications systems is proposed in [7] by considering Wideband Code Division Multiple Access (WCDMA) signals.

One of the reasons that explains the low number of measurement campaigns in high-speed environments is their complexity and cost. Furthermore, it is not possible,

*Correspondence: j.rpineiro@udc.es
[1]Department of Electronics and Systems, University of A Coruña, Facultade de Informática, Campus de Elviña, A Coruña 15071, Spain
Full list of author information is available at the end of the article

in most cases, to measure at high speeds in controlled environments in a reproducible and repeatable way. In addition, measuring in high-speed trains demands for specific hardware and software solutions (see [8]). In order to address those problems, we proposed a technique to induce the effects caused by highly time-varying channels in Orthogonal Frequency-Division Multiplexing (OFDM) signals while conducting the measurements at much lower speeds [9]. This technique consists basically in reducing the subcarrier spacing of the OFDM signal by scaling down the bandwidth of the whole OFDM signal. More specifically, we propose to interpolate the transmit OFDM signal in the time domain before its transmission. The time-interpolated signal still conveys exactly the same information as the original one but with a reduced subcarrier spacing, thus artificially increasing the sensitivity to the Inter-Carrier Interference (ICI). For example, if we time interpolate the transmit OFDM signal by a factor $I$, the subcarrier spacing will be reduced by the same factor $I$, which is similar to what would happen if the transmission was conducted at $I$ times the original speed.

In [9], we have proposed this novel methodology for evaluating the performance of OFDM transmissions in real-world scenarios affected by large Doppler spreads while conducting the measurements at low speeds. More specifically, in [9], we considered the transmission of standard-compliant WiMAX Mobile (IEEE 802.16e) signals, both through simulations and realistic outdoor measurements. When conducting measurements with movement in realistic environments and using off-the-shelf vehicles (e.g., cars, trains), the repeatability of the results is basically lost because the following issues arise:

- It is extremely difficult to keep the vehicle speed constant during the measurements.
- Reaching high-speed values with experimental user equipment is expensive and sometimes even not possible in realistic environments.
- Impacts from measurement control can always arise (e.g., another vehicle driving nearby) leading to non-repeatable results.
- Modifications in the measurement scenarios (e.g., the path of the road is modified, a huge vehicle is parked close to the measurement path) hinder fair comparisons with future measurements.
- It is quite challenging to drive several times along exactly the same path.

In order to validate the technique proposed in [9] while, at the same time, overcoming all the abovementioned issues found when conducting non-repeatable measurements using off-the-shelf vehicles, we performed the assessment employing a setup that allows for repeatable measurements at different speeds up to 200 km/h and considered LTE as the wireless communication standard. This setup consists in an antenna that is rotated around a central pivot at a constant speed, allowing for validating our previously proposed technique under repeatable as well as controlled conditions.

We complete the validation by means of simulations considering a channel model suited for high-speed train scenarios. More specifically, we consider the channel model associated with the D2a link of the D2 scenario of the Winner Phase II Channel Models [3]. Notice that our intention is not to model the measurement environment using a channel model existing in the literature. Our intention is to prove the validity of our results in a perfectly repeatable (and controlled) environment which is widely accepted for simulating high-speed train conditions. Therefore, measurement and simulation scenarios correspond to very different wireless communication environments since the simulations consider a rural macro-cell with Line-of-Sight (LoS) between transmitter and receiver, while an outdoor-to-indoor communication without LoS is considered for the measurements.

The presented results, which were obtained under repeatable conditions, both, through measurements and simulations, show that our technique induces highly time-varying channels with excellent agreement.

The rest of the paper is organized as follows. Section 2 explains the proposed time interpolation technique to induce high-speed effects on OFDM signals while conducting measurements at much lower speeds. Section 3 describes the setup and measurement methodology for measurements as well as for simulations. Different figures of merit for the results are also introduced. Section 4 presents both, measurement and simulation results, and shows the excellent agreement obtained with the proposed technique. Finally, Section 5 is devoted to conclusions.

## 2 Emulating high speeds by time interpolation

Let us consider an OFDM modulation where $N$ subcarriers are multiplexed to construct each OFDM symbol. OFDM symbols are cyclically extended by adding $N_g$ samples, thus having a total length of $N_t = N + N_g$ samples. Accordingly, the $k$-th OFDM symbol can be represented as:

$$\mathbf{s}_k = \mathbf{G}_1 \mathbf{F}^H \mathbf{x}_k, \tag{1}$$

where $\mathbf{x}_k$ is a $N \times 1$ vector containing the constellation symbols corresponding to the transmitted subcarriers in the $k$-th symbol, $\mathbf{F}$ is the standard $N \times N$ DFT matrix, $\mathbf{G}_1$ is a $N_t \times N$ matrix which cyclically extends the OFDM symbol, and $\mathbf{s}_k$ is a $N_t \times 1$ vector with the transmitted OFDM symbol in the time domain. This signal is transmitted at a sampling period $T_s$, hence creating symbols with a duration $T_t = T_s N_t$ and a bandwidth $F_s = 1/T_s$. When

transmitting $\mathbf{s}_k$ over a time-varying channel and assuming a sufficiently long cyclic prefix, the received signal is [10]:

$$\mathbf{r}_k = \mathbf{F}\mathbf{G}_2\left(\mathbf{H}_k^{(t)}\mathbf{G}_1\mathbf{F}^H\mathbf{x}_k + \mathbf{n}_k\right) = \mathbf{H}_k\mathbf{x}_k + \mathbf{w}_k, \quad (2)$$

where $\mathbf{H}_k^{(t)}$ is a $N_t \times N_t$ matrix with the time-varying channel impulse response experienced by $\mathbf{s}_k$, $\mathbf{G}_2$ is a $N \times N_t$ matrix to remove the cyclic prefix, $\mathbf{n}_k$ is a $N_t \times 1$ vector with uncorrelated complex-valued white Gaussian noise entries with power $\sigma^2$, $\mathbf{H}_k$ is a $N \times N$ matrix with the channel frequency response, and $\mathbf{w}_k$ is a $N \times 1$ vector containing uncorrelated complex-valued white Gaussian noise entries with variance $\sigma^2$.

If the channel is time invariant, $\mathbf{H}_k$ will be a diagonal matrix. In time-selective channels, however, non-zero entries will appear outside the main diagonal of $\mathbf{H}_k$ and ICI arises in the received signal. The amount of ICI relates to the normalized Doppler spread of the channel, which is given by $D_n = f_d T$, $f_d$ being the maximum Doppler frequency and $T = T_s N$ the duration of the OFDM symbol excluding the cyclic prefix. As proposed in our previous work [9], parameter $T$ can be adjusted by time interpolation by a factor $I$, yielding an OFDM symbol duration $T^I = IT_sN$. Therefore, given the actual velocity $v$ of the mobile receiver, the normalized Doppler spread, impacting the time-interpolated OFDM signal can be written as:

$$D_n^I = f_d T^I = f_d I T_s N = \frac{T_s N I f_c v}{c} = \frac{T_s N f_c}{c} v^I, \quad (3)$$

with $f_c$ the carrier frequency, $c$ the speed of light, and $v^I = Iv$ the emulated speed as a result of an actual measurement speed $v$ and an interpolation factor $I$. Consequently, enlarging the symbol length $T^I$ by adjusting $I$ allows for the emulation of a velocity $v^I$ while conducting measurements at an actual speed $v$. Notice that this procedure is also valid for time decimation of the signal, simply taking $0 < I < 1$, leading to an emulated speed lower than the actual one. Finally, note also that $I$ does not have to be an integer value. Fractional time interpolation and decimation factors are also possible, hence providing a great flexibility for adjusting $v^I$ from $v$.

In our setup, time interpolation factors $I \geq 1$ were applied to standard-compliant downlink LTE OFDM signals before the over-the-air transmission to emulate situations with $I$ times higher velocity than the actual receiver speed. The same principle was considered for the simulations.

## 3 Evaluation setup and procedure

We use the measurement setup shown in Figure 1 (measurement branch) to test the proposed technique of emulating high speeds by time interpolation of OFDM signals. The setup consists of:

1. *Signal generation (transmitter side) and signal processing (receiver side)*: at the transmitter side, standard-compliant LTE subframes are generated using the LTE Downlink Link-Level Simulator developed at the TU Wien [11]. At the receiver side, the same simulator is used to process the received signals and to estimate the following figures of merit: uncoded Bit Error Ratio (BER), coded BER, Error Vector Magnitude (EVM), and Signal-to-Noise Ratio (SNR).
2. *Time interpolation and time decimation*: the signal is time-interpolated by a factor $I$ at the transmitter and decimated by the same factor $I$ at the receiver side. This way, we emulate a Doppler spread similar to that obtained with a speed increase by a factor of $I$.
3. *Signal transmission and signal reception*: signals are transmitted over the air by using a testbed developed

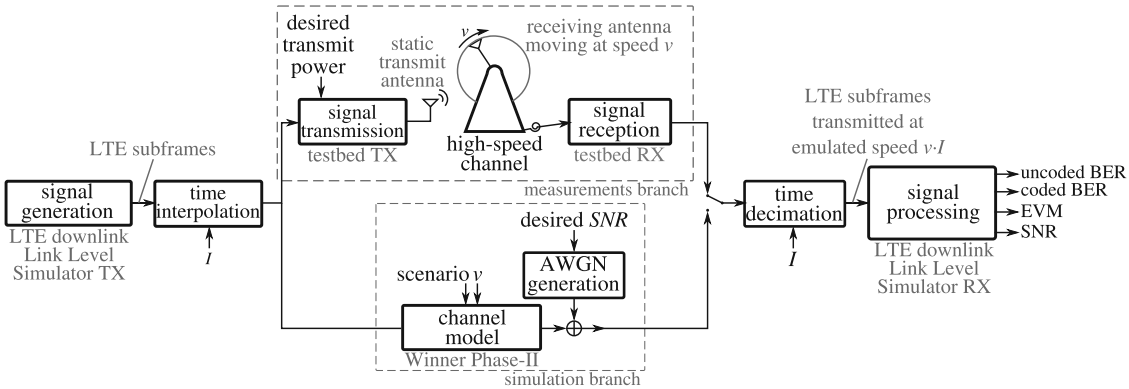


**Figure 1** Block diagram of the considered setup. 'Measurement branch' is considered for the measurements, while 'simulation branch' is used for the simulations.

at the TU Wien [12,13]. The testbed transmitter is placed outdoors on a roof of a building in downtown Vienna, Austria. The receiver is placed indoors in the fifth floor of an adjacent building at a distance of 150 m (see Figure 2), hence recreating an infrastructure-to-vehicle scenario. Note that no feedback channel was used in our experiments. Consequently, no adaptive modulation and coding schemes were applied. Channel Quality Indication (CQI) values were fixed in advance. Notice also that the testbed is equipped with a highly precise time and frequency synchronization system based on Global Positioning System (GPS)-disciplined rubidium oscillators and a custom-made synchronization unit [14]. As a result, we can assume perfectly time and frequency synchronized measurements. Thus, the results are not affected by time or frequency offsets due to imperfect synchronization.

4. *Generation of high-speed conditions*: high-speed conditions are generated by transmitting from a static transmit antenna to a receive antenna that is rotated around a central pivot in a controlled and repeatable way [15,16] (see Figure 3). Different channel realizations are created by measuring at different initial positions of the receive antenna. Note that the trajectory of the antenna is well approximated by a straight line since the diameter of the trajectory is 2 m and each LTE subframe is 1 ms long (see Figure 4).

### 3.1 Measurement setup

In order to evaluate the impact of high-speed conditions on LTE transmissions, actual velocities ranging from 50 to 200 km/h were considered. Furthermore, interpolation factors of $I = 1$ (no interpolation), $I = 2$, and $I = 3$ were used for generating Doppler spreads equivalent to those associated to velocities ranging from 50 to 600 km/h. Note that it is possible to generate exactly the same Doppler spread value from different combinations of the actual measurement velocity and the interpolation factor (see Table 1). We considered this fact to show that our technique allows for the evaluation of wireless communication systems at high speeds while measuring at much lower speeds. In order to do that, we generated the same Doppler spread by means of different velocities and interpolation factors, and then, we compared the obtained results. Table 1 shows the combinations of actual speeds and interpolation factors which lead to equal Doppler spreads (each row of the table corresponds to a different Doppler spread factor).

### 3.2 Measurement procedure

Several measurements are conducted for each velocity and interpolation factor. More specifically, three different positions of the whole receiver (including the antenna rotation unit) along its rails (see Figure 3) are considered. For each of these positions, 10 measurements per velocity and interpolation factor are carried out, each starting at a given angular shift on the circumference defined by the receive antenna rotating around a central pivot. Therefore, 30 different channel realizations are measured in total for each pair of velocity and interpolation factor. Furthermore, the whole set of measurements is repeated for each SNR value, among those specified in Table 2. The transmit power employed at the testbed transmitter

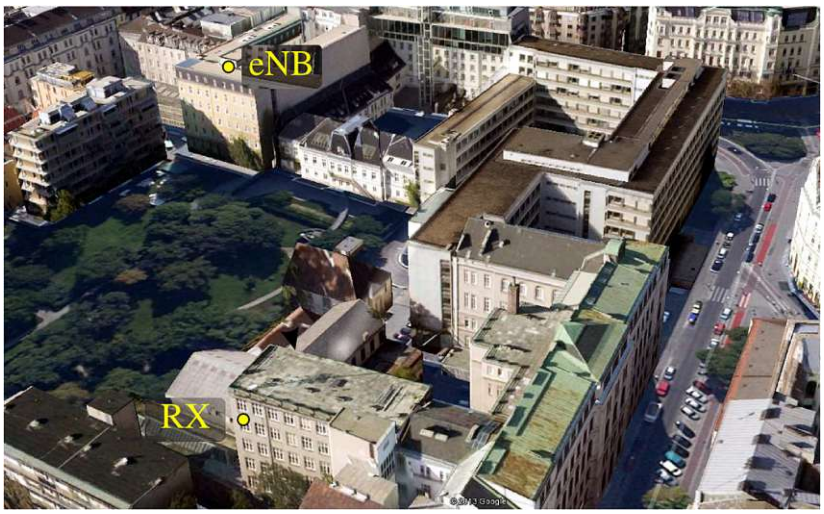


**Figure 2** Location of the transmitter and the receiver. Note that the transmitter is installed outdoors on a roof of a building, while the receiver is placed indoors in the fifth floor of an adjacent building. The distance between transmitter and receiver is approximately 150 m.

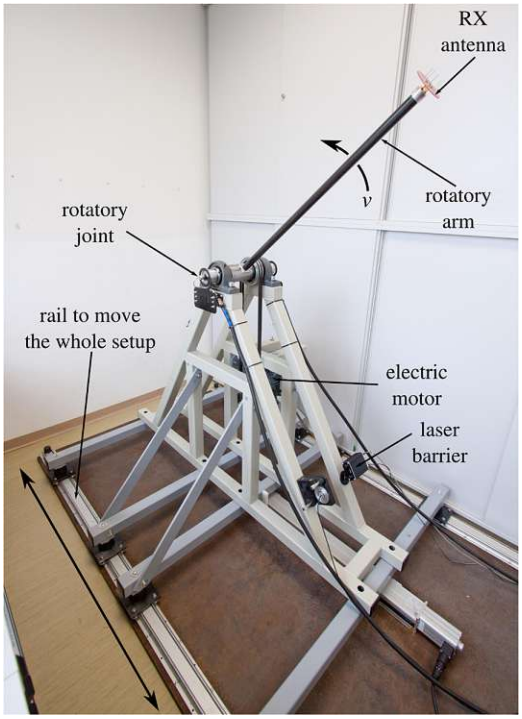


**Figure 3** Setup used for generating high-speed conditions. The receive antenna is rotated around a central pivot, generating high-speed conditions in a controlled and repeatable way.

is modified in order to achieve different average SNR values.

In order to be able to compare the results gathered from different interpolation factors, we have to ensure that the receive antenna trajectory, spectrum usage, and average OFDM symbol energy remain constant for each emulated velocity $v \cdot I$:

1. *Equal receive antenna trajectory*: in order to maintain a constant Doppler spread, the rotation speed has to be divided by the interpolation factor (see Table 1). Therefore, as it is shown in Figure 4, the trajectory of the receive antenna during the transmission of one LTE subframe does not vary when changing the interpolation factor and antenna velocity as long as the emulated speed is the same.
2. *Equal spectrum usage*: when a subframe is interpolated by a factor of $I$, its bandwidth is decreased by the same factor, which in principle reduces the effect of the channel frequency diversity. In order to experience the same spectrum, $I$ replicas of the interpolated signal are transmitted to ensure that the whole frequency range of the original signal is used. The results are then averaged. Figure 5 shows an example of this procedure for $I = 2$, $I = 3$, and for an arbitrary interpolation factor.

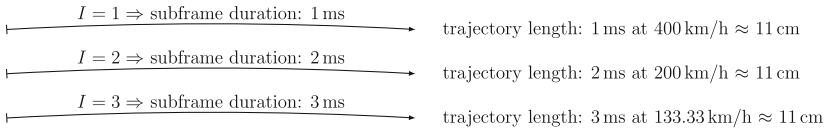


**Figure 4** Trajectory followed by the antenna during the acquisition of a single LTE subframe. An emulated speed of 400 km/h was used and the three interpolation factors $I = \{1, 2, 3\}$ were considered. Evaluating the results at a speed value of 400 km/h can be done 1) by measuring at the actual velocity of 400 km/h without time interpolation ($I = 1$); 2) by measuring at half the speed with $I = 2$; and 3) by measuring at 400/3 = 133.33 km/h with $I = 3$. In all cases, the length of the trajectory described by the antenna is the same (close to 11 cm) and can be approximated by a straight line since the antenna describes a circle with a diameter of 2 m while rotating around the central pivot.

**Table 1 Emulated speed values (expressed in km/h) that can be obtained from more than an actual velocity *v***

| Emulated speed, $v^I = Iv$ | $I = 1$ | $I = 2$ | $I = 3$ |
|---|---|---|---|
| 100 | $v = 100$ | $v = 50$ | – |
| 150 | $v = 150$ | $v = 75$ | $v = 50$ |
| 200 | $v = 200$ | $v = 100$ | $v = 66.6$ |
| 250 | – | $v = 125$ | $v = 83.3$ |
| 300 | – | $v = 150$ | $v = 100$ |

Notice that these are the speed values considered in the error curves in Figures 6, 7, 8, 9, 10, and 11.

3. *Equal average transmit energy per OFDM symbol*: in order to preserve the average energy per OFDM symbol, the interpolated signals are scaled in amplitude by a factor of $\sqrt{I}$ before being transmitted.

Notice that our main objective is to validate the proposed technique considering a realistic scenario while, at the same time, keeping its complexity under reasonable terms, hence simplifying the validation process and facilitating the comprehension of the results. Therefore, we consider over-the-air standard-compliant LTE transmissions as a good example of the state of the art in wireless communications. However, due to the abovementioned simplicity reasons, we restrict the evaluation to a single-user scenario without feedback channel, so modulation and coding scheme values are fixed beforehand instead of being adapted according to the channel quality.

**Table 2 Main parameters for measurements as well as for simulations**

| Parameters | Values | | |
|---|---|---|---|
| Bandwidth, $F_s$ (MHz) | 15.36 (9 occupied) | | |
| FFT size, $N$ | 1,024 | | |
| Used subcarriers | 600 (excluding DC) | | |
| Velocities, $v$ (km/h) | 50, 66.6, 75, 83.3, 100, 125, 150, and 200 | | |
| Carrier frequency, $f_c$ (GHz) | 2.5 | | |
| Interpolation factors, $I$ | 1, 2, and 3 | | |
| SNR (dB) | 38, 31, 21, 11, 1, and $\infty$ (simulations only) | | |
| CQI values | 1 | 8 | 12 |
| Modulation | 4-QAM | 16-QAM | 64-QAM |
| Code rate | 0.076 | 0.48 | 0.65 |
| Efficiency | 0.1523 | 1.9141 | 3.9023 |
| Source bits | 1,192 | 15,288 | 31,192 |
| Coded bits | 16,000 | 32,000 | 48,000 |
| Peak throughput (Mbit/s) | 1.192 | 15.288 | 31.192 |

Although three CQI values were evaluated and considered throughout the text to validate the proposed technique, results in the figures only consider CQI = 12.

Each LTE frame in the Frequency-Division Duplex (FDD) mode consists of ten subframes, each one following a different structure depending on the subframe index. For example, synchronization signals are always allocated in the first and sixth subframes, while broadcast channels are included, if necessary, in the first subframe. In order to make the comparison between channel realizations independent of the subframe structure, we always transmit the seventh subframe, considering only pilot and data symbols in subsequent evaluations. Consequently, we ensure the same payload for each channel realization, which enables us to fairly compare the results of different measurements as the subframe structure is kept invariant all the time. More specifically, the number of data symbols that can be transported in the seventh subframe according to the system configuration is 8,000, which leads to the number of coded bits, source bits, and peak throughput values specified in Table 2.

### 3.3 Simulation environment

We employ the setup shown in Figure 1 (simulation branch) to validate through simulations our technique of emulating high speeds by time interpolation. We select noise variance values that lead to the same SNR values estimated from the measurements. A channel model suited for high-speed train scenarios was considered, namely, the model defined by the D2a link of the D2 scenario of the Winner Phase II Channel Models [3]. This scenario models the channel between an antenna placed at the roof of a train carriage and a network of fixed eNodeBs installed in a rural environment, which usually leads to LoS propagation conditions. Speeds up to 350 km/h can be considered for the train movement.

Notice that the considered channel model does not intend to reproduce the wireless channel observed in the measurements. Our intention is to complement the evaluation of the proposed technique in a simulation environment while, at the same time, avoiding the process of characterizing the doubly selective wireless channel observed in the measurements, which is not the intention of this work. Finally, we selected the aforementioned channel model because it is specifically designed to model an outdoor-to-outdoor high-speed scenario with LoS between transmitter and receiver, while the measurement environment corresponds to an outdoor-to-indoor scenario with Non-Line-of-Sight (NLoS) between them.

### 3.4 Simulation procedure

The number of evaluated subframes by simulation was the same considered when measuring, i.e., 30 channel realizations for each velocity and interpolation factor pair. The values of SNR, velocity, and interpolation factors were also kept unchanged. We also guarantee an equal spectrum usage as well as equal average transmit energy per OFDM

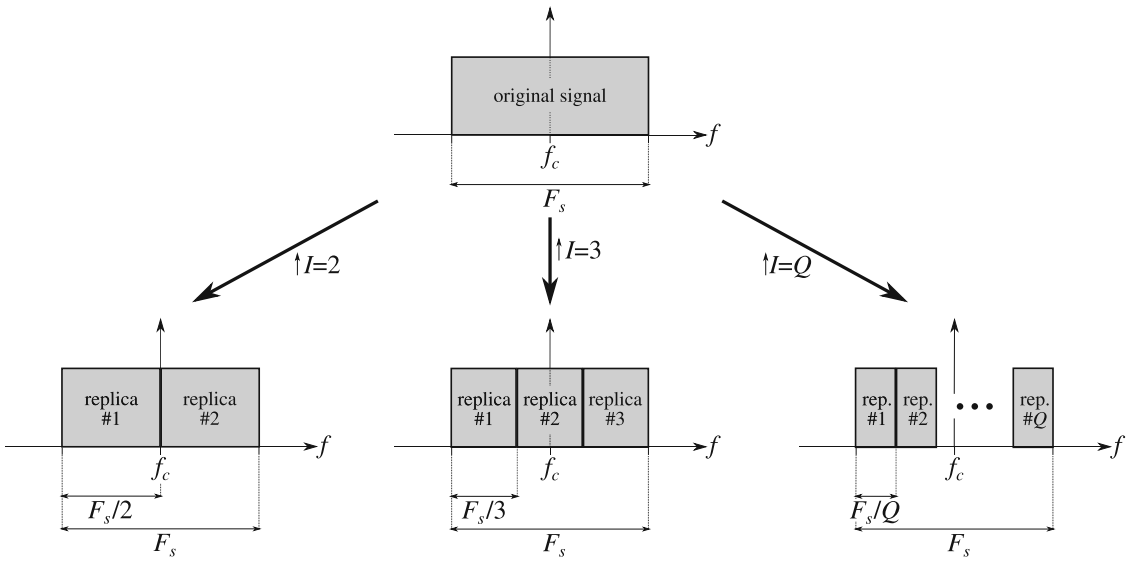


**Figure 5** Ensuring equal spectrum usage for interpolation factors $I = 2$, $I = 3$, and for an arbitrary integer interpolation factor $I = Q$. $I$ replicas of the interpolated signal are transmitted to ensure that the whole frequency range of the original signal (without interpolation) is used.

symbol. Furthermore, to fairly compare the results, the channel model was fed with identical initial conditions (e.g., delays and mean power per path) for each evaluated interpolation factor. This way, we model a situation in which the receiver moves along the same path for each interpolation factor.

Table 2 details the most relevant parameters for the experimental evaluations as well as for the simulations.

### 3.5 Figures of merit

We have selected three different figures of merit that evaluate the quality of the signal at different points in the receive signal processing chain: 1) EVM calculated without knowing the transmitted symbols; and 2) uncoded BER, which is the BER after the symbol decision, and coded BER, which corresponds to the BER at the output of the channel decoder.

Recall that our main objective is to inspect the level of agreement between the results obtained from those figures of merit when the wireless system is evaluated at actual speed conditions with respect to those obtained when the system is evaluated (under similar conditions) using emulated speeds by time interpolation. Given that the testbed employed for the measurements guarantees excellent time and frequency synchronization between transmitter and receiver, the results of the three figures of merit enumerated above greatly depend on the channel equalizer, which is strongly affected by ICI.

The main reason for considering both, EVM and uncoded BER, is that EVM is an unbounded and continuous metric, which is specially valuable when the SNR levels observed are high enough to saturate the BER to its minimum value of zero. On the other hand, considering uncoded BER in the evaluation is very convenient not only because it is one of the most used performance metrics in wireless communications but also because the EVM is calculated only from the received symbols. Hence, EVM results loose accuracy as the corresponding SNR value decreases. Finally, coded BER is specially relevant in our evaluation since the proposed technique causes a signal bandwidth reduction proportional to the time interpolation factor, hence reducing the frequency diversity and potentially degrading the channel decoder performance. Consequently, one could expect that, in terms of coded BER, the wireless system would perform differently when actual speeds are considered in comparison to emulated ones.

With the aim of evaluating of the level of agreement between the results obtained by means of actual speed with respect to emulated ones, we have included curves for the relative error values computed for those emulated speed values that can be obtained from more than one actual velocity (see Section 4). We considered the emulated speed values that can be obtained from at least two of the three interpolation factors considered (see Table 1).

The procedure followed to calculate each figure of merit is detailed below:

*SNR*. The SNR is estimated considering exclusively the data subcarriers. Thus, the guard subcarriers, Direct

Current (DC) subcarrier as well as the pilots are discarded. SNR is estimated by performing the following steps:

1. Noise samples for a given velocity $v$ and interpolation factor $I$ are captured directly (measurement case) or generated (simulation case). In the measurement case, noise samples in the time domain are captured with the transmitter switched off (hence, not transmitting any signal).
2. The captured noise samples in the time domain are then processed as if they were actual data samples, i.e., they are downsampled by the corresponding interpolation factor (if required), the cyclic prefix is removed, a Fast Fourier Transform (FFT) is performed, and both guard subcarriers, pilots, and also the DC subcarrier are discarded.
3. As a result, $w^{(l,k,s)}$ noise samples are obtained in the frequency domain, each one corresponding to the $l$-th subcarrier of the $k$-th OFDM symbol of the $s$-th subframe and for the values of $l$ corresponding to the indexes of the data subcarriers.
4. All previous steps are repeated when the transmitter is switched on, so $r^{(l,k,s)}$ data samples are obtained in the frequency domain.
5. The average SNR for a given velocity $v$ and interpolation factor $I$ is then estimated by averaging out the SNR values corresponding to each channel realization. Defining:

$$\bar{r} = \frac{1}{LKS} \sum_{l=1}^{L} \sum_{k=1}^{K} \sum_{s=1}^{S} \left| r^{(l,k,s)} \right|^2, \tag{4}$$

and:

$$\bar{w} = \frac{1}{LKS} \sum_{l=1}^{L} \sum_{k=1}^{K} \sum_{s=1}^{S} \left| w^{(l,k,s)} \right|^2, \tag{5}$$

then, the SNR is calculated as follows:

$$\text{SNR} = \frac{\bar{r} - \bar{w}}{\bar{w}}, \tag{6}$$

with $L$, $K$, $S$ the total number of data subcarriers, OFDM symbols, and subframes, respectively.

*EVM*. The EVM is obtained based on the equalized symbols which feed the receiver decision. The following steps are considered for the EVM estimation:

1. The dynamic range of the equalized symbols is bounded. This is realistic in a practical receiver. In this sense, real and imaginary parts of the symbols are clipped to a maximum value. This avoids symbols having extremely large modulus (e.g., due to imperfect zero-forcing channel equalization), hence distorting the EVM estimation. Clipping values were selected, taking into account the mean power of the equalized symbols in perfect conditions (flat channel in the absence of noise).
2. A hard decision unit is fed with the clipped symbols. Let $\mathbf{s}_c = \left(s_c^1, s_c^2, \ldots, s_c^S\right)^T$ be the vector of $S$ clipped symbols in a subframe and $\mathbf{s}_d = \left(s_d^1, s_d^2, \ldots, s_d^S\right)^T$ the vector of decided symbols.
3. The EVM per subframe, expressed in decibels, is obtained as:

$$\text{EVM} = 10 \log_{10} \left( \frac{P_r}{P_c} \right), \tag{7}$$

with $P_c = \frac{1}{S} \mathbf{s}_c^T \cdot \mathbf{s}_c$, $P_r = \frac{1}{S} \mathbf{s}_r^T \cdot \mathbf{s}_r$, and $\mathbf{s}_r = |\mathbf{s}_c - \mathbf{s}_d|$. Notice that the aforementioned procedure for calculating the EVM does not require knowing the transmitted symbols. However, the higher the uncoded BER, the more underestimated the EVM is.

## 4 Results

This section presents both, measurement and simulation results. Three types of performance curves are included in the result graphs, which are:

- *Red solid lines*: they correspond to the cases with no interpolation ($I = 1$). According to the speed values considered for the measurements as well as for the simulations, the red solid curves range from 50 to 200 km/h.
- *Green dashed lines*: they correspond to the cases with $I = 2$, so the emulated velocity is twice the measured or simulated speed. Therefore, the green curves range from 100 to 400 km/h.
- *Pink dotted lines*: they correspond to the cases where $I = 3$. In this case, the emulated velocity is three times the measured or simulated speed, and the curves range from 150 to 600 km/h.

Besides the performance curves, we have also included the relative error curves for all figures although in some cases not all error curves are plotted. Three types of relative error curves are included in the graphs presenting the results (see Table 1), which are:

- *Green dashed lines*: they correspond to the relative difference between the results obtained when the interpolation factor $I = 2$ is employed and when actual speeds are used.
- *Blue dashed lines*: they correspond to the relative difference of the results between the interpolation factors $I = 3$ and $I = 2$.
- *Pink dotted lines*: they correspond to the relative difference of the results between the interpolation factors $I = 3$ and $I = 1$ (actual speeds).

The relative error values are calculated differently for EVM and for BER (coded and uncoded):

- *Relative error for EVM*: given $\mathrm{EVM}_A$ and $\mathrm{EVM}_B$ the instantaneous EVM values, corresponding to a channel realization and obtained for the interpolation factors $I = A$ and $I = B$, respectively, we define the instantaneous relative error as:

$$E_{\mathrm{EVM}}(A,B) = 100 \cdot \frac{\mathrm{EVM}_A - \mathrm{EVM}_B}{\mathrm{EVM}_B} \quad [\%]. \tag{8}$$

- *Relative error for uncoded and coded BER*: given $W_A$ and $W_B$ the number of received bits estimated without errors, corresponding to a channel realization and obtained for the interpolation factors $I = A$ and $I = B$, respectively, we define the instantaneous relative error for the BER as:

$$E_{\mathrm{BER}}(A,B) = 100 \cdot \frac{W_A - W_B}{W_B} \quad [\%]. \tag{9}$$

Mean relative error values for both error types are calculated by averaging instantaneous relative error values for all channel realizations. These mean relative error values are plotted in Figures 6, 7, 8, 9, 10, and 11 together with their corresponding 95% BCa bootstrap confidence intervals for the mean [17]. These confidence intervals are plotted as an area around each curve and in the same color as the corresponding curve. We also gauge the precision of the results by calculating the 95% confidence intervals for the mean.

Due to limitations of the inverter driving the motor used to rotate the receive antenna (see Figure 3), the actual velocity range considered for the measurements (and also for the simulations) starts at 50 km/h, while the maximum actual speed value is set to 200 km/h. Given that we consider interpolation factors $I = 1, 2, 3$, in the speed range from 50 to 300 km/h, at least two curves overlap, thus allowing for evaluating the level of agreement of the results between different interpolation factors.

### 4.1 Measurement results

Figure 6 shows the measured EVM for CQI = 12 (64-QAM) for SNR values ranging from 38 to 11 dB. For high SNR values, it can be seen that the higher the emulated speed is, the worse the EVM becomes, as expected. However, it can be seen that the curves for different interpolation factors (as well as their associated confidence regions) overlap, which demonstrates that the proposed technique of emulating high speeds by time interpolation performs adequately. Results for CQI = 1 (4-QAM) and CQI = 8 (16-QAM) were not included, but they have been also evaluated, and they show that the achieved performance is very similar despite the considered modulation scheme. Figure 6 also shows that the quality of the received signal, in terms of EVM, is considerably affected by the speed for high SNR values, showing that the main source contributing to the signal distortion is the ICI. As the SNR decreases, however, the performance is less affected by the

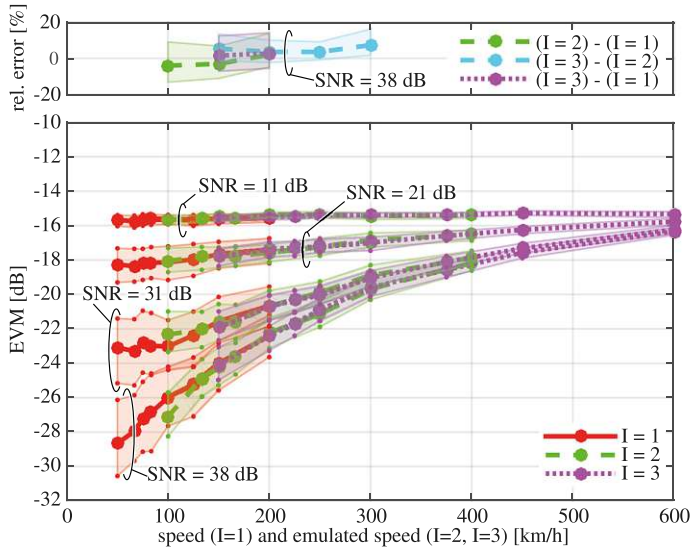


**Figure 6** Measured EVM for different SNR values. EVM results obtained by measuring when CQI = 12 and SNR ranges from 11 to 38 dB for the interpolation factors $I = 1, 2, 3$. 95% confidence regions are provided. We have also evaluated the EVM for CQI = 1 (4-QAM) and CQI = 8 (16-QAM), and the results are almost indistinguishable. Corresponding relative error curves are plotted when the SNR is set to 38 dB, showing an excellent agreement.

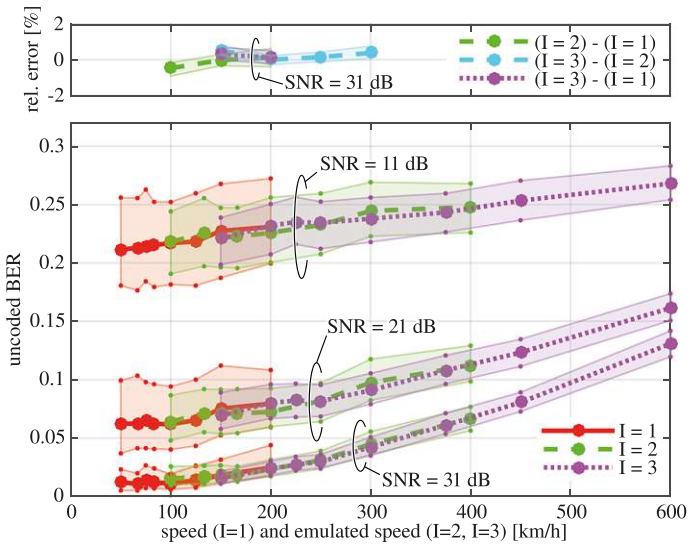


**Figure 7** Measured uncoded BER for different SNR values. Uncoded BER results obtained by measuring when CQI = 12 and SNR ranges from 11 to 31 dB for the interpolation factors $I = 1, 2, 3$. 95% confidence regions are provided. Corresponding relative error curves are plotted when the SNR is set to 31 dB, showing an excellent agreement.

emulated speed because the noise is the main contributor to the signal distortion.

The relative error curves in Figure 6 also demonstrate the excellent agreement of the results independently of the source of the Doppler spread: actual speed or emulated velocity from time interpolation. Note that the confidence intervals for the relative error values are mainly influenced by the number of realizations averaged. Hence, these confidence intervals could be decreased by increasing the number of realizations measured. However, as the

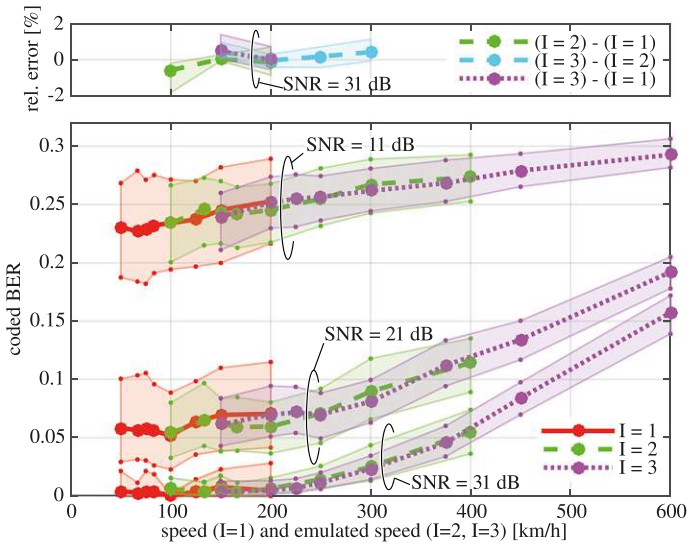


**Figure 8** Measured coded BER for different SNR values. Coded BER results obtained by measuring when CQI = 12 and SNR ranges from 11 to 31 dB for the interpolation factors $I = 1, 2, 3$. 95% confidence regions are provided. Corresponding relative error curves are plotted when the SNR is set to 31 dB, showing an excellent agreement.

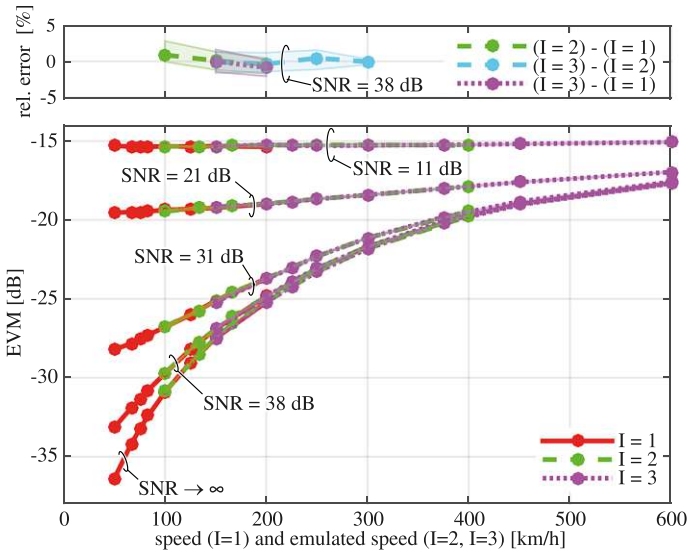


**Figure 9** Simulated EVM for different SNR values. EVM results obtained by simulation when CQI = 12 and SNR ranges from 11 dB to infinity for the interpolation factors $I = 1, 2, 3$. Note that the channel model associated to the D2a link of the D2 scenario of the Winner Phase II Channel Models was applied. 95% confidence regions are provided. We have also evaluated the EVM for CQI = 1 (4-QAM) and CQI = 8 (16-QAM), and the results are almost indistinguishable. Corresponding relative error curves are plotted when the SNR is set to 38 dB, showing an excellent agreement.

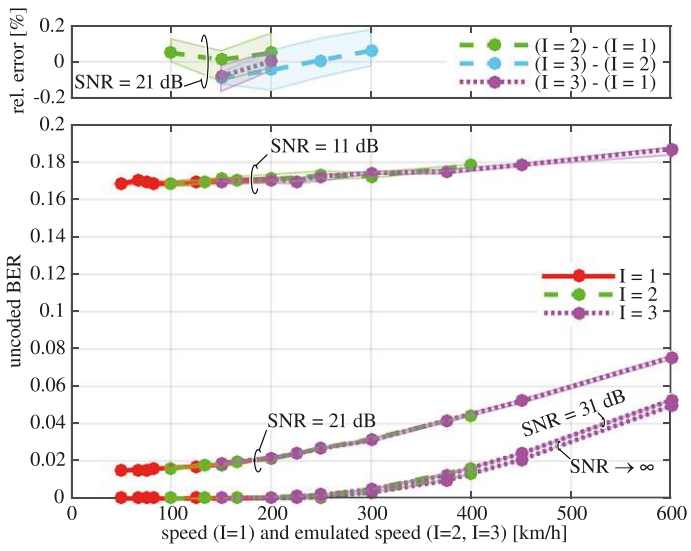


**Figure 10** Simulated uncoded BER for different SNR values. Uncoded BER results obtained by simulation when CQI = 12 and SNR ranges from 11 to 31 dB for the interpolation factors $I = 1, 2, 3$. Note that the channel model associated to the D2a link of the D2 scenario of the Winner Phase II Channel Models was applied. 95% confidence regions are provided. Corresponding relative error curves are plotted when the SNR is set to 21 dB, showing an excellent agreement. Note that for SNR values greater or equal than 31 dB, the BER curves are close to zero for speeds below 250 km/h; hence, the relative error curves do not provide much information.

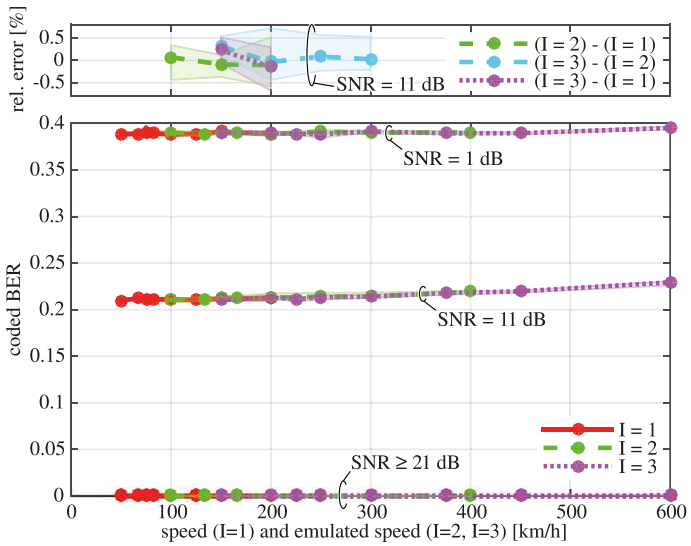


**Figure 11** Simulated coded BER for different SNR values. Uncoded BER results obtained by simulation when CQI = 12 and SNR ranges from 1 dB to infinity for the interpolation factors $I = 1, 2, 3$. Note that the channel model associated to the D2a link of the D2 scenario of the Winner Phase II Channel Models was applied. 95% confidence regions are provided. Corresponding relative error curves are plotted when the SNR is set to 11 dB, showing an excellent agreement. Note that for SNR values greater or equal than 21 dB, the BER curves are close to zero for all considered speeds; hence, the relative error curves do not provide much information.

receive antenna trajectory is kept constant between different interpolation factors, the relative error is mainly influenced by the repeatability of the setup, the noise, and the interpolation itself. For this reason, we can achieve relative agreements with mean error values below 10% in the worst case (i.e., the highest SNR value of 38 dB) without increasing the number of channel realizations.

Figures 7 and 8 show the measured uncoded BER and coded BER, respectively, for different SNR values when CQI = 12. Both, uncoded BER and coded BER, are strongly dependent on the emulated speed for high SNR values, while the noise is the main source of signal distortion when the SNR decreases. It can also be observed that curves for different interpolation factors overlap both for uncoded BER and coded BER, demonstrating again the excellent results of the proposed technique. Notice also that, as shown in the corresponding relative error curves in Figures 7 and 8, the agreement of the proposed technique is below 2 %, both in terms of uncoded BER and coded BER. Therefore, such a proposed technique can be effectively used for emulating high-speed effects at any point of the receive signal processing chain.

### 4.2 Simulation results

The channel model of the simulations was selected because of its suitability for the simulation of high-speed conditions. Notice that such a channel model leads to frequent LoS propagation conditions [3]. However, the receiver in the measurements is located inside a building, while the eNodeB is placed on a roof of another building (see Figure 2), and hence, NLoS propagation conditions arise, leading to a much more relevant multipath effect.

Figure 9 shows the simulated EVM for CQI = 12 (64-QAM) for SNR values ranging from 38 to 11 dB. Additionally, we have also evaluated the results in the absence of noise (infinite SNR). Note that the slopes of the curves are similar to those obtained by measurements as shown in Figure 6, while the obtained EVM values are always lower for the same SNR value. This result is expected because the channel model considered for the simulations is easier to equalize due to the lower variability of the simulated channel. However, when the SNR decreases (SNR = 11 dB and SNR = 21 dB in our case), the above-mentioned effect vanishes as the noise becomes the main contribution to the signal distortion and the corresponding curves approach each other for simulations and for measurements.

The variability of the results obtained by simulations is much lower than that of the measurements because, on the one hand, the simulated channel is less variable than that observed in the measurements. On the other hand, exactly the same initial channel conditions are applied in the simulations for each interpolation factor and velocity pair, thus ensuring much less variability between the different channel realizations generated for each interpolation factor and velocity pair. In fact, the confidence region

of each simulated curve completely overlaps the curve itself, which causes that the confidence regions cannot be appreciated although they are included. Additionally, curves simulated for different interpolation factors almost completely overlap, hence showing the good behavior of the proposed technique also in this case. This precise behavior is also confirmed by the corresponding relative error curves in Figure 9.

Finally, Figures 10 and 11 show the simulated uncoded BER and coded BER, respectively, for different SNR values when CQI = 12. Some level of dependency on the emulated speed for high SNR values can be still appreciated for the uncoded BER, while the coded BER is always zero for SNR values greater than or equal to 21 dB since the channel decoder is able to correct all errors. Notice that this is not the case for the measurements as the channel is much more difficult to equalize. Curves for different interpolation factors overlap both for uncoded BER and coded BER, thus showing the good behavior of the proposed interpolation technique. This is also confirmed by the corresponding error curves.

## 5 Conclusions

We have shown that time interpolating OFDM signals prior to their transmission followed by the corresponding decimation at the receiver is a suitable technique for inducing high-speed effects (mainly ICI) while actually measuring at much lower speeds. The key idea behind the proposed technique is that the ICI level experienced by the received signals after OFDM demodulation and before channel equalizer depends on the relative factor between subcarrier spacing and Doppler spread; thus, instead of changing the Doppler spread, one can change the subcarrier spacing by the same factor to obtain the same results. The main advantage of the proposed technique is its feature to offer experimental evaluation of OFDM-based wireless communication systems at very high velocities while conducting measurements at much lower speeds. The price to be paid is that the signal bandwidth is reduced proportionally to the time interpolation factor, and therefore, potential inaccuracies could arise due to the loss of frequency diversity. However, to combat this loss in diversity, we proposed to transmit different replicas of the interpolated signal to cover the same bandwidth as in the non-interpolated case.

We have designed a measurement methodology for validating our technique in a controlled environment and under repeatable conditions. The basic idea consists in evaluating different figures of merit for a certain range of actual speed values and to compare them with emulated speeds of the same magnitude under the same conditions. For example, when the figures of merit considered are evaluated at 150 km/h, three different cases are evaluated under the same conditions: 1) the receive antenna moves at the actual speed of 150 km/h; 2) the receive antenna moves at the actual speed of 75 km/h and a time interpolation factor $I = 2$ is used, hence the emulated speed is $75 \times 2 = 150$ km/h; and 3) the receive antenna moves at 50 km/h, and $I = 3$ is applied. Besides the measurement results, we have also evaluated the proposed technique through simulations based on a channel model specifically designed for modeling high-speed scenarios. We selected EVM, uncoded BER, and coded BER as figures of merit, all being evaluated for different SNR, CQI, and speed values. All results based on the three figures of merit have shown an excellent agreement between actual and emulated speeds for all the interpolation factors considered, hence validating the proposed technique as a good candidate to be considered not only for physical layer performance evaluations but also for higher layer ones.

Besides validating the proposed technique, we have also shed light on the effects caused by high and even extremely high speeds on OFDM signals. More specifically, we have selected LTE as a waveform example of the state of the art of current mobile wireless systems. As expected beforehand, received signals suffer a similar degradation (in terms of EVM, uncoded BER, and coded BER) when the SNR decreases or when the speed (and correspondingly the ICI level) increases. However, low SNR values can conceal the effects due to high speeds as the noise becomes the main contributor of the signal distortion. We have shown that the level of signal distortion (measured in terms of EVM) caused by high-speed conditions does not depend on the modulation scheme.

We have also shown that the proposed technique performs excellent not only in outdoor-to-indoor measurement scenarios but also in simulations for a channel model specifically designed for outdoor-to-outdoor high-speed scenarios. In both cases, the level of agreement between the results for actual speed and for emulated speeds is at the level of possible measurement accuracy, as the corresponding relative error curves have shown.

Finally, in the light of the excellent agreement of the results obtained under repeatable conditions for the three figures of merit considered (EVM, uncoded BER, and coded BER) and regardless actual or emulated speeds are considered, it can be concluded that the proposed technique is valid for inducing high-speed effects at any point in the signal processing chain at the receiver.

**Competing interests**

The authors declare that they have no competing interests.

**Acknowledgements**

This work has been funded by the Christian Doppler Laboratory for Wireless Technologies for Sustainable Mobility, KATHREIN Werke KG, and A1 Telekom Austria AG. This work was supported in part by the Xunta de Galicia, MINECO of Spain, and FEDER funds of the E.U. under Grant 2012/287, Grant IPT-2011-1034-370000, Grant TEC2013-47141-C4-1-R, Grant FPU12/04139, and Grant EST13/00272. The financial support by the Austrian Federal Ministry of

Economy, Family and Youth and the National Foundation for Research, Technology and Development is gratefully acknowledged.

**Author details**
[1]Department of Electronics and Systems, University of A Coruña, Facultade de Informática, Campus de Elviña, A Coruña 15071, Spain. [2]Institute of Telecommunications, TU Wien, Gusshausstrasse 25/389, A-1040 Vienna, Austria.

Received: 13 December 2014 Accepted: 25 March 2015
Published online: 18 April 2015

**References**

1. Radiocommunication Sector of International Telecommunication Union (ITU-R), Guidelines for evaluation of radio transmission technologies for IMT-2000. ITU-R Recommendation M.1225 (1997)
2. 3GPP TSG-RAN Working Group 4 (Radio), *High speed environment channel models (R4-050388). 3GPP TSG-RAN Working Group 4 (Radio) meeting #35*, (Athens, Greece, 2005)
3. P Kyosti, J Meinila, L Hentila, X Zhao, T Jamsa, C Schneider, M Narandzic, M Milojevic, AHJ Ylitalo, Veli-Matti, Holappa, M Alatossava, R Bultitude, Y de Jong, T Rautiainen, IST-4-027756 WINNER II D1.1.2 V1.1: WINNER II Channel Models (2007)
4. Radiocommunication Sector of International Telecommunication Union (ITU-R), Guidelines for evaluation of radio interface technologies for IMT-Advanced, Report ITU-R M.2135-1 (2009)
5. H Wei, Z Zhong, K Guan, B Ai, in *2010 IEEE 5th International ICST Conference on Communications and Networking in China*. Path loss models in viaduct and plain scenarios of the high-speed railway (IEEE, USA Beijing, China, 2011), pp. 1–5
6. K Guan, Z Zhong, B Ai, in *2011 IEEE Third International Conference on Communications and Mobile Computing (CMC)*. Assessment of LTE-R using high speed railway channel model (IEEE,USA, Quingdao, China, 2011), pp. 461–464. doi:10.1109/CMC.2011.34
7. L Liu, C Tao, T Zhou, Y Zhao, X Yin, H Chen, A highly efficient channel sounding method based on cellular communications for high-speed railway scenarios. EURASIP J. Wireless Commun. Netw. **2012**(1), 1–16 (2012)
8. J Rodríguez-Piñeiro, JA García-Naya, A Carro-Lagoa, L Castedo, in *2013 Euromicro Conference on Digital System Design*. A testbed for evaluating LTE in high-speed trains (IEEE, USA, Santander, Spain, 2013), pp. 175–182. doi:10.1109/DSD.2013.27
9. Rodríguez-Piñeiro, J, P Suárez-Casal, JA García-Naya, L Castedo, C Briso-Rodríguez, JI Alonso-Montes, in *2014 IEEE Eighth IEEE Sensor Array and Multichannel Signal Processing Workshop*. Experimental validation of ICI-aware OFDM receivers under time-varying conditions (IEEE, USA, A Coruña, Spain, 2014). doi:10.1109/SAM.2014.6882411
10. Z Wang, GB Giannakis, Wireless multicarrier communications. IEEE Signal Process. Mag. **17**(3), 29–48 (2000). doi:10.1109/79.841722
11. C Mehlführer, JC Ikuno, M Simko, S Schwarz, M Wrulich, M Rupp, The Vienna LTE simulators - enabling reproducibility in wireless communications research. EURASIP J. Adv. Signal Process. **2011**, 1–13 (2011)
12. M Lerch, S Caban, M Mayer, M Rupp, The Vienna MIMO testbed: evaluation of future mobile communication techniques. Intel Technol. J. **18**(3), 58–69 (2014)
13. S Caban, JA Garcia-Naya, M Rupp, Measuring the physical layer performance of wireless communication systems: part 33 in a series of tutorials on instrumentation and measurement. IEEE Instrum. Meas. Mag. **14**(5), 8–17 (2011). doi:10.1109/MIM.2011.6041377
14. S Caban, A Disslbacher-Fink, JA Garcia-Naya, M Rupp, in *Proc. International Instrumentation and Measurement Technology Conference (I2MTC 2011)*. Synchronization of wireless radio testbed measurements (IEEE, USA Binjiang, Hangzhou, China, 2011). doi:10.1109/IMTC.2011.5944089
15. S Caban, R Nissel, M Lerch, M Rupp, in *Proc. of 6th Extreme Conference on Communication and Computing (ExtremeCom)*. Controlled OFDM measurements at extreme velocities (Association for Computing Machinery (ACM), USA San Cristobal, Galapagos, Ecuador, 2014)
16. S Caban, J Rodas, JA Garcia-Naya, in *2011 IEEE Instrumentation and Measurement Technology Conference*. A methodology for repeatable, off-line, closed-loop wireless communication system measurements at very high velocities of up to 560 km/h (IEEE, USA Binjiang, China, 2011), pp. 1–5. doi:10.1109/IMTC.2011.5944019
17. B Efron, DV Hinkley, *An Introduction to the Bootstrap (CRC Monographs on Statistics & Applied Probability)*, 1st edn. (Chapman & Hall, USA, 1994)

## Scaled-time OFDM experiments for channels exceeding the cyclic prefix

M. Lerch✉, S. Caban, E. Zöchmann, P. Svoboda and M. Rupp

Wireless communications experiments at high user velocities can be performed with much less effort at lower velocities by using time-stretching techniques. In OFDM, state-of-the-art time-stretching techniques do not consider the case of channel impulse responses exceeding the length of the cyclic prefix (CP). This is the case in any real-world OFDM system. In particular, multipath scenarios caused by relay nodes commonly found in public railways have a late, strong channel tap. In this work, the authors propose a time-stretching technique that preserves the effects of the insufficient CP with negligible error and without channel knowledge.

*Introduction:* Wireless communications experiments at very high user velocities are costly and sometimes even not feasible. Scaled-time implementations of the desired experiment allow to still perform such experiments with a lower effort at much lower velocities. This is achieved by time-stretching the transmit signals by a factor $I$, moving $I$-times slower, and time-compressing the received signals by the same factor $I$, see Fig. 1 second panel. The implementation of this technique should be transparent to the transmitter and receiver under test. The transmitted signals shall thereby experience the same effects of the time-varying wireless channel as when moving with the original user velocity.

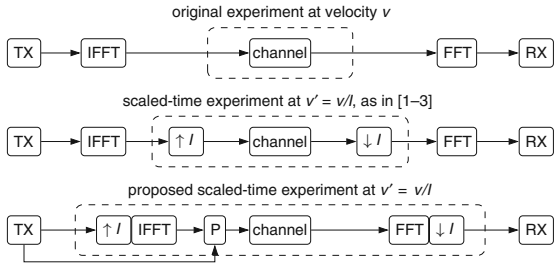


**Fig. 1** *Emulating channel conditions at higher velocities through time-stretching of the transmit signals and time-compression of the received signals. P is the proposed padding signal*

Historically, time-stretching techniques [1–3] only work with negligible error in line-of-sight channels because the channel does not compress in frequency as the transmit signal does. In other words, the transmitted orthogonal frequency division multiplexing (OFDM) signals including the cyclic prefix (CPs) are time-stretched while the relative path delays of the physical channel are not affected. Only are the temporal variations of the physical channel time-scaled by moving $I$-times slower. Hence, Lerch *et al*. [4] correct this error by maintaining the original bandwidth through inserting dummy subcarriers. This emulates the effects of time-varying wireless channels if the channel does not exceed the length of the CP.

In a real-world mobile communications system, however, setting the length of the CP is always a trade-off between increased overhead and a possible throughput loss due to interference. Hence, methods tailored for insufficient CP have been proposed, for example, in [5].

In this Letter, we propose a scaled-time experimental design for real-world channels, including those exceeding the CP [6]. We thereby allow to assess the performance of receiver algorithms (see again [5]) under such conditions.

*System model:* We consider time-stretching OFDM signals as in [4] by fixing the sample rate and using an $I$-times larger FFT-length $N'_{\mathrm{FFT}} = I \cdot N_{\mathrm{FFT}}$. Note that throughout this work, the prime symbol $()'$ denotes the variables for the case of $I > 1$. The $i$th OFDM symbol with its CP can be expressed by

$$x_i[n] = \sum_{l' \in \mathcal{S}'} s'_{i,\,l'} \cdot \mathrm{e}^{\mathrm{j}\frac{2\pi l'(n - iN'_{\mathrm{cp}})}{N'_{\mathrm{FFT}}}} \qquad i\tilde{N}' - N'_{\mathrm{cp}} \le n \le i\tilde{N}' + N'_{\mathrm{FFT}} - 1 \tag{1}$$

where $\tilde{N}' = N'_{\mathrm{FFT}} + N'_{\mathrm{cp}}$ is the total length of one time-stretched OFDM symbol including the CP with a length of $N'_{\mathrm{cp}}$, $s'_{i,\,l'}$ is the data symbol modulated on subcarrier $l'$, and $\mathcal{S}'$ is the set of non-zero subcarriers. As illustrated in Fig. 2*a*, we leave the original subcarriers at the original frequency positions. Therefore $l' = I \cdot l$ are the indices of the original subcarriers $l$. All other $l'$s are dummy subcarriers we insert between the original subcarriers to generate the correct inter-carrier-interference (ICI) due to Doppler. The dummy subcarriers are modulated with random symbols from the symbol alphabet used for the original subcarriers. At the receiver, the $i$th demodulated OFDM symbol

$$Y_i[k'] = \frac{1}{N'_{\mathrm{FFT}}} \sum_{n=0}^{N'_{\mathrm{FFT}}-1} y[n + i\tilde{N}'] \cdot \mathrm{e}^{-\mathrm{j}2\pi\frac{k'n}{N'_{\mathrm{FFT}}}} \tag{2}$$

is obtained through an $N'_{\mathrm{FFT}}$-point FFT of the received signal $y[n]$ before the dummy subcarriers are discarded and the demodulated OFDM symbol $Y_i[k']$ is evaluated at subcarriers $k' = I \cdot k$. The received signal

$$y[n] = \sum_{n=-\infty}^{\infty} x[n-m] \cdot h[m, n, I] \quad \text{with} \quad x[n] = \sum_{i=-\infty}^{\infty} x_i[n] \tag{3}$$

is the convolution of the transmit signal $x[n]$ with the time-stretched channel impulse response $h[m, n, I] = h\big(m \cdot T, (n \cdot T/I)\big)$ where $T = 1/(N_{\mathrm{FFT}}{}^{*}\Delta f)$ is the sampling period and $\Delta f$ is the subcarrier spacing of the original signal.

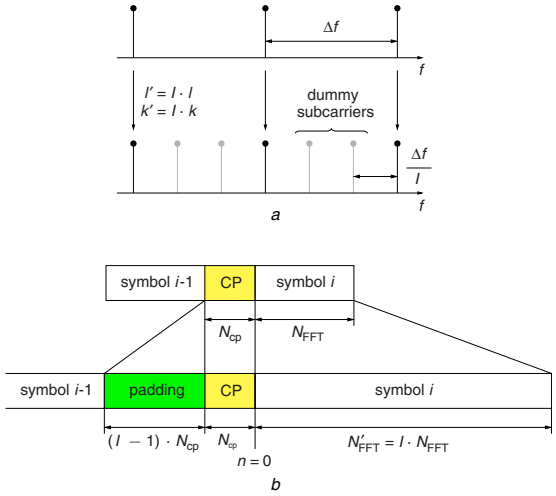


**Fig. 2** *Proposed method*

*a* We perform time-stretching (as in [4]) by increasing the FFT-length and inserting random, dummy subcarriers that generate the correct ICI due to Doppler
*b* We use the same CP length as in the original signal and fill the gap between the CP and the preceding symbol with a padding signal that generates the desired interference due to insufficient CP

*Effects of insufficient cyclic prefix:* Insufficient CP affects OFDM transmissions in two ways. Firstly, insufficient CP causes a loss of orthogonality. This effect is independent of the preceding symbols and causes ICI. Secondly, the preceding symbols cause inter-symbol-interference (ISI) onto the actual OFDM symbol. We consider channels where ISI onto symbol $i$ is caused by the preceding symbol $i-1$ only. Therefore, the possible length of channel impulse responses is upper-bounded by $L_h < 2N_{\mathrm{cp}} + N_{\mathrm{FFT}} + 2$ where $L_h$ is the number of relevant channel taps. Considering LTE with a standard CP, this bound corresponds to a maximum relative path delay of $\sim 77\,\mu\mathrm{s}$ (excess path length of ~23 km) that is unlikely to be observed in real wireless channels. If this condition is fulfilled for the original signal, it is naturally fulfilled for time-stretched signals. The contribution of data symbols $s_{i,\,l'}$ and $s_{i-1,\,l'}$ transmitted on subcarrier $l'$ to the symbol received on subcarrier $k'$ of the $i$th demodulated OFDM symbol can then be expressed by

$$\begin{aligned} Y_i[k', l', I] = {} & s_{i-1,\,l'} G_{\mathrm{ISI}}[k', l', I] + s_{i,\,l'} G_{\mathrm{ICI}}[k', l', I] \\ & + s_{i,\,l'} G[k', l', I], \end{aligned} \tag{4}$$

see [7, 8]. Without loss of generality, we evaluate the OFDM symbol $i$ starting at time index $n = 0$. The first term of (4) describes the ISI caused by the preceding symbol. The corresponding transfer function is given by

$$G_{\mathrm{ISI}}[k', l', I] = \mathrm{e}^{\mathrm{j}2\pi \frac{l' N'_{\mathrm{cp}}}{N'_{\mathrm{FFT}}}} \times \left( \frac{1}{N'_{\mathrm{FFT}}} \sum_{m=N'_{\mathrm{cp}}+1}^{L_h-1} \sum_{n=0}^{m-N'_{\mathrm{cp}}-1} h[m, n, I] \mathrm{e}^{\mathrm{j}2\pi \frac{l'(n-m)}{N'_{\mathrm{FFT}}}} \mathrm{e}^{-\mathrm{j}2\pi \frac{k' n}{N'_{\mathrm{FFT}}}} \right). \quad (5)$$

The second term of (4) describes the ICI due to loss of orthogonality. Its transfer function

$$G_{\mathrm{ICI}}[k', l', I] = -\left( \frac{1}{N'_{\mathrm{FFT}}} \sum_{m=N'_{\mathrm{cp}}+1}^{L_h-1} \sum_{n=0}^{m-N'_{\mathrm{cp}}-1} h[m, n, I] \mathrm{e}^{\mathrm{j}2\pi \frac{l'(n-m)}{N'_{\mathrm{FFT}}}} \mathrm{e}^{-\mathrm{j}2\pi \frac{k' n}{N'_{\mathrm{FFT}}}} \right) \quad (6)$$

differs from $G_{\mathrm{ISI}}[k', l', I]$ in phase only. Thus, independent of the actual channel, the transfer function of the ICI can be expressed by the corresponding ISI one

$$G_{\mathrm{ICI}}[k', l', I] = V[l', I] G_{\mathrm{ISI}}[k', l', I] \quad V[l', I] = -\mathrm{e}^{-\mathrm{j}2\pi \frac{l' N'_{\mathrm{cp}}}{N'_{\mathrm{FFT}}}}. \quad (7)$$

Note that the ICI is caused by symbol $i$ while the ISI is caused by the preceding symbol $i-1$. The last term of (4) does not depend on the length of the CP and corresponds to the demodulated symbols for the case of sufficient CP. For static channels

$$G[k', l', I] = \frac{1}{N'_{\mathrm{FFT}}} \sum_{m=0}^{L_h-1} \sum_{n=0}^{N'_{\mathrm{FFT}}-1} h[m, n, I] \cdot \mathrm{e}^{\mathrm{j}2\pi \frac{l'(n-m)}{N'_{\mathrm{FFT}}}} \cdot \mathrm{e}^{-\mathrm{j}2\pi \frac{k' n}{N'_{\mathrm{FFT}}}} \quad (8)$$

is non-zero for $k' = l'$ only. For time-variant channels, (8) describes the ICI due to Doppler on subcarriers $k' \neq l'$. For the special case of static channels, a fixed CP-length $N'_{\mathrm{cp}} = N_{\mathrm{cp}}$, and using the method where dummy subcarriers are inserted ($l' = I \cdot l$, $k' = I \cdot k$), ISI and ICI due to insufficient CP scale with $1/I$ while the signal is independent of $I$

$$\begin{aligned} G_{\mathrm{ISI}}[k', l', I] &= \frac{1}{I} G_{\mathrm{ISI}}[k, l, 1] \\ G_{\mathrm{ICI}}[k', l', I] &= \frac{1}{I} G_{\mathrm{ICI}}[k, l, 1] \\ G[k', k', I] &= G[k, k, 1]. \end{aligned} \quad (9)$$

Considering uncorrelated data symbols, the total interference power on subcarrier $k'$ is the sum of the ISI caused by all subcarriers $l'$ of the preceding symbol and the ICI caused by all subcarriers $l' \neq k'$ of the actual symbol $i$

$$\sigma^2_{\mathrm{int}}[k', I] = \sum_{l' \in \mathcal{S}'} |s_{i-1, l'} G_{\mathrm{ISI}}[k', l', I]|^2 + \sum_{l' \in \mathcal{S}' l' \neq k'} |s_{i, l'} G[k', l', I] + s_{i, l'} G_{\mathrm{ICI}}[k', l', I]|^2. \quad (10)$$

The received signal power at subcarrier position $k'$ of the $i$th symbol is the sum of all contributions caused by the data symbol $s_{i, l'}$ transmitted on subcarrier $l' = k'$

$$\sigma^2_{\mathrm{signal}}[k', I] = |s_{i, k'} G[k', k', I] + s_{i, k'} G_{\mathrm{ICI}}[k', k', I]|^2. \quad (11)$$

*Correct emulation:* To correctly emulate the interference due to insufficient CP, we propose the method illustrated in the third panel of Fig. 1. Firstly, we perform time-stretching by increasing the FFT-length and insert dummy subcarriers, see Fig. 2*a* for a frequency domain view, that generate the correct ICI due to Doppler. Secondly, we prepend a CP with the same length $N'_{\mathrm{cp}} = N_{\mathrm{cp}}$ as in the original signal and fill the gap between the CP and the preceding symbol with the padding signal

$$p_i[n] = \sum_{l' \in \mathcal{S}'} p_{i, l'} \cdot \mathrm{e}^{\mathrm{j} \frac{2\pi l'(n+N_{\mathrm{cp}})}{N'_{\mathrm{FFT}}}} \quad n = -IN_{\mathrm{cp}} \cdots - N_{\mathrm{cp}} - 1. \quad (12)$$

that generates the correct interference due to insufficient CP, see Fig. 2*b*. This padding signal consists of the last $(I-1) \cdot N_{\mathrm{cp}}$ samples of an OFDM symbol modulated with data symbols $p_{i, l'}$. For the case of $L_h < IN_{\mathrm{cp}} + 2$, there is no ISI caused by the preceding symbol. There is only ISI originating from the padding signal $p_i[n]$. The $i$th demodulated OFDM symbol can then be expressed by

$$Y_i[k', l', I] = p_{i, l'} G_{\mathrm{ISI}}[k', l', I] + s_{i, l'} G_{\mathrm{ICI}}[k', l', I] + s_{i, l'} G[k', l', I] \quad (13)$$

or, using (7) to express $G_{\mathrm{ICI}}$ through $G_{\mathrm{ISI}}$

$$Y_i[k', l', I] = p_{i, l'} G_{\mathrm{ISI}}[k', l', I] + s_{i, l'} V[l', I] \cdot G_{\mathrm{ISI}}[k', l', I] + s_{i, l'} G[k', l', I]. \quad (14)$$

We design the data symbols $p_{i, l'}$ of the padding signal such that the demodulated OFDM symbol $Y_i[k', l', I]$ is independent of $I$ for the case of static channels. The data symbols

$$p_{i, l'} = \begin{cases} -s_{i, l'} V[l', I] + I \cdot s_{i, l'} V[l', I] + I \cdot s_{i-1, l'} & l' = I \cdot l \\ -s_{i, l'} V[l', I] & \text{otherwise} \end{cases} \quad (15)$$

are independent of the actual channel and depend on the known data symbols $s_{i, l'}$ and $s_{i-1, l'}$ only. The first term of (15) completely eliminates the ICI. This is necessary as the ICI is smaller than for the original signal. Furthermore, the ICI caused by the dummy subcarriers does not exist for the original signal. The correct ICI is generated by the second term. Thereby, the padding signal generates scaled ISI to emulate the correct ICI, but only on the subcarriers $l' = I \cdot l$ that also exist in the original signal. The last term generates the correct ISI using the data symbols $s_{i-1, l'}$ from the preceding symbol. Note, that the factors $I$ in (15) linearly scale every $I$th subcarrier of the padding signal. Therefore, the peak-to-average power ratio (PAPR) of the transmit signal increases approximately linearly with increasing $I$. Note that the increased peak-powers occur in the padding signal while the actual OFDM symbol and the CP are not affected. For subcarriers $l' = I \cdot l$ that also exist in the original signal, the demodulated OFDM symbol calculates to

$$Y_i[k', I \cdot l, I] = s_{i-1, l'} I G_{\mathrm{ISI}}[k', l', I] + s_{i, l'} I G_{\mathrm{ICI}}[k', l', I] + s_{i, l'} G[k', l', I] \quad (16)$$

while the dummy subcarriers $l' \neq I \cdot l$ do not cause any interference due to insufficient CP,

$$Y_i[k', l', I] = s_{i, l'} G[k', l', I]. \quad (17)$$

Using (9) and evaluating the received signal at subcarrier positions $k' = I \cdot k$, the demodulated OFDM symbol is independent of $I$

$$Y_i[I \cdot k, I \cdot l, I] = Y_i[k, l, 1] = s_{i, l} G_{\mathrm{ICI}}[k, l, 1] + s_{i-1, l} G_{\mathrm{ISI}}[k, l, 1] + s_{i, l} G[k, l, 1]. \quad (18)$$

Note, that (18) is only exactly valid for static channels and for $L_h < IN_{\mathrm{cp}} + 2$.

*Numerical results:* We evaluate the proposed method with LTE-based OFDM signals with 72 subcarriersand the VehicularB channel model [9] where the impulse response exceeds the CP of LTE. The time-variations of the channel are based on the Jakes' model [10] at a centre frequency of 2.5 GHz. We evaluate the signal power $\sigma^2_{\mathrm{signal}}$ and the interference power $\sigma^2_{\mathrm{int}}$ at the centre subcarrier $k' = 0$.

Firstly, we evaluate the SIR for the *static* case, where the SIR should be independent of the time-stretching factor $I$ because the scenario is

static. Results for this case are shown in Fig. 3. While the signal power is independent of the stretching factor $I$ for any method, the interference decreases with increasing $I$ for the state-of-the-art methods shown. Therefore, the SIR increases for these two methods with increasing $I$. For the stretched CP case ($N'_{cp} = IN_{cp}$), the interference vanishes for CP lengths $N'_{cp}$ exceeding the length of the impulse response. For a fixed CP length $N'_{cp} = N_{cp}$, the SIR increases monotonically with increasing $I$. To evaluate the error of our method, we define

$$\begin{aligned}\epsilon_{\text{int}}[I] &= \sigma^2_{\text{int}}[0, I]\ (\text{dB}) - \sigma^2_{\text{int}}[0, 1]\ (\text{dB}) \\ \epsilon_{\text{signal}}[I] &= \sigma^2_{\text{signal}}[0, I]\ (\text{dB}) - \sigma^2_{\text{signal}}[0, 1]\ (\text{dB})\end{aligned} \tag{19}$$

as the logarithmic differences between the powers of the time-stretched signal and the powers of the original signal, see Fig. 4. For time-stretching factors $I$ that do not fulfil the condition $IN_{cp} + 2 > L_h$ we observe negligible errors of <0.2 dB due to ISI caused by the preceding symbol. For higher values of $I$, the error is zero.

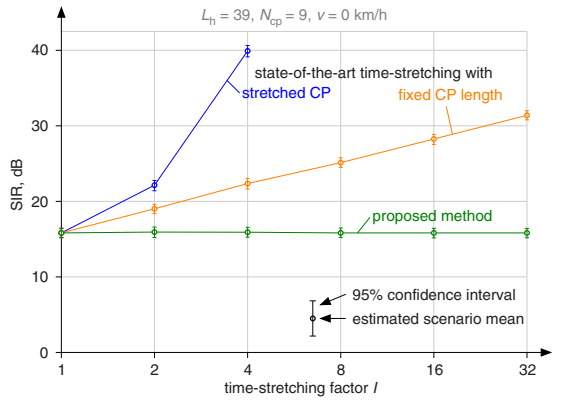


**Fig. 3** *Signal-to-interference power ratio (SIR) when time-stretching OFDM signals in a static scenario. In a static scenario, the SIR should be independent of the time-stretching factor I. Compared to state-of-the-art methods, the error of the method proposed is negligible*

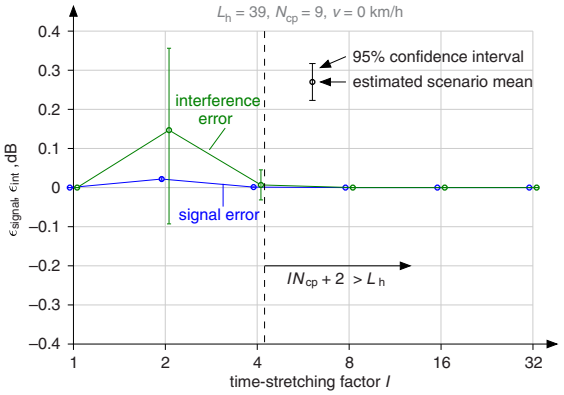


**Fig. 4** *Error of the method proposed in a static scenario. For time-stretching factors I that do not fulfil the condition $IN_{cp} + 2 > L_h$ we observe negligible errors of <0.2 dB. Otherwise, the errors are equal to zero*

Secondly, we evaluate the error for time-variant channels, see Fig. 5. For time-stretching factors that fulfil the condition $IN_{cp} + 2 > L_h$ small errors are observed. These small errors are caused by the fixed CP length $N'_{cp}$ and the fixed channel length $L_h$ in the limits of the sums in (5) and (6). While the time-variations of the channel are stretched in time, the limits are fixed.

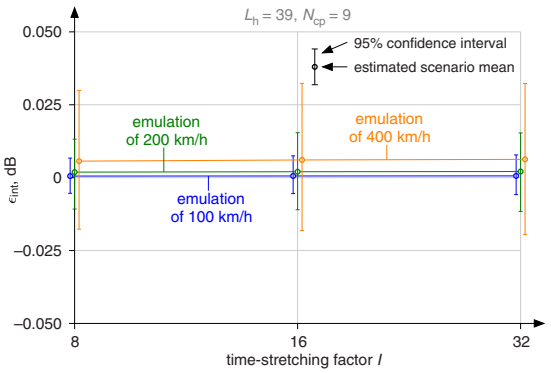


**Fig. 5** *Error of the method proposed for time-variant channels. For time-stretching factors that fulfil the condition $IN_{cp} + 2 > L_h$ the errors observed are smaller than 0.025 dB*

*Conclusion:* The time-stretching method proposed preserves the effects of insufficient CP without channel knowledge with negligible error.

*Acknowledgments:* This work was funded by the Christian Doppler Laboratory for Dependable Wireless Connectivity for the Society in Motion, the ITC, TU Wien and has been supported by the Austrian FFG, Bridge Project No. 871261. The financial support of the Austrian BMWFW and the National Foundation for Research, Technology, and Development is gratefully acknowledged.


Submitted: *30 August 2019* E-first: *22 October 2019*
doi: 10.1049/el.2019.2857
One or more of the Figures in this Letter are available in colour online.

M. Lerch, P. Svoboda and M. Rupp (*Institute of Telecommunications, TU Wien, Vienna, Austria*)

✉ E-mail: mlerch@nt.tuwien.ac.at

S. Caban and E. Zöchmann (*Christian Doppler Laboratory for Dependable Wireless Connectivity for the Society in Motion, Vienna, Austria*)

## References

1 Rodríguez-Piñeiro, J., Lerch, M., García-Naya, J.A., *et al.*: 'Emulating extreme velocities of mobile LTE receivers in the downlink', *EURASIP J. Wirel. Commun. Netw.*, 2015, **2015**, (106), pp. 1–14
2 Fei, D., Rodríguez-Piñeiro, J., García-Naya, J.A., *et al.*: 'TD-LTE downlink performance assessment in high speed scenarios'. IEEE 83rd Vehicular Technology Conf., Nanjing, China, May 2016, pp. 1–5
3 Rodríguez-Piñeiro, J., Suárez-Casal, P., García-Naya, J.A., *et al.*: 'Experimental validation of ICI-aware OFDM receivers under time-varying conditions'. IEEE 8th Sensor Array and Multichannel Signal Processing Workshop, A Coruna, Spain, June 2014, pp. 341–344
4 Lerch, M., Rodríguez-Piñeiro, J., García-Naya, J.A., *et al.*: 'Methods to perform high velocity LTE experiments at low velocities'. IEEE 83rd Vehicular Technology Conf., Nanjing, China, May 2016, pp. 1–5
5 Pham, T., Le-Ngoc, T., Woodward, G.K., *et al.*: 'Channel estimation and data detection for insufficient cyclic prefix MIMO-OFDM', *IEEE Trans. Veh. Technol.*, 2017, **66**, (6), pp. 4756–4768
6 Lerch, M., Svoboda, P., Platzgummer, V., *et al.*: 'Analysis of LTE in two-path vehicular repeater channels'. IEEE 90th Vehicular Technology Conf., Honolulu, HI, USA, September 2019, pp. 1–5
7 Chen, S., and Zhu, C.: 'ICI and ISI analysis and mitigation for OFDM systems with insufficient cyclic prefix in time-varying channels', *IEEE Trans. Consum. Electron.*, 2004, **50**, (1), pp. 78–83
8 Molisch, A.F., Toeltsch, M., Vermani, S., *et al.*: 'Iterative methods for cancellation of intercarrier interference in OFDM systems', *IEEE Trans. Veh. Technol.*, 2007, **56**, (4), pp. 2158–2167
9 Universal Mobile Telecommunications System: 'Selection procedures for the choice of radio transmission technologies of the UMTS'. Tech. Rep. TR 101.112, European Telecommunications Standards Institute, 1997
10 Zemen, T., and Mecklenbräuker, C.: 'Time-variant channel estimation using discrete prolate spheroidal sequences', *IEEE Trans. Signal Process.*, 2005, **53**, (9), pp. 3597–3607

IEEE Access
Multidisciplinary | Rapid Review | Open Access Journal

SPECIAL SECTION ON EMERGING TECHNOLOGIES ON VEHICLE TO EVERYTHING (V2X)

Received November 15, 2018, accepted December 22, 2018, date of publication January 15, 2019, date of current version February 8, 2019.

*Digital Object Identifier 10.1109/ACCESS.2019.2893136*

# Position-Specific Statistics of 60 GHz Vehicular Channels During Overtaking

**ERICH ZÖCHMANN[1,2,3], (Member, IEEE), MARKUS HOFER[4], (Student Member, IEEE), MARTIN LERCH[2], (Student Member, IEEE), STEFAN PRATSCHNER[1,2], (Student Member, IEEE), LAURA BERNADÓ[4], (Member, IEEE), JIRI BLUMENSTEIN[3], (Member, IEEE), SEBASTIAN CABAN[2], SEUN SANGODOYIN[5], (Student Member, IEEE), HERBERT GROLL[2], (Student Member, IEEE), THOMAS ZEMEN[4], (Senior Member, IEEE), ALEŠ PROKEŠ[3], MARKUS RUPP[2], (Fellow, IEEE), ANDREAS F. MOLISCH[5], (Fellow, IEEE), AND CHRISTOPH F. MECKLENBRÄUKER[2], (Senior Member, IEEE)**

[1]Christian Doppler Laboratory for Dependable Wireless Connectivity for the Society in Motion, Institute of Telecommunications, TU Wien, 1040 Vienna, Austria
[2]Institute of Telecommunications, TU Wien, 1040 Vienna, Austria
[3]Department of Radio Electronics, TU Brno, 616 00 Brno, Czech Republic
[4]Center for Digital Safety & Security, AIT Austrian Institute of Technology, 1210 Vienna, Austria
[5]Ming Hsieh Department of Electrical Engineering, University of Southern California, Los Angeles, CA 90007, USA

Corresponding author: Erich Zöchmann (ezoechma@nt.tuwien.ac.at)

This work was supported in part by the Austrian Federal Ministry for Digital and Economic Affairs, in part by the National Foundation for Research, Technology and Development, in part by the Czech Science Foundation under Project 17-27068S and Project 17-18675S, and in part by the National Sustainability Program under Grant LO1401. The work of S. Sangodoyin and A. F. Molisch was supported in part by NSF under Grant CNS-1457340, and in part by NIST under Grant 70NANB17H157. The authors acknowledge the TU Wien University Library for financial support through its Open Access Funding Program. For this research, the infrastructure of the SIX Center was used. This work was carried out in the framework of COST Action CA15104 IRACON.

**ABSTRACT** The time-variant vehicle-to-vehicle radio propagation channel in the frequency band from 59.75 to 60.25 GHz has been measured in an urban street in the city center of Vienna, Austria. We have measured a set of 30 vehicle-to-vehicle channel realizations to capture the effect of an overtaking vehicle. Our experiment was designed for characterizing the large-scale fading and the small-scale fading depending on the overtaking vehicle's position. We demonstrate that large overtaking vehicles boost the mean receive power by up to 10 dB. The analysis of the small-scale fading reveals that the two-wave with diffuse power (TWDP) fading model is adequate. By means of the model selection, we demonstrate the regions where the TWDP model is more favorable than the customarily used the Rician fading model. Furthermore, we analyze the time selectivity of our vehicular channel. To precisely define the Doppler and delay resolutions, a multitaper spectral estimator with discrete prolate spheroidal windows is used. The delay and Doppler profiles are inferred from the estimated local scattering function. Spatial filtering by the transmitting horn antenna decreases the delay and Doppler spread values. We observe that the RMS Doppler spread is below one-tenth of the maximum Doppler shift 2f v/c. For example, at 60 GHz, a relative speed of 30 km/h yields a maximum Doppler shift of approximately 3300 Hz. The maximum RMS Doppler spread of all observed vehicles is 450 Hz; the largest observed RMS delay spread is 4 ns.

**INDEX TERMS** 5G mobile communication, automotive engineering, communication channels, fading channels, intelligent vehicles, millimeter wave propagation, millimeter wave measurement, multipath channels, RMS delay spread, RMS Doppler spread, parameter extraction, time-varying channels, two-wave with diffuse power fading, wireless communication.

## I. INTRODUCTION

The idea of automated cars represents a tremendous attraction to both, industry and the research community. More than ten years ago, a first forward collision warning system based on a millimeter wave (mmWave) automotive radar was commercialized [3]. Nowadays, reliable mmWave communication systems, supporting vehicle-to-vehicle information exchange, are anticipated to be among the key enablers for automated vehicles [4]. Due to the large available bandwidth at mmWave bands, even raw sensor data exchange between vehicles is possible [4]. Millimeter wave vehicular communications has two main distinctive features as

compared to sub-6-GHz vehicular communications. Firstly, the use of directive antennas – at least at one link end – and secondly, the much higher maximum Doppler shift. This high maximum Doppler shift, being directly proportional to the carrier frequency, is also viewed as a possible stumbling stone for vehicular mmWave communications. It is, however, shown theoretically in [5] and [6] that directional antennas, anticipated for mmWaves, act as spatial filters. The Doppler spread, and hence the time-selectivity, may be drastically decreased by beamforming. Experimentally, this has first been demonstrated in our prior work [2].

### A. LITERATURE REVIEW

The analysis of static mmWave channels is already well advanced, see for example [7]–[29]. For static environments, frequency-domain channel sounding methods based on vector network analyzers are frequently used [30]. However, channel sounding concepts with sufficient sampling rates of the time-varying channel have been so far only treated by a few research papers [1], [2], [31]–[34].

Interestingly, mmWave frequency bands have been candidates for vehicular communications already for several decades [35], [36]. Millimeter wave train-to-infrastructure path loss is measured in [35], mmWave vehicle-to-vehicle communication performance is studied in [36]. Both works use narrowband transmissions. In [37] and [38], the focus is on inter-vehicle path loss results. Recent advances on mmWave circuit technology [39] renewed the interest in vehicular mmWave communications [40] and for joint vehicular communication and radar [41]. In [42], vehicle-to-vehicle (V2V) channel measurements at 38 GHz and 60 GHz, using a channel sounder with 1 GHz bandwidth, have been conducted. The antennas in [42] were put into the bumpers, thereby the dominating multipath components (MPCs) are the line-of-sight (LOS) component, a road reflection, and a delayed component reflected at the guard rails. In [43], 73 GHz V2V large-scale fading and small-scale fading analysis is provided for approaching vehicles. Intra-vehicular Doppler spectra of vibrations appearing while the vehicle is in operation are shown in [44] and [45]. In [46], signal-to-noise ratio (SNR) fluctuations for 60 GHz transmissions with 5 MHz bandwidth in a vehicle-to-infrastructure scenario are investigated. Time-varying receive power and time-varying small-scale fading for vehicular channels at 5.6 GHz are addressed in [47].

### B. CONTRIBUTIONS OF THIS PAPER

With this article, we contribute to the dynamic mmWave vehicle-to-vehicle channel research by analyzing the effect of an overtaking vehicle on the mmWave V2V wideband (510 MHz) channel. Our experiment in a real-world street environment is designed to make the experiment as controllable as possible. The wireless link is always LOS and unblocked. We demonstrate that the size and the relative position of the overtaking vehicle greatly influences the large-scale and small-scale fading parameters. Furthermore, Doppler dispersion is strongly suppressed by the transmit horn antenna. The data we analyze consist of channel impulse responses (CIRs) during the overtaking situations with 30 vehicles. For the statistical analysis we differentiate between cars, sport utility vehicles (SUVs), and trucks.

### C. ORGANIZATION OF THIS PAPER

In Section II, we present our measurement scenario in detail. In Section III, we analyze the receive power fluctuations as a function of the relative position of the overtaking vehicle. Regardless of the position of the overtaking vehicle and its size, approximately 50% of the receive power belongs to the channel tap corresponding to the LOS delay. Accordingly, in the following Section IV, we analyze the small-scale fading of the LOS tap. The two-wave with diffuse power (TWDP) model is briefly introduced and we show that it explains our data very well. In Section V, we focus on delay and Doppler dispersion. The analysis of the root mean square (RMS) Doppler spread is based on the local scattering function (LSF). The obtained RMS Doppler spread values are then compared against RMS Doppler spread values of commonly used models. We conclude with simple channel modeling guidelines.

### D. NOTATION

We mention here only notation that is not commonly in use. Estimated quantities are marked with $\hat{(\cdot)}$. Functions with discrete input variables are denoted by square brackets $f[\cdot]$; functions with continuous inputs are denoted by parentheses $f(\cdot)$. The floor function is indicated via $\lfloor\cdot\rfloor$ and the ceiling function is indicated via $\lceil\cdot\rceil$. "Corresponds to" is symbolized with $\triangleq$.

## II. SCENARIO DESCRIPTION

We have measured a set of 60 GHz vehicle-to-vehicle channel realizations to capture the effect of an overtaking vehicle. The motivation for our setup is the scenario of two cars driving, one behind the other, keeping constant distance, and communicating via a 60 GHz mmWave link. A third vehicle then overtakes this car platoon and thus influences the wireless channel, depending on the overtaking car's relative position.[1] The vehicular channel data evaluated for this contribution consists of 30 different measurement runs. We are observing the effect of overtaking vehicles with excess speeds of up to 13 m/s. At the transmitter (TX) site, a horn antenna with an 18° half power beam width is used and aligned towards the receiver (RX) car. Surrounding buildings are filtered out by the directive horn antenna. At the RX site, a custom-built omni-directional ($\lambda/4$) monopole antenna is used. The RX has an omni-directional pattern so that scattered[2] waves from the passing vehicle are not filtered out. This situation occurs,

[1] Similar results will be obtained, if the car platoon overtakes a vehicle.

[2] By scattering we refer to any kind of wave interaction such as diffuse reflection or diffraction.

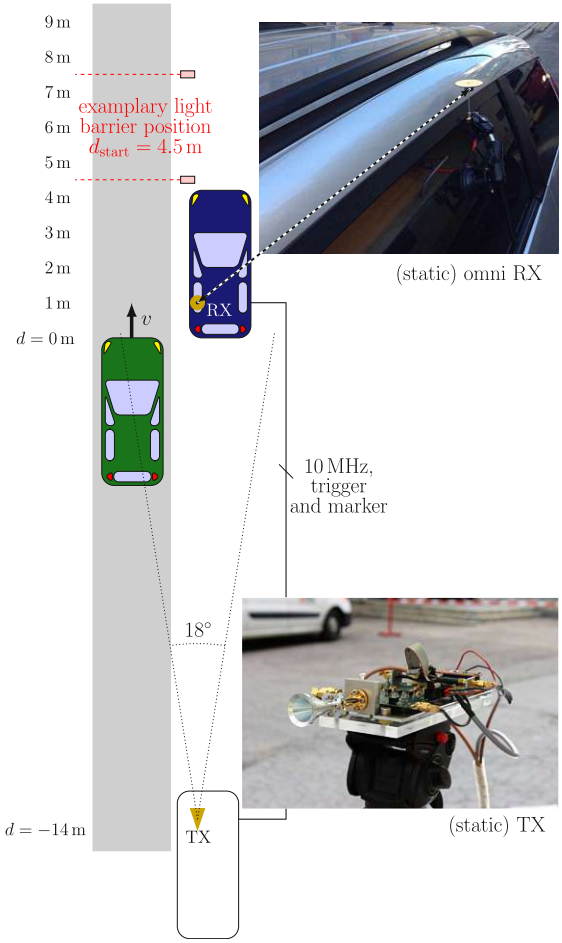


**FIGURE 1.** Bird's-eye view of the measurement site. TX and RX are static. The overtaking car is moving relative to the static vehicles with excess speed $v$. This models a moving car platoon being overtaken by a single vehicle. The overtaking vehicle is sketched at a bumper to bumper distance of $d = 0$ m.

for example, in directional neighbor discovery [48], where only one link end applies beamforming. Our RX equipment is put into a static (parked) car. The RX antenna is fixed to the left rear car window. Our TX is approximately 15 m behind the RX car. Single reflections at the TX car do not occur because of the directivity of the horn antenna, while double reflections involving the TX car are below the receiver sensitivity. Hence, the TX car is omitted and replaced by a simple tripod mounting. The TX and RX placement is shown in Figs. 1 and 2.

To simplify the measurements, we do not move TX and RX, but rather keep them static, and have the overtaking car emulated by regular street traffic passing by. As indicated above, this approach is valid because interaction by houses and other static objects are negligible due to the directivity of the TX horn antenna. Due to the spatial filtering, Doppler is mainly determined by the relative velocity of the overtaking vehicle. Our case corresponds to a "moving frame of reference". Keeping TX and RX static makes a very accurate time and frequency synchronization possible. The frequency synchronization is achieved via a 10 MHz reference signal distribution to all clocks. The time synchronization is achieved with a marker signal that triggers the receiver when the sounding signal is transmitted. A measurement is triggered once the overtaking vehicle is driving through a first light barrier, positioned at $d_{\text{start}}$. The distance $d_{\text{start}}$ is measured from the rear bumper of the parked receiver car. The mean velocity of the overtaking vehicle is estimated through a second light barrier, positioned 3 m after the first one. We measured the time $\Delta t$ it took for the vehicle to arrive at the second light barrier. By means of the mean velocity estimate $\hat{v}$ and the starting point $d_{\text{start}}$, we estimate the position of the overtaking vehicle at all time points $m$ to

$$\hat{d}[m] = \hat{v} \cdot m\, T_{\text{snap}} + d_{\text{start}} = \frac{3\,\text{m}}{\Delta t}\, m\, T_{\text{snap}} + d_{\text{start}}\,, \quad (1)$$

where $T_{\text{snap}}$ is the snapshot rate, provided in Appendix B. We hence take the front bumper of the overtaking vehicle and the rear bumper of the parked receiver car as reference planes. The distance $d$ is thus referred to as the "bumper to bumper distance". The range of interest is marked via meter marks on the left-hand side in Fig 1. Memory space is limiting the recording time of our 510 MHz broadband signal to 720 ms. Due to this limitation, the recorded measurements do not necessarily cover all distances of interest. To cover the distances shown in Fig. 1, the light barriers, triggering the measurements, are placed at three different positions. In other words, $d_{\text{start}}$ is varied. An exemplary light barrier position to cover the larger distances is illustrated in Fig 1.

## III. RECEIVE POWER FLUCTUATION (LARGE-SCALE FADING) DURING OVERTAKING

We have built a dedicated channel sounder for this experiment (for details see Appendix B) that provides estimates of the time-variant transfer function $H[m, q]$. The time index is denoted by $m \in \{0, \ldots, S-1\}$ and the frequency index is denoted by $q \in \{0, \ldots, K-1\}$, where $K = 103$. The time-variant CIR $h[m, n]$ with delay index $n$ is obtained via an inverse discrete Fourier transform[3]. The CIR $h$ exhibits a sparse structure. Therefore, the median of all samples of $h$ is used as estimator of the noise floor [49]. All values of the CIR below a threshold that is 6 dB above this noise floor are set to zero.

Similar as in [47], we estimate the large-scale fading by applying a moving average filter of length $L_{\text{f}}$. Likewise, we assume that the fading process is stationary as long as the movement of the scattering object (the overtaking vehicle) is within $L_{\text{c}} \triangleq 50\,\lambda = 50 \cdot 5\,\text{mm} = 0.25\,\text{m}$. The filter length $L_{\text{f}}$ depends on the velocity of the overtaking vehicles and is always chosen to cover $L_{\text{c}}$ and to extend it to the earlier and later time point by $\Delta L = 10$ samples [47]. It hence

[3]We do not apply window functions so that the temporal resolution will not be degraded. This will be important for the data evaluation in Section IV.

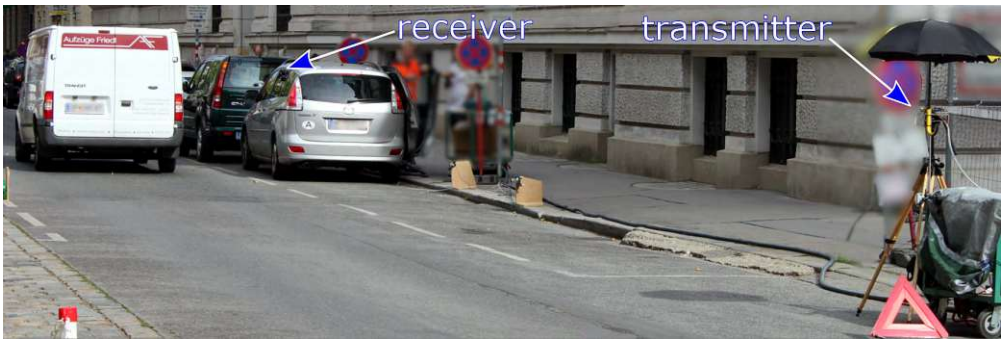


**FIGURE 2.** Measurement site. TX and RX are static. Urban street traffic is passing by. At this snapshot, the overtaking vehicle is at a bumper to bumper distance of approximately $d = 6$ m.

calculates to

$$L_\mathrm{f} = L_\mathrm{c} + 2\,\Delta L = \left\lfloor \frac{50\lambda}{v \cdot T_\mathrm{snap}} \right\rfloor + 2 \cdot 10\,. \tag{2}$$

The estimate of the time-varying second moment $\hat{\Omega}[m]$ is then calculated as

$$\hat{\Omega}[m] = \frac{1}{I_\mathrm{U}[m] - I_\mathrm{L}[m] + 1} \sum_{m'=I_\mathrm{L}[m]}^{I_\mathrm{U}[m]} \sum_{n=0}^{K-1} \left| h[n, m'] \right|^2 , \tag{3}$$

where the lower and the upper sum index are

$$I_\mathrm{L}[m] = \max(0, \lceil m - (L_f/2) \rceil)\,, \tag{4}$$

$$I_\mathrm{U}[m] = \min(\lceil m + (L_f/2) \rceil, S - 1)\,. \tag{5}$$

Our scenario is dominated by the LOS component. As we keep TX and RX static, this component will always appear at the same delay tap, called $n_\mathrm{LOS}$. To analyze the strength of the LOS delay tap relative to all taps, we estimate the second moment of the LOS tap as well.

$$\hat{\Omega}^\mathrm{LOS}[m] = \frac{1}{I_\mathrm{U}[m] - I_\mathrm{L}[m] + 1} \sum_{m'=I_\mathrm{L}[m]}^{I_\mathrm{U}[m]} \left| h[n_\mathrm{LOS}, m'] \right|^2 . \tag{6}$$

The delay index $n_\mathrm{LOS}$ is calculated based on the measured TX–RX distance. Both estimates $\hat{\Omega}[m]$ and $\hat{\Omega}^\mathrm{LOS}[m]$ are parameterized by the time index $m$. All time-dependent quantities are equally well parameterized by the relative position estimate (1). With an abuse of notation we denote, for example,

$$\hat{\Omega}[d] = \hat{\Omega}\left[\hat{d}^{-1}[d]\right]. \tag{7}$$

### A. STATISTICAL EVALUATION AND DISCUSSION

In this sub-section, we perform the statistical evaluation of the large-scale fading and then discuss the results. The experiment was conducted for 30 different vehicles, from which we derive ensemble statistics.

The first quantity of interest is the position-specific relative LOS tap gain, that is $\hat{\Omega}^\mathrm{LOS}[\hat{d}]/\hat{\Omega}[\hat{d}]$. This quantity is evaluated as boxplot in the top panel of Fig. 3. Our evaluation is based on a window size of $L_\mathrm{c} = 50\,\lambda = 0.25$ m length. For sake of illustration, we plot the graphs on a meter based grid by rounding $\hat{d}$ to the nearest integer meter value. In all the boxplots of our contribution, the bottom and top edges of the box indicate the 25$^\mathrm{th}$ and 75$^\mathrm{th}$ percentiles. The whiskers show the 5$^\mathrm{th}$ and 95$^\mathrm{th}$ percentiles. All observations outside the whiskers are marked with crosses. The bottom panel of Fig. 3 shows the number of samples we obtain for each meter bin. Please note that the maximum number of samples (per bin) is 120, since we observed 30 vehicles and obtain 4 samples per meter.

We observe that the LOS tap captures most of the channel gain and never drops below $-4$ dB. Cars (in red) and SUVs (in green) show a similar trend. For both vehicle types, the relative gain of the LOS tap increases when the overtaking car is at larger distances $d$. The additional MPC due to the overtaking vehicle fades out and the limiting value is reached after $d > 5$ m. Trucks show a different trend. If a truck is close to the RX, the relative gain of the LOS tap is increased, but for larger distances it approaches a lower limiting value. This is intuitively explained by strong MPCs generated at the side wall of trucks. Whenever a truck is "close enough", these MPCs are not resolved in the time domain and are binned in the LOS tap.

To further study the above mentioned side-wall wave interaction effect, we analyze the gain increase of the LOS tap versus the distance. The gain increase relative to no vehicle presence (indicated as $d \to \infty$) is plotted in the middle panel of Fig. 3. Cars and SUVs show no effect. In contrast, overtaking trucks potentially boost the LOS gain by more than 10 dB. The median result shows an increase of approximately 2 dB.

## IV. SMALL-SCALE FADING OF THE LOS TAP DURING OVERTAKING

As we discussed in the section above, the LOS tap is the dominating contribution of the channel gain. Here, we are interested in the small-scale fading behavior of this LOS tap. To suppress large-scale fading effects, the channel is normalized by the square root of the estimated second moment,

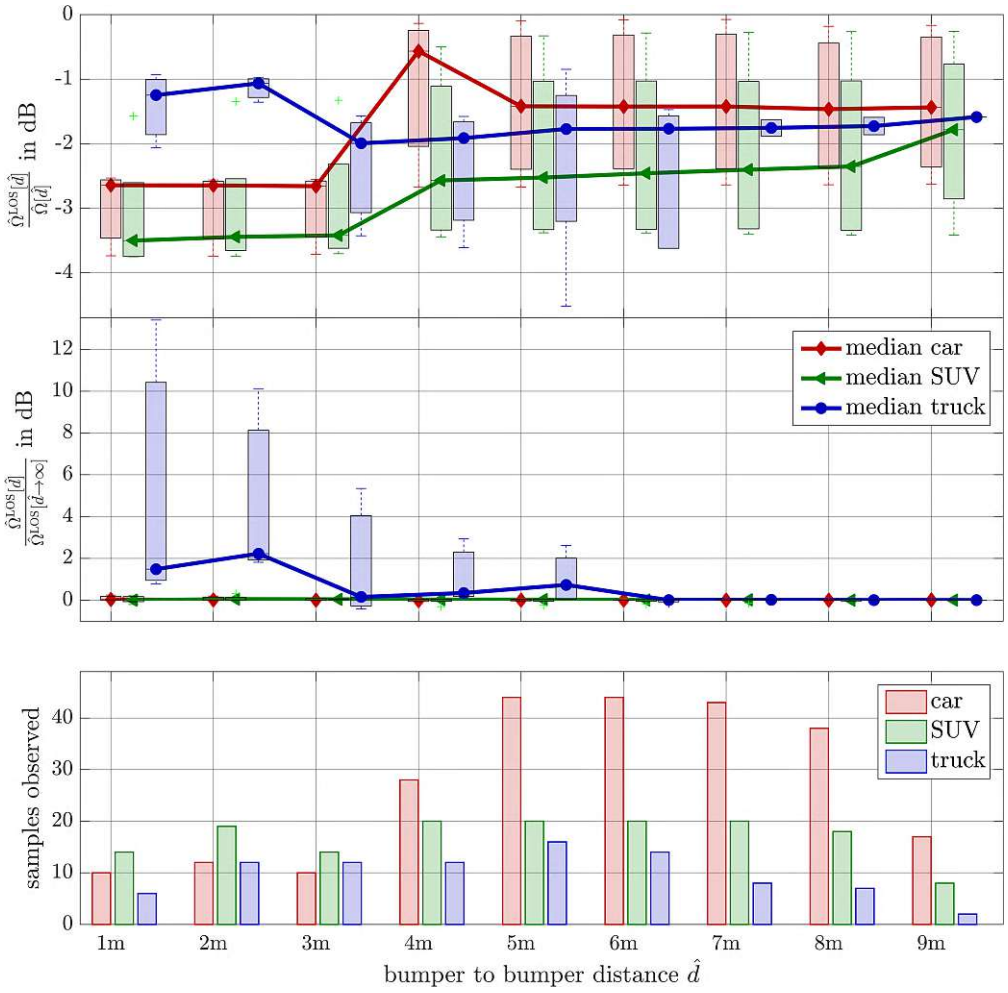


**FIGURE 3.** (top) Box plot of the LOS tap gain relative to the gain of all taps. When cars and SUVs are close to the RX antenna ($d = 1$ m), additional MPCs are created, thus decreasing the relative LOS gain. For trucks the converse is true because strong interactions with the side wall (scattering, diffraction) add power to the LOS tap. (middle) Box plot of the LOS tap gain increase by an overtaking vehicle compared to "no vehicle present". When cars and SUVs pass by, the LOS tap is hardly affected. The side walls of trucks strongly reflect impinging waves. (bottom) Number of samples used for the evaluation above.

that is

$$\tilde{h}[m, n_{\mathrm{LOS}}] = \frac{h[m, n_{\mathrm{LOS}}]}{\sqrt{\hat{\Omega}^{\mathrm{LOS}}[m]}}. \tag{8}$$

As a demonstrative example, we provide the channel impulse responses and estimates of the second moment for an overtaking truck, see Fig. 4 for a photograph of the truck and Fig. 5 for the LOS channel estimates. Before we study the small-scale fading statistics, we note that there is an oscillation with evolving instantaneous frequency visible in Fig. 5. The oscillations of the red curve with time-varying beating frequency can be explained by the Doppler shift changing with $d$, see Fig. 6 for the spectrogram[4] of $|\tilde{h}[m, n_{\mathrm{LOS}}]| - 1$.

[4]The spectrogram uses a Kaiser window of length 256 and shape parameter $\alpha = 5$. The Kaiser window approximates the discrete prolate spheroidal (DPS) sequence window [50, p. 232 ff.], that will be later extensively used for the Doppler analysis in Section V.

### A. GEOMETRIC ARGUMENTATION FOR TWDP SMALL-SCALE FADING

The TWDP small-scale fading model assumes fading due to the interference of two strong radio signals and numerous smaller, so called diffuse, signals. In our case, the two strong radio signals are the unblocked LOS and a scattered component from an overtaking vehicle that arrives at the same delay tap. Our measurement bandwidth of BW $= 510$ MHz allows to resolve MPCs that are separated by a delay of $\Delta\tau \approx 1/\mathrm{BW} \approx 2$ ns or a travel distance of $\Delta s \approx c_0/\mathrm{BW} \approx 60$ cm. Every MPC separated less than these values is not resolved and interpreted as fading. We define the Fresnel ellipsoids for the MPCs arriving at the same time tap (bin) as the component corresponding to LOS

$$|\tau_{\mathrm{LOS}} - \tau_{\mathrm{refl}}| \leq \frac{1}{\mathrm{BW}}. \tag{9}$$


**FIGURE 4.** Webcam snapshot of the exemplary overtaking truck ($d \approx 5$ m).

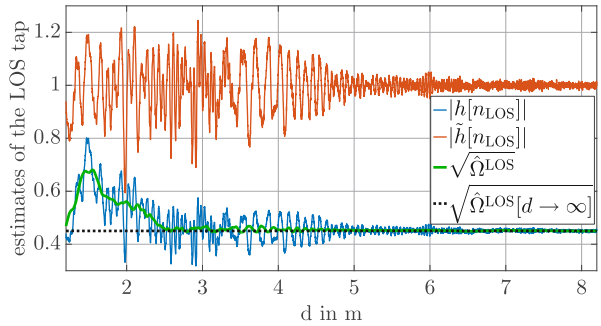


**FIGURE 5.** Result of the post-processing of the LOS tap for the exemplary truck shown in Fig. 4. The lower, blue curve shows the LOS channel tap $h[n_{\mathrm{LOS}}]$ including large-scale fading. The green, smooth curve shows the estimated large-scale fading $\sqrt{\hat{\Omega}^{\mathrm{LOS}}}$. The black dashed line is the estimate of the channel gain without a vehicle present. The red curve shows the normalized LOS channel tap $\tilde{h}[n_{\mathrm{LOS}}]$, that is, the small-scale fading only. The oscillatory behavior stops at approximately 5 m.

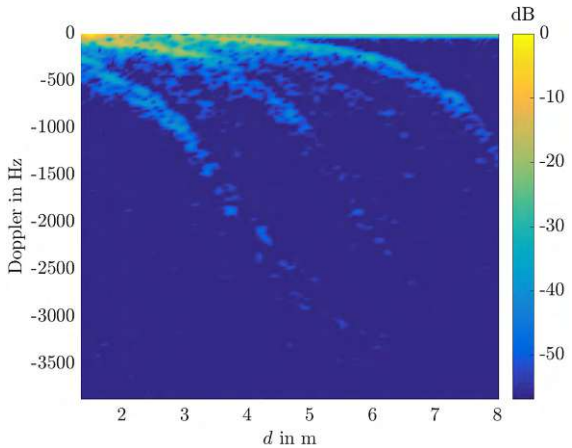


**FIGURE 6.** Spectrogram of the normalized LOS channel tap ($|\tilde{h}[n_{\mathrm{LOS}}]| - 1$) from Fig. 5. The oscillatory behavior is best explained by the two strong, yellow traces in the spectrogram.

In Fig. 7, this ellipse is shown in red. The green car in Fig. 7 shows the maximum distance values ($d \approx 4.5$ m) for which an overtaking car is producing TWDP fading. Figure 7 also

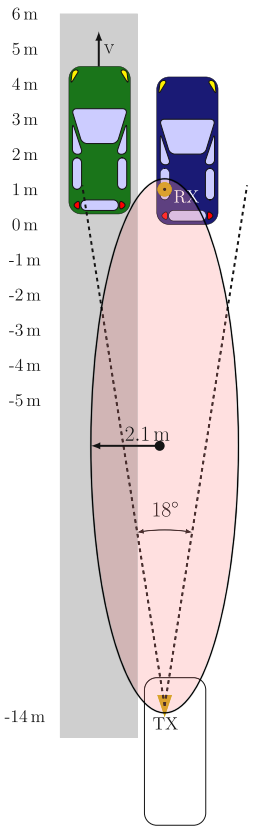


**FIGURE 7.** Scaled sketch (1:5000). The LOS tap fades if another object is within the red filled ellipse (semi-minor axis equals 2.1 m). The green car in this figure is sketched such that it just produces TWDP fading. If the car goes further on, its scattered component will be at the next channel tap.

shows the half power beam width of the TX horn. This illustrates that the distance region 0 . . . 4 m leads to a signal created by wave interaction with the overtaking vehicle that is not much weaker than the LOS component. Hence, we expect two MPCs at the same order of magnitude. In the region before, for example, −5 . . . 0 m the ellipsoid condition to experience TWDP fading is fulfilled but spatial filtering by the horn antenna suppresses the scattered component. By inspecting Fig. 5 again, one observes that the oscillatory behavior fades out after 5 m, as the overtaking truck is a rather short one. In the following subsection we briefly introduce the mathematics of the TWDP model. In Section IV-C, we focus on maximum likelihood estimation (MLE) of the model parameters and perform model selection to draw eventually statistical conclusions.

### B. MATHEMATICAL DESCRIPTION OF TWDP FADING

TWDP fading was first introduced in [51]. A more extensive mathematical description was provided in [52]. For the convenience of the reader, we briefly summarize [52]. The TWDP fading model in the complex-valued baseband is given as

$$r_{\mathrm{complex}} = V_1 e^{j\phi_1} + V_2 e^{j\phi_2} + X + jY \,, \tag{10}$$

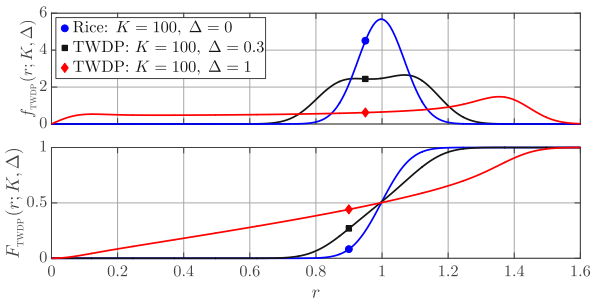


**FIGURE 8. Comparison of Rician, and TWDP fading. The TWDP distribution with $\Delta = 1$ deviates strongly from the Rice distribution. Smaller $\Delta$ values do not affect the shape of the distribution as severely.**

where $V_1 > 0$ and $V_2 \geq 0$ are the deterministic amplitudes of the non-fluctuating components. The phases $\phi_1$ and $\phi_2$ are independent and uniformly distributed in $(0, 2\pi)$. The diffuse components are modeled via the law of large numbers as $X + jY$, where $X, Y \sim \mathcal{N}(0, \sigma^2)$ are independent Gaussian random variables. The $K$-factor is defined analogously to the Rician K-factor as the power ratio of the non-fluctuating components and the diffuse components

$$K = \frac{V_1^2 + V_2^2}{2\sigma^2} . \tag{11}$$

The parameter $\Delta$ describes the amplitude relationship among the non-fluctuating components

$$\Delta = \frac{2V_1V_2}{V_1^2 + V_2^2} . \tag{12}$$

The $\Delta$-parameter is bounded between 0 and 1 and equals 1 iff both amplitudes are equal. Iff $\Delta = 0$, TWDP fading degenerates to Rician fading. This transition from TWDP fading to Rician fading is smooth. If the second non-fluctuating component becomes very small, it can be absorbed equally well in the diffuse components. This is discussed in detail in Appendix C.

The cumulative distribution function (CDF) of the envelope of (10) is

$$F_{\mathrm{TWDP}}(r; K, \Delta) = 1 - \frac{1}{2\pi} \int_0^{2\pi} Q_1\left(\sqrt{2K\,[1 + \Delta\cos(\alpha)]},\ \frac{r}{\sigma}\right) \mathrm{d}\alpha , \tag{13}$$

where $Q_1(\cdot, \cdot)$ is the Marcum Q-function. Figure 8 shows an example of the probability density function (PDF) $f_{\mathrm{TWDP}}(r; K, \Delta)$ and CDF $F_{\mathrm{TWDP}}(r; K, \Delta)$ of the TWDP fading distribution.

### C. MAXIMUM LIKELIHOOD ESTIMATION OF K AND Δ AND MODEL SELECTION

Based on the filtered envelope measurement data of the LOS delay $r[m] = \left|\tilde{h}[m, n_{\mathrm{LOS}}]\right|$, we are seeking the TWDP fading distribution of which the observed realizations appear most likely. To do so, we estimate the parameter tuple $(\hat{K}[m], \hat{\Delta}[m])$ via MLE

$$(\hat{K}[m], \hat{\Delta}[m]) = \arg\max_{K,\Delta} \sum_{m'=m-(L_c/2)}^{m+(L_c/2)-1} \ln f_{\mathrm{TWDP}}(r[m']; K, \Delta) \tag{14}$$

For the MLE, we take all samples within the assumed stationary length of $L_c \triangleq 50\lambda$. The maximization is implemented as exhaustive search on a $(K, \Delta)$ grid specified in Appendix C. We also perform MLE for the Rician $K$-factor. To do so, we restrict the maximization (14) to the parameter tuple $(K, \Delta \equiv 0)$. Taking the data of the exemplary truck (Figs. 4 to 6), the estimated CDFs and their evolution is shown in Fig. 9. The three smallest distances (in Fig. 9) show CDFs where the truck is in proximity of the receive antenna. There we observe fading that is not well explained by a Rician fit. The proposed TWDP fading model shows a superior fit. Only the last example at a distance of 6 m clearly fades according to a Rice distribution. Of course, TWDP fits must always be better than Rician fits as the Rician model is a special case of TWDP. However, the TWDP model introduces an additional parameter, which is not desirable.

Thus, to select between Rician fading and TWDP fading, we employ Akaike's information criterion (AIC). The AIC is a rigorous way to estimate the Kullback-Leibler divergence, the relative entropy based on MLE [53]. Given the MLE fitted parameter tuple $(\hat{K}[m], \hat{\Delta}[m])$ of TWDP fading and Rician fading, we calculate the sample size $N$ corrected AIC [53, p. 66] for Rician fading ($\Delta \equiv 0$) and TWDP fading

$$\mathrm{AIC}[m] = -2 \sum_{m'=m-(L_c/2)}^{m+(L_c/2)-1} \ln f_{\mathrm{TWDP}}(r[m']; \hat{K}, \hat{\Delta}) + 2U + \frac{2U(U+1)}{N - U - 1}, \tag{15}$$

where the model orders $U$ for Rician and TWDP fading are 1 and 2, respectively. We choose between Rician fading and TWDP fading based on the lower AIC value. Due to the model order penalization in the AIC we avoid over-fitting. For our exemplary truck, the fitted parameters as well as the selected model are shown in Fig. 10.

### D. STATISTICAL EVALUATION AND DISCUSSION

In this sub-section, we show the ensemble statistics of small-scale fading. Depending on the selected model, we take either the TWDP $K$-factor or the Rician $K$-factor. For Rician fits we set $\Delta \equiv 0$. Notice, however, that we rely then on the success of the model selection algorithm. Especially for very small $\Delta$-parameters, very likely, we decide for Rician fading and hence bias the found $\Delta$-parameters towards smaller values. This is discussed in Appendix C.

Figure 11 illustrates the fitted $K$-factors and $\Delta$-parameters. The $K$-factor is smaller if the vehicle is closer to the RX antenna (closer to the rear bumper of the car). If the vehicle passes the static RX car, the $K$-factor saturates. Basically the LOS tap does not fade any longer. As mentioned above,

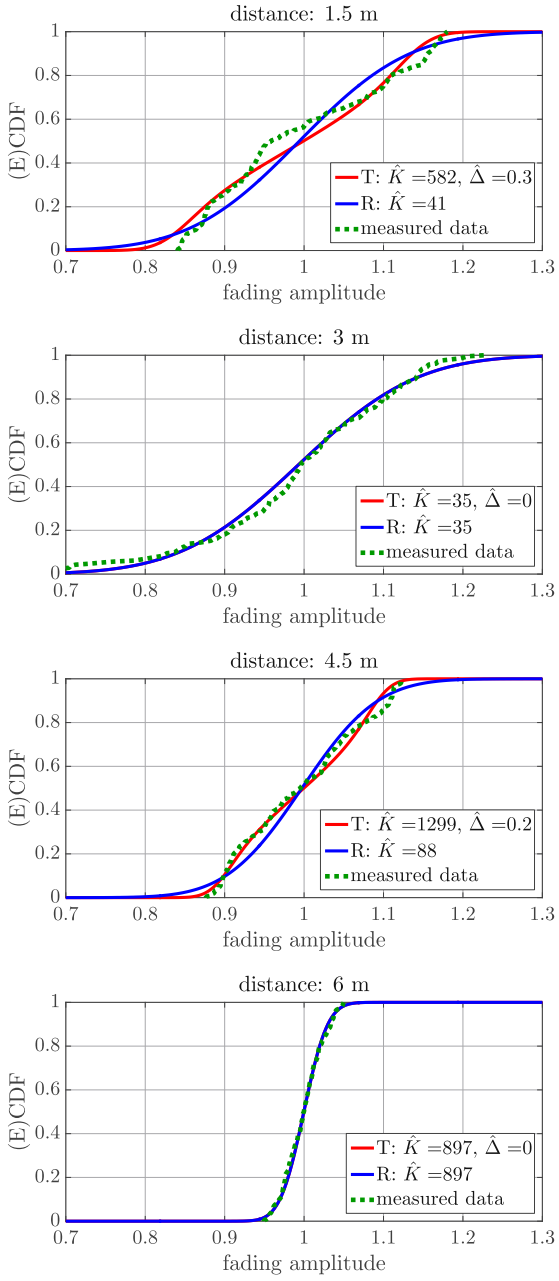


**FIGURE 9.** CDF evolution over distance. The data is again from our example, see Figs. 4 to 7. For distances smaller than 5 m, TWDP fading leads to a superior fit. At first glance, the Rician model seems to achieve a good fit as well, however, the $K$-factors of both models are not in the same order of magnitude. Rician fading underestimates the power in the non-fluctuating components.

the vehicle size is translated to the distance $d$. For longer vehicles such as trucks, it takes longer until the $K$-factor starts rising. SUVs lie in between cars and trucks.

Next, we focus on the $\Delta$-parameter. We see that the length of the vehicle also affects this parameter. We observe TWDP fading, that is, $\Delta > 0$, whenever a part of the vehicle is still

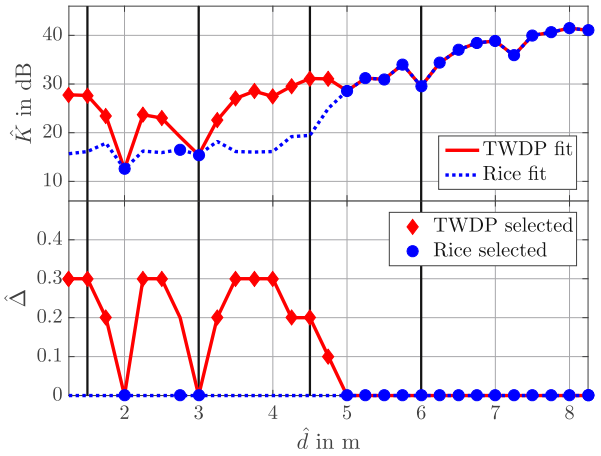


**FIGURE 10.** MLE fitted parameter tuple $(\hat{K}, \hat{\Delta})$ for the exemplary truck channel from Fig. 5. The Rician $K$-factor (blue dashed line) underestimates the power within the non-fluctuating components. If AIC selects TWDP fading, a red diamond marks the parameter tuple. If Rician fading is selected, a blue circle is used. The black vertical lines illustrate the positions evaluated in Fig. 9.

close to the RX antenna. The longer the vehicle, the longer this effect is visible. Remember that the median $\Delta$ value has a slight negative bias, as we set $\Delta$ to zero if we decide for Rician fading. This explains why the SUV median is zero at 2 m, although the $\Delta$ values are spread out; since in case of SUVs, the AIC decides for Rician fading more than half of the time. The AIC model selection decisions are color-coded in the histogram in the bottom panel of Fig. 11. The histogram in lighter shades is identical to the histogram of Figure 3. The darker shades show the number of samples where the AIC decided for TWDP fading. Again, looking at the maximum distances where TWDP fading occurs, we see a correlation with the vehicle length.

## V. DELAY-DOPPLER DISPERSION EVALUATED VIA THE LOCAL SCATTERING FUNCTION

To study the delay-Doppler dispersion of our vehicular channel, we characterize the channel by the LSF, as explained in [47], [54], and [55]. Similar to the previous sections, we assume that the fading process is locally stationary within a region of $M$ samples in time and all samples in frequency domain. We hence estimate the LSF for consecutive stationarity regions in time. We use a multitaper based estimator in order to obtain multiple independent spectral estimates from the same measurement and being able to average them. The estimate of the LSF is defined as [54]

$$\hat{C}[k_t; n, p] = \frac{1}{IJ} \sum_{w=0}^{IJ-1} \left| \mathcal{H}^{(G_w)}[k_t; n, p] \right|^2 . \tag{16}$$

By $p \in \{-K/2, \ldots, K/2\}$ we denote the Doppler index, and as in the previous sections, we denote by $n \in \{0, \ldots, M-1\}$ the delay index. The delay and Doppler shift resolutions are given by $\tau_s = 1/(K\Delta f)$ and $\nu_s = 1/(MT_{\text{snap}})$. The time index

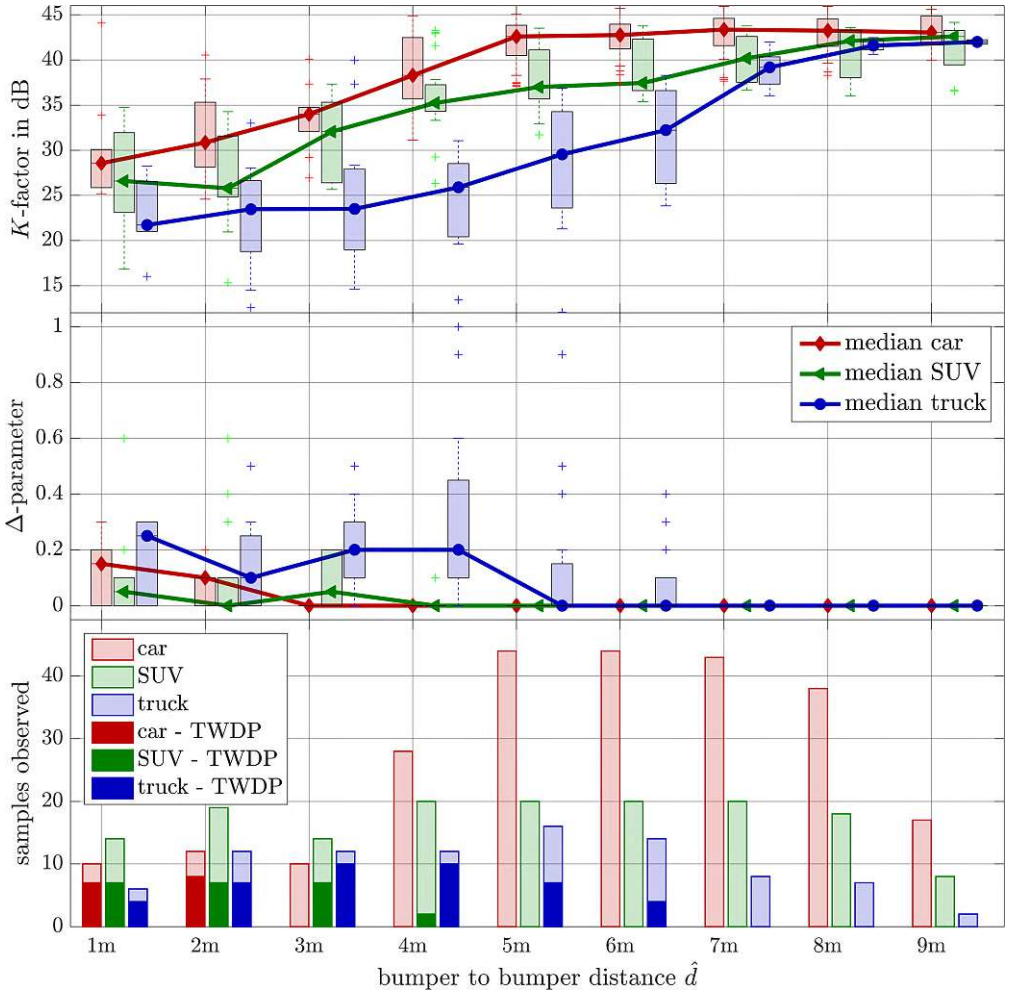


**FIGURE 11.** (top) Boxplot of the Rician fading and TWDP fading $K$-factor. The closer the vehicle to the RX and the larger the vehicle, the stronger are the diffuse components. (middle) Boxplots of the $\Delta$-parameter. The larger the vehicle, the stronger is the second non-fluctuating component. For example, $\Delta = 0.2$ (for trucks) correponds to a second non-fluctuating component that is 20 dB smaller than the LOS component, see Fig. 15 in Appendix C. (bottom) Histogram of all samples observed and the TWDP samples. This shows the TWDP selection ratio.

of each stationarity region is $k_t \in \{0, \ldots, \lfloor (S/M - 1 \rfloor)\}$ and corresponds to the center of the stationarity regions. The windowed spreading function $\mathcal{H}^{(G_w)}$ is calculated by

$$\mathcal{H}^{(G_w)}[k_t; n, p] = \sum_{\substack{m= \\ -M/2}}^{M/2-1} \sum_{\substack{q= \\ -K/2}}^{K/2} H[m + Mk_t, q]\, G_w[m, q]\, \mathrm{e}^{-\mathrm{j}2\pi(pm-nq)}, \tag{17}$$

where the tapers $G_w[m, q]$ are the DPS sequences [56], explained in detail in [54]. The number of tapers in time domain is $I = 3$ and in frequency domain $J = 3$ .

We set $M = 233$ which corresponds to a stationarity region of 30 ms in time. The power delay profile (PDP) and the Doppler spectral density (DSD) are calculated as a summation (marginalization) of the LSF over the Doppler domain or delay domain [54],

$$\mathrm{PDP}[k_t; n] = \sum_{p=-M/2}^{M/2-1} \hat{C}[k_t; n, p]\,, \tag{18}$$

$$\mathrm{DSD}[k_t; p] = \sum_{n=0}^{K-1} \hat{C}[k_t; n, p]\,. \tag{19}$$

Based on the PDP and DSD, we analyze the time-varying RMS delay spread and the RMS Doppler spread. To obtain these quantities, we use the formulas (10) – (13) from [54].

Our measurements were carried out in a street with 30 km/h speed limit. The average vehicle speed is in this order, but some vehicles significantly deviate from the

average speed. To compare vehicles at different speed, the Doppler profile of each vehicle is first normalized w.r.t. to its maximum Doppler shift

$$\nu_{\max} = \frac{2\hat{v}}{\lambda}\,. \tag{20}$$

Next the Doppler profile is re-scaled to a common speed of $v = 30\,\text{km/h} \approx 8.33\,\text{m/s}$. The data post-processing for our exemplary truck is shown in Fig. 12. Figure 12(a) shows the PDP as it evolves over distance. A bandwidth of 510 MHz is not sufficient to distinguish the MPCs in the time-domain. A small channel gain increase in the delay range $10 - 30\,\text{ns}$ is visible after approximately 5 m. Figure 12(c) shows the corresponding DSD. The additional MPCs from the overtaking truck are clearly visible as negative Doppler shift traces. Note that these traces are already partially demonstrated in Fig. 6. Figure 12(b) shows the respective RMS spread values.

### A. STATISTICAL EVALUATION AND DISCUSSION

The results for the whole data ensemble are illustrated in Fig. 13. The bottom panel shows again the number of samples used for the evaluation at each individual position. Note, that the histogram is slightly different to the previous ones. Previously we performed the evaluation on $50\lambda$ in space, which equals 30 ms evaluation time exactly only for a vehicle at a speed of $v \approx 8.25\,\text{m/s} = 29.7\,\text{km/h}$.

The RMS delay spread, illustrated in the top panel of Fig. 13, is only slightly affected by an overtaking vehicle. There is only a total swing of 1.5 ns for the median values of the truck. If a truck is close to the RX antenna (at approx. 1 m to 2 m) it shadows the background, boosts the already dominating LOS delay and $\sigma_\tau$ is smallest. Cars and SUVs barely alter $\sigma_\tau$. For both vehicle types the median swing is less than 1 ns. Generally, the RMS delay spread values of different vehicles are all in the same order.

The RMS Doppler spread of cars and SUVs at distances close to the antenna ($< 3\,\text{m}$) is mainly due to phase noise of our equipment. Cars show the strongest effect on $\sigma_\nu$ at approximately 3 m to 4 m. SUVs show their maximum a bit later at around 4 m to 5 m. At larger distances the MPC belonging to the overtaking car (SUV) fades out. Note the similarity of $\sigma_\nu$ for cars and SUVs after 6 m. In this region only the rear part of the vehicles is illuminated. Trucks produce an RMS Doppler spread twice as strong as cars and as SUVs. Again, due to trucks' larger extent the maximum RMS Doppler spread occurs later, at approximately 7 m.

Keep in mind, however, that due to the spatial filtering of the horn antenna combined with the existence of a strong LOS, the RMS Doppler spread is less than 12% of the maximum Doppler shift ($\sigma_\nu \leq 0.12\,\nu_{\max}$). In the median case, $\sigma_\nu$ is even below one-tenth of the maximum Doppler shift $\nu_{\max}$. For comparison, a Doppler shift uniformly distributed in $(-\nu_{\max}, 0)$ yields $\sigma_\nu = \nu_{\max}/\sqrt{12} \approx 0.3\,\nu_{\max}$, a Doppler shift distributed according to a half-Jakes' spectrum yields $\sigma_\nu = \nu_{\max}\sqrt{(\pi^2 - 2^2)/(2\pi)^2} \approx 0.4\,\nu_{\max}$, and a Doppler shift according to a Jakes' spectrum even $\sigma_\nu = \nu_{\max}/\sqrt{2} \approx 0.7\,\nu_{\max}$. Modeling $\sigma_\nu$ with these models is therefore not appropriate. The calculations of the RMS

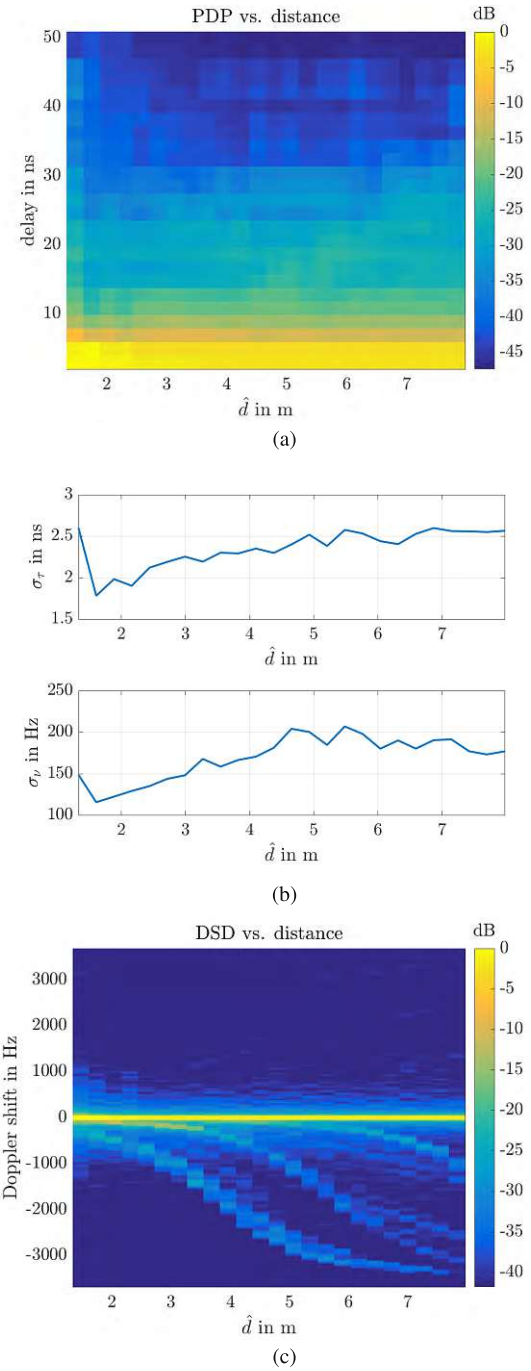


**FIGURE 12.** Post-processing steps to obtain the RMS delay spread and RMS Doppler spread from the LSF.(a) Time aligned PDP of the exemplary truck. The time resolution obtained with 510 MHz bandwidth is not sufficient to resolve strong MPCs. (b)Estimated RMS delay spread (top) and estimated RMS Doppler spread (bottom) are calculated on a 30 ms time grid. (c)DSD of the exemplary truck. MPC reflected at the truck are clearly visible via their Doppler shift.

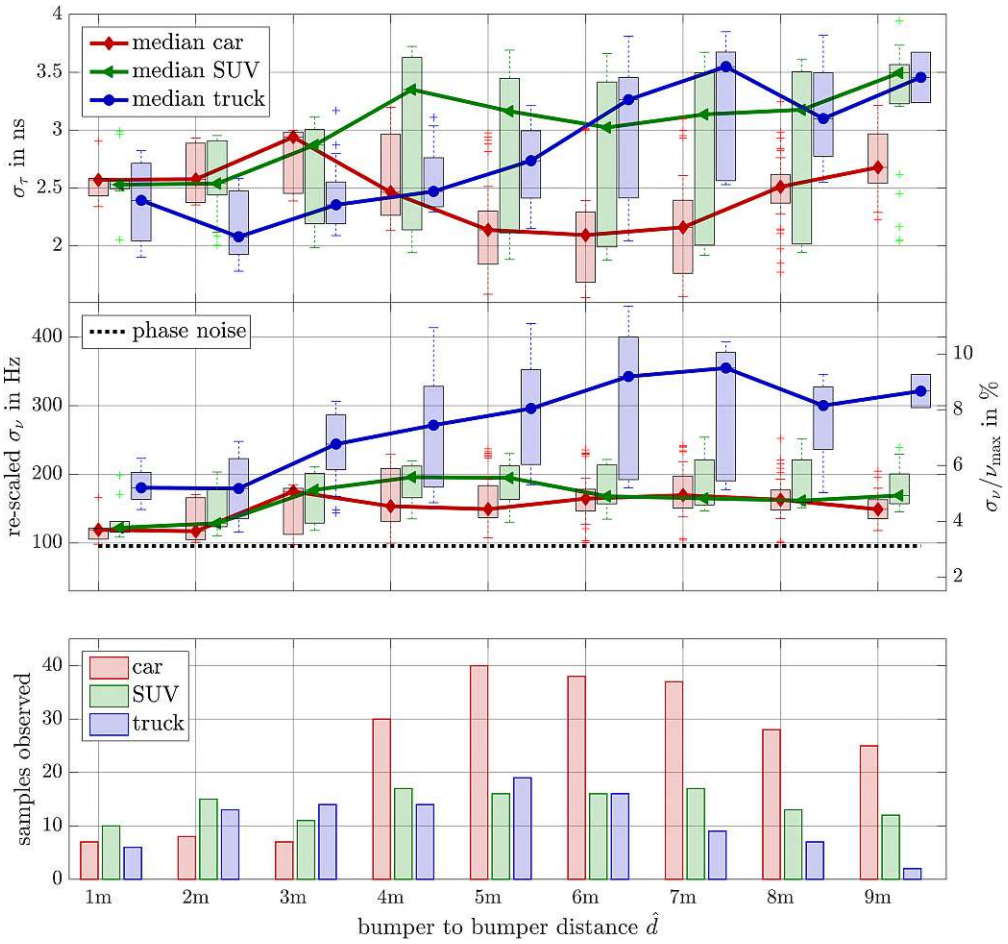


**FIGURE 13.** (top) Box plots of RMS delay spread as a function of bumper to bumper distance. The position of the overtaking vehicle does not have a strong impact on the RMS delay spread. (middle) Box plots of RMS Doppler spread re-scaled to a common vehicle speed of 30 km/h at the left axis. RMS Doppler spread normalized to the maximum Doppler shift is labelled at the right axis. The black dotted line shows the estimate for the RMS Doppler spread obtained through the phase noise of our measurement system. The RMS Doppler spread of cars and SUVs is only twice as much the values obtained with the phase noise only. In system without "perfect" frequency synchronization or worse reference clocks, the increase might not be visible. (bottom) Number of samples used for the evaluation above based on 30 ms sample lengths.

Doppler spread values for known distributions is provided in Appendix D.

## VI. CONCLUSION

The size of the overtaking vehicle plays a crucial role for the statistics of the vehicular channel during an overtaking maneuver. Our statistical evaluation of an overtaking process has shown that large-scale fading is essentially only influenced by very large objects such as trucks and buses. Large vehicles potentially increase the receive power through scattering on their side wall by several dB. For smaller vehicles, a change of large-scale fading was not observed.

Rician fading is a good model for small-scale fading, unless a vehicle is in the "bandwidth ellipse" in which case the TWDP distribution provides a better fit. The larger the vehicle, the larger is the $\Delta$-parameter. With the same $K$-factor, TWDP fading experiences deeper fades than predicted with a Rice distribution.

Furthermore, we have seen that the RMS delay spread is hardly affected by overtaking vehicles. This parameter does not need to be modeled position specific.

The analysis of Doppler dispersion has shown that the increased Doppler effect at millimeter waves is not directly translated to the RMS Doppler spread in our scenario. The RMS Doppler spread is extremely low due to spatial filtering of the horn antenna and the very strong LOS component. Only for large vehicles, this value increases significantly during overtaking. Note that the observed maximum value is a lot smaller than standard models (uniform, Jakes) would predict. The maximum observed RMS Doppler spread is approximately four times larger than the phase noise of our

measurement system. A commercial system without "perfect" frequency synchronization or worse reference clocks will very likely not experience this relatively small increase of the RMS Doppler spread at all.

## APPENDIX A: ACRONYMS

| | |
|---|---|
| **AIC** | Akaike's information criterion |
| **AWG** | arbitrary waveform generator |
| **CDF** | cumulative distribution function |
| **CIR** | channel impulse response |
| **DFT** | discrete Fourier transform |
| **DPS** | discrete prolate spheroidal |
| **DSD** | Doppler spectral density |
| **LO** | local oscillator |
| **LOS** | line-of-sight |
| **LSF** | local scattering function |
| **MLE** | maximum likelihood estimation |
| **mmWave** | millimeter wave |
| **MPC** | multipath component |
| **OEW** | open-ended waveguide |
| **PDP** | power delay profile |
| **PDF** | probability density function |
| **PLL** | phase-locked loop |
| **RF** | radio frequency |
| **RMS** | root mean square |
| **RX** | receiver |
| **SA** | signal analyzer |
| **SNR** | signal-to-noise ratio |
| **SUV** | sport utility vehicle |
| **TWDP** | two-wave with diffuse power |
| **TX** | transmitter |
| **V2V** | vehicle-to-vehicle |

## APPENDIX B: MEASUREMENT SETUP

The hardware setup is illustrated in Fig. 14. Our transmitter consists of an arbitrary waveform generator (AWG). Once triggered, it continuously repeats a baseband sounding sequence. This baseband sequence described in the following subsection is up-converted by an external mixer module. The external mixer module employs a synthesizer phase-locked loop (PLL) for generating the internal local oscillator (LO). The synthesizer PLL is fed by a 285.714 MHz reference, and uses a counter (divider) value of 210 to generate the center frequency of $f_0 = 59.99994$ GHz. Our receiver is a Rohde and Schwarz signal analyzer (SA) R&S FSW67. Its sensitivity is $P_{\mathrm{SA,min}} = -150$ dBm/Hz at 60 GHz. All radio frequency (RF) devices are synchronized with a 10 MHz reference.

When a vehicle passes the first light barrier, the AWG is triggered and plays back the baseband sequence and a sample synchronous marker signal. The marker triggers the recording of the receive samples. We directly access the IQ samples at a rate of 600 MSamples/s. From the receive IQ samples we calculate the time-variant channel transfer function $H'[m', q]$ by a discrete Fourier transform (DFT). This transforms the channel convolution into a multiplication in the frequency domain. Here $m'$ denotes the symbol time

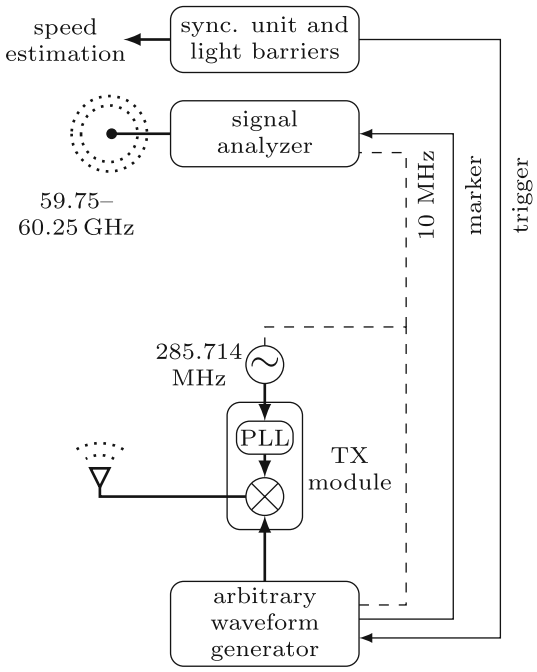


**FIGURE 14.** Measurement setup.

index and $q = 0, \ldots, 102$ the frequency index. After coherent averaging over $N$ baseband symbols, we divide the resulting channel transfer function by the calibration function, obtained from back-to-back measurements, to equalize the frequency characteristics of our equipment.

### EXCITATION SIGNAL

The excitation signal generated by the AWG is a multi-tone waveform. The use of a multi-tone waveform affords us several advantages such as i) ideally flat frequency spectrum, ii) design flexibility, iii) controllable crest factor, and iv) high SNR through processing gain. These advantages are important for channel transfer function extraction. Using an approach similar to a procedure implemented in [57], the excitation signal is given by $x(n) = \mathrm{Re}\left(\sum_{k=1}^{K/2} e^{j\pi \frac{k^2}{K}} e^{-j2\pi k \frac{n}{Q}}\right)$, where $n = 0, \ldots, Q-1$ is the time index and $k$ the sub-carrier index. To minimize the crest factor of the signal, the tone phases are chosen quadratic. The crest factor is reduced in order to maximize the average transmitted power while ensuring that all RF components encountered by the excitation signals operate in their linear regions.

For the geometry of our scenario, the excess length (w.r.t. LOS length) of the MPC resulting from an overtaking car is on the order of 15 m. Ignoring multiple reflections between the parked RX car and the overtaking car, we assume that the path length difference will never be larger than 30 m. Thus, 100 ns is our maximum excess delay. To make the symbols shorter and less susceptible to inter-carrier interference caused by phase noise and Doppler, we choose the sub-carrier spacing $\Delta f$ as large as possible. To still obey the sampling theorem in the frequency domain, we need to fulfil $\Delta f \leq$

$(1/(2\tau_{\max})) = 5\,\text{MHz}$, where $\tau_{\max}$ is the maximum excess delay. With our sampling rate of 600 MSamples/s this gives $Q = 121$ sub-carriers spaced by $\Delta f = 600\,\text{MHz}/121 = 4.96\,\text{MHz}$. Due to the sharp (anti-aliasing) filter of the SA, from the $Q = 121$ sub-carriers we effectively utilize only $K = 103$ sub-carriers, which is equal to a measurement bandwidth BW $\approx 510\,\text{MHz}$. With these parameters the delay resolution of the channel sounder is $\tau_{\min} = 1/\text{BW} \approx 1.96\,\text{ns}$. The receiver sensitivity is approximated to $P_{\text{RX,min}} = P_{\text{SA,min}} + 10\log_{10}(\Delta f) + 10\log_{10} K = -63\,\text{dBm}$.

### *LINK BUDGET AND OTHER LIMITATIONS*

For the LOS component, the propagation loss including antenna gains sums up to $P_{\text{L}} = 75.5\,\text{dB}$. For the design of our setup, we assume that reflected paths are $P_{\text{R}} = 10\,\text{dB}$ weaker than the LOS component. Next, we require an SNR at each sub-carrier of the reflected component of $\text{SNR}_{\text{refl}} = 10\,\text{dB}$. These requirements directly translate to the necessary transmit power $P_{\text{TX,min}} = P_{\text{RX,min}} + P_{\text{L}} + P_{\text{R}} + \text{SNR}_{\text{refl}} = 32.5\,\text{dBm}$. The maximum power of the TX module is 7 dBm. Thus, an additional processing gain of 25.5 dB is needed. The processing gain is realized by coherently averaging over $N = \{480, 560, 640\}$ multi-tone symbols. The number of averaging symbols is chosen such that the averaged channel is still aliasing free. The least processing gain for fast vehicles ($N = 480$) is 27 dB. Remember, our multi-tone system has a sub-carrier spacing of $\Delta f = 4.96\,\text{MHz}$ and a sounding sequence length of $\tau_{\text{sym}} = 1/\Delta f = 202\,\text{ns}$. The overall pulse length including 480 repetitions, sums up to $T_{\text{snap}} = 96.8\,\mu\text{s}$. Applying the sampling theorem for the Doppler support, we obtain a maximum alias-free Doppler frequency of $\nu_{\max} = 1/(2T_{\text{snap}}) = 5.2\,\text{kHz}$, which limits the speed of overtaking cars to $v_{\text{car}} = (\lambda\nu_{\max})/2 = 12.9\,\text{m/s} = 46.5\,\text{km/h}$ . This value is sufficient for our measurements, as the street, were the measurements took place, has a speed limit of 30 km/h. Our receiver is limited to a memory depth of approximately 420 MSamples or equivalently, with a sampling rate of 600 MSamples/s, we are recording $T_{\text{rec}} = 720\,\text{ms}$ of the channel evolution. At 12.9 m/s this equals a driving distance of 9.29 m. An overview of the channel sounder parameters is given in Table 1.

**TABLE 1. Channel sounder parameters.**

| Parameter | Value |
|---|---|
| transmit antenna | 20 dBi conical horn |
| transmit antenna heights | 70, 110, 146, 156 cm |
| receive antenna | $\lambda/4$ monopole |
| receive antenna height | 156 cm |
| transmit power | $P_{\text{TX}} = 7\,\text{dBm}$ |
| receiver sensitivity | $P_{\text{RX,min}} = -63\,\text{dBm}$ |
| sub-carrier spacing | $\Delta f = 4.96\,\text{MHz}$ |
| number of sub-carriers | $K = 103$ |
| center frequency | $f_0 = 59.99994\,\text{GHz}$ |
| maximum alias free delay | $\tau_{\max} = 100.83\,\text{ns}$ |
| delay resolution | $\Delta\tau = 1.96\,\text{ns}$ |
| recording time | $T_{\text{rec}} = 720\,\text{ms}$ |
| snapshot rate | $T_{\text{snap}} = \begin{cases} 129.1\,\mu\text{s}, & \text{if } N = 640 \\ 112.9\,\mu\text{s}, & \text{if } N = 560 \\ 96.8\,\mu\text{s}, & \text{if } N = 480 \end{cases}$ |
| maximum car speed | $v_{\text{car}} = \begin{cases} 9.68\,\text{m/s}, & \text{if } N = 640 \\ 11.06\,\text{m/s}, & \text{if } N = 560 \\ 12.91\,\text{m/s}, & \text{if } N = 480 \end{cases}$ |
| maximum recording distance | $d_{\max} = 9.29\,\text{m}$ |

## APPENDIX C: THE TRANSITION OF TWDP FADING TO RICIAN FADING

To study the TWDP to Rice distribution transition, we first express the $\Delta$-parameter, defined in (12) through amplitudes, via the power ratio

$$\delta P = \frac{V_2^2}{V_1^2}, \quad V_2 \le V_1 \Rightarrow \delta P \le 1. \tag{21}$$

Equation (12) becomes now

$$\Delta(\delta P) = \frac{2\sqrt{\delta P}}{1+\delta P} \tag{22}$$

The expression (22) is demonstrated in Fig. 15 with $\delta P$ plotted in decibels.

For $\delta P < -20\,\text{dB}$ even an exponential power decrease is barely translated to different $\Delta$ values.

For $\Delta \to 0$, depending on the $K$-factor, the second much weaker component might be no longer large enough to change the distribution sufficiently from the Rician distribution. Mathematically this is expressed through the variance of the diffuse components. Given that $\Omega \equiv 1$, $\sigma$ solely depends on the $K$-factor [58]

$$\sigma^2 = \frac{1}{2(1+K)}. \tag{23}$$

For $K \gg 0$, the power of the diffuse components (in decibels) is

$$20\log_{10}\sigma \approx -10\log_{10} K - 3\,\text{dB}. \tag{24}$$

Hence, TWDP fading differs from Rician fading only if $10\log_{10}\delta P \gg -10\log_{10} K - 3\,\text{dB}$, otherwise the second non-fluctuating component appears as strong as the diffuse components.

This behavior directly translates to the model selection algorithm. To demonstrate this, we run Monte Carlo simulations with synthetic data. Our test data is generated equivalently to the search grid used for MLE. The $K$-factor is linearly spaced in $\{0, 1, \ldots, 100\}$ and logarithmically spaced with 150 points for each decade above $K = 100$. The $\Delta$-parameter is linearly spaced in $\{0, 0.1, \ldots, 1\}$. We generate 300 realizations of each pair $(K, \Delta)$ and perform the fitting and selection approach of subsection IV-C. A success is defined whenever AIC decides correctly for the TWDP model. The success rate of TWDP selection is plotted in Fig. 16. We plotted on top (as red dashed line) the relationship (22). From the considerations above, we already know that the $K$-factor must be at least above 3 dB. Observe that the transition region matches fairly well with those values, where the power of the second non-fluctuating component

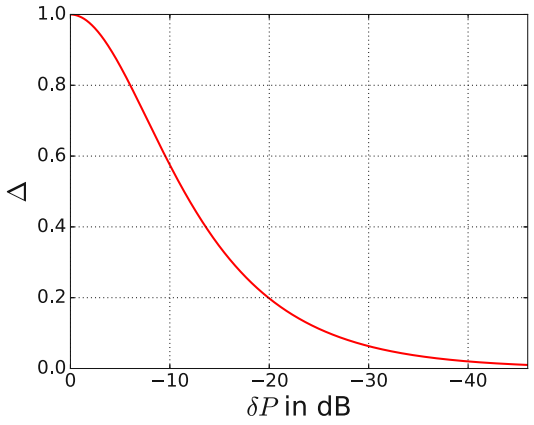


**FIGURE 15.** The Δ-parameter as a function of the power ratio $\delta P$ of both non-fluctuating waves.

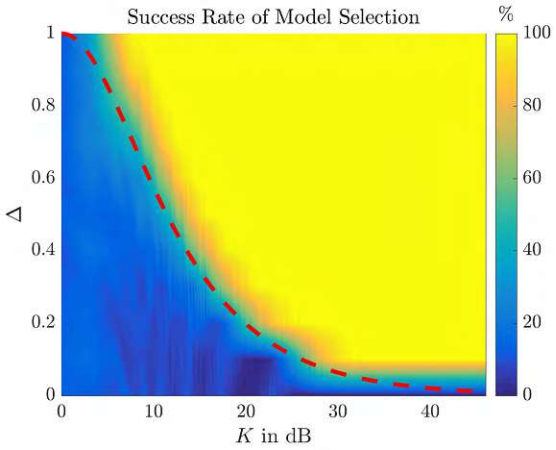


**FIGURE 16.** Success rate of selecting TWDP fading for all parameter tuples $(K, \Delta)$ of the grid search space. Whenever the second non-fluctuating component is in the order of the diffuse components, the AIC model selection fails. The red dashed line replaces $\delta P$ of (22) with $(1/K)$ to show this border.

becomes as strong at the diffuse components. However, there is a minimum $\Delta \approx 0.1$ where TWDP fading selection fails even for $K \to \infty$. From Fig. 15 we read that this value corresponds to a power difference of the LOS component and the reflected component of approximately 25 dB. With the proposed approach we are hence not capable of selecting the appropriate fading distribution for smaller, weak-reflecting vehicles. The found Δ-parameter for the statistical analysis in Subsection IV-D is therefore biased towards lower values.

## APPENDIX D: RMS DOPPLER SPREAD OF KNOWN DISTRIBUTIONS

In this appendix, we derive the normalized RMS Doppler spread values $\sigma_\nu$ for known Doppler distributions. This yields a reference for our statistical analysis.

### UNIFORM DISTRIBUTION (- LEFT SIDE)

Based on 3D uniform scattering the Doppler spectrum becomes a symmetric uniform distribution. This is simply the left half of it. Hence, the Doppler is uniformly distributed within $(-\nu_{\max}, 0)$.

$$\sigma_\nu^2 = \int_{-\nu_{\max}}^{0} \frac{1}{\nu_{\max}} \nu^2 \mathrm{d}\nu - \bar{\nu}^2 = \frac{\nu_{\max}^2}{12} \tag{25}$$

$$\boxed{\frac{\sigma_\nu}{\nu_{\max}} = \frac{1}{\sqrt{12}} = \frac{1}{2\sqrt{3}} \approx 0.2887} \tag{26}$$

### JAKES' SPECTRUM

This assumes that the angle of arrival is uniformly distributed (in a plane). Through the non-linear cosine relationship between the angle of arrival and the Doppler shift, the Doppler spectrum becomes the "double horn"

$$P(\nu) = \frac{1}{\pi \sqrt{\nu_{\max}^2 - \nu^2}}. \tag{27}$$

The RMS Doppler spread is

$$\sigma_\nu^2 = \frac{1}{\pi \nu_{\max}} \int_{-\nu_{\max}}^{\nu_{\max}} \frac{1}{\sqrt{1 - \left(\frac{\nu}{\nu_{\max}}\right)^2}} \nu^2 \mathrm{d}\nu = \frac{\nu_{\max}^2}{2}. \tag{28}$$

$$\boxed{\frac{\sigma_\nu}{\nu_{\max}} = \frac{1}{\sqrt{2}} \approx 0.7071} \tag{29}$$

### HALF JAKES' (- LEFT SIDE)

The half Jakes' distribution sets all positive Doppler shift to zero. Here, we re-use the result from above. We only need to calculate the mean of a half Jakes' distribution.

$$\bar{\nu} = \frac{1}{\pi \nu_{\max}} \int_{-\nu_{\max}}^{\nu_{\max}} \frac{1}{\sqrt{1 - \left(\frac{\nu}{\nu_{\max}}\right)^2}} \nu \mathrm{d}\nu = -\frac{\nu_{\max}}{\pi} \tag{30}$$

Reusing the result from above, the 2nd moment of the half-Jakes is $\frac{\nu_{\max}^2}{2} \cdot \frac{1}{2}$. Hence,

$$\sigma_\nu^2 = \frac{\nu_{\max}^2}{4} - \bar{\nu}^2 = \nu_{\max}^2 \frac{\pi^2 - 2^2}{(2\pi)^2} \tag{31}$$

$$\boxed{\frac{\sigma_\nu}{\nu_{\max}} = \sqrt{\frac{\pi^2 - 2^2}{(2\pi)^2}} \approx 0.3856} \tag{32}$$

## ACKNOWLEDGMENT

This paper was presented at the Proceedings of the 12th European Conference on Antennas and Propagation, 2018 [1] and at the Proceedings of IEEE-APS Topical Conference on Antennas and Propagation in Wireless Communications, 2018 [2].

## REFERENCES


[1] E. Zöchmann *et al.*, "Measured delay and Doppler profiles of overtaking vehicles at 60 GHz," in *Proc. 12th Eur. Conf. Antennas Propag. (EuCAP)*, 2018, pp. 1–5.

[2] E. Zöchmann *et al.*, "Statistical evaluation of delay and Doppler spread in 60 GHz vehicle-to-vehicle channels during overtaking," in *Proc. IEEE-APS Top. Conf. Antennas Propag. Wireless Commun. (APWC)*, Sep. 2018, pp. 1–4.

[3] T. Tokumitsu, M. Kubota, K. Sakai, and T. Kawai, "Application of GaAs device technology to millimeter-waves," *SEI Tech. Rev.*, no. 79, pp. 57–65, Oct. 2014.

[4] J. Choi, V. Va, N. González-Prelcic, R. Daniels, C. R. Bhat, and R. W. Heath, Jr., "Millimeter-wave vehicular communication to support massive automotive sensing," *IEEE Commun. Mag.*, vol. 54, no. 12, pp. 160–167, Dec. 2016.

[5] V. Va, J. Choi, and R. W. Heath, Jr., "The impact of beamwidth on temporal channel variation in vehicular channels and its implications," *IEEE Trans. Veh. Technol.*, vol. 66, no. 6, pp. 5014–5029, Jun. 2017.

[6] J. Lorca, M. Hunukumbure, and Y. Wang, "On overcoming the impact of Doppler spectrum in millimeter-wave V2I communications," in *Proc. IEEE Globecom Workshops (GC Wkshps)*, Dec. 2017, pp. 1–6.

[7] P. L. C. Cheong, "Multipath component estimation for indoor radio channels," in *Proc. IEEE Global Telecommun. Conf. (GLOBECOM)*, vol. 2, Nov. 1996, pp. 1177–1181.

[8] F. J. Velez, L. M. Correia, and J. M. Brázio, "Frequency reuse and system capacity in mobile broadband systems: Comparison between the 40 and 60 GHz bands," *Wireless Pers. Commun.*, vol. 19, no. 1, pp. 1–24, 2001.

[9] A. G. Siamarou, "Wideband propagation measurements and channel implications for indoor broadband wireless local area networks at the 60 GHz band," *Wireless Pers. Commun.*, vol. 27, no. 1, pp. 89–98, 2003.

[10] C. R. Anderson and T. S. Rappaport, "In-building wideband partition loss measurements at 2.5 and 60 GHz," *IEEE Trans. Wireless Commun.*, vol. 3, no. 3, pp. 922–928, May 2004.

[11] F. J. Velez, M. Dinis, and J. Fernandes, "Mobile broadband systems: Research and visions," *IEEE Veh. Technol. Soc. News*, vol. 52, no. 2, pp. 4–12, May 2005.

[12] N. Moraitis and P. Constantinou, "Measurements and characterization of wideband indoor radio channel at 60 GHz," *IEEE Trans. Wireless Commun.*, vol. 5, no. 4, pp. 880–889, Apr. 2006.

[13] S. Ranvier, J. Kivinen, and P. Vainikainen, "Millimeter-wave MIMO radio channel sounder," *IEEE Trans. Instrum. Meas.*, vol. 56, no. 3, pp. 1018–1024, Jun. 2007.

[14] S. Geng, J. Kivinen, X. Zhao, and P. Vainikainen, "Millimeter-wave propagation channel characterization for short-range wireless communications," *IEEE Trans. Veh. Technol.*, vol. 58, no. 1, pp. 3–13, Jan. 2009.

[15] P. F. M. Smulders, "Statistical characterization of 60-GHz indoor radio channels," *IEEE Trans. Antennas Propag.*, vol. 57, no. 10, pp. 2820–2829, Oct. 2009.

[16] K. Haneda, C. Gustafson, and S. Wyne, "60 GHz spatial radio transmission: Multiplexing or beamforming?" *IEEE Trans. Antennas Propag.*, vol. 61, no. 11, pp. 5735–5743, Nov. 2013.

[17] C. Gustafson, K. Haneda, S. Wyne, and F. Tufvesson, "On mm-wave multipath clustering and channel modeling," *IEEE Trans. Antennas Propag.*, vol. 62, no. 3, pp. 1445–1455, Mar. 2014.

[18] S. Salous, S. M. Feeney, X. Raimundo, and A. A. Cheema, "Wideband MIMO channel sounder for radio measurements in the 60 GHz band," *IEEE Trans. Wireless Commun.*, vol. 15, no. 4, pp. 2825–2832, Apr. 2016.

[19] J. Lee, J. Liang, M.-D. Kim, J.-J. Park, B. Park, and H. K. Chung, "Measurement-based propagation channel characteristics for millimeter-wave 5G Giga communication systems," *Electron. Telecommun. Res. Inst. J.*, vol. 38, no. 6, pp. 1031–1041, 2016.

[20] J. Vehmas, J. Jarvelainen, S. Le Hong Nguyen, R. Naderpour, and K. Haneda, "Millimeter-wave channel characterization at Helsinki airport in the 15, 28, and 60 GHz bands," in *Proc. IEEE 84th Veh. Technol. Conf. (VTC-Fall)*, Sep. 2016, pp. 1–5.

[21] E. Zöchmann, M. Lerch, S. Caban, R. Langwieser, C. F. Mecklenbräuker, and M. Rupp, "Directional evaluation of receive power, Rician K-factor and RMS delay spread obtained from power measurements of 60 GHz indoor channels," in *Proc. IEEE-APS Top. Conf. Antennas Propag. Wireless Commun. (APWC)*, Sep. 2016, pp. 246–249.

[22] G. R. MacCartney and T. S. Rappaport, "A flexible millimeter-wave channel sounder with absolute timing," *IEEE J. Sel. Areas Commun.*, vol. 35, no. 6, pp. 1402–1418, Jun. 2017.

[23] J. Ko *et al.*, "Millimeter-wave channel measurements and analysis for statistical spatial channel model in in-building and urban environments at 28 GHz," *IEEE Trans. Wireless Commun.*, vol. 16, no. 9, pp. 5853–5868, Sep. 2017.

[24] D. Dupleich *et al.*, "Influence of system aspects on fading at mm-waves," *IET Microw., Antennas Propag.*, vol. 12, no. 4, pp. 516–524, 2018.

[25] F. Fuschini *et al.*, "Analysis of in-room mm-Wave propagation: Directional channel measurements and ray tracing simulations," *J. Infr., Millim., Terahertz Waves*, vol. 38, no. 6, pp. 727–744, 2017.

[26] X. Wu *et al.*, "60-GHz millimeter-wave channel measurements and modeling for indoor office environments," *IEEE Trans. Antennas Propag.*, vol. 65, no. 4, pp. 1912–1924, Apr. 2017.

[27] B. Ai *et al.*, "On indoor millimeter wave massive MIMO channels: Measurement and simulation," *IEEE J. Sel. Areas Commun.*, vol. 35, no. 7, pp. 1678–1690, Jul. 2017.

[28] E. Zöchmann, M. Lerch, S. Pratschner, R. Nissel, S. Caban, and M. Rupp, "Associating spatial information to directional millimeter wave channel measurements," in *Proc. IEEE 86th Veh. Technol. Conf. (VTC-Fall)*, Sep. 2017, pp. 1–5.

[29] J. Blumenstein *et al.*, "In-vehicle channel measurement, characterization, and spatial consistency comparison of 30–11 GHz and 55–65 GHz frequency bands," *IEEE Trans. Veh. Technol.*, vol. 66, no. 5, pp. 3526–3537, May 2017.

[30] A. Chandra *et al.*, "Frequency-domain in-vehicle UWB channel modeling," *IEEE Trans. Veh. Technol.*, vol. 65, no. 6, pp. 3929–3940, Jun. 2016.

[31] P. B. Papazian, C. Gentile, K. A. Remley, and N. Golmie, "A radio channel sounder for mobile millimeter-wave communications: System implementation and measurement assessment," *IEEE Trans. Microw. Theory Techn.*, vol. 64, no. 9, pp. 2924–2932, Sep. 2016.

[32] E. Zöchmann, S. Caban, M. Lerch, and M. Rupp, "Resolving the angular profile of 60 GHz wireless channels by delay-Doppler measurements," in *Proc. IEEE Sensor Array Multichannel Signal Process. Workshop (SAM)*, Jul. 2016, pp. 1–5.

[33] C. U. Bas *et al.* (2018). "Real-time Millimeter-Wave MIMO channel sounder for dynamic directional measurements." [Online]. Available: https://arxiv.org/abs/1807.11921

[34] C. U. Bas *et al.*, "Dynamic double directional propagation channel measurements at 28 GHz—Invited paper," in *Proc. IEEE 87th Veh. Technol. Conf. (VTC Spring)*, Jun. 2018, pp. 1–6.

[35] H. Meinel and A. Plattner, "Millimetre-wave propagation along railway lines," *IEE Proc. F Commun., Radar Signal Process.*, vol. 130, no. 7, pp. 688–694, Dec. 1983.

[36] A. Kato, K. Sato, M. Fujise, and S. Kawakami, "Propagation characteristics of 60-GHz millimeter waves for ITS inter-vehicle communications," *IEICE Trans. Commun.*, vol. 84, no. 9, pp. 2530–2539, 2001.

[37] S. Takahashi, A. Kato, K. Sato, and M. Fujise, "Distance dependence of path loss for millimeter wave inter-vehicle communications," *Radioengineering*, vol. 13, no. 4, pp. 8–13, 2004.

[38] A. Yamamoto, K. Ogawa, T. Horimatsu, A. Kato, and M. Fujise, "Path-loss prediction models for intervehicle communication at 60 GHz," *IEEE Trans. Veh. Technol.*, vol. 57, no. 1, pp. 65–78, Jan. 2008.

[39] T. S. Rappaport, J. N. Murdock, and F. Gutierrez, Jr., "State of the art in 60-GHz integrated circuits and systems for wireless communications," *Proc. IEEE*, vol. 99, no. 8, pp. 1390–1436, Aug. 2011.

[40] V. Va, T. Shimizu, G. Bansal, and R. W. Heath, Jr., "Millimeter wave vehicular communications: A survey," *Found. Trends Netw.*, vol. 10, no. 1, pp. 1–113, Jun. 2016.

[41] P. Kumari, J. Choi, N. González-Prelcic, and R. W. Heath, Jr., "IEEE 802.11ad-based radar: An approach to joint vehicular communication-radar system," *IEEE Trans. Veh. Technol.*, vol. 67, no. 4, pp. 3012–3027, Apr. 2018.

[42] M. G. Sánchez, M. P. Táboas, and E. L. Cid, "Millimeter wave radio channel characterization for 5G vehicle-to-vehicle communications," *Measurement*, vol. 95, pp. 223–229, Jan. 2017.

[43] H. Wang, X. Yin, X. Cai, H. Wang, Z. Yu, and J. Lee, "Fading characterization of 73 GHz millimeter-wave V2V channel based on real measurements," in *Proc. 13th Int. Workshop Commun. Technol. Vehicles, Nets4Cars/Nets4Trains/Nets4Aircraft*, Madrid, Spain, May 2018, pp. 159–168.

[44] A. Prokes, J. Vychodil, M. Pospisil, J. Blumenstein, T. Mikulasek, and A. Chandra, "Time-domain nonstationary intra-car channel measurement in 60 GHz band," in *Proc. Int. Conf. Adv. Technol. Commun. (ATC)*, 2016, pp. 1–6.

[45] J. Blumenstein, A. Prokes, J. Vychodil, M. Pospisil, and T. Mikulasek, "Time-varying K factor of the mm-Wave vehicular channel: Velocity, vibrations and the road quality influence," in *Proc. IEEE 28th Annu. Int. Symp. Pers., Indoor, Mobile Radio Commun. (PIMRC)*, Oct. 2017, pp. 1–5.
[46] A. Loch, A. Asadi, G. H. Sim, J. Widmer, and M. Hollick, "mm-Wave on wheels: Practical 60 GHz vehicular communication without beam training," in *Proc. 9th Int. Conf. Commun. Syst. Netw. (COMSNETS)*, 2017, pp. 1–8.
[47] L. Bernadó, T. Zemen, F. Tufvesson, A. F. Molisch, and C. F. Mecklenbräuker, "Time-and frequency-varying *K*-factor of non-stationary vehicular channels for safety-relevant scenarios," *IEEE Trans. Intell. Transp. Syst.*, vol. 16, no. 2, pp. 1007–1017, Apr. 2015.
[48] R. Ramanathan, J. Redi, C. Santivanez, D. Wiggins, and S. Polit, "Ad hoc networking with directional antennas: A complete system solution," *IEEE J. Sel. Areas Commun.*, vol. 23, no. 3, pp. 496–506, Mar. 2005.
[49] E. S. Sousa, V. M. Jovanovic, and C. Daigneault, "Delay spread measurements for the digital cellular channel in Toronto," *IEEE Trans. Veh. Technol.*, vol. 43, no. 4, pp. 837–847, Nov. 1994.
[50] F. F. Kuo and J. F. Kaiser, *System Analysis By Digital Computer*. New York, NY, USA: Wiley, 1966.
[51] G. D. Durgin, T. S. Rappaport, and D. A. de Wolf, "New analytical models and probability density functions for fading in wireless communications," *IEEE Trans. Commun.*, vol. 50, no. 6, pp. 1005–1015, Jun. 2002.
[52] M. Rao, F. J. Lopez-Martinez, M.-S. Alouini, and A. Goldsmith, "MGF approach to the analysis of generalized two-ray fading models," *IEEE Trans. Wireless Commun.*, vol. 14, no. 5, pp. 2548–2561, May 2015.
[53] K. P. Burnham and D. R. Anderson, *Model Selection and Multimodel Inference: A Practical Information-Theoretic Approach*. New York, NY, USA: Springer, 2003.
[54] L. Bernadó, T. Zemen, F. Tufvesson, A. F. Molisch, and C. F. Mecklenbräuker, "Delay and Doppler spreads of nonstationary vehicular channels for safety-relevant scenarios," *IEEE Trans. Veh. Technol.*, vol. 63, no. 1, pp. 82–93, Jan. 2014.
[55] D. J. Thomson, "Spectrum estimation and harmonic analysis," *Proc. IEEE*, vol. 70, no. 9, pp. 1055–1096, Sep. 1982.
[56] D. Slepian, "Prolate spheroidal wave functions, Fourier analysis, and uncertainty—V: The discrete case," *Bell Syst. Tech. J.*, vol. 57, no. 5, pp. 1371–1430, May/Jun. 1978.
[57] S. Sangodoyin, J. Salmi, S. Niranjayan, and A. F. Molisch, "Real-time ultrawideband MIMO channel sounding," in *Proc. 6th Eur. Conf. Antennas Propag. (EUCAP)*, 2012, pp. 2303–2307.
[58] D. Kim, H. Lee, and J. Kang, "Comments on "Near-body shadowing analysis at 60 GHz,""*IEEE Trans. Antennas Propag.*, vol. 65, no. 6, p. 3314, Jun. 2017.

**ERICH ZÖCHMANN** (M'18) received the B.Sc. and Dipl.Ing. (M.Sc.) degrees (Hons.) in electrical engineering from TU Wien, in 2013 and 2015, respectively. From 2013 to 2015, he was a Project Assistant with the Institute of Telecommunications, where he co-developed the Vienna LTE-A uplink link level simulator and conducted research on physical layer signal processing for 4G mobile communication systems. From 2017 to 2018, he was a Visiting Scholar with The University of Texas at Austin. His current interests include experimental characterization and modeling of millimeter-wave propagation, physical layer signal processing, array signal processing, compressed sensing, and convex optimization.

**MARKUS HOFER** received the Dipl.Ing. degree (Hons.) in telecommunications from TU Wien, in 2013. He is currently pursuing the Ph.D. degree in telecommunications. From 2013 to 2015, he was a Researcher with the Telecommunications Research Center Vienna (FTW), Signal and Information Processing Department. Since 2015, he has been a Junior Scientist with the Research Group for Ultra-Reliable Wireless Machine-to-Machine Communications, AIT Austrian Institute of Technology. His research interests include low-latency wireless communications, vehicular channel measurements, modeling and emulation, time-variant channel estimation, mmwave, massive MIMO, cooperative communication systems, and interference management.

**MARTIN LERCH** received the master's degree in electrical engineering from TU Wien, where he is currently with the Institute of Telecommunications, developing test beds and measurement methodologies for controlled and reproducible wireless experiments at high velocities.

**STEFAN PRATSCHNER** was born in Vienna, Austria, in 1990. He received the B.Sc. degree in electrical engineering and the M.Sc. degree (Hons.) in telecommunications from TU Wien, in 2014 and 2016, respectively, where he is currently pursuing the Ph.D. degree with a main focus on massive MIMO technologies for mobile communications. Since 2013, he has been a Project Assistant with the Institute of Telecommunications, TU Wien.

**LAURA BERNADÓ** received the M.Sc. degree in telecommunications engineering from the Technical University of Catalonia (UPC), Spain, in 2007, and the Ph.D. degree from TU Wien, in 2012. She is currently a Scientist with the Austrian Institute of Technology. Her research interests include the characterization and modeling of fast time-varying and non-stationary fading processes for ultra-reliable and low-latency communications for future radio communication systems.

**JIRI BLUMENSTEIN** (M'17) received the Ph.D. degree from the Brno University of Technology, in 2013. In 2011, he was a Researcher with the Institute of Telecommunications, TU Wien. He has cooperated with several companies, including Racom, Volkswagen, and ON Semiconductor in the area of applied research of wireless systems and in the area of the fundamental research funded by the Czech Science Foundation. He is currently a Researcher with the Department of Radio Electronics, Brno University of Technology. His research interests include signal processing, physical layer of communication systems, channel characterization and modeling, and wireless system design.

**SEBASTIAN CABAN** received the master's degree in business administration from the University of Vienna, Vienna, Austria, and the master's and Ph.D. degrees in telecommunications from TU Wien. His current research interest includes measurements in wireless communications.

**SEUN SANGODOYIN** received the B.Sc. degree in electrical engineering from Oklahoma State University, in 2007, and the M.Sc. and Ph.D. degrees in electrical engineering from the University of Southern California, in 2009 and 2018, respectively. He is currently a Postdoctoral Research Fellow with the Georgia Institute of Technology. His research interests include millimeter-wave (measurement-based) MIMO channel modeling and analysis, terahertz communications, UWB MIMO radar, parameter estimation, body area networks, and stochastic dynamical systems.

**HERBERT GROLL** received the B.Sc. and Dipl.Ing. (M.Sc.) degrees in electrical engineering from TU Wien, in 2014 and 2017, respectively, where he is currently pursuing the Ph.D. degree, under the supervision of Prof. C. Mecklenbräuker. His research interest includes vehicular wireless communication with an emphasis on millimeter-wave propagation for future wireless systems.

**THOMAS ZEMEN** was with FTW Forschungszentrum Telekommunikation Wien, Austria, and Siemens, Austria. He is currently a Senior Scientist with the AIT Austrian Institute of Technology, where he is also leading the Reliable Wireless Communications Group. He is also an External Lecturer with TU Wien. He has authored four books chapters, 37 journal papers, more than 110 conference communications, as well as two patents. His research interests include wireless ultra-reliable low-latency communications, massive MIMO systems, time-variant channel measurements, modeling and real-time emulation, as well as software-defined radio rapid prototyping. He has served as an Editor for the IEEE Transactions on Wireless Communications, from 2011 to 2017.

**ALEŠ PROKEŠ** received the M.Sc., Ph.D., and the Habilitation degrees from the Brno University of Technology (BUT), in 1988, 1999, and 2006, respectively. Since 1990, he has been with the Faculty of Electrical Engineering and Communication, BUT, where he is currently a Professor. Since 2013, he has been the Head of the Research Center of Sensor, Information and Communication Systems, Radio-Frequency Systems Group. He has (co)authored 30 journal publications and more than 40 conference papers. His research interests include measurement and modeling of channels for V2X communication, optimization, and design of optical receivers and transmitters for free-space optics (FSO) systems, influence of atmospheric effects on optical signal propagation, evaluation of FSO availability and reliability, higher order non-uniform sampling and signal reconstruction, and software-defined radio.

**MARKUS RUPP** received the Dipl.Ing. degree from the University of Saarbrücken, Germany, in 1988, and the Dr.Ing. degree from the Technische Universität Darmstadt, Germany, in 1993. Until 1995, he held a Postdoctoral position with the University of California at Santa Barbara, Santa Barbara, CA, USA. From 1995 to 2001, he was with the Wireless Technology Research Department, Nokia Bell Labs, Holmdel, NJ, USA. Since 2001, he has been a Full Professor of digital signal processing in mobile communications with TU Wien.

**ANDREAS F. MOLISCH** was with TU Vienna, AT&T (Bell) Labs, Lund University, and Mitsubishi Electric Research Labs. He is currently the Solomon Golomb - Andrew and Erna Viterbi Chair Professor with the University of Southern California. He is the author of four books, 19 book chapters, more than 240 journal papers, 320 conference papers, as well as 80 patents. His research interests include wireless communications, with an emphasis on wireless propagation channels, multi-antenna systems, ultrawideband signaling and localization, novel modulation methods, and caching for wireless content distribution. He is a Fellow of the National Academy of Inventors, the IEEE, AAAS, and IET, as well as a member of the Austrian Academy of Sciences. He was a recipient of numerous awards.

**CHRISTOPH F. MECKLENBRÄUKER** (S'88–M'97–SM'08) received the Dipl.Ing. degree (Hons.) in electrical engineering from TU Wien, in 1992, and the Dr.Ing. degree (Hons.) from the Ruhr-Universität Bochum, Bochum, Germany, in 1998. From 1997 to 2000, he was with Siemens AG, Austria, where he was engaged in the standardization of the radio access network for UMTS. From 2000 to 2006, he was a Senior Research with the Telecommunications Research Center Vienna (FTW), Vienna. In 2006, he joined the Institute of Communications and Radio Frequency Engineering, TU Wien, as a Full Professor. From 2009 to 2016, he led the Christian Doppler Laboratory for Wireless Technologies for Sustainable Mobility. He has authored approximately 250 papers in international journals and conferences, for which he has also served as a reviewer. He holds several patents in the field of mobile cellular networks. His current research interests include radio interfaces for peer-to-peer networks (vehicular connectivity and sensor networks), ultra-wideband radio, and MIMO transceivers. He is a member of the Antennas and Propagation Society, the Intelligent Transportation Society, the Vehicular Technology Society, the Signal Processing society, VDE, and EURASIP. He is the Councilor of the IEEE Student Branch Wien. His doctoral dissertation received the Gert-Massenberg Prize, in 1998.